Modelling quantum dynamics in molecular photoswitches

Luke Daniel Smith

University of Leeds

School of Chemistry

Submitted in accordance with the requirements for the degree of

Doctor of Philosophy

October 2021

For my father, who only saw the beginning of my academic journey.

Intellectual Property Statement

The candidate confirms that the work submitted is his own, except where work which has formed part of jointly authored publications has been included. The contribution of the candidate and the other authors to this work has been explicitly indicated below. The candidate confirms that appropriate credit has been given within the thesis where reference has been made to the work of others.

Work in Chapter 4 and 5 has appeared in publication as follows: The Journal of Chemical Physics, 2019, Volume 151, Page 164109, by L. D. Smith and A. G. Dijkstra. The candidate was responsible for the theoretical work, writing the program, generating results through simulations, and writing the manuscript, producing all figures and tables. The contribution of A. G. Dijkstra was to discuss results, supervise work, and suggest edits to the manuscript.

Acknowledgements

There are several people who I want to thank in helping me throughout my PhD, and guiding me to become the researcher I am today. First and foremost, I have had the pleasure of working with and learning from two excellent supervisors Arend Dijkstra and Dmitry Shalashilin. Their guidance and experience allowed me to explore interconnections in interdisciplinary topics and develop the skills in communicating to diverse audiences. I will be forever grateful for their advice, expertise, and time dedicated to me.

During my PhD I have had the pleasure of collaborating with excellent researchers and colleagues Animesh Datta, George Knee, and Max Marcus at the University of Warwick. I would also like to thank James Green, Dale Green, Dominic Branford, Yoshitaka Tanimura, Garth Jones, and all of my office colleagues for interesting discussions that helped me to develop my understanding of complex quantum systems and other intriguing fields of research.

I am thankful to my parents who instilled in me a sense of wonder about the beauty of the world around me and how to creatively interpret it. I also thank my brother Jordan Douglas-Banks who helped to nurture and refine this into a passion for science and research.

I am grateful to Javed Singh, who shared and encouraged my appreciation for the intricacies of mathematics and its ability to describe the universe, and Sue Grimsey who always believed in my capabilities.

Thank you to my extended family and friends for bringing me joy and to Tom Simons, Mark Skelton, and Robert Wardrop for their continued friendship through my PhD which allowed me to broaden my interests and preserve my sanity.

Lastly, my heartfelt thanks to Emma Ramsey for her love and support which provided me with a solid foundation to pursue my academic passions, helping me to celebrate my accomplishments, and to persevere through challenging times.

Abstract

Quantum dynamics and effects in complex systems is an increasingly important area of research with wide impact to several areas of physics, chemistry, and biology. Progress in this field promises the advancement of our understanding of the fundamental behaviour of nature, and crucial developments for future technologies. Molecular photoswitches present a key example with applications to medicine, molecular motors and machines, and understanding the first stages of vision. Significant challenges arise in the modelling of these complex quantum systems due to the need to account for several degrees of freedom in combination with quantum effects. Furthermore, such systems constitute a difficult regime of quantum dynamics far from equilibrium that necessitates an anharmonic description. This thesis addresses the challenge with the development of efficient quantum stochastic methods. As a result, a method is produced capable of simulating quantum dynamics on several anharmonic surfaces in contact with an environment.

Firstly, model systems that go beyond the standard harmonic approximation are used to investigate molecular photoswitch potentials, and tools are identified to predict potential energy surface curvature and assist in the interpretation of linear absorption spectroscopy.

Secondly, a stochastic Schrödinger equation approach is developed for the investigation of the absorption spectra of anharmonic systems, in the presence of an environment. Through this it is demonstrated that photoswitching may be stabilised via damping caused by interaction with the environment.

Lastly, a numerically exact method, the hierarchy of stochastic pure states, is extended for the study of molecular photoswitch dynamics. It is found that a combination of potential energy surface shape, damped quantum dynamics, thermally activated dynamics, and environment memory play significant roles in the observed dynamics of the stiff-stilbene photoswitch. Subsequently, it is established that dynamics produced with the method and single coordinate models agree well with transient absorption spectroscopy experiments.

Contents

List of Figures

List of Tables

Abbreviations

BCF	Bath Correlation Function
CCS	Coupled Coherent States
ESA	Excited State Absorption
FCC	Franck-Condon Coefficients
HEOM	Hierarchical Equations of Motion
HOPS	Hierarchy of Pure States
LME	Lindblad Master Equation
MCE	Multiconfigurational Ehrenfest
MCTDH	Multiconfigurational Time-Dependent Hartree
NMSSE	Non-Markovian Stochastic Schrödinger Equation
OQS	Open Quantum Systems
QME	Quantum Master Equation
QCF	Quantum Time-Correlation Functions
RK4	Fourth Order Runge-Kutta
SSE	Stochastic Schrödinger Equation
TEMPO	Time-Evolving Matrix Product Operator
ZPL	Zero Phonon Line

Chapter 1

Introduction and background

Quantum mechanics was an innovation of the early 20th century providing fundamental theory that formed the foundations for several areas of modern physics and chemistry. It gives a description for the counter-intuitive behaviour of the universe at atomic and subatomic scales underpinning complex chemical systems [5, 6], many of which have technological and biological relevance. For example, understanding of this theory drove the development of several technologies, such as computers, smartphones, MRI scanners, and lasers. Furthermore, in the 21st century we have witnessed the emergence of technologies, such as quantum computers and sensors, that seek to harness quantum physics to gain an advantage that is otherwise unattainable [7].

Photochemical reactions [8] are fundamentally quantum due to the time and size scales involved and the nature of light induced excitation. Such reactions are ubiquitous in nature and include photosynthesis [9], and the first stages of vision which involves the cis-trans photoisomerisation of the retinal molecular photoswitch [10]. This reaction constitutes one of the fastest known chemical reactions with photoproduct formation within 200 fs [11]. Quantum dynamics of this reaction takes place in a rhodopsin protein environment, which consequently undergoes a conformational change leading to the visual signal [12].

Interactions of photoswitch systems with an environment leads to damped dynamics, and consequently to effects such as quantum decoherence and dissipation [13, 14]. Additionally, a common feature among photoswitch reactions is that the nuclear motion induced by electronic excitation is very large. Thus the system is displaced far from equilibrium negating descriptions that are commonly used, such as the harmonic oscillator description. Quantum mechanical modelling of the electronic and nuclear motion with anharmonic descriptions in the presence of condensed phase environments, such as a protein or solvent, presents a challenging problem.

Beyond their natural occurrence, photoswitches have numerous applications and potential [15–18], examples include, molecular machines and motors [19–22], energy storage [23, 24], photopharmacology [25], and the restoration of vision [26–29] for degenerative retinal diseases such as age-related macular degeneration. Theory is thus required in order to understand the underlying physics of natural systems, interpret and predict the results of ultrafast spectroscopy experiments, and make improvements to artificial systems and technology. However, feasible computational implementation of a quantum system plus its condensed phase environment requires efficient yet accurate

treatments that account for quantum mechanics.

Several methods have been developed capable of treating multidimensional quantum problems with favourable system size scaling [30]. One strategy is to use a large but formally closed finite system to treat the full many-body wavefunction. Examples include the Multiconfigurational Ehrenfest (MCE) and the Coupled Coherent States (CCS) methods [31–40] which have been implemented in system-environment studies.

Alternatively, in the area of open quantum systems (OQS) [41–43] common methods deal with the reduced system, such as the reduced system density matrix, by tracing over the many environment degrees of freedom. Examples of this include quantum master equations (QME), and stochastic Schrödinger equation (SSE) approaches [44, 45]. These OQS methods are often derived in the limit of weak coupling of the system to the environment, where processes that transfer from system to environment retain no memory (Markovian) and so energy and information is simply lost to the environment. However, non-Markovian extensions and methods are possible that go beyond weak coupling approximations [46, 47]. These can model system-environment correlations that persist on timescales relevant to the system dynamics leading to a flow of information back into the system from the environment [48]. Furthermore, there are numerically exact methods such as time-evolving matrix product operator (TEMPO) [49, 50], and methods that allow systematic convergence of the reduced system dynamics such as the hierarchical equations of motion (HEOM) [51–58] and the hierarchy of pure states (HOPS) [59–62]. The latter provides a method to solve the non-Markovian stochastic Schrödinger equation (NMSSE) [63–67] and allows a wider applicability of the method whilst retaining the OQS structure.

The above techniques provide theory of open quantum system dynamics and computational methods that can be used to interpret and predict experimental results of condensed-phase chemical dynamics. Notable experiments for probing the dynamics, with a temporal resolution down to femtoseconds, and absorption of light for photo-excited systems include linear and non-linear ultrafast laser spectroscopies, such as 2D spectroscopy [68, 69]. Beyond this, the methods have wide applications in understanding environment interaction with a quantum system, which is crucial in developing quantum technology that relies on sustaining quantum effects in noisy environments. Furthermore, OQS techniques have been applied in assessing whether non-trivial quantum effects play a functional role in systems that are of relevance to biological and

life processes [70–74]. Prominent examples include magnetoreception and the quantum theory of bird migration [75–81], and energy transport in photosynthesis [82–89]. It has also been proposed that vibrational coherence, conical intersections, and shaping of the ground-state and excited state potentials may play important roles in the quantum dynamics of retinal [70, 90–96]. These remain innovative, interdisciplinary, and actively debated topics. Development of OQS techniques that can accurately model these processes is not only of importance to our fundamental understanding of nature but also in developing technological enhancements that are inspired by nature and biological systems.

This thesis develops OQS theory to describe molecular photoswitch quantum dynamics in the condensed phase. The focus is on development of quantum stochastic wavefunction methods with several motivations behind this choice. Firstly, the stochastic wavefunction approach scales with the system Hilbert space size, whereas alternative density matrix approaches scale as the square of the system Hilbert space size. Thus, there is reduced computational demand with the stochastic wavefunction method as computations and storage involve a smaller object of interest. Additionally, implementation of the stochastic wavefunction approach is easily simulated in parallel, which allows for a reduction in the required computation time. Furthermore, the method provides a framework to develop an anharmonic description of the open quantum system with large displacement of nuclear coordinates, by treating degrees of freedom that deviate from the harmonic approximation explicitly whilst treating the rest in a reduced manner, as a harmonic bath. The reduced computational demand of the method becomes increasingly important as more degrees of freedom are treated explicitly. Furthermore, the method offers a natural connection to stochastic differential equations and classical methods historically used to approach the topic such as Langevin and generalised Langevin equations. Lastly, extensions to non-Markovian regimes are possible with viable implementation through the HOPS approach, providing a numerically exact treatment to reveal the most important underlying physical phenomena and assess essential resources for desired photoswitch properties, such as speed or efficiency [97]. In addition, there are close relations of the NMSSE to the CCS method, which provides further steps in connecting the different strategies of treating open quantum system dynamics.

The remainder of this introductory chapter details statistical mechanics, stochastic

methods and classical models of photoswitching. This is followed by a review of quantum theory and dynamics. In Chapter 2 general OQS theory is presented. In Chapter 3 SSE approaches are introduced, the non-Markovian extension is detailed and its solution via HOPS. Chapter 4 uses model systems to investigate the effects of going beyond the harmonic approximation on spectroscopic results. Following this, Chapter 5 analyses model dissipative quantum systems that feature anharmonicity and applies the SSE method to a photoswitch study. Subsequently, Chapter 6 extends the method to the non-Markovian regime, and a normalised and non-linear version of HOPS is presented and applied to a spin-boson model study. Furthermore, a reaction coordinate version of HOPS is derived and applied to model photoswitching in a non-Markovian environment that includes an interplay of damped quantum dynamics and thermal fuctuations, and results are compared to recent ultrafast spectroscopy experiments. Chapter 7 provides a summary of the results of previous chapters and considers wider field relations, conclusions are then presented and the future direction of the research is discussed.

1.1 Overview of classical physics and stochastic dynamics

Although the bulk of this thesis will focus on quantum mechanical treatments, it is important to first provide a rough background on classical treatments and stochastic methods. This gives a conceptual foundation for theories presented and an understanding of classical methodologies used to study photoswitches and isomerisation reactions. A comprehensive review will not be given as we will only consider the most relevant theory, a more general overview is provided by Valkunas [13] and a detailed review can be found in textbooks [98–103].

Classical mechanics provides a set of rules and principles that govern a physical system where the uncertainty of quantum mechanics is negligible. Within this theory if everything is known about the physical system at an initial time, and there is a dynamical equation that models how it evolves, then it can be determined at a later time, in other words it is deterministic. Additionally, if the principle is invariant under time inversion, that is to say we consider the past time and replace t with $-t$ and the equation is unchanged, then it is known as reversible. Formally, the physical system is described by idealised point particles, occupying spatial coordinates, that may interact with one another through forces. These particle coordinates along with their velocities

describe the system's state. The concept of the state of the system is also of importance more generally and we will revisit this notion further with respect to quantum mechanics. Furthermore, a system that is either comprised of the entire universe or isolated such that it does not interact with anything else is known as a closed system. This is usually an idealisation as perfect isolation is not realistic and most systems are instead open.

The laws that govern the dynamics of classical mechanics are the three Newton's laws of motion. The first law states that particles in motion will move with constant velocity, and particles at rest will remain so, unless acted upon by a force. The second law provides a way of determining the velocity change due to the presence of external forces. Specifically, it states that the rate of change of momentum, with respect to time, is proportional to the force. This can be mathematically defined, for example, the dynamics of N particles is given by [13, 98, 102, 103]

$$m_i \ddot{r}_i = \sum_j F_{ij}(r_1 \dots r_N), \tag{1.1}$$

where m_i is the mass, assumed to be constant with respect to time, $\ddot{r}_i = d^2 r_i / dt^2$ and F_{ij} is the force. If we are considering one particle, or object, this takes the well known form

$$F = m\ddot{r} = ma, \tag{1.2}$$

where a is the acceleration. The momenta $p_i = m_i \dot{r}_i$ and coordinates r_i form the phase space of the system. Notably Newton's second law equation thus defines a principle that is both reversible and deterministic. With respect to this mechanical system a single point in phase space defines a state of the system at an instant in time, the dynamical equation of Newton's second law then defines a trajectory in phase space. Different initial conditions each correspond to an initial state of the system and these give different trajectories through the phase space. Furthermore, the energy of the system is conserved if there are no external forces acting, and the trajectories are associated with a particular energy value. We will later explore how damping and irreversible dynamics arise in a microscopic description of an open system. Firstly, we shall consider alternative representations, namely the Lagrangian and Hamiltonian formulations, which form important foundations for quantum mechanics.

1.1.1 Lagrangian Mechanics

This formulation of classical mechanics provides a structure in which the mechanical equations of motion take the same form in arbitrary coordinate systems. Thus, there are simple means to transform between coordinate systems. In addition, it can also deal with complex constraints providing a very useful formulation of classical mechanics. The starting point of this reformulation is Newton's second law Eq. 1.1 and a full derivation from this point can be found in several books on the topic [13, 99, 100, 102] which we shall follow in this section to provide an overview.

In the derivation one finds that the variation of kinetic energy is equal but opposite in sign to the variation of the potential energy. This motivates the definition of the Lagrangian

$$L = T - V, \tag{1.3}$$

where $T = \sum_i (1/2) m_i |\dot{r}_i|^2$ represents the kinetic energy and V represents the potential energy. From this, the action is introduced as

$$S = \int_{t_1}^{t_2} L \, dt. \tag{1.4}$$

These definitions allow the problem to be reformulated as a variational one, the process of which is known as Hamilton's principle, and involves finding the solution to

$$\delta S = 0. \tag{1.5}$$

This tells us that of all possible trajectories that a dynamical system could follow, the actual path is an extremum of the action, and is commonly known as the principle of stationary action.

As stated earlier the choice of coordinates is arbitrary, and so this result could be expressed in different coordinates to the chosen Cartesian ones. Therefore, to generalise the result one may consider generalised coordinates q_i and express the Lagrangian in terms of these and their time derivatives $\dot{q}_i$. By following this process [98–103] one obtains the Euler-Lagrange equation, also known as the Lagrange equation,

$$\frac{d}{dt}\left(\frac{\partial}{\partial \dot{q}_i} L\right) - \frac{\partial}{\partial q_i} L = 0, \tag{1.6}$$

solutions of which describe the evolution of a physical system for the action. The more mathematically inclined may be interested in the general setting of calculus of variations and derivation of the Euler-Lagrange equations [104–106].

1.1.2 Hamiltonian mechanics

The Lagrangian provides a reformulation of classical mechanics with wide applicability even outside of mechanics. Examples include, the field of optics, and quantum mechanics where it forms an important foundation for Feynman's path integral approach. Within this formalism the state of the system is represented by a point in an n-dimensional configuration space of the generalised coordinates q_i, and their derivatives $\dot{q}_i$. We will now look at the Hamiltonian formulation, which provides important structure for modern statistical mechanics and quantum mechanics.

Whilst the Lagrangian is second order and requires $2n$ initial values to be specified, the Hamiltonian formulation provides a description in terms of first order equations of motion. However, there must still be $2n$ independent variables that describe $2n$ independent first order equations. Thus, the $2n$ equations describe the mechanics in a phase space, for which an intuitive choice of variables are n as the generalised coordinates q_i and the remaining n as the conjugate generalised momenta p_i. Mathematically the change from the Lagrangian to Hamiltonian formulations corresponds to a transformation of variables $(q_i, \dot{q}_i, t) \rightarrow (q_i, p_i, t)$. This change of variables is defined by the Legendre transformation [102].

Equations of the Hamiltonian formulation follow by considering a small change in the Lagrangian [13, 102]

$$dL = \sum_i \dot{p}_i \, dq_i + \sum_i p_i \, d\dot{q}_i + \frac{\partial L}{\partial t} dt \tag{1.7}$$

where the expression for generalised (canonical) momentum

$$p_i = \frac{\partial L}{\partial \dot{q}_i} \tag{1.8}$$

has been substituted. The Legendre transformation then defines a change of variables and provides the definition of the Hamiltonian

$$H(q, p, t) = \sum_i \dot{q}_i p_i - L(q, \dot{q}, t). \tag{1.9}$$

To obtain equations of motion from this, consider the differential of the Hamiltonian using Eq. 1.9

$$dH = \sum_i \dot{q}_i \, dp_i - \sum_i \dot{p}_i \, dq_i - \frac{\partial L}{\partial t} dt. \tag{1.10}$$

If we compare this to like terms of the general definition of the differential of the Hamiltonian

$$dH = \sum_i \frac{\partial H}{\partial q_i} dq_i + \frac{\partial H}{\partial p_i} dp_i + \frac{\partial H}{\partial t} dt, \tag{1.11}$$

then we obtain the $2n$ relations

$$-\dot{p}_i = \frac{\partial H}{\partial q_i} \tag{1.12}$$

$$\dot{q}_i = \frac{\partial H}{\partial p_i}, \tag{1.13}$$

which are known as the canonical or Hamilton equations of classical mechanics. In addition to this, by comparing the equations it is clear to see that

$$-\frac{\partial L}{\partial t} = \frac{\partial H}{\partial t}. \tag{1.14}$$

Furthermore, by taking the time derivative of H in Eq. 1.9 we obtain

$$\frac{dH}{dt} = -\frac{\partial L}{\partial t}, \tag{1.15}$$

and so if the system is invariant under time translation then H is conserved. In most cases $H = T + V$ represents the total energy, and thus for this case this time invariance represents a statement on the conservation of energy. Furthermore, the Hamiltonian as the total energy provides an intuitive quantity that describes the dynamics of a system.

In summary, the Hamiltonian formulation focuses on a trajectory through phase space (q, p) rather than coordinate space. This allows the Hamiltonian formulation to represent mechanics elegantly and concisely a set of first-order differential equations. Additionally, Hamiltonian mechanics forms an important foundation for quantum mechanics through the Schrödinger approach which we shall discuss in the introduction to quantum theory given in the latter half of this chapter. It is important to note that the Hamiltonian and Lagrangian formulations require the systems to have gradient forces, which means that they can be described as derivatives of potentials. Frictional forces do not satisfy this and thus cannot be described in terms of some friction potential. This means the formulations alone are unable to describe friction phenomena, which will be essential in describing dynamics of molecular photoswitches in contact with a condensed phase environment. In order to achieve this, microscopic relaxation theory and an open system are required, for which statistics and stochastic methods provide an essential background.

1.1.3 Introduction to stochastic methods

Much of theoretical science up to the late 1800s involved the study of deterministic solutions of differential equations to model natural phenomena. It is a known false notion that, with knowledge of all initial data, one can predict the future of a real system. This has come to light via the advent of quantum mechanics, which has fundamentally a statistical element to it, and also in the concept of chaos. Consequently, stochastic descriptions were required [107, 108], which permit a description through random probability distributions. Historically, one of the best known stochastic process studied was that of Brownian motion, developed from the observation that small pollen grains suspended in water are found to be in a highly animated and irregular state of motion. This phenomena was first studied by Robert Brown in 1827, although, a rigorous explanation was not provided until 1905 by Einstein. This explanation gave indirect evidence for the existence of atoms and molecules in which the motion is caused by frequent impacts between the pollen grain and the molecules of the liquid surrounding it. Furthermore, the complex nature of the dynamics of the molecules and interaction with the pollen grain resulted in a description possible only through probabilistic means. Smoluchowski also independently came to the same explanation [108]. Einstein's explanation of the nature of Brownian motion is seen as the beginning of stochastic modelling of natural phenomena. Since its initial introduction, the field of stochastic methods has been developed and applied to many areas of research and disciplines. These include applications to mathematical finance, statistical physics, physical chemistry, and quantum optics and electronics. In this section I will not aim to cover a complete theory of stochastic methods, but a more complete review can be found in [13, 108, 109], which this section follows. From these sources I present: basic probability concepts, stochastic processes and stochastic differential equations, open system dynamics and classical treatments of isomerisation reactions. This provides structure for the quantum stochastic methods presented in Chapter 3.

Probability theory provides the mathematical framework by which random processes can be described. Often there are occurrences in a system of interest which we aim to assign probabilities to. For example, that a Brownian particle is at a position x in space, or that a molecule in a photoisomerisation reaction is in its cis state. These occurrences constitute realisations of events, which construct the probability space. An event is then a member of this space which can generally be characterised, for example,

by a vector of real numbers $x = (x_1, x_2, x_3, \dots)$. It is of convenience to group together events into the concept of a set of events A, where $q \in A$ is used to represent that the event q is contained in the set A.

Firstly, there are some concepts relating to sets of which it is useful to state in order to understand the mathematical structure. If a set A is contained in another set B then we say A is a subset of B and denote this by

$$A \subset B. \tag{1.16}$$

The elements of A and B can form a new set C which consists of elements contained in A or B or both. This is called the union of sets A and B and is denoted by

$$C = A \cup B. \tag{1.17}$$

If elements are shared by A and B then this forms a set D, and is called the intersection of sets A and B denoted

$$D = A \cap B. \tag{1.18}$$

With respect to the space of events there is also the set of all events Ω known as the full set, and the set of no events $\emptyset$ known as an empty set. In addition to these concepts there is the complementarity operation

$$C = B \setminus A, \tag{1.19}$$

which removes any elements of B that are contained in A.

The framework of set theory allows us to define random events in terms of sets. An occurrence of an event relating to a set happens upon realisation of an element belonging to that set. In order to quantify an event A we introduce the probability of A, $P(A)$, as a function that must satisfy several probability axioms [108]. The first is that the probability must be nonnegative

$$P(A) \geq 0, \forall\, A. \tag{1.20}$$

Secondly, the full set which contains all events, must have unit probability

$$P(\Omega) = 1. \tag{1.21}$$

The third and final required axiom is that the union of nonintersecting sets is additive. For example, if

$$A_i \cap A_j = \emptyset, \forall\, i \neq j \tag{1.22}$$

then we have

$$P(\cup_i A_i) = \sum_i P(A_i). \tag{1.23}$$

A key concept regarding probability and a stochastic dynamical description is that of conditional probability. Consider two events A and B, in some cases where A is realised B might be realised at the same time and this is associated with the set $A \cap B$. The probability that this occurs is then proportional to $P(A \cap B)$. If the event B is a necessary condition in describing the event A, then this limits the possible events. As the event B, with its own probability $P(B)$ is also a necessary condition, the conditional probability must be defined only on the collection of sets contained in B. Therefore, the conditional probability is given by dividing the joint probability by the probability of event B

$$P(A|B) = \frac{P(A \cap B)}{P(B)}. \tag{1.24}$$

This can also be defined from the other direction,

$$P(A \cap B) = P(A|B)P(B) = P(B|A)P(A). \tag{1.25}$$

If the events are independent then the conditional probability simplifies to just the probability of A, as B is no longer a necessary condition, and we obtain

$$\frac{P(A \cap B)}{P(B)} = P(A). \tag{1.26}$$

It follows that for independent results we also have the relation

$$P(A \cap B) = P(A)P(B). \tag{1.27}$$

Furthermore, consider a collection of disjoint events which fill the entire space such that

$$B_i \cap B_j = \emptyset, \tag{1.28}$$

$$\cup_i B_i = \Omega, \tag{1.29}$$

which means the space is formed from sets that do not overlap. Under these considerations, an event A can be given as

$$A = U_i(A \cap B_i), \tag{1.30}$$

which by the third probability axiom gives

$$P(A) = \sum_i P(A \cap B_i). \tag{1.31}$$

Using the relation for conditional probabilities we obtain

$$P(A) = \sum_i P(A|B_i)P(B_i), \tag{1.32}$$

which is an important result in the development of stochastic processes. It suggests the following: consider a system that at a time t_1 is described by a set of states B_i with associated probabilities $P(B_i)$. At a later time t_2 if the system is in the state A with probability $P(A)$ then $P(A|B_i)$ conveys the probability of a transition from state B_i to A. The sum total of probability of transitions to A is then the probability $P(A)$.

We also require another concept, the random variable, which is central to topics discussed in this thesis. Consider a probability space whose events can be written x. A random variable is then a specific mapping of the event. Formally we can introduce the random variable as $F(x)$, which is a function of x and takes on values for each x. The identity of x is written as $X(x) = x$. Often for events w that have a complicated description, we may omit explicit inclusion of w because the events are associated with the values of x. To exemplify this, consider a molecule, in a condensed phase environment, that we want to know the position of. In this case w might include all of the positions, orientations, and momenta of each molecule in the condensed phase environment which presents a complex description that it is not always necessary to make explicit. Random variables play an important role in stochastic differential equations which presents a description of the time evolution of random variables in a representation which is somewhat analogous to the differential equations of nonprobabilistic systems.

The characterisation of random variables can be achieved in several ways such as moments, where the nth moment is defined as the average

$$\langle x^n \rangle = \sum_w x^n(w)P(w). \tag{1.33}$$

Often the most important quantities are related to the first and second order moments. For example, $\langle x^1 \rangle$, represents the mean. The second, known as dispersion, is a measure of the spread of the random numbers. We will also make use of correlation functions, described later in the thesis, which give the statistical correlation between random variables.

1.1.4 Stochastic process

A system that evolves probabilistically in time, that is to say such that a time dependent random variable $X(t)$ exists, can be described as a stochastic process. For example, in the process there is a random variable x_1 at time t_1, and x_2 at a later time t_2, and a random variable at all subsequent times up to x_n at t_n. The probability of this composite event is given by

$$P(x_n, t_n; \ldots; x_2, t_2; x_1, t_1), \tag{1.34}$$

which is a description in terms of the entire time trajectory. The conditional probability may also be defined in which we want to know the probability of the composite event if preceding it there was a process $y_1, t_1; y_2, t_2; \ldots; y_m, t_m$. Let the probability of the composite event be defined as

$$P(x_n, t_n; \ldots; x_2, t_2; x_1, t_1; y_m, \tau_m; \ldots; y_2, \tau_2; y_1, \tau_1), \tag{1.35}$$

then the conditional probability is given by

$$\begin{aligned} &P(x_n, t_n; \ldots; x_2, t_2; x_1, t_1 | y_m, \tau_m; \ldots; y_2, \tau_2; y_1, \tau_1) \\ &= \frac{P(x_n, t_n; \ldots; x_2, t_2; x_1, t_1; y_m, \tau_m; \ldots; y_2, \tau_2; y_1, \tau_1)}{P(y_m, \tau_m; \ldots; y_2, \tau_2; y_1, \tau_1)}. \end{aligned} \tag{1.36}$$

With respect to an evolution equation, we thus consider conditional probabilities as a prediction of future values of $x_1, x_2, \ldots, x_n$ given the knowledge of the past $y_1, y_2, \ldots, y_n$. Therefore, there is a relation between n and m points in time. For example, if $t_n > \cdots > t_1 > \tau_m > \ldots \tau_1$, then a long memory of the process is implied as the present state depends on the knowledge of a chain of past events.

An important class of processes which forms a subset of the ones previously discussed is the Markov process. In this the so called Markov assumption is made in which the process only depends on the most recent preceding time. This means the composite

probability reduces to

$$P(x_n, t_n; \dots; x_2, t_2; x_1, t_1; y_m, \tau_m), \tag{1.37}$$

which is an important statement which means that everything can be defined in terms of simple conditional probabilities $(x_1, t_1|y_1, \tau_1)$. In general, for an arbitrary joint probability we have

$$P(x_n, t_n; \dots; x_2, t_2; x_1, t_1) = P(x_n, t_n|x_{n-1}, t_{n-1}) \dots P(x_2, t_2|x_1, t_1)P(x_1, t_1). \tag{1.38}$$

Markovian processes form the foundation for many stochastic methods both in classical and quantum settings. In addition, an important property which will be made use of is that the Markovian process can be characterised by Gaussian white noise.

1.1.5 Stochastic differential equations

Many situations in nature can be described with a system of one or few degrees of freedom that is in contact with some complex environment with a large number of degrees of freedom, possibly tending to an infinite amount. Dynamics of an open system of this type in the classical limit can be modelled by a type of stochastic differential equation named the Langevin equation [13, 108]

$$\frac{dx}{dt} = \gamma(x) + \xi(t), \tag{1.39}$$

where $\gamma(x)$ is a force that is dependent on the dynamical variables $x = (x_1, x_2, \dots)$ and could, for example, represent a frictional or damping, force. The second term $\xi(t)$ represents the fluctuations, or stochastic force, which introduces irreversible dynamics. This stochastic force doesn't have an explicit definition and is instead characterised by its moments, specifically its ensemble averages and correlation function given by

$$\langle \xi(t) \rangle = 0, \tag{1.40}$$

and

$$\langle \xi(t)\xi(t') \rangle = K(t - t'), \tag{1.41}$$

respectively. For white noise characterising the fluctuating force, the friction force is local in time and the Langevin equation takes the Markovian form

$$m\ddot{q}(t) + m\gamma\dot{q}(t) + V'(q) = \xi(t), \tag{1.42}$$

where

$$\langle \xi(t)\xi(t')\rangle = 2m\gamma k_B T\delta(t-t'), \tag{1.43}$$

for which T is the temperature, m is the mass, k_B is the Boltzmann constant, and a driving force $F = -V'(q)$ has been included where $V(q)$ is a potential. This equation is capable of describing a heavy Brownian particle, driven by a force, whilst immersed in a fluid environment of light particles. An equation of this type is also widely used as the starting point in the Kramers model of the reactive motion of photoisomerisation as the escape of a particle over a potential barrier in one dimension [8, 110]. The coordinate of interest is then the isomerisation coordinate, for example a molecular rotation parametrised by an angle. In addition to this the Kramers model [111] can be generalised to the Grote-Hynes model [112–114] through the generalised Langevin equation in which the fluctuations are characterised by coloured noise

$$m\ddot{q}(t) + m\int_0^t dt'\,\gamma(t-t')\dot{q}(t') + V'(q) = \xi(t). \tag{1.44}$$

In this equation the friction force is time (or frequency) dependent representing non-Markovian dynamics. The correlation function is related to the frequency-dependent friction by a Green-Kubo formula [115, 116]

$$\tilde{\gamma}(\omega) = \frac{1}{mk_BT}\int_0^\infty dt\exp(i\omega t)\langle\xi(t)\xi(0)\rangle, \tag{1.45}$$

where the frequency-dependent friction is related to the time-dependent friction by

$$\tilde{\gamma}(\omega) = \int_0^\infty dt\,\gamma(t)\exp(i\omega t). \tag{1.46}$$

Using this and comparing against the classical regime power spectrum of the stochastic force

$$\tilde{K}(\omega) = \int_{-\infty}^{\infty} dt\,K(t)\cos(\omega t) = \int_{-\infty}^{\infty} dt\,\langle\xi(t)\xi(0)\rangle\cos(\omega t), \tag{1.47}$$

we can see it relates to the real part of the friction function $\tilde{\gamma}(\omega) = \tilde{\gamma}'(\omega) + i\tilde{\gamma}'(\omega)$ through the relation

$$\tilde{K}(\omega) = 2mk_BT\tilde{\gamma}'(\omega). \tag{1.48}$$

These form important classical models that have been used to study photoswitching in the condensed phase and will be referred to later in the thesis when discussing the comparison to quantum models.

1.2 Introduction to quantum theory

Quantum theory marks a departure from the classical physics discussed thus far which corresponds more with our intuitive experience of the macroscopic world. In this section the required mathematics and fundamental principles of quantum mechanics will be detailed that will be necessary for an understanding of the ensuing chapters. For a more complete assessment, a good overview is provided by Valkunas [13], and there are several books that introduce and delve into the topic [117–122]. The remainder of this chapter will summarise the most relevant information to this thesis from these sources. A review of open quantum systems will be reserved for Chapter 2.

Core concepts in classical physics concern the physical behaviour of waves, and separately particles. However, at the start of the 20th century observations were at odds with a strict adherence to ascribing purely a wave-like or particle-like behaviour. Instead it arose that there must be a dual property that, for example, light that was previously thought to behave only as a wave could behave as a particle, and matter such as electrons, which were thought to have a particle-like behaviour, could behave as a wave. Thus, physical phenomena relating to these are neither described as just waves or particles but can have properties of both. Furthermore, observation of a particular type of behaviour can be altered through the act of measurement. As a consequence of this dual nature there is an uncertainty in the position and momentum of a system that dictates a limit on how well both can be known. The formal relation associated with this is the Heisenberg uncertainty principle

$$\Delta x \Delta p_x \approx h \tag{1.49}$$

where Δx and Δp_x are the uncertainty in the position and momentum in a particular direction x, and h is the Planck constant. To account for this we must change the usual functions of classical mechanics to mathematical operators $f \to \hat{f}$ and the system state to a vector with an associated space in which these operators act. Another consequence is that for measurements of a quantum system predictions of outcomes are probabilistic. This is not the stochastic nature of classical mechanics that we discussed earlier in this section, but a fundamental statistical aspect of the quantum world. Quantum mechanics provides the mathematical framework for the development of physical laws through which a quantum system will behave.

1.2.1 Mathematical structure of quantum mechanics

As discussed in the introduction, in the more abstract formalism the state of the quantum system is described by a unit vector which is called the state vector $|\psi\rangle$. Equivalently, when representing physical variables of a quantum system, the state is known as the wavefunction $\psi(x,t)$. Note, in some cases where the operator nature is evident from context, we shall drop the hat notation for readability. An important property of the wavefunction is that it satisfies the condition of normalisation

$$\int \psi^*(x)\psi(x)\,dx = 1. \tag{1.50}$$

The wavefunction incorporates the wavelike properties of the quantum system and contains the relevant information for determining the probability amplitude that a system is in a given state. The space associated with this, and which operators act in, is called the Hilbert space $\mathcal{H}$. Thus, in the vector formalism of the state the operator can be represented by a matrix and both of these act within $\mathcal{H}$. In this formalism an operator can act on a state through usual matrix vector multiplication to produce another state within the same space. A simple example is of the identity operator $\hat{I}$, which acts on the state as

$$\hat{I}|\psi\rangle = |\psi\rangle. \tag{1.51}$$

In a matrix representation $\hat{I}$ is given by an n dimensional identity matrix, where n is the dimension of the Hilbert space. There is also another useful description of a quantum state known as a density operator, or density matrix, which we shall discuss in the next chapter on open quantum systems. Beyond this postulate, quantum mechanics does not specify what the state for a system is or the state space, and this depends on the physical system studied.

1.2.2 Closed quantum system dynamics and basis representations

The dynamics of the state $|\psi\rangle$ is determined by the Schrödinger equation

$$i\hbar\frac{d|\psi\rangle}{dt} = \hat{H}|\psi\rangle, \tag{1.52}$$

where $\hbar = h/2\pi$ is the reduced Planck's constant which is experimentally determined and $\hat{H}$ is a Hermitian operator equivalent of the Hamiltonian. In quantum mechanics the Hamiltonian $\hat{H}$ is the operator that corresponds to the total energy of the system.

In this thesis it was first presented earlier in the context of classical mechanics, but the importance of it in quantum mechanics is now clear. Once we have knowledge of the Hamiltonian of a system (along with the value of $\hbar$) then we understand the closed system dynamics of the wavefunction completely. However, it is not always an easy task to connect a Hamiltonian to particular physical system. Furthermore, no real quantum system is truly closed, but if the system interacts only very weakly and slowly with an environment, then closed system dynamics can be a useful approximation to gain insight. Later in this thesis, we shall find that this does not suffice for many chemical physics and biochemical physics problems, for which the environment is often complex and strongly coupled to the system. For example, a complete modelling of molecular photoswitches in a condensed phase environment will require us to adopt a more advanced treatment that takes into account the interaction with the environment. Nonetheless, the closed system treatments discussed here offer an important means of comparison and allow us to elucidate features in the quantum dynamics of molecules.

It has not yet been stipulated as to what the physical variables the wavefunction depends on. This can be defined in particular ways through so called basis representations. A common representation is the coordinate representation where $\psi(q,t)$ represents the wavefunction with respect to a coordinate basis q. The Schrödinger equation in this basis is given by

$$i\hbar\frac{d\psi(q,t)}{dt} = \left[\frac{-\hbar^2}{2m}\frac{\partial^2}{\partial q^2} + \hat{V}(q)\right]\psi(q,t), \tag{1.53}$$

where the first term on the right hand side represents the kinetic energy operator $\hat{T}$, and the second represents the potential energy operator $\hat{V}$. To understand the concept of basis expansion further consider an ansatz

$$\Psi(q,t) = \psi(t)\varphi(q), \tag{1.54}$$

and a time-independent Hamiltonian for the Schrödinger equation. This allows us to separate the equations into one for the time variable and one for the coordinate and write an eigenvalue equation

$$\hat{H}\varphi(q) = E\varphi(q), \tag{1.55}$$

for the coordinate wavefunction $\varphi(q)$ known as the stationary or time-independent Schrödinger equation. The quantities E and $\varphi(x)$ in the equation represent the eigenvalue and eigenfunction respectively. These quantities often correspond to a set of

eigenvalues E_n with corresponding eigenfunctions $\varphi_n(x)$. The numbers n then form an index by which the state may be identified, for example, an energy level corresponding to the nth eigenenergy, or reference to the nth eigenstate. Then for the time variable equation we have

$$i\hbar\frac{d\psi(t)}{dt} = E\psi(t), \tag{1.56}$$

which can be solved for known values of E_n. Specifically a solution of the Schrödinger equation is provided by $\exp(-iE_nt/\hbar)\varphi_n$. The full wavefunction, of coordinate and time, can then be computed as linear superpositions of these solutions

$$\begin{aligned}\Psi(q,t) &= \sum_n c_n(0)e^{-\frac{i}{\hbar}E_nt}\varphi_n(q) \\ &= \sum_n c_n(t)\varphi_n(q),\end{aligned} \tag{1.57}$$

where

$$c_n(t) = c_n(0)e^{-\frac{i}{\hbar}E_nt}. \tag{1.58}$$

The general result is that an arbitrary wavefunction $\psi(q,t)$ can be expanded in this manner in a basis that is complete, which means the basis vectors span the entire vector space. Note that for $t = 0$, the initial wavefunction $\psi(q,0)$ is the summation of only expansion coefficients c_n multiplied by associated eigenfunctions φ_n

$$\psi(q,0) = \sum_n c_n\varphi_n(q). \tag{1.59}$$

As the wavefunction is normalised and the eigenfunctions of the Hamiltonian form an orthogonal and orthonormal set such that

$$\int \varphi_n^*(q)\varphi_m(q)\,dq = \delta_{nm}, \tag{1.60}$$

the expansion coefficients are given by

$$c_n(t) = \int \varphi_n^*(q)\psi(q,t)\,dq. \tag{1.61}$$

Additionally, other basis representations are possible, for example the momentum representation, and the energy representation in which the eigenstates $|n\rangle$ form the basis vectors. This differs to the above discussion where we remained in a coordinate representation of the state but performed the expansion of the state with respect to eigenenergies and eigenstates. An important class of evolutions is formed from considering the

dynamics of the eigenstates. This can be defined succinctly in the $|n\rangle$ basis. Firstly, as the Hamiltonian is Hermitian, it can be diagonalised allowing it to be brought into the form

$$\hat{H} = \sum_n E_n |n\rangle\langle n|, \tag{1.62}$$

where E_n are the eigenvalues of the Hamiltonian, $|n\rangle$ are the eigenvectors and $|n\rangle\langle n|$ represent elements of a diagonal matrix. The states $|n\rangle$ are commonly known as the energy eigenstates, also known as the stationary states, and E_n corresponds to the energy associated with the state $|n\rangle$. The lowest of these states $|0\rangle$ is known as the ground state, whilst E_0 is known as the ground state energy. Dynamics of the energy eigenstates is rather simple and rationalises their interpretation as stationary states, as they only acquire a numerical factor also known as a phase factor,

$$|n(t)\rangle = \exp(-iE_n t/\hbar)|n(0)\rangle. \tag{1.63}$$

Furthermore, if we perform the expansion of $|\psi(t)\rangle$ with respect to the energy eigenstate basis $|n\rangle$ we obtain

$$|\psi(t)\rangle = \sum_n c_n(t)|n\rangle, \tag{1.64}$$

and

$$|\psi(t)\rangle = \sum_n e^{-iE_n t/\hbar} c_n(0)|n\rangle, \tag{1.65}$$

which are the results of 1.57 and 1.58 but written in the $|n\rangle$ basis. In addition, due to normalisation it follows that

$$1 = \langle\psi(t)|\psi(t)\rangle = \sum_n \sum_m c_n^*(t) c_m(t)\langle n|m\rangle, \tag{1.66}$$

which due to orthonormality becomes

$$\begin{aligned} 1 &= \sum_n |c_n(t)|^2 \\ &= \sum_n |c_n(0)|^2. \end{aligned} \tag{1.67}$$

Thus each of the values of $|c_n(0)|^2$ contribute to the normalisation of the state.

1.2.3 Quantum probability and expectation values

In the last section we obtained the expansion coefficients c_n. In the standard interpretation of quantum mechanics, and without the inclusion of measurement, the square modulus of the expansion coefficient $|c_n(0)|^2$ provides the probability density of finding the system in its nth state. Similarly, $|\varphi_n(x)|^2$ defines the probability for finding the system in the nth eigenstate with a coordinate value of x. This is commonly known as the Born rule for probability. With respect to this the probability density represents a real nonnegative value whereas the wavefunction itself is complex and is not a measurable quantity.

As with functions in classical mechanics, the operators of quantum mechanics often represent some physical quantities of interest. The expectation of an operator represents the probabilistic expected value of experimental observation. For example, the probability that a molecule may be found in a particular conformation. This generally corresponds to outcomes of repeated experimental observation. Mathematically the expectation value of operator $\hat{A}$ is given by an equation also known as the Born rule

$$\langle \hat{A} \rangle = \int dx\, \psi^*(x) \hat{A} \psi(x). \tag{1.68}$$

Notably, the expectation can take values that there is a zero probability of the system attaining in any single observation. Furthermore, an operator which represents a physically measurable quantity must have real expectation values and eigenvalues. This is true for a class of operators known as Hermitian operators which satisfy

$$\int dx\, \psi_1^* \hat{A} \psi_2 = \int dx\, (\hat{A}\psi_1)^* \psi_2. \tag{1.69}$$

To see that expectation values of such operators are real, consider

$$\begin{aligned} (\langle \hat{A} \rangle)^* &= \int dx\, \psi(x) (\hat{A}\psi(x))^* \\ &= \int dx\, (\hat{A}\psi(x))^* \psi(x) \end{aligned} \tag{1.70}$$

which, by using the property that $\hat{A}$ is Hermitian, may be written as

$$\begin{aligned} &\int dx\, \psi(x)^* \hat{A} \psi(x) \\ &= \langle \hat{A} \rangle. \end{aligned} \tag{1.71}$$

Thus, we have the result for Hermitian operators that

$$(\langle \hat{A} \rangle)^* = \langle \hat{A} \rangle, \tag{1.72}$$

which is true if the expectation value is real. In addition, by introducing the Hermitian conjugate as

$$(\hat{A}^T)^* = \hat{A}^\dagger, \tag{1.73}$$

a Hermitian operator can be defined as an operator that satisfies

$$\hat{A}^\dagger = \hat{A}. \tag{1.74}$$

1.2.4 Time evolution operator

The aforementioned Schrödinger equation allows the description of the time evolution of a quantum state in continuous time. Another useful description is possible in which we define the time evolution between two discrete times t_1 and t_2 through a so called unitary operator. A matrix, or equivalently operator, $\hat{U}$ is said to be unitary if $\hat{U}^\dagger \hat{U} = \hat{U}\hat{U}^\dagger = \hat{I}$. Unitary operators are of particular importance as they can be used to describe the time evolution of a closed quantum system. For example if the state of the system at time t_0 is $|\psi(t_0)\rangle$, then the state $|\psi(t_1)\rangle$ which the state is in at time t_1 is connected to the state at t_0 via a unitary operator

$$|\psi(t_1)\rangle = \hat{U}(t_1, t_0)|\psi(t_0)\rangle. \tag{1.75}$$

Furthermore, if we consider the solution to the Schrödinger equation we can make the connection between evolution in the Hamiltonian picture and unitary evolution. The solution, for a time-independent Hamiltonian, is as follows

$$\begin{aligned} |\psi(t_1)\rangle &= \exp\Big[\Big(-\frac{i}{\hbar}\hat{H}(t_1 - t_0)\Big)/\hbar\Big]|\psi(t_0)\rangle \\ &= \hat{U}(t_1, t_0)|\psi(t_0)\rangle, \end{aligned} \tag{1.76}$$

where the time evolution operator $\hat{U}$, which is unitary, is defined as

$$\hat{U}(t_1, t_0) \equiv \exp\Big[\Big(-\frac{i}{\hbar}\hat{H}(t_1 - t_0)\Big)/\hbar\Big]. \tag{1.77}$$

Thus it can be seen that there is a bijection, that is to say a one to one correspondence, between the discrete unitary and continuous time Hamiltonian implementing pictures.

It is noteworthy that the time evolution operator can also be defined in terms of time-dependent Hamiltonians. Firstly, by observing that the time evolution operator satisfies

$$\hat{U}(t_0, t_0) = 1 \tag{1.78}$$

and by considering the time evolution with respect to the Schrödinger equation we obtain

$$\hat{U}(t_1, t_0) = 1 - \frac{i}{\hbar} \int_{t_0}^{t_1} \hat{H}(\tau)\hat{U}(\tau, t_0)\, d\tau. \tag{1.79}$$

The integral in this equation can then be considered in an iterative manner, in the first iteration the equation becomes

$$\hat{U}(t_1, t_0) = 1 - \frac{i}{\hbar} \int_{t_0}^{t_1} \hat{H}(\tau)\, d\tau + \left(\frac{-i}{\hbar}\right)^2 \int_{t_0}^{t_1} d\tau \int_{t_0}^{\tau} d\tau_1\, \hat{H}(\tau)\hat{H}(\tau_1)\hat{U}(\tau_1, t_0). \tag{1.80}$$

Applying this iterative procedure repeatedly gives

$$\hat{U}(t_1, t_0) = 1 + \sum_{n=1}^{\infty} \left(-\frac{i}{\hbar}\right)^n \int_{t_0}^{t_1} d\tau_n \int_{t_0}^{\tau_n} d\tau_{n-1} \cdots \int_{t_0}^{\tau_2} d\tau_1\, \hat{H}(\tau_n)\hat{H}(\tau_{n-1}) \ldots \hat{H}(\tau_1), \tag{1.81}$$

where there is time ordering such that $t_0 \leq \tau_1 \leq \cdots \leq \tau_{n-1} \leq \tau_n \leq t_1$. The upper limits of the integrals can be made equal to t_1, for which the equation takes the form of a Dyson series

$$\hat{U}(t_1, t_0) = 1 + \sum_{n=1}^{\infty} \frac{(-\frac{i}{\hbar})^n}{n!} \int_{t_0}^{t_1} d\tau_n \int_{t_0}^{t_1} d\tau_{n-1} \cdots \int_{t_0}^{t_1} d\tau_1\, \hat{H}(\tau_n)\hat{H}(\tau_{n-1}) \ldots \hat{H}(\tau_1), \tag{1.82}$$

where the same time ordering applies. From this it follows that the time evolution operator can be written as

$$\hat{U}(t_1, t_0) = T\exp\left(-\frac{i}{\hbar} \int_{t_0}^{t_1} d\tau\, \hat{H}(\tau)\right), \tag{1.83}$$

where T is the time ordering operator.

1.2.5 Dirac notation

A useful way of representing the mathematical expressions of quantum mechanics that shall be used in this thesis is provided by the Dirac notation, also known as bra-ket

notation. Consider the wavefunction $\varphi_n(x)$ of state n in a coordinate representation. In Dirac notation this representation of the state vector n with respect to a basis x is given by

$$\varphi_n(x) = \langle x|n\rangle, \tag{1.84}$$

where the term on the right hand side of the equation represents the scalar product of two vectors $|x\rangle$ and $|n\rangle$. This defines the projection of $|n\rangle$ on $|x\rangle$ in the Hilbert space. The vector $|n\rangle$ is known as a ket-vector, and $\langle n|$ is called the bra-vector which motivates the Dirac notation also being referred to as bra-ket notation. Regarding this notation the bra and ket vectors are related through hermitian conjugation

$$|n\rangle = (\langle n|)^\dagger \tag{1.85}$$

and thus it follows

$$\langle x|n\rangle = \big(\langle n|x\rangle\big)^*. \tag{1.86}$$

Dirac notation also allows relations to be condensed such as the integral of two wavefunctions

$$\langle b|a\rangle = \int \varphi_b^*(x)\varphi_a(x)\,dx \tag{1.87}$$

and the integral

$$\langle b|\hat{A}|a\rangle = \int \varphi_b^*(x)\hat{A}\varphi_a(x)\,dx. \tag{1.88}$$

If the state vectors are equivalent, then we obtain the normalisation condition

$$\langle a|a\rangle = 1 \tag{1.89}$$

and the expectation value of an operator with respect to a becomes

$$\langle a|\hat{A}|a\rangle = \int \varphi_a^*(x)\hat{A}\varphi_a(x)\,dx. \tag{1.90}$$

Similarly, the expectation value of $\hat{A}$ for a system in a given state $\psi(x)$ is given by

$$\langle\hat{A}\rangle = \langle\psi(x)|\hat{A}|\psi(x)\rangle = \int \psi^*(x)\hat{A}\psi(x)\,dx. \tag{1.91}$$

1.2.6 Formulations of quantum mechanics

Formulations, also known as representations or pictures, represent equivalent methods of formulating the dynamics of a quantum system. We have already discussed one formulation, the Schrödinger picture, in which the system state is evolved in time via the Schrödinger equation, and operators are time-independent. Another formulation, known as the Heisenberg picture, transfers the time dependency to the operators of the system, whilst the state vectors become time-independent. Formulations are covered in more detail by Breuer and Petruccione [41]. However, we shall review the most relevant elements of this source in this section.

Indexing Heisenberg picture operators with an H, the relation between Heisenberg and Schrödinger picture operators is given by

$$\hat{A}_H(t) = \hat{U}^\dagger(t, t_0)\hat{A}(t_0)\hat{U}(t, t_0). \tag{1.92}$$

Thus, at time t_0 the pictures coincide and $\hat{A}_H(t_0) = \hat{A}(t_0)$. Similarly, the relation between Heisenberg picture wavefunctions is given by

$$|\psi(t)\rangle = \hat{U}(t, t_0)|\psi_H\rangle. \tag{1.93}$$

Additionally, we have

$$\begin{aligned} |\psi_H\rangle &= \hat{U}^\dagger(t, t_0)|\psi(t)\rangle \\ &= |\psi(t_0)\rangle. \end{aligned} \tag{1.94}$$

Using these expressions, the equivalence between pictures becomes clear when taking the expectation value of an observable

$$\begin{aligned} \langle\hat{A}\rangle =& \langle\psi(t)|\hat{A}|\psi(t)\rangle \\ =& \langle\psi(t_0)|\hat{U}^\dagger(t, t_0)\hat{A}\hat{U}(t, t_0)|\psi(t_0)\rangle \\ =& \langle\psi_H|\hat{A}_H(t)|\psi_H\rangle, \end{aligned} \tag{1.95}$$

where $\hat{A} = \hat{A}(t_0)$. Using the above relations and

$$\frac{d}{dt}\hat{U}(t, t_0) = -\frac{i\hat{H}}{\hbar}\hat{U}(t, t_0), \tag{1.96}$$

the equation of motion in the Heisenberg picture for $\hat{A}_H(t)$ can be derived as follows

$$\begin{aligned}\frac{d\hat{A}_H(t)}{dt} =& \frac{d}{dt}\Big(\hat{U}^\dagger(t,t_0)\hat{A}(t_0)\hat{U}(t,t_0)\Big)\\ =& \frac{i}{\hbar}\hat{U}^\dagger(t,t_0)\hat{H}\hat{A}\hat{U}(t,t_0) + \hat{U}^\dagger(t,t_0)\Big(\frac{\partial\hat{A}}{\partial t}\Big)\hat{U}(t,t_0)\\ & - \frac{i}{\hbar}\hat{U}^\dagger(t,t_0)\hat{A}\hat{H}\hat{U}(t,t_0)\\ =& \frac{i}{\hbar}\Big(\hat{H}_H\hat{A}_H - \hat{A}_H\hat{H}_H\Big) + \hat{U}^\dagger(t,t_0)\Big(\frac{\partial\hat{A}}{\partial t}\Big)\hat{U}(t,t_0)\\ =& \frac{i}{\hbar}[\hat{H}_H,\hat{A}_H] + \hat{U}^\dagger(t,t_0)\Big(\frac{\partial\hat{A}}{\partial t}\Big)\hat{U}(t,t_0).\end{aligned} \tag{1.97}$$

For the Schrödinger operator $\hat{A}$, without explicit time dependence, the Heisenberg equation of motion reduces to

$$\frac{d\hat{A}_H(t)}{dt} = \frac{i}{\hbar}[\hat{H}_H,\hat{A}_H]. \tag{1.98}$$

In the special case of a time-independent Hamiltonian, this further reduces to

$$\frac{d\hat{A}_H(t)}{dt} = \frac{i}{\hbar}[\hat{H},\hat{A}_H]. \tag{1.99}$$

An equation of motion can also be found for the expectation value of an arbitrary Schrödinger observable $\hat{A}$, the derivation of which is most easily carried out in the Heisenberg picture as follows

$$\begin{aligned}\frac{d}{dt}\langle\hat{A}\rangle =& \Big\langle\frac{d}{dt}\hat{A}_H(t)\Big\rangle\\ =& \frac{i}{\hbar}\Big\langle[\hat{H}_H,\hat{A}_H]\Big\rangle + \Big\langle\frac{\partial\hat{A}_H}{\partial t}\Big\rangle.\end{aligned} \tag{1.100}$$

This is known as the Ehrenfest equation, and as before, for a Schrödinger operator $\hat{A}$, without explicit time dependence this equation reduces to

$$\frac{d}{dt}\langle\hat{A}_H\rangle = \frac{i}{\hbar}\Big\langle[\hat{H}_H,\hat{A}_H]\Big\rangle. \tag{1.101}$$

The Schrödinger and Heisenberg pictures are both limiting cases of the interaction picture which will be of use to us in later derivations. To operate in the interaction picture we first divide the Hamiltonian into two parts

$$\hat{H}(t) = \hat{H}_0 + \hat{H}_I(t), \tag{1.102}$$

the details of the partition depend on the physical system under study. Generally, the free part $\hat{H}_0$ represents the sum of the energies of the two systems when interaction is ignored, and the division is usually done such that it is time independent. The interaction between systems is then given by $\hat{H}_I$. As before, we denote the time evolution of the total system by $\hat{U}(t, t_0)$. Furthermore, we introduce the unitary time evolution operators

$$\hat{U}_0(t, t_0) = \exp\Big[-\frac{i}{\hbar}\hat{H}_0(t - t_0)\Big] \tag{1.103}$$

and

$$\hat{U}_I(t, t_0) = \hat{U}_0^\dagger(t, t_0)\hat{U}(t, t_0). \tag{1.104}$$

The expectation value of an observable is then equivalently given by

$$\begin{aligned}\langle \hat{A} \rangle &= \langle \psi(t_0)|\hat{U}_I^\dagger(t, t_0)\hat{U}_0^\dagger \hat{A}\hat{U}_0\hat{U}_I(t, t_0)|\psi(t_0)\rangle \\ &= \langle \psi_I(t)|\hat{A}_I(t)|\psi_I(t)\rangle,\end{aligned} \tag{1.105}$$

where we have introduced the interaction picture operator

$$\hat{A}_I(t) = \hat{U}_0^\dagger(t, t_0)\hat{A}\hat{U}_0(t, t_0), \tag{1.106}$$

and the interaction wavefunction

$$|\psi_I(t)\rangle = \hat{U}_0^\dagger(t, t_0)|\psi(t)\rangle. \tag{1.107}$$

As in the Heisenberg picture there is a time dependence on operators, however, this comes from the free part of the Hamiltonian $\hat{H}_0$ rather than the total Hamiltonian. The limiting case of the Heisenberg picture arises if $\hat{H}_I(t) = 0$, in which case $\hat{U}_0(t, t_0) = \hat{U}(t, t_0)$ and $\hat{U}_I(t, t_0) = \hat{I}$. Alternatively, the Schrödinger picture is obtained if the free Hamiltonian $\hat{H}_0 = 0$, which means $\hat{H}_I(t) = \hat{H}(t)$, such that $\hat{U}_0(t, t_0) = \hat{I}$ and $\hat{U}_I(t, t_0) = \hat{U}(t, t_0)$. The time evolution of the interaction picture wavefunction can be easily determined by substituting Eq. 1.107 into the Schrödinger equation to give

$$\begin{aligned}\frac{d}{dt}\hat{U}_0(t, t_0)|\psi_I(t)\rangle &= -\frac{i}{\hbar}\hat{H}(t)\hat{U}_0(t, t_0)|\psi_I(t)\rangle \\ -\frac{i}{\hbar}\hat{H}_0\hat{U}_0(t, t_0)|\psi_I(t)\rangle + \hat{U}_0(t, t_0)\frac{\partial|\psi_I(t)\rangle}{\partial t} &= -\frac{i}{\hbar}\Big(\hat{H}_0 + \hat{H}_I(t)\Big)\hat{U}_0(t, t_0)|\psi_I(t)\rangle,\end{aligned} \tag{1.108}$$

which means that

$$\frac{d}{dt}|\psi_I(t)\rangle = -\frac{i}{\hbar}\hat{H}_I(t)|\psi_I(t)\rangle. \tag{1.109}$$

Thus, the time evolution of the interaction picture wavefunction is determined by the interaction part of the Hamiltonian. Whereas, following the same argument as for the Heisenberg picture equation of motion, the time evolution of interaction picture operators is determined by the free Hamiltonian as

$$\frac{d}{dt}\hat{A}_I(t) = \left[\hat{H}_0, \hat{A}_I(t)\right]. \tag{1.110}$$

The interaction picture forms a useful formulation of quantum mechanics when dealing with changes to wavefunctions and operators due to interactions. Consequently, as we shall see in later chapters, changing to the interaction picture is often an important step in the derivation of open quantum system methods.

Chapter 2

Open quantum system theory

Most realistic quantum systems of interest constitute an open quantum system (OQS). These correspond to a quantum system that is coupled to an environment through which energy and particles can be exchanged. Interaction with the environment results in time irreversible processes in addition to the deterministic closed quantum system dynamics defined by the Schrödinger equation. Furthermore, this induces quantum dissipation and decoherence leading to a loss of quantum behaviour of the system.

Open quantum dynamics are of importance to a wide variety of fields. Examples include: condensed matter physics, quantum thermodynamics, quantum optics, quantum information and technology, chemical physics, and quantum biology. Within these fields the theory and simulation of OQS dynamics is crucial in understanding quantum effects in complex systems, modelling condensed phase reactions, and predicting and interpreting experimental results such as ultrafast spectroscopy. Such considerations were, in part, a driving motivation that helped with the formation of the field with initial studies concerning line shape analysis in laser spectra and nuclear magnetic resonance (NMR).

In many open quantum systems modelling all degrees of freedom explicitly is undesirable or not feasible. Moreover, it can be of importance to understand what the fundamental features of a quantum system are in order to replicate observed phenomena. There are several methods of treating the problem with two main representations of the OQS that exist. In one approach a large but finite and formally closed system is used. Some examples are the multiconfigurational time-dependent Hartree (MCTDH) approach [123–126], time evolving density matrix using orthogonal polynomials algorithm (TEDOPA) [127–129], multiconfigurational erenfhest (MCE) and the coupled coherent states (CCS) methods [31–40]. Many of these approaches have wide applicability and are capable of treating nonlinear system-environment coupling and anharmonic environment modes. Common challenges with approaches of this type are that the number of environment modes accounted for in the total system must be large enough for convergence. Additionally, the total system wave-function describes time-reversible dynamics and so challenges arise in describing the thermal equilibrium state.

Alternatively, the problem can be separated into a quantum system interacting with an environment (also known as a bath) to form a reduced system approach [41–43]. Formally, the bath is typically modelled by an infinite number of harmonic oscillators. Through this system-bath model approach it is possible to describe the time-irreversible

dynamics that lead to the thermal equilibrium state. For such a state in this formalism, processes that provide energy from the bath to system are balanced, dependent on the temperature, by dissipative processes from system to bath. In addition to these two approaches to treating the system and environment there is a choice of what quantity is simulated and the method of solution. Choices of quantity include the wave function, correlation functions, and the density matrix which is a useful representation of a quantum state commonly used for open systems which we shall discuss later in this chapter. Methods that implement these quantities include the quantum master equation (QME) for density matrix approaches, and the stochastic Schrödinger equation (SSE) [44, 45] for wavefunction based approaches. We will discuss the methods for simulating dynamics, focusing on SSE approaches, in the next chapter.

In this chapter we will review the necessary theory of open quantum systems following the sources [13, 41, 122, 130]. Firstly, the density matrix representation of the quantum state will be presented and its usefulness to open quantum systems descriptions shall be discussed. We will then define the mathematical foundation of an open quantum system. Following this, we shall review quantum statistics and thermodynamics that provide the tools for describing an environment at finite temperature. Subsequently, we will see how the mathematical structure of quantum systems may be extended via the thermofield method to account for an environment and finite temperature.

2.1 Density matrix representation of the quantum state

In the previous chapter we formulated quantum mechanics in terms of state vectors and the wavefunction. An alternative formulation of the state is given by the density matrix ρ, which is also known as the density operator [13, 41, 122]. This provides a useful state representation for describing individual subsystems of a composite quantum system. Furthermore, it provides a convenient means through which statistical and quantum uncertainty can be accounted for. It has a natural description in terms of bra-ket notation but firstly we shall discuss its connection to the previous representation.

The density matrix is a $d \times d$ matrix, where d is the Hilbert space dimension, that is defined with respect to a specific basis. The diagonal entries of this matrix represent probabilities of finding the quantum system in a corresponding state. The off-diagonal elements, which are referred to as coherences, quantify the superposition of states, and

by definition of the density matrix are a basis dependent quantity [131].

Formally consider the wavefunction

$$\psi(x) = \sum_i c_i \varphi_i(x), \tag{2.1}$$

which is defined with respect to a basis of wavefunctions φ_i. As defined in Chapter 1 the probability of finding the system in state φ_i is given by $|c_i|^2$. Additionally, the expectation value of an operator $\hat{A}$ with respect to the state $\psi(x)$ is given by

$$\langle \hat{A} \rangle = \sum_{ij} A_{ji} c_i c_j^*, \tag{2.2}$$

where

$$A_{ji} = \int dx\, \varphi_j^*(x) \hat{A} \varphi_i(x). \tag{2.3}$$

Thus if a particular basis is chosen, and A_{ij} is represented with respect to this, then one need only know the expansion coefficients c_i in order to calculate the expectation value. This suggests that the state of the system can be characterised in terms of these expansion coefficients and thus we obtain the density matrix elements

$$\rho_{ij} = c_i c_j^*. \tag{2.4}$$

Using this expression the expectation value of an operator is given by

$$\langle \hat{A} \rangle = \sum_{ij} A_{ji} \rho_{ij}. \tag{2.5}$$

Consider that A_{ji} and ρ_{ij} are elements of matrices $\hat{A}$ and ρ. Then it follows that the expectation value is represented by the sum of the diagonal elements of the matrix multiplication of $\hat{A}$ and ρ. This mathematical operation of the sum of diagonal elements of a matrix is known as the trace and so the expectation value can be represented as

$$\langle \hat{A} \rangle = \mathrm{tr}(\hat{A}\rho). \tag{2.6}$$

In the mathematical description, the probabilities are given by diagonal elements ρ_{ii}, sometimes called populations, and the coherences are given by ρ_{ij} where $i \neq j$. The density matrix is succinctly represented in bra-ket notation as

$$\rho = \sum_{ij} \rho_{ij} |i\rangle\langle j|. \tag{2.7}$$

It is important to note that the density matrix doesn't provide more information than the wavefunction about a pure quantum state, which is one we know exactly up to quantum uncertainty and can be represented by a state vector $|\psi\rangle$. However, it provides a representation that can have practical advantages that are of use to condensed phase relaxation phenomena and spectroscopy. In particular, it is useful for mixed states which describe statistical mixtures representing incomplete knowledge of the quantum state. Additionally, the density matrix can also represent a pure state simply as

$$\rho = |\psi\rangle\langle\psi|. \tag{2.8}$$

If the state cannot be expressed in this form, then it is a mixed state. As a proper mixed state this is represented as a statistical mixture of pure states such that there is a probability p_i that the system is in the state $|\psi_i\rangle$. Thus, generally the density matrix can be written in the form

$$\rho = \sum_i p_i |\psi_i\rangle\langle\psi_i|. \tag{2.9}$$

The expectation value of an operator $\hat{A}$ is then represented by

$$\begin{aligned}
\langle\hat{A}\rangle &= \sum_i p_i \langle\psi_i|\hat{A}|\psi_i\rangle \\
&= \sum_i p_i \,\mathrm{tr}(|\psi_i\rangle\langle\psi_i|\hat{A}) \\
&= \mathrm{tr}\left(\sum_i p_i |\psi_i\rangle\langle\psi_i|\hat{A}\right) \\
&= \mathrm{tr}\Big(\rho\hat{A}\Big),
\end{aligned} \tag{2.10}$$

where the cyclic property of the trace has been used going from line one to two. A proper mixed state thus captures our uncertainty about which of a number of pure states the system might be in. Alternatively, one can obtain an improper mixed state when considering composite systems and a reduced density matrix which represents the state of a subsystem. We will discuss this concept in more detail in Section 2.2.

Furthermore, there are some noteworthy properties of the density matrix. Firstly, as diagonal entries represent probabilities, which are normalised, the density matrix must have unit trace

$$\mathrm{tr}(\rho) = \sum_i p_i \,\mathrm{tr}(|\psi_i\rangle\langle\psi_i|) = \sum_i p_i = 1. \tag{2.11}$$

Secondly, it follows from its definition that the density matrix is hermitian as $\rho_{ji}^* = \rho_{ij}$. Lastly, the degree of how pure a state is can be quantified by its purity, $\mathrm{tr}(\rho^2)$, where

$$\mathrm{tr}(\rho^2) = 1 \tag{2.12}$$

if ρ is a pure state, and

$$\mathrm{tr}(\rho^2) < 1 \tag{2.13}$$

if ρ is a mixed state. This section has presented how the density matrix offers a useful representation of the quantum state but its time evolution must still be defined.

2.1.1 Time-evolution of the density matrix

In the last chapter we defined evolution of a quantum state via the time-dependent Schrödinger equation. By considering this, the equation of motion for the density matrix can be obtained [41, 122]

$$\frac{\partial \rho}{\partial t} = \frac{\partial}{\partial t}(|\psi\rangle\langle\psi|) = \left(\frac{\partial}{\partial t}|\psi\rangle\right)\langle\psi| + |\psi\rangle\frac{\partial}{\partial t}\langle\psi| = -\frac{i}{\hbar}\hat{H}|\psi\rangle\langle\psi| + \frac{i}{\hbar}|\psi\rangle\langle\psi|\hat{H}, \tag{2.14}$$

where the time-dependent Schrödinger equation and its conjugate have been substituted. Using a commutation relation this can be written more concisely as

$$\frac{\partial \rho}{\partial t} = -\frac{i}{\hbar}[\hat{H}, \rho], \tag{2.15}$$

which is known as the Liouville-Von Neumann equation. In Chapter 1 we introduced the concept of the time evolution operator $\hat{U}$, this can also be extended to the density matrix to give

$$\rho(t_1) = \hat{U}(t_1, t_0)\rho(t_0)\hat{U}^\dagger(t_1, t_0). \tag{2.16}$$

Furthermore, if we take the trace we obtain

$$\mathrm{tr}(\rho(t_1)) = \mathrm{tr}\Big(\hat{U}(t_1, t_0)\rho(t_0)\hat{U}^\dagger(t_1, t_0)\Big) \tag{2.17}$$

$$= \mathrm{tr}(\rho(t_0)), \tag{2.18}$$

from which it can be deduced that unitary evolution is trace preserving. Additionally, for a time-independent Hamiltonian the density matrix elements, in the energy

eigenbasis, evolve as

$$\begin{aligned}\rho_{ij}(t_1) &= \langle i|\rho(t)|j\rangle \\ &= \langle i|\hat{U}|\psi(t_0)\rangle\langle\psi(t_0)|\hat{U}^\dagger|j\rangle \\ &= e^{-i(\omega_i-\omega_j)(t_1-t_0)}\rho_{ij}(t_0) \\ &= e^{-i\omega_{ij}(t_1-t_0)}\rho_{ij}(t_0). \end{aligned} \tag{2.19}$$

It thus follows that under unitary evolution population elements, $\rho_{ii}(t_1) = \rho_{ii}(t_0)$, are time invariant whereas coherences oscillate due to the exponential and the energy splitting $\omega_{ij} = \omega_i - \omega_j$.

2.2 Composite systems and the reduced density matrix

Beyond the useful description of mixed states provided by the density matrix they are also a key tool in the description of composite systems and their dynamics [122]. Firstly, consider quantum systems A and B to which a pure state can be defined in each of the associated Hilbert spaces,

$$|\psi_A\rangle \in H_A, \tag{2.20}$$

$$|\psi_B\rangle \in H_B. \tag{2.21}$$

The larger composite space can then be formed from the tensor product of these Hilbert spaces which then form subsystems of the total space $H_A \otimes H_B$. The composite state can then be defined as

$$|\Psi\rangle = |\psi_A\rangle \otimes |\psi_B\rangle, \tag{2.22}$$

which is known as a product state, where importantly the assumption has been made that the subsystems are separable. The density matrix of the composite system follows in the same manner

$$\rho = \rho_A \otimes \rho_B. \tag{2.23}$$

Throughout this thesis such states will primarily form the initial state of the open quantum system. However, it is important to note that not every state is separable in this manner and interaction between systems can lead to entanglement and inseparable

states. A state that cannot be written as a product state is referred to as an entangled state. To represent this formally consider a general state of the form

$$|\psi_{AB}\rangle = \sum_{ij} c_{ij}|i_A\rangle \otimes |j_B\rangle. \tag{2.24}$$

The state is separable if the coefficient can be represented by $c_{ij} = c_i^A c_j^B$, otherwise it is inseparable and thus an entangled state. The state of a subsystem of the composite system is known as the reduced state and can be found by taking the partial trace. For example, by taking the partial trace over system B we obtain

$$\rho_A = \mathrm{tr}_B(\rho_{AB}). \tag{2.25}$$

To understand how the partial trace works, as an example, consider two vectors $|v_1\rangle, |v_2\rangle$ belonging to the state space of system A and two vectors $|u_1\rangle, |u_2\rangle$ belonging to another state space of system B. As in Eq. 2.24 we take the composite system state, but here $|v_1\rangle, |v_2\rangle$ are in place of vectors $|i_A\rangle$ and $|u_1\rangle, |u_2\rangle$ are in place of vectors $|j_B\rangle$. It follows that the partial trace over system B of the composite system state formed by these, is given by

$$\begin{aligned}\mathrm{tr}_B(|v_1\rangle\langle v_2| \otimes |u_1\rangle\langle u_2|) &= |v_1\rangle\langle v_2|\mathrm{tr}(|u_1\rangle\langle u_2|) \\ &= |v_1\rangle\langle v_2|\langle u_2|u_1\rangle.\end{aligned} \tag{2.26}$$

The partial trace can thus be seen as averaging over the degrees of freedom of other subsystems. The property that the state of a subsystem of a composite system can be obtained via the partial trace is a core concept to reduced equation of motion open quantum system approaches. Further interesting concepts regarding entanglement and composite systems, such as purification, and the Schmidt decomposition theorem which allows one to identify if a state is entangled, are covered in detail in books by Breuer and Petruccione [41], and Nielsen and Chuang [122]. Briefly summarising some of these concepts, the Schmidt decomposition theorem states that if $|\psi\rangle$ is a pure state of a composite system AB, then there is a representation of this state as

$$|\psi\rangle = \sum_i \lambda_i |i_A\rangle|i_B\rangle, \tag{2.27}$$

where $|i_A\rangle$ and $|i_B\rangle$ are orthonormal states for systems A and B respectively and λ_i is known as the Schmidt coefficient. The Schmidt coefficients are non-negative real

numbers that satisfy the relation $\sum_i \lambda_i^2 = 1$. The Schmidt number is then defined as the number of non-zero values λ_i. There are some interesting results that relate to this, for example, the state $|\psi\rangle$ of a composite system AB is a product state if and only if it has a Schmidt number of 1. To see this, note that if $|\psi\rangle$ is a product state of composite system AB, then there exist φ_A and φ_B, that are orthonormal states of A and B respectively, such that $|\psi\rangle = |\varphi_A\rangle \otimes |\varphi_B\rangle$. Via the Schmidt decomposition theorem it follows that this has a Schmidt number of 1. Conversely, if the Schmidt number for a state $|\psi\rangle$ is 1, then there exist orthonormal states such that

$$|\psi\rangle = \lambda|\varphi_A\rangle|\varphi_B\rangle \tag{2.28}$$

$$= |\varphi_A\rangle|\varphi_B\rangle, \tag{2.29}$$

where, via the rule of Schmidt coefficients that states $\sum \lambda_i = 1$, we must have $\lambda = 1$. A related result is that a state $|\psi\rangle$ of a composite system AB is a product state if and only if ρ_A and ρ_B are pure states. To prove this, consider the composite product state $|\psi\rangle = |a\rangle|b\rangle$, where $|a\rangle$ and $|b\rangle$ are pure states of systems A and B respectively. Let ρ represent the density matrix $|a\rangle\langle a|$ for system A and σ represent the density matrix $|b\rangle\langle b|$ for system B. Then the composite system density matrix reads

$$\rho_{AB} = \rho \otimes \sigma. \tag{2.30}$$

By taking the partial trace over system B as in Eq. 2.25, and by using the property that a density matrix has unit trace it follows that

$$\rho_A = \mathrm{tr}_B(\rho \otimes \sigma) = \rho \mathrm{tr}(\sigma) = \rho, \tag{2.31}$$

and thus as ρ is pure it follows that $\mathrm{tr}(\rho_A^2) = 1$ and the reduced system density matrix is pure. Proving this in the other direction, suppose we have a pure state $|\psi\rangle$, then by the Schmidt decomposition theorem

$$|\psi\rangle = \sum_i \lambda_i |i_A\rangle. \tag{2.32}$$

Furthermore, we obtain the reduced state via the partial trace

$$\rho_A = \mathrm{tr}_B(|\psi\rangle\langle\psi|) = \sum_i \lambda_i^2 |i_A\rangle\langle i_A|. \tag{2.33}$$

Making the assumption that ρ_A is a pure state, then for a particular state $i = \varphi$, $\lambda_\varphi = 1$ and for all other i, $\lambda_i = 0$. From this it follows that the Schmidt number is 1 and the state can be represented as a product

$$|\psi\rangle = |\varphi_A\rangle|\varphi_B\rangle. \tag{2.34}$$

Crucially the converse result informs us that if the state is entangled then the reduced subsystem state must be mixed. As we have seen, such mixed states can more conveniently be represented within the density matrix representation.

2.3 Mathematical foundations of open quantum systems

In the previous chapter we defined the mathematical foundation of a quantum system in terms of the quantum state and Hilbert space. This shall be extended in this section to open quantum systems [41, 42]. An open quantum system is a composite quantum system made up by a system S which is coupled to another system B called the environment (or bath). For example, this could be comprised of a molecular motion that occurs in a protein or solvent condensed phase environment. As an aside, note that in some literature the nomenclature has some subtleties where reservoir refers to an environment with an infinite number of degrees of freedom, and bath refers to a reservoir in a thermal equilibrium state. It follows that S constitutes a subsystem of the combined total system $S + B$. If there is no interaction between systems then the dynamics of the subsystem S follows the closed system dynamics of the previous chapter. However, when there is interaction between system and environment, the system S will not evolve according to just its own internal dynamics. Whilst the combined system will evolve according to unitary time evolution, the interaction negates a unitary time evolution description for the dynamics of S. Thus a new equation of the reduced system dynamics must be derived for the time evolution of the reduced system state. Although the desired result is an OQS treatment of the reduced part of the entire combined system, which is inclusive of both environment and the reduced system, the derivation begins with treating a full model of system and environment. Such a starting point is advantageous as it allows one to understand where the dynamical effects on the reduced system state, due to the environment, originate. It also provides a starting point that extends the mathematical foundations of a closed quantum system and allows a derivation of the open quantum dynamics from the Schrödinger equation.

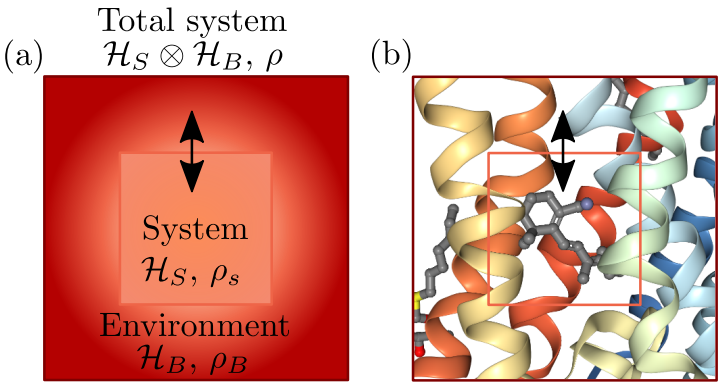

Figure 2.1: (a) Representation of an open quantum system comprised of a system part, with associated Hilbert space $\mathcal{H}_S$ and state ρ_S, and environment part with associated Hilbert space $\mathcal{H}_B$ and state ρ_B. The black arrow represents an interaction between system and environment. (b) An example of an open quantum system comprised of a retinal photoswitch molecule acting as the system part, and rhodopsin protein [1] acting as the environment. The system density matrix is defined with respect to a parameter (or parameters) important to the reaction, such as a bond rotation of the retinal molecule.

In an open quantum system there are three dynamical processes that need to be accounted for, the system dynamics, the bath dynamics, and the interaction between them. The state spaces consist of the Hilbert space for the system $\mathcal{H}_S$, the Hilbert space for the bath $\mathcal{H}_\mathcal{B}$, and the composite total system Hilbert space $\mathcal{H} = \mathcal{H}_S \otimes \mathcal{H}_\mathcal{B}$. The total Hamiltonian representing this is given by

$$H = H_S + H_B + H_I, \tag{2.35}$$

where H_S is the system Hamiltonian, H_B is the bath Hamiltonian, and H_I defines the interaction. The quantities of interest will be that of observables of the subsystem S. Following the techniques of composite quantum systems discussed in the last section, the total composite system can be described by a density matrix ρ. The key quantity that describes the dynamics of the system S is given by the reduced density matrix

$$\rho_S = \mathrm{tr}_B(\rho), \tag{2.36}$$

where the partial trace is performed over the bath degrees of freedom. Figure 2.1 shows a representation of the open quantum system and example. It follows that expectation

values for an operator of the open quantum system $A \otimes I_B$, where I_B is the identity of the bath Hilbert space, can be described by

$$\langle A \rangle = \mathrm{tr}_S(A\rho_S). \tag{2.37}$$

It is often assumed that the initial state is a product state of system and the vacuum state of the environment

$$|\Psi_0\rangle = |\psi_0\rangle \otimes |\mathbf{0}\rangle, \tag{2.38}$$

where $|\mathbf{0}\rangle$ is the vacuum state for all environment annihilation operators. This is required for the stochastic wavefunction methods derived in this thesis, as a thermal state represents a mixed state. As a result, methods using this initial state correspond to a zero temperature limit, however, we will discuss how a finite temperature bath state can be mapped to this case in the section on thermofield theory in order to extend to non-zero temperatures. Many OQS methods rely on an initial product state and system-environment correlations that are generated through interaction over time. OQS treatments of a wider range of initial states, such as entangled states, is an interesting topic in itself [46] but not the focus of this thesis.

Equation 2.35 defines the general structure of the OQS, to proceed a form of the bath must be chosen. Commonly the environment is modelled as a set of harmonic oscillators, which here is labelled with index λ. This set is not necessarily finite and generalising to an infinite number can be done in a similar manner. Notationally this extension requires adopting infinite series or integrals. For a harmonic oscillator bath the corresponding bath Hamiltonian is represented by

$$H_B = \sum_\lambda \omega_\lambda a_\lambda^\dagger a_\lambda, \tag{2.39}$$

where $a_\lambda^\dagger$ and a_λ are the creation and annihilation operators with frequency ω_λ of the mode with index λ. The interaction between system and environment under the standard model of open quantum systems is a system linearly coupled to the environment. The Hamiltonian representing this is

$$H_I = \sum_\lambda \left(g_\lambda^* L a_\lambda^\dagger + g_\lambda L^\dagger a_\lambda \right), \tag{2.40}$$

where L is an operator that mediates the influence of the environment interaction, and g_λ is the coupling strength of mode λ.

It is of use at this point to change to an interaction picture with respect to the bath, an intermediate between the Schrödinger and Heisenberg pictures discussed in the previous chapter. In this representation the Hamiltonian is split as

$$H(t) = H_0 + H_I(t), \tag{2.41}$$

where H_0 often represents a well understood exactly solvable part, describing some system of interest such as a molecule, while $H_I(t)$ can be considered a perturbation, describing some external system. In general, H_0 represents the sum of energies of the two systems when interaction between them is ignored, whilst $H_I(t)$ represents the interaction between the systems. Time dependence is imposed on the environment operators in a similar manner to the time evolution of operators in a Heisenberg picture, and the total Hamiltonian is written as

$$H(t) = H_S + \sum_\lambda (g_\lambda^* e^{iH_B t} L a_\lambda^\dagger e^{-iH_B t} + g_\lambda e^{iH_B t} L^\dagger a_\lambda e^{-iH_B t}). \tag{2.42}$$

A simplification of this expression is now given in a formal manner, however, a more succinct simplification is presented in Eq. 2.51. Consider the action of the exponential on the annihilation operator

$$\sum_\lambda e^{iH_B t} a_\lambda e^{-iH_B t} = \sum_\lambda \prod_k \left(e^{i\omega_k t N_k}\right) a_\lambda \prod_k \left(e^{-i\omega_k t N_k}\right), \tag{2.43}$$

where $N_k = a_k^\dagger a_k$, and the commutativity of operators of different modes k is used to split the summation in the exponential into a product of exponentials. Furthermore, only the exponentials with $k = \lambda$ will act on a_λ thus

$$\sum_\lambda \prod_k \left(e^{i\omega_k t N_k}\right) a_\lambda \prod_k \left(e^{-i\omega_k t N_k}\right) = \sum_\lambda e^{i\omega_\lambda t N_\lambda} a_\lambda e^{-i\omega_\lambda t N_\lambda}. \tag{2.44}$$

Using bra-ket notation for the operators

$$a_\lambda = \sum_n \sqrt{n_\lambda} |n_\lambda - 1\rangle\langle n_\lambda|, \tag{2.45}$$

$$N_\lambda = \sum_l l_\lambda \left|l_\lambda\right\rangle \left\langle l_\lambda\right|, \tag{2.46}$$

and rules for exponentiation of a diagonal operator from which it follows that

$$e^{i\omega_\lambda t N_\lambda} = \sum_l e^{i\omega_\lambda t l_\lambda} \left|l_\lambda\right\rangle \left\langle l_\lambda\right|, \tag{2.47}$$

equation 2.44 can be rewritten as

$$\begin{aligned}
&\sum_{\lambda}\sum_{n}\sum_{lm} e^{i\omega_\lambda t l_\lambda}\sqrt{n_\lambda}\,|l_\lambda\rangle\,\langle l_\lambda|\,n_\lambda-1\rangle\langle n_\lambda\,|m_\lambda\rangle\,\langle m_\lambda|\,e^{-i\omega_\lambda t m_\lambda}\\
&=\sum_{\lambda}\sum_{n} e^{i\omega_\lambda t(n_\lambda-1)}\sqrt{n_\lambda}\;|n_\lambda-1\rangle\langle n_\lambda|e^{-i\omega_\lambda t n_\lambda}\\
&=\sum_{\lambda} e^{-i\omega_\lambda t}a_\lambda. \qquad (2.48)
\end{aligned}$$

Thus the result

$$\sum_{\lambda} e^{iH_B t}a_\lambda e^{-iH_B t}=\sum_{\lambda} e^{-i\omega_\lambda t}a_\lambda \qquad (2.49)$$

is obtained and a similar reasoning leads to the expression

$$\sum_{\lambda} e^{iH_B t}a_\lambda^\dagger e^{-iH_B t}=\sum_{\lambda} e^{i\omega_\lambda t}a_\lambda^\dagger. \qquad (2.50)$$

Alternatively, these results can be obtained more succinctly by using the Baker-Campbell-Hausdorff relation

$$e^A B e^{-A}=B+[A,B]+\frac{1}{2!}[A,[A,B]]+\frac{1}{3!}[A,[A,[A,B]]]+\dots\ , \qquad (2.51)$$

which can be useful in determining the time evolution of an operator in the Heisenberg or interaction picture. With $A=i\omega_\lambda t N_\lambda$, $B=a_\lambda$, and the commutator result of $[N_\lambda,a_\lambda]$ the relation gives

$$\begin{aligned}
e^{i\omega_\lambda t N_\lambda}a_\lambda e^{-i\omega_\lambda t N_\lambda}&=a_\lambda-i\omega_\lambda t a_\lambda+\frac{1}{2!}(i\omega_\lambda t)^2 a_\lambda+\dots\\
&=a_\lambda\sum_{n}^{\infty}\frac{(-i\omega_\lambda t)^n}{n!}\\
&=e^{-i\omega_\lambda t}a_\lambda, \qquad (2.52)
\end{aligned}$$

where the Taylor expansion of $e^{-i\omega_\lambda t}$ has been used. Summation over the modes λ swiftly leads once again to the result of Eq. 2.49. Substituting Eq. 2.49 and Eq. 2.50 into Eq. 2.42 allows the total Hamiltonian to be written as

$$H(t)=H_S+\sum_{\lambda}\left(g_\lambda^* e^{i\omega_\lambda t}L a_\lambda^\dagger+g_\lambda e^{-i\omega_\lambda t}L^\dagger a_\lambda\right), \qquad (2.53)$$

where now the time dependence of the environment operators is incorporated through the phase $e^{\pm i\omega_\lambda t}$. It is useful to introduce a term which is often referred to as the force

$$B(t)=\sum_{\lambda} g_\lambda a_\lambda e^{-i\omega_\lambda t}, \qquad (2.54)$$

which allows the total Hamiltonian to be rewritten as

$$H(t) = H_S + LB(t)^\dagger + L^\dagger B(t). \tag{2.55}$$

From this equation, as H_S is the system Hamiltonian and L and $L^\dagger$ are system operators, we see that the force represents the environment part of the interaction. Furthermore, it can be used to define a quantity called the bath correlation function (BCF) that parameterises the environment. Before the BCF is presented we shall review necessary concepts in thermodynamics and statistics in the quantum regime, and time correlation functions.

2.4 Quantum statistics and thermodynamics

Thus far we have introduced the concept of mixed states, density matrix representation, and also the notion of a bath at thermal equilibrium. The intersection of these topics is of central importance in defining the thermal equilibrium state as such states are mixed. In this section we will not aim to give a complete background of the topic, a more detailed view of which can be found in several books [13, 130, 132–136]. Instead, we shall focus on the necessary details from these sources in order to describe the thermal equilibrium state of a quantum system that will enter in the OQS theory presented later in this chapter. Statistical physics provides the framework in which the microscopic properties of molecules and atoms can be related to the macroscopic properties that are observed. Core concepts include the microstate, the probability density, and ensembles. The microstate is related to entropy and defines a particular microscopic configuration (the coordinates and momenta of particles) that is occupied with a certain probability. Thermodynamics provides a characterisation of the system in terms of the macroscopic state. Statistical physics links the thermodynamic observed properties to the statistical distribution of an ensemble of microstates. An important quantity with respect to ensembles is the probability density $\rho(q_i, p_j)$. With this the average value of a variable A is given by

$$\langle A \rangle = \int dp\, dq\, A(p,q)\rho(p,q). \tag{2.56}$$

There are three thermodynamic ensembles that are central to statistical physics. Firstly, there is the microcanonical ensemble, which defines the case where copies of the system can be in different microstates, but where each configuration has the same average

energy. Secondly, the canonical ensemble describes a system that is fixed in composition and in thermal equilibrium with a bath. In contrast to the microcanonical ensemble, whilst the total system plus bath has an energy at a constant value, the system part is not fixed. Thus there is a probability p_i of the system being in a microstate with an associated energy E_i. Lastly, the grand canonical ensemble describes systems where the number of particles is not fixed and the exchange of energy and matter is allowed. For an equilibrium system at temperature T the canonical probability distribution is given by

$$\rho_{eq} = \frac{e^{-\beta H}}{Z}, \tag{2.57}$$

where Z is the canonical partition function associated with the statistical properties of the canonical ensemble and $\beta = 1/(k_B T)$, where k_B is the Boltzmann constant. Extending to quantum mechanics, the density matrix at thermal equilibrium ρ_{eq} is a diagonal matrix with Boltzmann weighted populations such that

$$\rho_{mn} = p_n = \frac{e^{-\beta E_n}}{Z}, \tag{2.58}$$

where

$$Z = \sum_n \exp(-\beta E_n). \tag{2.59}$$

Therefore, we can see that in the canonical ensemble the probabilities of states depends on their energy. In operator form, by noting that $\hat{H}|n\rangle = E_n|n\rangle$, the equilibrium density matrix can be written as

$$\rho_{eq} = \frac{\exp(-\beta \hat{H})}{\mathrm{tr}(\exp(-\beta \hat{H}))}, \tag{2.60}$$

where $\hat{H}$ represents the Hamiltonian operator of the system. The expectation value of an operator $\hat{A}$ is then given by

$$\langle \hat{A} \rangle = \mathrm{tr}(\hat{A} \rho_{eq}). \tag{2.61}$$

Therefore, there is a clear correspondence between the classical and quantum cases. In the classical case an ensemble averaging is performed with an integral over the probability density. In the quantum case, the density matrix takes the place of the probability density and the trace operation takes the place of the integrals. The equilibrium density matrix will constitute an important part of defining the time correlation function for an ensemble at finite temperature, which we shall discuss in the next section.

2.5 Time correlation functions

Time correlation functions are a useful tool in describing the dynamics of a system, the equilibrium state, and linear response [68]. They give a statistical description of the time evolution of an expectation value for an ensemble at finite temperature, and are useful in describing random (stochastic) and irreversible processes in condensed phases. A full description can be found in the literature [68, 130], which we shall follow in this section to outline important details and derivations.

For a single time-dependent trajectory of a molecular variable A, the expectation value can appear noisy and highly random. However, the noise arises as a consequence of interactions with the environment and so information on this interaction is contained in the trajectory. It is possible to encode the characteristic time-scales and amplitudes of these interactions by comparing the value of A at a time t with the value of A at a later time t'. This action defines the time-correlation function

$$\begin{aligned} C_{AA}(t,t') &= \langle A(t)A(t')\rangle_{eq} \\ &= \mathrm{tr}\big[\rho_{eq}A(t)A(t')\big] \\ &= \sum_n p_n \langle n|A(t)A(t')|n\rangle, \end{aligned} \tag{2.62}$$

for which ρ_{eq} is the thermal equilibrium density matrix and

$$p_n = e^{-\beta E_n}/Z, \tag{2.63}$$

$$\beta = 1/(k_B T), \tag{2.64}$$

where Z is the partition function, E_n are the energies, k_B is the Boltzmann constant, and T is the temperature.

As the correlation function involves the same variable A it is also known as an auto-correlation function, the cross correlation function describes the correlation function of two different variables. The time correlation function describes how long a property of a system persists until averaged out by microscopic fluctuations and interactions with its environment. Thus, it provides information on a statistical relationship and how long it persists.

Quantum time-correlation functions (QCF) involve the thermal equilibrium average over a product of Hermitian operators evaluated at two times. It is commonly written

in the form

$$C_{AA}(\tau) = \langle A(\tau)A(0)\rangle, \tag{2.65}$$

where the thermal average is implicitly implied, and a Heisenberg representation has been used. Explicitly the QCF is given by

$$C_{AA}(\tau) = \langle \frac{e^{-\beta H}}{Z} A(\tau)A(0)\rangle, \tag{2.66}$$

where H is the Hamiltonian, and the partition function is defined as

$$Z = \mathrm{Tr}[e^{-\beta H}]. \tag{2.67}$$

Evaluating the QCF for a time dependent Hamiltonian in a basis of states $|n\rangle$ gives

$$C_{AA}(\tau) = \sum_n p_n \langle n|A(\tau)A(0)|n\rangle. \tag{2.68}$$

If the eigenstates are known then, in the Schrödinger representation, the QCF is given by

$$\begin{aligned} C_{AA}(\tau) &= \sum_n p_n \langle n|U^\dagger(\tau)AU(\tau)A|n\rangle \\ &= \sum_{n,m} p_n \langle n|A|m\rangle\langle m|A|n\rangle e^{-i\omega_{nm}\tau} \\ &= \sum_{n,m} p_n |A_{nm}|^2 e^{-i\omega_{nm}\tau}, \end{aligned} \tag{2.69}$$

where U is the time evolution operator, and ω_{nm} are the frequencies associated with the eigenstates.

2.5.1 Bath correlation function

The bath correlation function (BCF) is an auto-correlation function that is useful in describing the dynamical and thermal properties of a bath. In this section it is derived following [130] for a harmonic bath with relaxation between two states where the result can be extended to the consideration of multiple states. Firstly, assume the system is prepared in an excited vibrational state $\nu = |1\rangle$ and we want to describe relaxation to $\nu = |0\rangle$. The system and bath Hamiltonian are given by

$$H_S = \hbar\omega_0(P^2 + Q^2), \tag{2.70}$$

$$H_B = \sum_\alpha \hbar\omega_\alpha(p_\alpha^2 + q_\alpha^2) = \sum_\alpha \hbar\omega_\alpha(a_\alpha^\dagger a_\alpha + \frac{1}{2}), \tag{2.71}$$

where P, Q, and ω_0 are the momentum, coordinate, and frequency of the system respectively, and p_α, q_α, and ω_α are the momentum, coordinate, and frequency respectively of bath mode α. Furthermore, $a_\alpha^\dagger$ and a_α are the creation and annihilation operators of bath mode α. The system-bath interaction is taken to be linear in the bath coordinate such that

$$H_{SB} = \sum_\alpha c_\alpha Q q_\alpha, \tag{2.72}$$

where c_α represents the coupling strength to bath mode α. In order to define relaxation from $a = |1\rangle$ to $b = |0\rangle$ let the system-bath interaction be denoted by

$$V_{ba} = \sum_\alpha \xi_{ab,\alpha}(a_\alpha^\dagger + a_\alpha), \tag{2.73}$$

which is a specific case of the more general interaction Hamiltonian of Eq. 2.40, where

$$\xi_{ab,\alpha} = c_\alpha \frac{\sqrt{m_Q m_q \omega_0 \omega_\alpha}}{2\hbar} \langle b|Q|a\rangle, \tag{2.74}$$

for which m_Q and m_q represent the mass for system, and masses of the bath modes assumed here to be equal for each mode. Then the correlation function is given by

$$\begin{aligned}
\langle V_{ab}(t) V_{ba}(0)\rangle &= \langle e^{iH_B t} V_{ab} e^{-iH_B t} V_{ba}\rangle \\
&= \langle e^{iH_B t} \sum_\alpha \xi_{ab,\alpha}(a_\alpha^\dagger + a_\alpha) e^{-iH_B t} \sum_{\alpha'} \xi_{ba,\alpha'}(a_{\alpha'}^\dagger + a_{\alpha'})\rangle \\
&= \langle \sum_\alpha \xi_{ab,\alpha}(a_\alpha^\dagger e^{i\omega_\alpha t} + a_\alpha e^{-i\omega_\alpha t}) \sum_{\alpha'} \xi_{ba,\alpha'}(a_{\alpha'}^\dagger + a_{\alpha'})\rangle \\
&= \sum_\alpha \xi_\alpha^2 [(\bar{n}_\alpha + 1) e^{-i\omega_\alpha t} + (\bar{n}_\alpha e^{i\omega_\alpha t})],
\end{aligned} \tag{2.75}$$

where

$$\bar{n}_\alpha = \frac{1}{e^{\beta\hbar\omega_\alpha} - 1}, \tag{2.76}$$

and equations 2.49 and 2.50 are used in going from the second line to the third. The final step makes use of the following relations

$$\langle a_\alpha a_{\alpha'}^\dagger\rangle = (\bar{n}_\alpha + 1)\delta_{\alpha\alpha'} \tag{2.77}$$

$$\langle a_\alpha^\dagger a_{\alpha'}\rangle = \bar{n}_\alpha \delta_{\alpha\alpha'}. \tag{2.78}$$

$$\langle a_\alpha a_{\alpha'}\rangle = 0 \tag{2.79}$$

$$\langle a_\alpha^\dagger a_{\alpha'}^\dagger\rangle = 0, \tag{2.80}$$

where the latter two relations follow simply from the orthogonality of $|n\rangle$ as

$$\begin{aligned}\langle aa\rangle &= \langle n|aa|n\rangle \\ &= \sqrt{n(n-1)}\langle n|n-2\rangle \\ &= 0,\end{aligned} \tag{2.81}$$

and

$$\begin{aligned}\langle a^\dagger a^\dagger\rangle &= \langle n|a^\dagger a^\dagger|n\rangle \\ &= \sqrt{(n+1)(n+2)}\langle n|n+2\rangle \\ &= 0.\end{aligned} \tag{2.82}$$

The relation of Eq. 2.78, is proven as follows

$$\begin{aligned}\langle a_\alpha^\dagger a_\alpha\rangle &= \mathrm{tr}(a_\alpha^\dagger a_\alpha \frac{e^{-\beta H}}{Z}) \\ &= \sum_n \frac{\langle n|a_\alpha^\dagger a_\alpha e^{-\beta H}|n\rangle}{\sum_n \langle n|e^{-\beta H}|n\rangle} \\ &= \sum_n \frac{n e^{-\beta E_n}}{\sum_n e^{-\beta E_n}}.\end{aligned} \tag{2.83}$$

Using

$$E_n = \hbar\omega_\alpha(n+\frac{1}{2}), \tag{2.84}$$

the equation can be written as

$$\frac{e^{-\beta\hbar\omega_\alpha/2}}{e^{-\beta\hbar\omega_\alpha/2}}\sum_n \frac{n e^{-\beta\hbar\omega_\alpha n}}{\sum_n e^{-\beta\hbar\omega_\alpha n}}, \tag{2.85}$$

which, using geometric series relations can be simplified to

$$\begin{aligned}\frac{e^{-\beta\hbar\omega_\alpha}}{(e^{-\beta\hbar\omega_\alpha}-1)^2}\left(\frac{e^{-\beta\hbar\omega_\alpha}-1}{e^{-\beta\hbar\omega_\alpha}}\right) &= \frac{1}{(e^{-\beta\hbar\omega_\alpha}-1)} \\ &= \bar{n}_\alpha,\end{aligned} \tag{2.86}$$

which provides the required result and corresponds to the Bose-Einstein distribution, the expected number of bosonic particles that occupy a set of discrete energy levels at thermal equilibrium. The relation of Eq. 2.77 follows from a similar proof. Continuing

with the derivation from Eq. 2.75 we obtain

$$\begin{aligned}
&\sum_{\alpha} \xi_{\alpha}^2 [\bar{n}_{\alpha}(e^{-i\omega_{\alpha}t} + e^{i\omega_{\alpha}t}) + e^{-i\omega_{\alpha}t}] \\
&= \sum_{\alpha} \xi_{\alpha}^2 [2\bar{n}_{\alpha}\cos(\omega_{\alpha}t) + \cos(\omega_{\alpha}t) - i\sin(\omega_{\alpha}t)] \\
&= \sum_{\alpha} \xi_{\alpha}^2 [(2\bar{n}_{\alpha} + 1)\cos(\omega_{\alpha}t) - i\sin(\omega_{\alpha}t)] \\
&= \sum_{\alpha} \xi_{\alpha}^2 [\coth\left(\frac{\beta\hbar\omega_{\alpha}}{2}\right)\cos(\omega_{\alpha}t) - i\sin(\omega_{\alpha}t)],
\end{aligned} \tag{2.87}$$

where standard exponential trigonometric relations have been used going from the first line to the second. For the final step from the third to the fourth line note

$$\begin{aligned}
2\bar{n}_{\alpha} + 1 &= \frac{2}{e^{\beta\hbar\omega_{\alpha}} - 1} + 1 \\
&= \frac{e^{\beta\hbar\omega_{\alpha}} + 1}{e^{\beta\hbar\omega_{\alpha}} - 1},
\end{aligned} \tag{2.88}$$

multiplying numerator and denominator by $e^{-\beta\hbar\omega_{\alpha}/2}$ gives

$$\frac{e^{\beta\hbar\omega_{\alpha}/2} + e^{-\beta\hbar\omega_{\alpha}/2}}{e^{\beta\hbar\omega_{\alpha}/2} - e^{-\beta\hbar\omega_{\alpha}/2}} = \coth\left(\frac{\beta\hbar\omega_{\alpha}}{2}\right), \tag{2.89}$$

where the hyperbolic identity

$$\coth(x) = \frac{e^{x} + e^{-x}}{e^{x} - e^{-x}} \tag{2.90}$$

has been utilised. Equation 2.87 is the common form of the bath correlation function. In section 2.3 of this chapter we defined the force term as

$$B(t) = \sum_{\alpha} g_{\alpha} a_{\alpha} e^{-i\omega_{\alpha}t}, \tag{2.91}$$

which is a term defined from the interaction Hamiltonian that fully described the interaction with the environment, where g_{α} is the coupling strength of mode α. As such it is closely related to the bath correlation function through the relation

$$\alpha(t-s) = \langle (B(t) + B^{\dagger}(t))(B(s) + B^{\dagger}(s)) \rangle. \tag{2.92}$$

Generalising the two state relaxation, the dynamical properties and temperature of the environment determine the form of the BCF such that for a thermal state at temperature T

$$\alpha(\tau) = \int_0^{\infty} d\omega\, J(\omega) \Big[\coth\Big(\frac{\omega}{2T}\Big)\cos(\omega\tau) - i\sin(\omega\tau)\Big], \tag{2.93}$$

where the spectral density $J(\omega) = \sum_\lambda |g_\lambda|^2 \delta(\omega - \omega_\lambda)$ has been introduced which encodes the frequency dependence of the interaction strength. Note also, that as a physical spectral density is real, the bath correlation function is hermitian $\alpha(-\tau) = \alpha^*(\tau)$.

If a zero temperature assumption is made, which will be necessary for some of the derivations presented, then all modes of the bath are in the vacuum state and so the bath correlation function reduces to

$$\begin{aligned} \alpha_{T=0}(t-s) &= \langle B(t) B^\dagger(s) \rangle \\ &= \int_0^\infty J(\omega) e^{-i\omega(t-s)} \, d\omega. \end{aligned} \tag{2.94}$$

2.6 Thermofield theory

The stochastic wavefunction methods derived in this thesis require a pure state description of the initial state. However, thermal states are mixed and thus described by a density matrix. This presents a problem if we wish to maintain the mathematical structure of the pure state methods whilst including finite temperature. The thermofield method [137–139] offers a solution to this problem by providing a means of describing the mixed thermal state as an entangled pure state in a doubled state space. Thus, thermal averages are able to be expressed as vacuum expectation values for a temperature dependent vacuum state. Interestingly, such a feat can be generalised allowing a pure state description for any mixed state in the process of purification [122, 140]. In this section, following the results of [137], the thermofield method is detailed to demonstrate how to achieve a pure state description of a thermal state. A summary is provided at the end of the section to explain the main results and how they are used in this thesis.

The expectation value of an observable A for a quantum system in a thermal state is given by

$$\langle A \rangle = \mathrm{tr}(A \rho_{eq}) = Z^{-1} \mathrm{tr}(A e^{-\beta H}), \tag{2.95}$$

where Z is the partition function, $\beta = (k_B T)^{-1}$ is the inverse temperature, H is the Hamiltonian and

$$\rho_{eq} = \frac{e^{-\beta H}}{Z}, \tag{2.96}$$

is the thermal equilibrium state. The thermofield representation seeks to express the expectation value of the mixed state as a pure-state expectation value which satisfies

$$\begin{aligned}\langle A\rangle &= \langle 0(\beta)|A|0(\beta)\rangle \\ &= Z^{-1}\sum_n \langle n|A|n\rangle e^{-\beta E_n},\end{aligned} \tag{2.97}$$

where $|0(\beta)\rangle$ is introduced as the so called temperature dependent vacuum state and

$$H|n\rangle = E_n|n\rangle, \tag{2.98}$$

$$\langle n|m\rangle = \delta_{nm}. \tag{2.99}$$

If we try to construct the state $|0(\beta)\rangle$ simply as a superposition of energy eigenstates of the Hilbert space

$$|0(\beta)\rangle = \sum_n |n\rangle f_n(\beta), \tag{2.100}$$

then one requires that

$$f_n^*(\beta) f_m(\beta) = Z^{-1} e^{-\beta E_n}\delta_{nm}, \tag{2.101}$$

which is not possible for numbers alone, but it is satisfied if $f_n(\beta)$ are orthogonal vectors. This can be achieved by introducing a fictitious space, which is denoted by a tilde, and represents an identical dynamical system such that for every state $|\psi\rangle$ in H, there is a copy $|\tilde{\psi}\rangle$ in $\tilde{H}$ [138]. The fictitious system Hamiltonian $\tilde{H}$ and the state vector space spanned by vectors $|\tilde{n}\rangle$ satisfy

$$\tilde{H}|\tilde{n}\rangle = E_n|\tilde{n}\rangle \tag{2.102}$$

$$\langle\tilde{n}|\tilde{m}\rangle = \delta_{nm} \tag{2.103}$$

where by definition E_n is the same as in Eq. 2.99. Consider the space spanned by $|n,\tilde{m}\rangle$, the direct product of $|n\rangle$ and $|\tilde{m}\rangle$. The matrix element of A is

$$\langle\tilde{m},n|A|n',\tilde{m}'\rangle = \langle n|A|n'\rangle\delta_{mm'}, \tag{2.104}$$

where the prime is used to indicate a different element. It should be noted that only the vectors belonging to the space of the operator act directly, the remaining tilde vectors, due to orthogonality, result in the dirac delta. Likewise, the matrix element of $\tilde{A}$ is

$$\langle\tilde{m},n|\tilde{A}|n',\tilde{m}'\rangle = \langle\tilde{m}|\tilde{A}|\tilde{m}'\rangle\delta_{nn'}. \tag{2.105}$$

Thus if we assume

$$f_n(\beta) = |\tilde{n}\rangle e^{-\beta E_n/2} Z^{-1/2} \tag{2.106}$$

then the required property of $f_n(\beta)$ is obtained as

$$\begin{aligned} f_n^*(\beta) f_m(\beta) &= Z^{-1} e^{-\beta E_n/2} \langle \tilde{n}|\tilde{m}\rangle \\ &= Z^{-1} e^{-\beta E_n} \delta_{nm}. \end{aligned} \tag{2.107}$$

Therefore, the temperature dependent vacuum state $|0(\beta)\rangle$ can be obtained by substituting Eq. 2.106 into Eq. 2.100

$$|0(\beta)\rangle = Z^{-1/2} \sum_n e^{-\beta E_n/2} |n, \tilde{n}\rangle, \tag{2.108}$$

which is a pure state of two identical systems that are entangled in their energy. It follows that the state $|0(\beta)\rangle$ satisfies

$$\begin{aligned} \langle 0(\beta)|A|0(\beta)\rangle &= Z^{-1} \sum_{n,m} e^{-\beta E_n/2} e^{-\beta E_m/2} \langle \tilde{n}, n|A|m, \tilde{m}\rangle \\ &= Z^{-1} \sum_n e^{-\beta E_n} \langle n|A|n\rangle. \end{aligned} \tag{2.109}$$

Thus, the correct thermal equilibrium statistical average is obtained and it can be seen that the tilde degrees of freedom are not explicit in the end result as they do not directly act on A. Instead, as they represent an identical copied space, if $\tilde{n} = \tilde{m}$ then we must also have $n = m$. Thus the fictitious space vectors act akin to a delta function allowing the selection of diagonal elements of A with respect to n, just as a trace operation would allow for a density matrix.

Applying these concepts to an ensemble of free bosons with frequency ω, the physical Hamiltonian is given by

$$H = \omega a^\dagger a \tag{2.110}$$

where the usual bosonic commutation relations for creation and annihilation operators hold as

$$[a, a^\dagger] = 1, \tag{2.111}$$

$$[a, a] = 0. \tag{2.112}$$

The fictitious state space is introduced with Hamiltonian

$$\tilde{H} = \omega \tilde{a}^\dagger \tilde{a}, \tag{2.113}$$

and the commutation relations are given by

$$[\tilde{a}, \tilde{a}^\dagger] = 1, \tag{2.114}$$

$$[\tilde{a}, \tilde{a}] = 0, \tag{2.115}$$

and we assume that

$$[a, \tilde{a}] = [a, \tilde{a}^\dagger] = 0. \tag{2.116}$$

The temperature dependent vacuum state for this system can then be related to the direct product of the physical and fictitious vacuum states

$$\begin{aligned} |0(\beta)\rangle &= Z^{-1/2} \sum_n e^{-\beta n\omega/2} \frac{1}{n!} (a^\dagger)^n (\tilde{a}^\dagger)^n |0, \tilde{0}\rangle \\ &= \sqrt{(1 - e^{-\beta\omega})} \exp\Big\{ (e^{-\beta\omega/2} a^\dagger \tilde{a}^\dagger) \Big\} |0, \tilde{0}\rangle. \end{aligned} \tag{2.117}$$

Furthermore, it is of use to define temperature dependent operators that act on the temperature dependent vacuum state, and transformations to and from the physical and fictitious operators and states. To achieve this first let

$$u(\beta) = (1 - e^{-\beta\omega})^{-1/2} = \sqrt{(1 + \bar{n})} \tag{2.118}$$

$$v(\beta) = (e^{\beta\omega} - 1)^{-1/2} = \sqrt{\bar{n}} \tag{2.119}$$

$$G_B = -i\theta(\beta)(\tilde{a}a - a^\dagger \tilde{a}^\dagger), \tag{2.120}$$

where $|u(\beta)|^2 - |v(\beta)|^2 = 1$, $\cosh\theta(\beta) = u(\beta)$ and, as in Eq. 2.76, $\bar{n}$ represents the expected number of particles following Bose-Einstein statistics. Consequently, this allows the following parametrisation

$$\sinh\theta(\beta) = v(\beta). \tag{2.121}$$

We can thus write $|0(\beta)\rangle$ as

$$|0(\beta)\rangle = u^{-1}(\beta) \exp\left(\frac{v(\beta)}{u(\beta)} a^\dagger \tilde{a}^\dagger \right) |0, \tilde{0}\rangle \tag{2.122}$$

$$= e^{-iG_B} |0, \tilde{0}\rangle, \tag{2.123}$$

which has a similar form to the displacement operator, which can be applied to a vacuum state to obtain a coherent state. The transformation can be applied to define temperature dependent operators

$$a(\beta) = e^{-iG_B} a e^{iG_B} = u(\beta)a - v(\beta)\tilde{a}^\dagger, \tag{2.124}$$

$$\tilde{a}(\beta) = e^{-iG_B} \tilde{a} e^{iG_B} = u(\beta)\tilde{a} - v(\beta)a^\dagger, \tag{2.125}$$

$$a^\dagger(\beta) = e^{-iG_B} a^\dagger e^{iG_B} = u(\beta)a^\dagger - v(\beta)\tilde{a}, \tag{2.126}$$

$$\tilde{a}^\dagger(\beta) = e^{-iG_B} \tilde{a}^\dagger e^{iG_B} = u(\beta)\tilde{a}^\dagger - v(\beta)a. \tag{2.127}$$

The inverse transformations are given by

$$a = u(\beta)a(\beta) + v(\beta)\tilde{a}^\dagger(\beta), \tag{2.128}$$

$$\tilde{a} = u(\beta)\tilde{a}(\beta) + v(\beta)a^\dagger(\beta), \tag{2.129}$$

$$a^\dagger = u(\beta)a^\dagger(\beta) + v(\beta)\tilde{a}(\beta), \tag{2.130}$$

$$\tilde{a}^\dagger = u(\beta)\tilde{a}^\dagger(\beta) + v(\beta)a(\beta). \tag{2.131}$$

Note that, for the temperature dependent operators, we regain annihilation properties of the vacuum state

$$a(\beta)|0(\beta)\rangle = \tilde{a}(\beta)|0(\beta)\rangle = 0, \tag{2.132}$$

as the same transformation to the state has been applied to the creation and annihilation operators. The new state space is spanned by

$$|0(\beta)\rangle, a^\dagger(\beta)|0(\beta)\rangle, \tilde{a}^\dagger(\beta)|0(\beta)\rangle, \ldots, \frac{1}{\sqrt{n!}}\frac{1}{\sqrt{m!}}\Big(a^\dagger(\beta)\Big)^n\Big(\tilde{a}^\dagger(\beta)\Big)^m|0(\beta)\rangle, \ldots \tag{2.133}$$

However, these are not eigenstates of the Hamiltonian H. Instead, the relation

$$a^\dagger a - \tilde{a}^\dagger\tilde{a} = a^\dagger(\beta)a(\beta) - \tilde{a}^\dagger(\beta)\tilde{a}(\beta) \tag{2.134}$$

implies that $\hat{H} = H - \tilde{H}$ is diagonal, where the hat notation is simply used to distinguish the operator $\hat{H}$ from operators H and $\tilde{H}$, and the following relations hold:

$$\hat{H}|0(\beta)\rangle = 0, \tag{2.135}$$

$$\hat{H}a^\dagger(\beta)|0(\beta)\rangle = \omega a^\dagger(\beta)|0(\beta)\rangle, \tag{2.136}$$

$$\hat{H}\tilde{a}^\dagger(\beta)|0(\beta)\rangle = -\omega\tilde{a}^\dagger(\beta)|0(\beta)\rangle, \tag{2.137}$$

$$\hat{H}a^\dagger(\beta)\tilde{a}^\dagger(\beta)|0(\beta)\rangle = 0. \tag{2.138}$$

An illuminating example of using the temperature dependent operators is the calculation of the statistical average of $a^\dagger a$

$$\begin{aligned}\langle 0(\beta)|a^\dagger a|0(\beta)\rangle =&\langle 0(\beta)|u^2(\beta)a^\dagger(\beta)a(\beta) + u(\beta)v(\beta)(a^\dagger(\beta)\tilde{a}^\dagger(\beta) + \tilde{a}(\beta)a(\beta))\\ &+ v^2(\beta)\tilde{a}(\beta)\tilde{a}^\dagger(\beta)|0(\beta)\rangle. \end{aligned} \tag{2.139}$$

The only surviving term is the last, whilst the other terms are zero as they annihilate the temperature dependent vacuum state, therefore we obtain

$$\begin{aligned}\langle 0(\beta)|a^\dagger a|0(\beta)\rangle &= v^2(\beta)\\ &= \sinh^2\theta(\beta)\\ &= \frac{1}{e^{\beta\omega}-1}\\ &= \bar{n}, \end{aligned} \tag{2.140}$$

which was the result of Eq. 2.86 using the thermal equilibrium density matrix and the original physical space operators.

Much of the derivation thus far is motivated by satisfying required mathematical properties to achieve correct statistical averages. As a result, it is of use at this point to discuss the physical interpretation. Firstly, note that for the thermal equilibrium state $|0(\beta)\rangle$ the average energy $\langle H\rangle$ is equal to $\langle\tilde{H}\rangle$. Consider

$$\tilde{a}|0(\beta)\rangle = \Big(u(\beta)\tilde{a} - v(\beta)a^\dagger\Big)|0(\beta)\rangle, \tag{2.141}$$

from which it follows that as $\tilde{a}|0(\beta)\rangle = 0$ we have

$$\frac{1}{v(\beta)}\tilde{a}|0(\beta)\rangle = \frac{1}{u(\beta)}a^\dagger|0(\beta)\rangle. \tag{2.142}$$

Using the inverse relation Eq. 2.129 we can rewrite this equation in terms of the temperature dependent operators, substituting for the left hand side gives

$$\begin{aligned}\frac{u(\beta)}{v(\beta)}\tilde{a}(\beta)|0(\beta)\rangle + a^\dagger(\beta)|0(\beta)\rangle &= a^\dagger(\beta)|0(\beta)\rangle\\ &= \frac{1}{u(\beta)}a^\dagger|0(\beta)\rangle. \end{aligned} \tag{2.143}$$

In contrast, substituting for the right hand side using Eq. 2.130 gives

$$\begin{aligned}\frac{v(\beta)}{u(\beta)}\tilde{a}(\beta)|0(\beta)\rangle + a^\dagger(\beta)|0(\beta)\rangle &= a^\dagger(\beta)|0(\beta)\rangle\\ &= \frac{1}{v(\beta)}\tilde{a}|0(\beta)\rangle. \end{aligned} \tag{2.144}$$

Therefore, these results show that $a^\dagger(\beta)|0(\beta)\rangle$ can be formed either by creating a physical boson or by annihilating a fictitious tilde boson. This result provides the interpretation that the tilde boson is the hole of the physical one. An interesting observation is that as $T \to 0$, $v(\beta) \to 0$ and $u(\beta) \to 1$. Therefore, $a(\beta) \to a$ and $\tilde{a}(\beta) \to \tilde{a}$, and the temperature dependent operators reduce to original operators. Each of these are then only dependent on a tilde operator or physical operator. As the temperature increases then the temperature dependent operators become mixed between tilde and physical operations. Thus they can be interpreted as bound quasiparticles, sometimes known as collective excitations when referring to bosons, of thermal physical particles and holes. This is similar to how an exciton is a bound state of an electron and electron hole. In the case of the temperature dependent operators it describes an aggregate behaviour. The temperature is included through a balance of physical and tilde particles. The temperature dependent vacuum state $|0(\beta)\rangle$ is then the state that is balanced between physical and tilde particles in such a way to achieve thermal equilibrium statistics. Furthermore, $a(\beta)$ applied to this state would annihilate the physical particle and create a tilde particle weighted with $u(\beta)$ and $-v(\beta)$ respectively. However, as $a(\beta)|0(\beta)\rangle = 0$, this implies the action of the operators cancel and the thermal equilibrium balance of particles is met. These notions will be explored further in section 3.3 in the context of the finite temperature non-Markovian stochastic Schrödinger equation.

In this section we have used thermofield theory to allow us to define a pure state, for which expectation values taken with respect to it can satisfy thermal statistics. Normally, to achieve correct thermal statistics one would require a mixed state given by the equilibrium density matrix ρ_{eq}. Instead, in the thermofield theory one begins by questioning what properties would be required for a pure state expectation value to give the correct thermal statistics. Through this reasoning it was found that a second fictitious space must be introduced which is a copy of the physical space. Whilst the fictitious space does not directly interact with the physical space, it is linked by its definition and, as a result, acts as the trace does for the density matrix. This allowed us to define the required pure state, the so called temperature dependent vacuum state, in terms of an entangled physical and fictitious state. Furthermore, we identified the transformation that takes one from the physical and fictitious states to the temperature dependent state and the creation and annihilation operators that act on it. Thermofield theory thus provides a framework that allows us to maintain the wavefunction structure

of the stochastic methods discussed in this thesis and include finite temperature.

Chapter 3

Stochastic Schrödinger equations

Throughout the last chapter the mathematical foundation and tools for describing an OQS have been presented. In this chapter we will discuss methods that provide the time-evolution and simulation of the dynamics of an OQS. Since its formation there have been many developments in the field of modelling OQS dynamics both theoretical, numerical, and computational, and a broad and recent overview is presented in the special topic on dynamics of open quantum systems [30]. We will focus on the stochastic Schrödinger equation (SSE) class of methods that gives the time-evolution in terms of a pure state description. Such approaches can offer a computational advantage. For example, the SSE deals with the wave function in the Hilbert space of the system following a stochastic trajectory. Thus the size of the state evolved only scales as the system basis dimension d rather than d^2 for the density matrix approaches.

In some methods that use system-bath models, assumptions are made such as the weak-coupling or Markov approximation. This leads to memoryless environment interaction processes in which there is a continuous flow of information from the system to the environment. Whilst useful for describing a range of phenomena and reducing computational cost, there are many interesting systems for which this approximation is not appropriate and a higher degree of accuracy is required. Specifically, the approximation fails when correlation times of the environment are not small compared to the systems relaxation or decoherence time. In these cases a non-Markovian method must be utilised [46, 47]. This property can be important in many problems of relevance to chemical physics and biochemistry, where the environment can be structured or strongly coupled to the system at finite temperature. Some examples of studies of dynamics of systems beyond the Markov approximation include photosynthetic complexes, and molecular physics [141–143].

Numerically exact approaches form an important class of methods that can account for non-Markovian dynamics of an OQS. Examples include the time-evolving matrix product operator (TEMPO) [49, 50], hierarchical equations of motion (HEOM) family of methods [51–53, 56], and the hierarchy of pure states (HOPS) [59–62]. These approaches are capable of calculating the dynamical and thermal properties of a reduced quantum system with an accuracy that can be incrementally increased to a desired level. Often the methods work best for smaller systems sizes and particular characterisations of the bath. Many HEOM methods utilise a density matrix representation of the system state. However, there exist equivalent numerically exact wavefunction ap-

proaches such as HOPS [59], an alternative realization of the non-Markovian stochastic Schrödinger equation [144], the hierarchy of stochastic Schrödinger equations [145], and hierarchical Schrödinger equations of motion [146]. The entire scope of methods used to simulate an OQS is too vast to cover in this chapter in detail, but reviews are available for the reader interested in the wider field and alternative methods [30, 46, 47, 53].

In this chapter the Markovian SSE shall be described and an application to a harmonic oscillator shall be presented, with a comparison to a master equation method, to demonstrate damped evolution. Following this, the non-Markovian stochastic Schrödinger equation (NMSSE) shall be discussed which accounts for memory of system-environment interaction processes. Subsequently, we will see how finite temperature is introduced to the NMSSE through the thermofield method that was presented in the last chapter. A solution scheme for the NMSSE is then presented that uses the HOPS method [59]. Lastly the non-linear version of the NMSSE is presented which has advantageous properties regarding convergence. Throughout this chapter we shall analyse the respective advantages of the SSE method which has links to other methods such as the quantum master equation, quantum Langevin equation, and coupled coherent states (CCS). In the following section we will predominantly follow the sources [41, 44] which the reader may be interested in for a more complete review.

3.1 Markovian SSE and Lindblad equation

The starting point of deriving the Markovian SSE is to model the environment as a heat bath consisting of harmonic oscillators such that [44, 108]

$$H_B = \hbar \int_{-\infty}^{\infty} d\omega\, \omega b^\dagger(\omega) b(\omega), \tag{3.1}$$

and

$$H_I = i\hbar \int_{-\infty}^{\infty} d\omega\, \kappa(\omega)[b^\dagger(\omega)L - L^\dagger b(\omega)], \tag{3.2}$$

where $b(\omega)$ are boson annihilation operators for the bath that have the relation

$$[b(\omega), b^\dagger(\omega)] = \delta(\omega - \omega'), \tag{3.3}$$

and where L is a system operator, and $\kappa(\omega)$ represents the strength of the coupling of the bath modes to the system. In this formalism the rotating wave approximation has already been made which provides the given form of the interaction Hamiltonian. In

brief, this requires a restriction of the range of frequencies in the integral of H_I and assumption that rapidly oscillating terms will quickly average to zero and may thus be neglected. Subsequently, a white noise approximation provides the extension of the lower limit of ω to $-\infty$, which admits a mathematically simple form. Additionally, an approximation commonly called the first Markov approximation is often made in which the coupling is assumed independent of the frequency such that

$$\kappa(\omega) = \sqrt{\frac{\gamma}{2\pi}}, \tag{3.4}$$

where γ represents the strength of coupling to the environment. A more complete derivation and explanation of these approximations is given by Gardiner and Zoller [44, 147], and Breuer and Petruccione [41]. Under these approximations we can derive the linear Itô stochastic Schrödinger equation

$$\begin{aligned} d|\Psi(t)\rangle = &\Bigg(\Big(-\frac{i}{\hbar} H_S - \frac{1}{2}\gamma L^\dagger L \Big) dt \\ &+ \sqrt{\gamma} dB^\dagger(t) L - \sqrt{\gamma} dB(t) L^\dagger \Bigg) |\Psi(t)\rangle, \end{aligned} \tag{3.5}$$

where H_S is the system Hamiltonian, $dB(t) = B(t+dt) - B(t)$, and

$$B(t) = \int_0^t b_{in}(s)\, ds, \tag{3.6}$$

is the quantum Wiener process for which the input noise is defined as

$$b_{in}(t) = \frac{1}{\sqrt{2\pi}} \int_{-\infty}^{\infty} d\omega\, e^{-i\omega t} b_0(\omega), \tag{3.7}$$

where $b_0(\omega) = b(\omega)|_{t=0}$. The Wiener process is a stochastic process that is continuous in t, and is commonly associated with Brownian motion. Furthermore, it satisfies the following properties: it is zero at $t = 0$, it has Gaussian increments which are normally distributed with a mean of zero and unit variance, and increments are independent of past values. The second term of Eq. 3.5 corresponds to the drift of the state, whilst the third and fourth terms correspond to random fluctuations due to the interaction of system with environment. Furthermore, the fluctuation terms with $dB^\dagger(t)L$ and $dB(t)L^\dagger$ are associated with processes from system to bath and bath to system, respectively.

In the low temperature regime we consider $|\Psi(0)\rangle = |\psi\rangle \otimes |\mathbf{0}\rangle$, where $|\mathbf{0}\rangle$ is the vacuum state for all bath annihilation operators in the bath Hilbert space, corresponding to a zero temperature approximation. Thus $dB(t)|\Psi(t)\rangle = 0$ and the linear Itô

stochastic Schrödinger equation reduces to the form

$$d|\Psi(t)\rangle = \Big(\big(-\frac{i}{\hbar} H_S - \frac{1}{2}\gamma L^\dagger L \big) dt + \sqrt{\gamma} dB^\dagger(t) L \Big) |\Psi(t)\rangle. \tag{3.8}$$

The linear form of the equation has some drawbacks for numerical simulation. In particular, the norm of the states generated via this evolution can become very small [45]. However, a non-linear version of the equation, which is suitable for numerical simulations, may be derived with the linear form as a starting point [148]. Whilst the nature of individual trajectories is different for each version, the averaged results are equivalent if there are a sufficient number of trajectories for convergence. It should be noted that there exist several forms of the equation and simulation methods that define time evolution in terms of either jump-processes [44, 149] or continuous diffusive processes [41, 150, 151]. Some of these may be interpreted in terms of a particular measurement scheme or, as in our treatment, act as a convenient method of simulating the equations of motion for an environment that continuously monitors the system.

Under the aforementioned approximations, a quantum white noise formalism is obtained and a non-linear Itô stochastic Schrödinger equation may be defined as [41, 44]

$$d|\psi(t)\rangle = D_1\big(|\psi(t)\rangle\big) dt + D_2\big(|\psi(t)\rangle\big) dW(t), \tag{3.9}$$

in which we have denoted $dW(t)$ as the increment of a Wiener process, and D_1 is called the drift term, given by

$$\begin{aligned} D_1\big(|\psi(t)\rangle\big) = &-\frac{i}{\hbar} H_S |\psi(t)\rangle \\ &+ \frac{\gamma}{2}\Big(\langle L + L^\dagger \rangle_\psi L \\ &- L^\dagger L - \frac{1}{4}\langle L + L^\dagger \rangle_\psi^2 \Big) |\psi(t)\rangle, \end{aligned} \tag{3.10}$$

where L and $L^\dagger$ are system operators often called Lindblad operators, γ quantifies the strength of coupling to the bath, and $\langle L + L^\dagger \rangle_\psi$ is concise notation for $\langle \psi(t)|L + L^\dagger|\psi(t)\rangle$. D_2 is the diffusion term, which is given by

$$D_2\big(|\psi(t)\rangle\big) = \sqrt{\gamma}\Big(L - \frac{1}{2}\langle L + L^\dagger \rangle_\psi \Big) |\psi(t)\rangle. \tag{3.11}$$

The Wiener process in the above equations must represent independent Gaussian random variables, with zero mean, and a variance of Δt. This is satisfied if

$$\Delta W_k = \sqrt{\Delta t}\,\xi_k, \tag{3.12}$$

where ΔW_k, and Δt, represent discretisations of the Wiener process and time respectively, and ξ_k is a Gaussian distributed random variable that has a mean of zero and unit variance. The closed system evolution of $|\psi(t)\rangle$ is represented by the first term in $D_1(|\psi(t)\rangle)$, whereas the open system is incorporated through the additional terms and Lindblad operators. It should be noted that for simplicity the above equations include interaction defined by a single Lindblad operator only, though the extension to multiple interactions is possible with ease. With regard to the open system terms, the drift term represents the drift of the state vector, and the diffusion term represents the random fluctuations due to the interaction of the system with the environment [152]. Equation 3.9 is also known as a quantum state diffusion equation and is a Markovian SSE. It also represents a stochastic unravelling [65, 150], which is a stochastic Schrödinger equation driven by a noise such that the mean of the solutions equals the density operator. Through this it provides an alternate solution of the density matrix equation given by the Markovian Lindblad master equation (LME) [41]

$$\begin{aligned}\frac{d}{dt}\rho(t) = &-\frac{i}{\hbar}[H_S, \rho(t)] \\ &+\gamma\Big(L\rho(t)L^\dagger - \frac{1}{2}L^\dagger L\rho(t) - \frac{1}{2}\rho(t)L^\dagger L\Big),\end{aligned} \tag{3.13}$$

where as before γ represents the strength of coupling to the environment. How the quantum state diffusion equation may be derived from a Lindblad master equation is shown by Gisin and Percival [150].

In addition, operator expectation values follow a similar relationship

$$\langle A\rangle_{\rho(t)} = \mathrm{tr}(A\rho(t)) = \mathbb{E}[\langle\psi(t)|A|\psi(t)\rangle], \tag{3.14}$$

where $\mathbb{E}$ represents taking the mean over stochastic realisations of the state $|\psi(t)\rangle$. It follows that, whilst in the mean normalisation is preserved, the norm of individual realisations may fluctuate [149]. The Lindblad equation is a simple example of an equation of motion for a reduced density matrix. Although many successful density matrix studies have been carried out which include the effect of the bath in detail [153], it is still of interest to develop wavefunction based methods because of reduced computational cost for multi-dimensional systems. An advantage of the SSE approach is that for a state space of dimension d the state vector requires only d complex numbers to define it whereas density matrix approaches require $d^2/2$. Such a reduction becomes important when considering systems with several degrees of freedom as may be required for photoswitch systems that have multiple coordinates that are relevant to the

photoisomerisation mechanism. In the following sections we shall consider extensions to non-Markovian treatments of the environment and solution through the hierarchy of pure states (HOPS) approach [59].

To formulate the SSE and the LME only the Hamiltonian and the Lindblad operators are required. Whilst Lindblad operators may be derived, they may also arbitrarily be chosen up to the requirement of being a system operator in order to represent desired phenomena [154]. A common choice is relaxation through resonant energy transfer between system and bath, for which the Lindblad operators are chosen to be the creation and annihilation operators of the systems manifold. One such example is the case of a damped quantum harmonic oscillator for which $L = a$, where a represents the lowering ladder operator for the harmonic oscillator [41, 47, 150]. Similarly, in the Markovian SSE approaches of this thesis, the Lindblad operator is chosen to be a lowering operator in order to to generate damped dynamics on respective potential energy surfaces (PESs) such that the system relaxes to the lowest vibrational eigenstate on each PES.

To simulate the stochastic Schrödinger equation an appropriate numerical method that can solve stochastic differential equations must be implemented. This is performed, on the wavepacket dynamics, for many iterations of the stochastic process, and a Monte Carlo average is taken. The Markovian SSE is applied further in Chapter 5 for the study of damped dynamics on anharmonic potentials and a photoswitch PES. However, in the next section the Markovian SSE is applied to the harmonic oscillator potential to provide an example of damped dynamics and comparison to LME results.

3.1.1 Example: damped quantum harmonic oscillator

In this example we consider a displaced harmonic oscillator system coupled to a bath. The system part of this can be described by a Hamiltonian of the form

$$H_S = \frac{p^2}{2} + \frac{\omega_0^2 x^2}{2}|g\rangle\langle g| + \Big(E_e + \frac{\omega_e^2 (x-\Delta_x)^2}{2}\Big)|e\rangle\langle e|, \tag{3.15}$$

where x is the nuclear coordinate, p is the nuclear momentum, ω_0 and ω_e denote the ground state and excited state vibrational frequency respectively, $|e\rangle$ and $|g\rangle$ each represent an electronic state and E_e is the electronic excitation energy. Such models can be used to represent photoexcitation dynamics wherein initially the wavepacket is stationary in the ground electronic state and is vertically excited via light to the

excited electronic state. Subsequently, wavepacket dynamics ensue on the excited state PES, if it is displaced with respect to the ground state PES. For this example, we shall analyse the electronic excited state dynamics after photoexcitation in the presence of a harmonic oscillator bath and assume that no transference occurs to the electronic ground state. Thus, the electronic ground state is only included in the above model for clarity with respect to photoexcitation and displacement of the electronic excited state.

As discussed earlier in this chapter the overall Hamiltonian is given by

$$H = H_S + H_B + H_I, \tag{3.16}$$

where H_S is the system Hamiltonian, H_B is the bath Hamiltonian and the interaction Hamiltonian is given by H_I. From the system Hamiltonian it can be seen that the excited state PES, which we shall generate wavepacket dynamics along, is given by

$$V_e = E_e + \frac{1}{2}\omega_e^2(x - \Delta_x)^2. \tag{3.17}$$

As discussed in the previous section a method which is able to account for the effects of an OQS, with a Markovian environment, is the LME. In this section I present the results of a LME using the model system with a harmonic PES. The motivation for this is twofold, for one it allows some initial insight into the differences between the evolution of a closed and an open system and the expectation value of observables. Secondly, this provides an important benchmark and limiting case in the development of SSE approaches.

Firstly, the LME is chosen to have the lowering operator a of the electronic excited harmonic PES as the environment coupling operator L_j such that

$$\dot{\rho}(t) = -\frac{i}{\hbar}[H, \rho(t)] + \frac{\Gamma}{2}\left[2a\rho(t)a^\dagger - \{a^\dagger a, \rho(t)\}\right], \tag{3.18}$$

where Γ represents the strength of coupling to the environment and $\rho(t)$ is the system density matrix. To simplify the definition of a in this example, the potentials have been shifted such that the minima of the electronic state PES is located at $x = 0$. Temperature may be included phenomenologically by including $a^\dagger$ as a second environment coupling operator and weighting the environment coupling strengths appropriately. However, for our current purposes of exploring damped quantum dynamics and comparing the LME to the SSE we shall only couple to the environment via a. In some

forms of the Lindblad equation the Γ term is absorbed into the Lindblad operator such that $L_j = \sqrt{\Gamma_j} A_j$, where L_j defines the collapse operator and A_j are the operators through which the environment couples to the system in the interaction Hamiltonian with a corresponding rate Γ_j.

In this section the energy representation is chosen and the basis $|n\rangle$ with each n representing an eigenstate of the system. In choosing the initial displaced wavefunction, a single eigenstate will not suffice. That is to say if $|\psi(t=0)\rangle = |n\rangle$ then $\langle x\rangle = 0$ and $\langle p\rangle = 0$. To demonstrate this the x operator in terms of the raising and lowering operators $a^\dagger$ and a is

$$x = \sqrt{\frac{\hbar}{2m\omega}}(a^\dagger + a), \tag{3.19}$$

where m is the mass and w is the oscillator frequency. When acting with the raising and lowering operators on eigenstates the following relations are obtained

$$a^\dagger|n\rangle = \sqrt{n+1}|n+1\rangle, \tag{3.20}$$

$$a|n\rangle = \sqrt{n}|n-1\rangle. \tag{3.21}$$

Thus for the expectation of the position we have

$$\begin{aligned}
\langle x\rangle =& \langle n|x|n\rangle \\
=& \sqrt{\frac{\hbar}{2m\omega}}\langle n|(a^\dagger + a)|n\rangle \\
=& \sqrt{\frac{\hbar}{2m\omega}}(\langle n|a^\dagger|n\rangle + \langle n|a|n\rangle|) \\
=& \sqrt{\frac{\hbar}{2m\omega}}(\sqrt{n+1}\langle n|n+1\rangle + \sqrt{n}\langle n|n-1\rangle) \\
=& \, 0,
\end{aligned} \tag{3.22}$$

due to orthogonality between the different eigenstates. By writing the momentum operator as

$$p = i\sqrt{\frac{\hbar m\omega}{2}}(a^\dagger - a), \tag{3.23}$$

the expectation of the momentum can similarly be found to be zero. To convert the wavefunction to an energy basis the wavefunction is written as a linear combination of

the eigenstates as

$$\psi(x,t) = \sum_{n=1}^{N} c_n(t)\phi_n(x,t), \tag{3.24}$$

where N has to be sufficiently large to correctly describe $\psi(x,t)$. The expansion coefficients c_n are given by

$$c_n(t) = \int_{-\infty}^{\infty} dx\, \phi_n^*(x,t)\psi(x,t). \tag{3.25}$$

This is then applied to the initial state $\psi(x,t)$ to find the coefficients required to linearly combine the eigenstates to form the initial state in the energy representation. To this end, the eigenstate functions are required. For the Harmonic oscillator these are well known and given by

$$\phi_n(x) = \frac{1}{\sqrt{2^n n!}}\left(\frac{m\omega}{\pi\hbar}\right)^{1/4} e^{-\frac{m\omega x^2}{2\hbar}} H_n\left(\sqrt{\frac{m\omega}{\hbar}}x\right), \tag{3.26}$$

where H_n represents the Hermite polynomials,

$$H_n(z) = (-1)^n e^{z^2}\frac{d^n}{dz^n}\left(e^{-z^2}\right). \tag{3.27}$$

The aforementioned quantities, such as the Hermite polynomials and expansion coefficients, are numerically calculated using Python which provides built in commands for the Hermite polynomials and evaluation of integrals. The Lindblad master equation is simulated using the QuTiP quantum toolbox for Python [155]. Expectation values are then calculated with the density matrix via the Born rule

$$\langle A\rangle = \mathrm{tr}(\rho A). \tag{3.28}$$

Using this relation the expectation of the position (coordinate) is calculated, which is displayed in Fig. 3.1. Planck's reduced constant is set to 1 in these simulations, $\hbar = m = \omega = 1$, such that the units are atomic units (a.u.). Furthermore, simulations are conducted on a spatial grid of 1000 points with a time step of $\Delta t = 0.001$ unless otherwise stated. The wavepacket at initial time is centred at $x = 1$. In contrast to the closed system evolution the expectation values are seen to tend towards zero as time proceeds and the system settles at the minimum of the potential well. The damped dynamics thus also dissipate energy and this can be seen in Fig. 3.2. In this figure the expectation values of the kinetic energy, the potential energy, and the total energy are

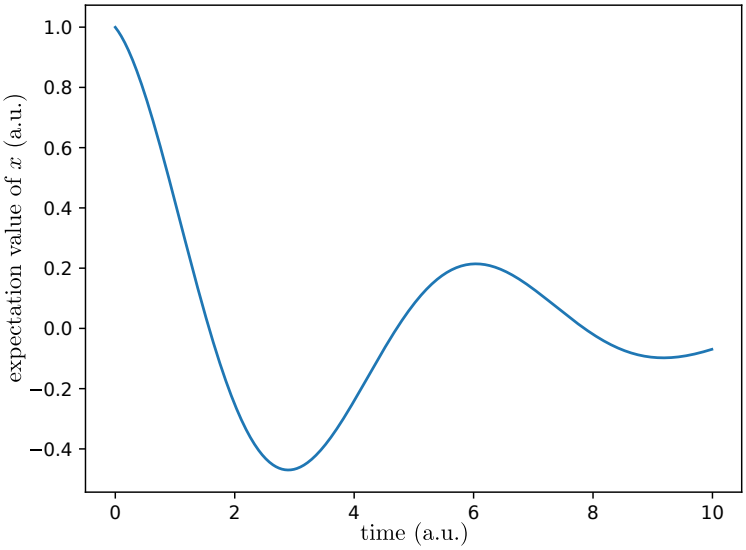

Figure 3.1: The expectation value of the position is shown for the damped harmonic oscillator with $\Gamma = 0.5$. In contrast to the closed system evolution, the expectation of the position no longer oscillates between 1 and -1. Instead, it undergoes damped motion as it approaches the equilibrium point located at the minimum of the potential energy located at $x = 0$.

displayed. The Hamiltonian acts as the total energy operator, the expectation value for which is the sum of the expectation of the potential and kinetic energies. For the closed quantum system the total energy would remain constant, however, here it is seen to decay to 0.5. The reason for this can be seen by looking at the Hamiltonian operator and its expectation value

$$\begin{aligned} H|n\rangle =& \hbar\omega\Big(N + \frac{1}{2}\Big)|n\rangle \\ =& \hbar\omega\Big(n + \frac{1}{2}\Big)|n\rangle, \end{aligned} \tag{3.29}$$

where $N = a^\dagger a$ is the number operator. Thus the expectation value gives

$$\langle n|H|n\rangle = \hbar\omega\Big(n + \frac{1}{2}\Big). \tag{3.30}$$

Therefore, the minimum of this occurs when $n = 0$ and gives the value $\hbar\omega/2$, which is 0.5 for the present choice of parameters. Thus as the expectation of the number operator decreases it would be expected that the total energy also shows this behaviour. This relationship is observed in Fig. 3.3. As the expectation of the number operator tends to

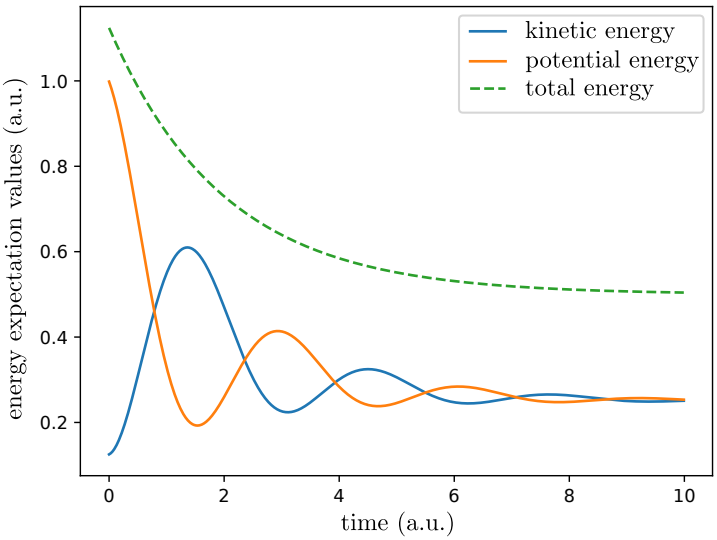

Figure 3.2: The expectation value of energy operators is shown for $\Gamma = 0.5$. Three energy operators are plotted which are the kinetic energy, potential energy, and the total energy operators. All show a dissipation towards a minimum value, the total energy dissipates to 0.5 and the other two energy expectations dissipate to 0.25. The total energy is provided by the sum of the potential energy and kinetic energy, which is equivalently the expectation of the Hamiltonian operator.

zero over time the total energy tends to its minimum value. This property sets apart the quantum harmonic oscillator from its classical counterpart as the energy can never be zero in the former case. A similar property is found with the kinetic energy and potential energy.

Within these simulations the rate of dissipation can be controlled via the parameter Γ. By increasing Γ the different regimes of the damped oscillator can be achieved. Thus the shift between an open system and a closed system can be achieved, where the closed system and unitary evolution is a limiting case when $\Gamma = 0$.

The Markovian SSE, provides equivalent results to the LME. Here the non-linear version is used [41] and, as with the LME, the lowering operator a is chosen as the

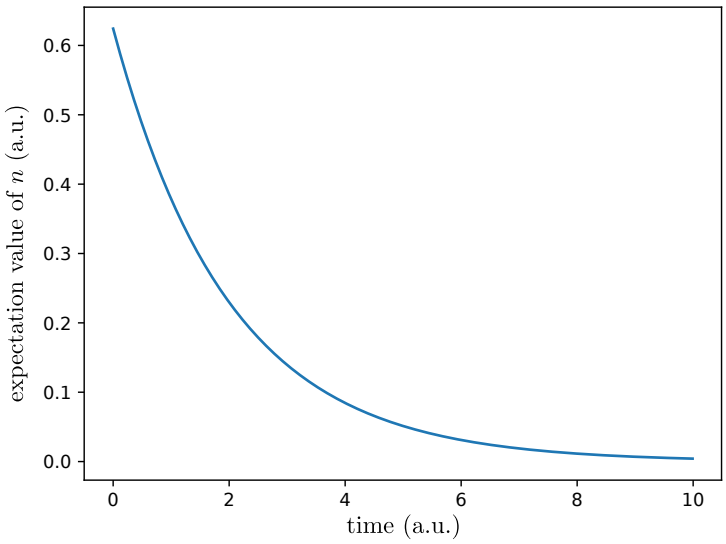

Figure 3.3: The expectation value of the number operator is shown for damped evolution of the harmonic oscillator and displays a decay over time to 0.

environment coupling operator L. This gives the equation

$$\begin{aligned} d\psi(t) = &\Big[-\frac{i}{\hbar}H\psi(t) + \frac{\Gamma}{2}\Big(\langle a + a^\dagger\rangle_\psi a - a^\dagger a - \frac{1}{4}\langle a + a^\dagger\rangle_\psi^2\Big)\psi(t)\Big]dt \\ &+ \Big[\sqrt{\Gamma}\Big(a - \frac{1}{2}\langle a + a^\dagger\rangle_\psi\Big)\psi(t)\Big]dW(t), \end{aligned} \tag{3.31}$$

where Γ represents the strength of environment coupling and $dW(t)$ is the Wiener increment, introduced in section 3.1. The Wiener increment term represents the stochastic process and is the term through which noise enters. Simulations with this equation thus result in a single noisy trajectory, and to obtain converged results that equate dynamics generated through the LME several trajectories must be simulated and the mean value with respect to these must be taken when calculating the density matrix or expectation values.

Using a choice of parameters $\hbar = m = \omega = 1$ the results of the numerical solution to this equation, which is calculated using a Runge-Kutta fourth-order method [41], is shown in Fig. 3.4. Further details on the computational method for closed system evolution can be found in Appendix A.1, and damped evolution via SSE approach in Appendix A.2. As can be seen, for the results to converge to the Lindblad method

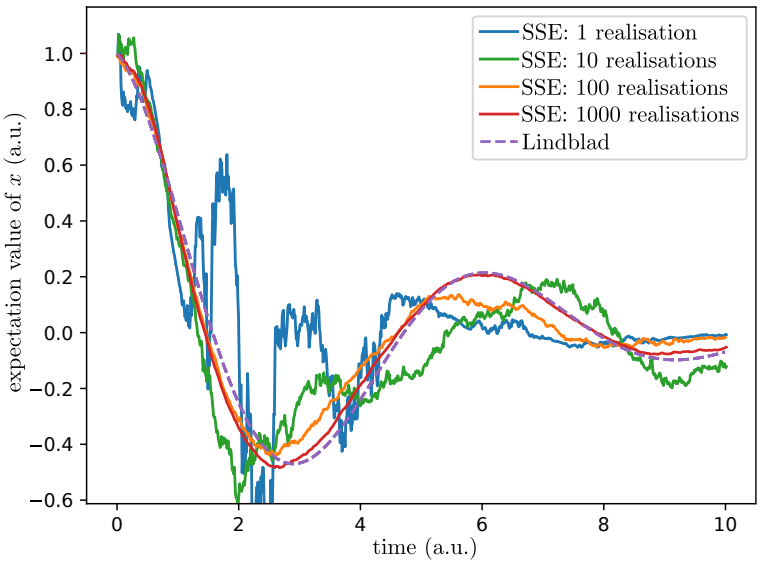

Figure 3.4: The expectation value of the position is shown for evolution via the Markovian SSE with an increasing number of realisations. As the number of realisations increases the results become smoother as the fluctuations are averaged out and the results converge to the Lindblad evolution results.

many realisations must be carried out and the ensemble average taken. By taking more realisations the SSE results approach the corresponding Lindblad results, however, for full convergence and concurrence of results many realisations may need to be taken.

This example demonstrates that the Markovian SSE provides a wavepacket method to simulate results that are equivalently given by the LME method for the density matrix. In the next section the extension to non-Markovian dynamics is derived.

3.2 Linear NMSSE

Several derivations of the non-Markovian stochastic Schrödinger equations (NMSSE) exist, however the first extension of the quantum state diffusion SSE equations to non-Markovian environments was provided by Diósi and Strunz [65, 156]. We shall summarise the derivation in this section and additional relevant details from sources [46, 47, 157]. The linear NMSSE determines the time evolution of the reduced state for non-Markovian environments and its derivation is the objective of this section.

Essentially the linear NMSSE is a reformulation of the interaction picture Schrödinger equation

$$\partial_t|\Psi_t\rangle = -iH(t)|\Psi_t\rangle, \tag{3.32}$$

that defines the closed evolution of the total state where

$$|\Psi_0\rangle = |\psi_0\rangle \otimes |\mathbf{0}\rangle_B, \tag{3.33}$$

and the subscript B corresponds to the bath. This derivation makes use of a coherent state basis for the environmental degrees of freedom. In particular expressing these in the Bargmann Hilbert space of anti-holomorphic functions provides a route to a stochastic description of non-Markovian open systems [63]. At this point it is of use to review some relevant properties of coherent states, which are often described as states with dynamics in close correspondence to the oscillatory behaviour of the classical harmonic oscillator. Formally the Bargmann coherent states are unnormalised eigenstates of the annihilation operator defined in terms of the vacuum state as

$$|z\rangle = e^{za^\dagger}\,|0\rangle\,. \tag{3.34}$$

Coherent states have the following properties with respect to annihilation and creation operators

$$a\,|z\rangle = z\,|z\rangle\,, \tag{3.35}$$

$$\langle z|\,a^\dagger = \langle z|\,z^*, \tag{3.36}$$

$$\langle z|\,a = \langle z|\,\frac{\partial}{\partial z^*}, \tag{3.37}$$

the last of which can be seen from acting on the definition in terms of the vacuum state. In the coherent state basis the resolution of identity is

$$I = \int d^2z\, e^{-|z|^2}|z\rangle\langle z| = 1, \tag{3.38}$$

where $d^2a = \ \mathrm{Re}(dz)\ \mathrm{Im}(dz)/\pi$. Using this relation the total state can now be expanded in the time independent environment basis $|z\rangle \equiv |z_1\rangle \otimes |z_2\rangle \otimes \ldots$ for the environment degrees of freedom z_λ,

$$|\Psi_t\rangle = I|\Psi_t\rangle = \int \mu(z)|\psi_t(z^*)\rangle \otimes |z\rangle\, d^{2N}z, \tag{3.39}$$

where $|\psi_t(z^*)\rangle = \langle z|\Psi_t\rangle$ and

$$\mu(z) = \pi^{-N}e^{-|z|^2} \tag{3.40}$$

has been introduced to drop explicit reference to N and whether the environment is finite or infinite. The $|\psi_t(z^*)\rangle$ states of the system correspond to a particular configuration z of the environment. Another crucial quality for the following derivation is that $|\psi_t(z^*)\rangle$ is analytic.

By tracing over the environment in this representation of the total state, the reduced density operator for the system using Eq. 3.38 and Eq. 3.39 is given by

$$\rho_S(t) = \mathrm{tr}_B|\Psi_t\rangle\langle\Psi_t| = \int \mu(z)|\psi_t(z^*)\rangle\langle\psi_t(z^*)|\, d^{2N}z. \tag{3.41}$$

The expectation value of an operator A can be found similarly as for example $\langle\psi_t|A|\psi_t\rangle = \mathrm{tr}(\rho_S(t)A)$. Thus to determine the reduced dynamics it suffices to know the time evolution of $|\psi_t(z^*)\rangle = \langle z|\Psi_t\rangle$ and perform the integration with respect to the Gaussian integration measure. Using the stated properties of coherent states, and the definition of the total Hamiltonian in Eq. 2.53, the dynamical equation for $|\psi_t(z^*)\rangle = \langle z|\Psi_t\rangle$ can be defined as

$$\partial_t\,|\psi_t(z^*)\rangle = -iH_S\,|\psi_t(z^*)\rangle - iL\sum_\lambda g_\lambda^* e^{i\omega_\lambda t} z_\lambda^*\,|\psi_t(z^*)\rangle - iL^\dagger\sum_\lambda g_\lambda e^{-i\omega_\lambda t}\frac{\partial\,|\psi_t(z^*)\rangle}{\partial z_\lambda}. \tag{3.42}$$

In like manner to the force defined in the previous sections an effective bath operator can be defined as

$$\zeta_t^* = -i\sum_\lambda g_\lambda^* e^{i\omega_\lambda t} z_\lambda^*. \tag{3.43}$$

Subsequently, by substituting Eq. 3.43 into Eq. 3.42, and using the chain rule

$$\frac{\partial}{\partial z_\lambda^*} = \int \frac{\partial\zeta_s^*}{\partial z_\lambda^*}\frac{\delta}{\delta\zeta_s^*}\, ds, \tag{3.44}$$

the non-Markovian stochastic Schrödinger equation is obtained

$$\partial_t|\psi_t\rangle = -iH_S|\psi_t\rangle + L\zeta_t^*|\psi_t\rangle - L^\dagger\int_0^t \alpha_{T=0}(t-s)\frac{\delta|\psi_t\rangle}{\delta\zeta_s^*}\, ds, \tag{3.45}$$

where $\alpha_{T=0}(t-s) = \sum_\lambda |g_\lambda|^2 e^{-i\omega_\lambda(t-s)}$ is the zero temperature BCF. Note the above equation gives the form of the NMSSE but so far has only been a reformulation of the Schrödinger equation. To understand how this can be interpreted as a stochastic equation it is fruitful to rewrite

$$\rho_S(t) = \mathbb{E}[|\psi_t\rangle\langle\psi_t|], \tag{3.46}$$

where $\mathbb{E}$ represents the average is taken over $\mu(z)$. Thus the reduced density matrix arises from averaging over stochastic pure state projectors $|\psi_t(z^*)\rangle\langle\psi_t(z^*)|$ with Gaussian weight $\mu(z)$. Therefore, the NMSSE can be regarded as a stochastic differential equation for realisations $|\psi_t(z^*)\rangle$ which are referred to as a quantum trajectory. Coherent state labels are dropped in Eq. 3.45 as the initial state is noise independent and $|\psi_t\rangle$ depends on the coherent state z^* only through the noise process. The stochastic process ζ_t^* is a complex Gaussian process with the following properties

$$\mathbb{E}[\zeta_t] = 0, \tag{3.47}$$

$$\mathbb{E}[\zeta_t\zeta_s] = 0, \tag{3.48}$$

$$\mathbb{E}[\zeta_t\zeta_s^*] = \alpha_{T=0}(t-s), \tag{3.49}$$

designed in such a way as to mimic the force in Eq. 3.43. In this manner the influence of the environment, encoded in the BCF $\alpha_{T=0}(t-s)$, which also influences the memory integral term, is implemented as a stochastic process. It is through these means that non-Markovian behaviour arises in the time correlated noise process and also in the memory integral, which involves the complete history of $|\psi_t(z^*)\rangle$. However, it is the presence of this term that makes the NMSSE difficult to solve as compared to its Markovian counterpart, overcoming this difficulty is achieved through the HOPS solution discussed in section 3.4. However, before this is presented it is of use to consider how finite temperature can enter in the wavepacket formalism through the use of the thermofield method.

3.3 Derivation of the finite temperature NMSSE

The derivation of the NMSSE presented in the previous section relied on the zero temperature approximation, characterised by the initial product state

$$|\Psi_0\rangle = |\psi_0\rangle \otimes |\mathbf{0}\rangle_B, \tag{3.50}$$

where the environment, here indexed by B, is in the vacuum state. Conversely, for the inclusion of temperature, the initial thermal product state

$$\rho_0 = |\psi_0\rangle\langle\psi_0| \otimes \rho_{eq} \tag{3.51}$$

is required, where

$$\rho_{eq} = Z^{-1} e^{-\beta H_B}, \tag{3.52}$$

$$Z = \mathrm{tr}[e^{-\beta H_B}], \tag{3.53}$$

is the equilibrium density matrix, and H_B is the bath Hamiltonian. As shown earlier in the chapter, the thermofield method provides the means to represent the expectation of an operator with respect to the equilibrium density matrix, as the expectation value of a pure state. Such a derivation preserves the structure of the derived NMSSE by retaining a pure state representation. We will now review the derivation shown in [67] supplemented with concepts from [137–139, 157].

Firstly, following the thermofield method a second fictitious bath is required. This is achieved by introducing a second bath of harmonic oscillators $\mathcal{B}$, along with the the physical bath $\mathcal{A}$. The bath $\mathcal{B}$ then represents the tilde fictitious degrees of freedom and is defined such that it does not interact with the system degrees of freedom. Consequently, any issues caused by its inclusion are negated, and the correct reduced system dynamics is produced once the environment has been traced out. Figure 3.5(a) shows the open quantum system representation of this. Therefore, we obtain

$$\hat{H} = H_S + \sum_{\lambda} (g_\lambda^* L a_\lambda^\dagger + g_\lambda L^\dagger a_\lambda) + \sum_{\lambda} \omega_\lambda (a_\lambda^\dagger a_\lambda - b_\lambda^\dagger b_\lambda), \tag{3.54}$$

where the operators a_λ and $a_\lambda^\dagger$ are associated with $\mathcal{A}$, whereas b_λ and $b_\lambda^\dagger$ are associated with $\mathcal{B}$. Following thermofield theory, the temperature dependent operators are defined as,

$$A_\lambda(\beta) = u(\beta) a_\lambda - v(\beta) b_\lambda^\dagger, \tag{3.55}$$

$$A_\lambda^\dagger(\beta) = u(\beta) a_\lambda^\dagger - v(\beta) b_\lambda, \tag{3.56}$$

$$B_\lambda(\beta) = u(\beta) b_\lambda - v(\beta) a_\lambda^\dagger, \tag{3.57}$$

$$B_\lambda^\dagger(\beta) = u(\beta) b_\lambda^\dagger - v(\beta) a_\lambda, \tag{3.58}$$

where we recall $u(\beta) = \sqrt{(1+\bar{n})}$, $v(\beta) = \sqrt{\bar{n}}$, and $\bar{n}$ represents the expected number of particles following Bose-Einstein statistics. The inverse transformations are given by,

$$a_\lambda = u(\beta) A_\lambda(\beta) + v(\beta) B_\lambda^\dagger(\beta), \tag{3.59}$$

$$a_\lambda^\dagger = u(\beta) A_\lambda^\dagger(\beta) + v(\beta) B_\lambda(\beta), \tag{3.60}$$

$$b_\lambda = u(\beta) B_\lambda(\beta) + v(\beta) A_\lambda^\dagger(\beta), \tag{3.61}$$

$$b_\lambda^\dagger = u(\beta) B_\lambda^\dagger(\beta) + v(\beta) A_\lambda(\beta). \tag{3.62}$$

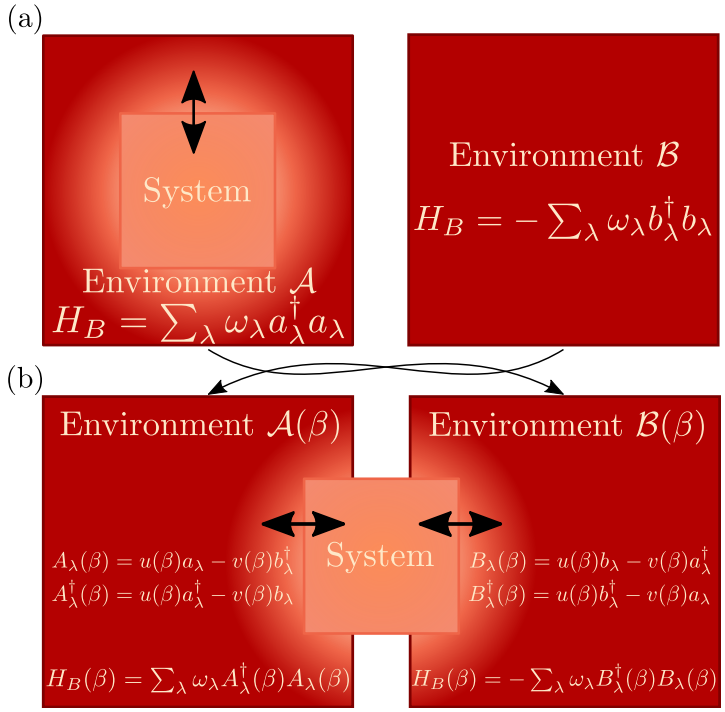

Figure 3.5: Open quantum system representation of system and environment for the inclusion of finite temperature via thermofield theory. (a) The system is coupled to an environment $\mathcal{A}$, and a second uncoupled environment $\mathcal{B}$ is introduced which is copy of environment $\mathcal{A}$. The overall bath Hamiltonian is given by $H_B = \sum_\lambda \omega_\lambda (a_\lambda^\dagger a_\lambda - b_\lambda^\dagger b_\lambda)$. (b) Transforming to temperature dependent operators $A_\lambda(\beta)$ and $B_\lambda(\beta)$ allows this to be equivalently represented in terms of two environments $\mathcal{A}(\beta)$ and $\mathcal{B}(\beta)$ that each couple to the system.

Using these transformations Eq. 3.54 is written in terms of the temperature dependent operators to give

$$\begin{aligned}\hat{H} =& H_S + \sum_\lambda \Big[g_\lambda^* L\Big(u(\beta)A_\lambda^\dagger(\beta) + v(\beta)B_\lambda(\beta)\Big) + g_\lambda L^\dagger\Big(u(\beta)A_\lambda(\beta) + v(\beta)B_\lambda^\dagger(\beta)\Big)\Big] \\ &+ \sum_\lambda \omega_\lambda \Big[\Big(u^2(\beta)A_\lambda^\dagger(\beta)A_\lambda(\beta) + u(\beta)v(\beta)\Big(A_\lambda^\dagger(\beta)B_\lambda^\dagger(\beta) + B_\lambda(\beta)A_\lambda(\beta)\Big) \\ &+ v^2(\beta)B_\lambda(\beta)B_\lambda^\dagger(\beta)\Big) - \Big(u^2(\beta)B_\lambda^\dagger(\beta)B_\lambda(\beta) + u(\beta)v(\beta)\Big(B_\lambda^\dagger(\beta)A_\lambda^\dagger(\beta) \\ &+ A_\lambda(\beta)B_\lambda(\beta)\Big) + v^2(\beta)A_\lambda(\beta)A_\lambda^\dagger(\beta)\Big)\Big]. \end{aligned} \tag{3.63}$$

Note the transformations are constructed such that they preserve the commutation

relations

$$[A_\lambda^\dagger(\beta), A_\lambda(\beta)] = [B_\lambda(\beta), B_\lambda^\dagger(\beta)] = 1, \tag{3.64}$$

$$[A_\lambda(\beta), B_\lambda(\beta)] = [A_\lambda(\beta), B_\lambda^\dagger(\beta)] = 0. \tag{3.65}$$

Collecting $v(\beta)$ and $u(\beta)$ terms, and using the commutation relations, Eq. 3.63 becomes

$$\begin{aligned}\hat{H} =& H_S + \sum_\lambda u(\beta)\Big(g_\lambda^* L A_\lambda^\dagger(\beta) + g_\lambda L^\dagger A_\lambda(\beta)\Big) + \sum_\lambda v(\beta)\Big(g_\lambda^* L B_\lambda(\beta) + g_\lambda L^\dagger B_\lambda^\dagger(\beta)\Big) \\ &+ \sum_\lambda \omega_\lambda \Big[\Big(u^2(\beta) - v^2(\beta)\Big) A_\lambda^\dagger(\beta) A_\lambda(\beta) - 1 - \Big(u^2(\beta) - v^2(\beta)\Big) B_\lambda^\dagger(\beta) B_\lambda(\beta) + 1\Big].\end{aligned} \tag{3.66}$$

Using $u^2(\beta) - v^2(\beta) = 1$, and substituting for $\bar{n}_\lambda$ Eq. 3.66 simplifies to

$$\begin{aligned}\hat{H} =& H_S + \sum_\lambda \sqrt{\bar{n}_\lambda + 1}\Big(g_\lambda^* L A_\lambda^\dagger(\beta) + g_\lambda L^\dagger A_\lambda(\beta)\Big) \\ &+ \sum_\lambda \sqrt{\bar{n}_\lambda}\Big(g_\lambda^* L B_\lambda(\beta) + g_\lambda L^\dagger B_\lambda^\dagger(\beta)\Big) \\ &+ \sum_\lambda \omega_\lambda \Big[A_\lambda^\dagger(\beta) A_\lambda(\beta) - B_\lambda^\dagger(\beta) B_\lambda(\beta)\Big],\end{aligned} \tag{3.67}$$

which is of a similar form to the zero temperature derivation but the system is now coupled to two separate baths, which are associated with the temperature dependent operators. Thus it should be noted that each bath does not represent the physical or tilde oscillators, but a bound quasiparticle of both. This representation is shown in Fig. 3.5(b). Interpreting this further, note that the boson Bogoliubov transformation can be formulated as a hyperbolic rotation matrix

$$\begin{bmatrix} a \\ \tilde{a}^\dagger \end{bmatrix} = \begin{bmatrix} u(\beta) & v(\beta) \\ v(\beta) & u(\beta) \end{bmatrix} \begin{bmatrix} a(\beta) \\ \tilde{a}^\dagger(\beta) \end{bmatrix}, \tag{3.68}$$

where $u(\beta) = \cosh\theta(\beta)$ and $v(\beta) = \sinh\theta(\beta)$, and the transformation has been demonstrated using operators a and $\tilde{a}^\dagger$. As an aside, such hyperbolic rotations of Minkowski space can be used to describe Lorentz transformations. In general, Bogoliubov transformations can be interpreted as a rotation of phase space that allows a change of basis to one where the Hamiltonian is diagonal. In summary, the second bath incorporates the negative frequency oscillators of the environment. These are required in the construction of a anti-symmetrised spectral density associated with a BCF at $T > 0$

$$\bar{J}(\omega) = J(\omega) - J(-\omega). \tag{3.69}$$

A Fourier transform of the time dependent BCF to obtain a frequency dependent version shows that at finite temperature both negative and positive oscillator frequencies are required associated with either upward or downward transitions. The implication is that a loss of energy of the system is balanced by an equal rise in energy of the bath and vice versa. Furthermore, the bath $\mathcal{B}$ does not directly interact with the system in the original representation. However, its inclusion allows transformation to the representation where there are finite temperature system-bath interaction terms. Starting from the transformed Hamiltonian Eq. 3.67 the derivation of the NMSSE follows similarly to the zero temperature assumption case. This is because the finite-temperature problem has been mapped to the zero-temperature one, which results in the requirement of coupling to two separate harmonic baths. Note, the bath Hamiltonian in the original equation (Eq. 3.54) reads

$$\hat{H}_B = \sum_\lambda \omega_\lambda \left[a_\lambda^\dagger a_\lambda - b_\lambda^\dagger b_\lambda \right]. \tag{3.70}$$

Equation 2.134, along with the above derivation of the transformed Hamiltonian, motivates the relation

$$\begin{aligned} \hat{H}_B(\beta) &= \sum_\lambda \omega_\lambda \left[A_\lambda^\dagger(\beta) A_\lambda(\beta) - B_\lambda^\dagger(\beta) B_\lambda(\beta) \right] \\ &= \hat{H}_B. \end{aligned} \tag{3.71}$$

Together with Eqs. 2.135–2.138, and using the result of Eq. 2.49 & 2.50, this implies

$$\sum_\lambda e^{i\hat{H}_B(\beta)t} A_\lambda(\beta) e^{-i\hat{H}_B(\beta)t} = \sum_\lambda e^{-i\omega_\lambda t} A_\lambda(\beta), \tag{3.72}$$

$$\sum_\lambda e^{i\hat{H}_B(\beta)t} B_\lambda(\beta) e^{-i\hat{H}_B(\beta)t} = \sum_\lambda e^{i\omega_\lambda t} B_\lambda(\beta). \tag{3.73}$$

The coherent state properties used in the zero-temperature results can be extended for both temperature dependent operators

$$\langle z, w | A_\lambda^\dagger(\beta) = \langle z, w | z_\lambda^*, \tag{3.74}$$

$$\langle z, w | B_\lambda^\dagger(\beta) = \langle z, w | w_\lambda^*. \tag{3.75}$$

Thus following a similar derivation to the zero-temperature case, the time evolution of

the pure state $|\psi_t\rangle = |\psi_t(z^*, w^*)\rangle$ can be determined

$$\begin{aligned}\partial_t|\psi_t\rangle =& -iH_S - iL\sum_\lambda \sqrt{\bar{n}_\lambda} g_\lambda^* w_\lambda^* e^{-i\omega_\lambda t}|\psi_t\rangle - iL^\dagger \sum_\lambda \sqrt{\bar{n}_\lambda} g_\lambda e^{i\omega_\lambda t}\frac{\partial|\psi_t\rangle}{\partial\omega_\lambda^*} \\ & - iL\sum_\lambda \sqrt{\bar{n}_\lambda + 1} g_\lambda^* e^{i\omega_\lambda t} z_\lambda^*|\psi_t\rangle - iL^\dagger \sum_\lambda \sqrt{\bar{n}_\lambda + 1} g_\lambda e^{-i\omega_\lambda t}\frac{\partial|\psi_t\rangle}{\partial z_\lambda^*}. \end{aligned} \tag{3.76}$$

Subsequently, let

$$\zeta_t^* = -i\sum_\lambda \sqrt{\bar{n}_\lambda + 1} g_\lambda^* z_\lambda^* e^{i\omega_\lambda t}, \tag{3.77}$$

$$\xi_t^* = -i\sum_\lambda \sqrt{\bar{n}_\lambda} g_\lambda^* w_\lambda^* e^{-i\omega_\lambda t}, \tag{3.78}$$

be interpreted as two independent, coloured, complex Gaussian noises, then the functional derivative chain rule can be used to give

$$\frac{\partial}{\partial z_\lambda^*} = \int \frac{\partial\zeta_s^*}{\partial z_\lambda^*}\frac{\delta}{\delta\zeta_s^*}\, ds, \tag{3.79}$$

$$\frac{\partial}{\partial w_\lambda^*} = \int \frac{\partial\xi_s^*}{\partial w_\lambda^*}\frac{\delta}{\delta\xi_s*}\, ds. \tag{3.80}$$

The functional derivative terms shall be investigated further in the physical interpretation of the NMSSE section. Noting that

$$\frac{\partial\zeta_s^*}{\partial z_\lambda^*} = -i\sum_\lambda \sqrt{\bar{n}_\lambda + 1} g_\lambda^* e^{i\omega_\lambda s}, \tag{3.81}$$

$$\frac{\partial\xi_s^*}{\partial w_\lambda^*} = -i\sum_\lambda \sqrt{\bar{n}_\lambda} g_\lambda^* e^{-i\omega_\lambda s}, \tag{3.82}$$

Eq. 3.76 can be written as

$$\begin{aligned}\partial_t|\psi_t\rangle =& -iH_S|\psi_t\rangle + L\zeta_t^*|\psi_t\rangle - L^\dagger\int_0^t \sum_\lambda (\bar{n}_\lambda + 1)|g_\lambda|^2 e^{-i\omega_\lambda(t-s)}\frac{\delta|\psi_t\rangle}{\delta\zeta_s^*}\, ds \\ & + L^\dagger\xi_t^*|\psi_t\rangle - L\int_0^t \sum_\lambda \bar{n}_\lambda|g_\lambda|^2 e^{i\omega_\lambda(t-s)}\frac{\delta|\psi_t\rangle}{\delta\xi_s^*}\, ds. \end{aligned} \tag{3.83}$$

This can be simplified by noticing the bath correlation functions can be defined as

$$\alpha_1(t-s) = \sum_\lambda (\bar{n}_\lambda + 1)|g_\lambda|^2 e^{-i\omega_\lambda(t-s)}, \tag{3.84}$$

$$\alpha_2(t-s) = \sum_\lambda \bar{n}_\lambda|g_\lambda|^2 e^{i\omega_\lambda(t-s)}, \tag{3.85}$$

where

$$\alpha(t-s) = \alpha_1(t-s) + \alpha_2(t-s) \tag{3.86}$$

is the bath correlation function derived in section 2.5.1. Substituting Eq. 3.84 & 3.85 in Eq. 3.83 gives the finite temperature NMSSE

$$\begin{aligned}\partial_t|\psi_t\rangle = &-iH_S|\psi_t\rangle + L\zeta_t^*|\psi_t\rangle - L^\dagger\int_0^t \alpha_1(t-s)\frac{\delta}{\delta\zeta_s^*}\,ds \\ &+ L^\dagger\xi_t^*|\psi_t\rangle - L\int_0^t \alpha_2(t-s)\frac{\delta}{\delta\xi_s^*}\,ds,\end{aligned} \tag{3.87}$$

where the noise processes satisfy

$$\mathbb{E}[\zeta_t] = \mathbb{E}[\zeta_t\zeta_s] = 0, \tag{3.88}$$

$$\mathbb{E}[\zeta_t^*\zeta_s] = \alpha_1(t-s), \tag{3.89}$$

$$\mathbb{E}[\xi_t^*] = \mathbb{E}[\xi_t\xi_s] = 0, \tag{3.90}$$

$$\mathbb{E}[\xi_t^*\xi_s] = \alpha_2(t-s). \tag{3.91}$$

3.3.1 Interpretation of NMSSE finite temperature and memory

In the finite-temperature NMSSE Eq. 3.87 the term $L\zeta_t^*$ is related to emissions from the system to the bath and associated with the $A_\lambda^\dagger(\beta)$ operator. Both vacuum spontaneous emissions present at zero temperature, and temperature dependent stimulated emissions are accounted for. The term with $\alpha_1(t-s)$ defines the memory of the emission processes and is associated with the $A_\lambda(\beta)$ operator. Conversely, $L^\dagger\xi_t^*$ is related to temperature dependent absorption stimulated from the bath to the system and is associated with the $B_\lambda^\dagger(\beta)$ operator. Similarly, the memory term with $\alpha_2(t-s)$ defines the memory of the absorption process associated with the $B_\lambda(\beta)$ operator. Furthermore, if the Eqs. 3.55–3.58 that relate the temperature dependent operators to physical and fictitious degrees of freedom are considered, then it is revealed that system to bath processes involve creation of the physical degrees of freedom and annihilation of the fictitious. The opposite applies to bath to system processes, which involve the creation of the fictitious degrees of freedom whilst annihilating the physical. In this way a temperature related process involving a creation or annihilation in the physical or fictitious space is conversely recorded by the other space. The memory terms act counter to the connected process, for example whilst $L\zeta_t^*$ defines emission from system to bath, the

memory term defines the back transfer into the system over time related to the emission process. Temperature is not required for such a memory effect to occur as it is present for the vacuum spontaneous emission, however, it does also introduce memory for the extra processes. To understand the memory terms in more detail it is of use to consider the simpler setting of the zero-temperature case again.

Consider the zero-temperature NMSSE introduced in section 3.2

$$\partial|\psi_t\rangle = -iH_S|\psi_t\rangle + L\zeta_t^*|\psi_t\rangle - L^\dagger \int_0^t \alpha_{T=0}(t-s)\frac{\delta|\psi_t\rangle}{\delta\zeta_s^*}\,ds, \tag{3.92}$$

where, because $\bar{n}_\lambda = 0$, the noise process becomes

$$\zeta_t^* = -i\sum_\lambda g_\lambda^* z_\lambda^* e^{i\omega_\lambda t} \tag{3.93}$$

and the BCF reduces to

$$\alpha_{T=0} = \sum_\lambda |g_\lambda|^2 e^{-i\omega_\lambda(t-s)}. \tag{3.94}$$

The noise process ζ_t^* represents an ensemble of modes λ that have been acted on by the creation operator $A_\lambda^\dagger(\beta)$ and evolved in time via the multiplication of a phase factor $e^{i\omega_\lambda t}$. It thus acts as a time local ensemble creation operator. On first observation one might assume the third term in Eq. 3.92 acts as the corresponding annihilation for this. Note however, that it represents $\partial/\partial z_\lambda^*$ which is the action of annihilation and is performed for all modes. Therefore, the configuration of bath modes is of importance and depends on previous times. ζ_t^* is time local and can be formulated as a noise process providing a tractable way of dealing with it, whereas the annihilation is more challenging. To solve this issue note that ζ_t^* is closely related to z_λ^* and $\partial/\partial z_\lambda^*$. The chain rule (for functionals), allows the annihilation $\partial/\partial z_\lambda^*$ to be recast in terms of a time local action that is evaluated at previous times. Therefore, the overall term does not represent a time local annihilation, which is instead achieved by the functional derivative $\delta|\psi_t\rangle/\delta\zeta_s^*$. Considering the entire term

$$\int_0^t \alpha_{T=0}(t-s)\frac{\delta|\psi_t\rangle}{\delta\zeta_s^*}\,ds, \tag{3.95}$$

along with the functional derivative there is also the presence of the BCF which is formed from the consideration of the variation of ζ_t^* with respect to z_λ^*. Thus at all times s preceding the present time t the ensemble of modes is annihilated by the functional

derivative providing back transfer, weighted by the BCF, to the system. It thus defines the time delay between when the environment receives the transfer, to when it returns it to the system due to the structure, or strong-coupling, of the environment. In the Markov limit this becomes time-local, and so the memory vanishes as it does not involve the ensemble of modes at previous times s. We know that the BCF provides information on how long a statistical property persists, in this case it defines the strength of and how long the back transfer can occur for. In turn this is dependent on the physical properties of the environment and the coupling to the system.

3.4 The HOPS Solution to the NMSSE

The form of the NMSSE that has been derived is formally exact; however, difficulty arises in the solution due to the appearance of a functional derivative with respect to a stochastic process. The hierarchy of pure states (HOPS) [59] approach offers a method of dealing with the functional derivative term and providing a solvable NMSSE equation. The approach involves derivation of a hierarchy of coupled stochastic differential equations for pure states in the Hilbert space, termed quantum trajectories. The reduced density operator, or desired expectation values, can then be obtained as an ensemble average over the trajectories. Some methods of dealing with the functional derivative term of the NMSSE have used an operator ansatz to replace it, for which in some few cases an exact explicit expression is known [65]. In other cases it is possible to obtain the replacement operator approximately. Alternatively, the hierarchy of pure states provides a general approach without these approximations. In this section we shall present the derivation following the results of [59, 60, 157].

First it is instructive to rewrite the NMSSE, for $T = 0$, as

$$\partial_t|\psi_t\rangle = -iH_S|\psi_t\rangle + L\zeta_t^*|\psi_t\rangle - L^\dagger|\psi_t^{(1)}\rangle, \tag{3.96}$$

where the central idea is to absorb the action of the functional derivative on ψ_t into an auxiliary pure state

$$|\psi_t^{(1)}\rangle = \int_0^t ds\, \alpha_{T=0}(t-s)\frac{\delta|\psi_t\rangle}{\delta\zeta_s^*}. \tag{3.97}$$

This can be rewritten in the form

$$|\psi_t^{(1)}\rangle = D_t|\psi_t\rangle, \tag{3.98}$$

$$D_t = \int_{-\infty}^{\infty} ds\, \alpha_{T=0}(t-s)\frac{\delta}{\delta\zeta_s^*}, \tag{3.99}$$

in which D_t can be understood as an auxiliary pure state operator, that acts on $|\psi_t\rangle$ to create an auxiliary state. The obstacle in solving Eq. 3.96 is $|\psi_t^{(1)}\rangle$, if the time evolution of this term can be understood then this issue will be overcome. Thus considering the time derivative of $|\psi_t^{(1)}\rangle$,

$$\begin{aligned}|\dot{\psi}_t^{(1)}\rangle &= \partial_t(D_t|\psi_t\rangle) \\ &= \dot{D}_t|\psi_t\rangle + D_t|\dot{\psi}_t\rangle,\end{aligned} \tag{3.100}$$

where

$$\dot{D}_t|\psi_t\rangle = \int_0^t ds\, \dot{\alpha}_{T=0}(t-s)\frac{\delta|\psi_t\rangle}{\delta\zeta_s^*}, \tag{3.101}$$

and the integral bounds of $[0,t]$ are acquired due to the fact that $|\psi_t\rangle$ is independent of noise for $s>t$ and $s<0$ [59]. Therefore, if $\dot{D}_t$ can be expressed in terms of D_t and other terms that are already known a tractable scheme can be developed. Indeed this is the case, and most simply shown, if the bath correlation function is of exponential form

$$\alpha_{T=0}(\tau) = ge^{-w\tau}, \tag{3.102}$$

where $w=\gamma+i\Omega$, $\tau\geq 0$, and

$$\alpha(\tau) = \alpha^*(-\tau). \tag{3.103}$$

For a bath correlation of this form $\dot{D}_t|\psi_t\rangle = -wD_t|\psi_t\rangle$. Note similar relations hold for bath correlations that are sums of exponentials, which can be used to approximate many spectral densities [158, 159], such as Lorentzian, and include finite temperature. Thus the derivative of the first auxiliary state, by using Eq. 3.96 and the property that D_t commutes with all system operators, can be written as

$$|\dot{\psi}_t^{(1)}\rangle = -wD_t|\psi_t\rangle - iHD_t|\psi_t\rangle + LD_t\zeta_t^*|\psi_t\rangle - L^\dagger D_t^2|\psi_t\rangle. \tag{3.104}$$

Then using the commutator relation $[D_t,\zeta_s^*] = \alpha_{T=0}(t-s)$ it follows that

$$[D_t,\zeta_t^*] = D_t\zeta_t^* - \zeta_t^*D_t = \alpha_{T=0}(0). \tag{3.105}$$

Thus by rewriting the term $LD_t\zeta_t^*|\psi_t\rangle$ using this relation

$$|\dot{\psi}_t^{(1)}\rangle = (-iH - w + L\zeta_t^*)|\psi_t^{(1)}\rangle + \alpha_{T=0}(0)L|\psi_t^{(0)}\rangle - L^\dagger|\psi_t^{(2)}\rangle, \tag{3.106}$$

where $|\psi_t^{(k)}\rangle = D_t|\psi_t^{(k-1)}\rangle = D_t^k|\psi_t\rangle$. As can be seen the functional derivative has reappeared in the time derivative of the first auxiliary pure state in the form $D_t|\psi_t^{(1)}\rangle = D_t^2|\psi_t\rangle$. This introduces a secondary auxiliary pure state of which the time evolution must be found. Crucially the commutation relation creates a term involving $|\psi_t^{(0)}\rangle$. Following in the manner laid out a hierarchy can thus be developed in which each auxiliary pure state depends only on the order directly above and directly below.

Explicitly one considers the time derivatives of $|\psi_t^{(k)}\rangle$ and obtains coupled stochastic differential equations for an infinite hierarchy of pure states

$$|\dot{\psi}_t^{(k)}\rangle = (-iH - w + L\zeta_t^*)|\psi_t^{(k)}\rangle + \alpha_{T=0}(0)L|\psi_t^{(k-1)}\rangle - L^\dagger|\psi_t^{(k+1)}\rangle, \tag{3.107}$$

where the noise is represented by ζ_t^*, and $|\psi_{t=0}^{(0)}\rangle = |\psi_0\rangle$ and $|\psi_{t=0}^{(k)}\rangle = 0$ for $k > 0$. Solving the infinite set of equations in the HOPS approach of Eq. 3.107 would lead to an exact solution for $|\psi_t\rangle$ as according to the NMSSE of Eq. 3.45. In practice one must turn to a method of truncation by using a terminator, such as [59]

$$|\psi_t^{(k+1)}\rangle \approx \frac{\alpha_{T=0}(0)}{w}L|\psi_t^{(k)}\rangle, \tag{3.108}$$

for an appropriate k that is large enough. This closes the HOPS scheme to a set of $k+1$ coupled equations. In essence this terminator provides a term akin to the Markovian SSE of the form $-L^\dagger L|\psi_t^{(k)}\rangle$ though with a different prefactor. Furthermore, with a delta function form of the bath correlation and zeroth order HOPS the Markov limit is replicated. As an additional note it is not the only terminator that gives good performance and in some cases it is possible to just negate terms for an appropriate k setting $|\psi_t^{(k+1)}\rangle = 0$.

3.4.1 Truncation of HOPS via a terminator

It is insightful to consider the motivation of the terminator of Eq. 3.108 and how it arises by summarising [59]. The linear version of the hierarchy can be rewritten as an integral equation

$$|\psi_t^{(k)}\rangle = \int_0^t e^{-k\gamma(t-s)-ik\Omega(t-s)}\hat{O}e^{\int_s^t(-iH+Lz_r^*)dr}\Big(k\alpha_{T=0}(0)L|\psi_s^{(k-1)}\rangle - L^\dagger|\psi_s^{(k+1)}\rangle\Big)\,ds, \tag{3.109}$$

where $\hat{O}$ is the time ordering operator denoting positive time-ordering. With the condition $k\gamma \gg \omega_{sys}$, where ω_{sys} is the frequency associated with the systems free evolution, the first exponential tends to zero before any noticeable change in the remaining integrand. Thus by setting $s \approx t$

$$|\psi_t^{(k)}\rangle = \left(k\alpha_{T=0}(0)L|\psi_t^{(k-1)}\rangle - L^\dagger|\psi_t^{(k+1)}\rangle\right)\int_0^t e^{-kw(t-s)}\,ds. \tag{3.110}$$

Evaluation of the above integral gives

$$\int_0^t e^{-kw(t-s)}\,ds = \frac{1-e^{-kwt}}{kw} \approx \frac{1}{kw}, \tag{3.111}$$

as $-kwt \ll 1$ for $t > 0$. Thus by considering these parameter and time scales an approximate expression for the kth auxiliary state is given by

$$|\psi_t^{(k)}\rangle = \frac{\alpha_{T=0}(0)}{w}L|\psi_t^{(k-1)}\rangle - \frac{1}{kw}L^\dagger|\psi_t^{(k+1)}\rangle. \tag{3.112}$$

As $k \to \infty$ the second term tends to zero, so for k large enough the second term is assumed to be negligible and the terminator is given by

$$|\psi_t^{(k)}\rangle = \frac{\alpha_{T=0}(0)}{w}L|\psi_t^{(k-1)}\rangle. \tag{3.113}$$

Note there is no clear way to determine at what value of k the second term is negligible. Thus to check for convergence in simulations one must successively increase k and see if the results are in agreement.

3.5 Non-linear NMSSE

For simulation purposes the linear version of the NMSSE has drawbacks as the quality of averaging over individual pure state projectors is reduced due to large contributions from some trajectories. Also, the norm of many trajectories tend to zero and so to preserve the norm on average many trajectories must be taken. A non-linear version solves this issue and was derived by Diosi et al [65] which we shall review in this section.

The linear version of the NMSE does not preserve the norm of the state. In contrast, its non-linear version allows the derivation in terms of normalised states. However, in order to maintain the correct ensemble mean a change in the probability distribution is required.

Crucially, the average that yields the density operator is not unique. Additionally, a change in the integration measure $u(z)$ of Eq. 3.41 can be accounted for using a Girsanov transformation

$$\rho_t = \int d^{2N}z\, P_t(z,z^*)\frac{|\psi_t(z^*)\rangle\langle\psi_t(z^*)|}{\langle\psi_t(z^*)|\psi_t(z^*)\rangle} \tag{3.114}$$

with a time dependent density function

$$P_t(z,z^*) = \frac{e^{-|z|^2}}{\pi^N}\langle\psi_t(z^*)|\psi_t(z^*)\rangle. \tag{3.115}$$

This corresponds to a Husimi distribution which is a quasiprobability distribution in phase space obtained effectively by a trace of the density matrix over the basis of coherent states. Note that, as a quasiprobability distribution requires, the distribution function satisfies

$$\int P(z,z^*)\,dz = \int \|\psi_t(z^*)\|\mu(z)\,dz = 1 \tag{3.116}$$

and it is also non-negative and bounded. Furthermore, a coherent state $|z\rangle$ in this representation represents a wavepacket localised about $z = (q+ip)/\sqrt{2}$. The norm of the trajectory $|\psi_t(z^*)\rangle$ thus represents the probability of finding the environment in a quantum state localised about (q,p) in phase space. Therefore, crucial improvements can be achieved by incorporating dynamics of the environment through a moving coherent basis. Firstly, the assumption is made that at $t = 0$ the initial state $|\psi_0\rangle$ is normalised. Thus at $t = 0$ the probability distribution $P_0(z,z^*)$ is identical to the original distribution. The time evolution of $P_t(z,z^*)$ is given by

$$\partial_t P_t(z,z^*) = \frac{e^{-|z|^2}}{\pi^N}\langle\psi_t(z^*)|\partial_t|\psi_t(z^*)\rangle + \text{c.c.} \tag{3.117}$$

An important observation is that the solution of $|\psi_t\rangle$, with initial condition $|\psi_t(z^*)\rangle = |\psi_0\rangle$, is analytic in z^*. Consequently, $\partial|\psi_t(z^*)\rangle/\partial z = \partial\langle\psi_t(z^*)|/\partial z^* = 0$. This condition implies that

$$\langle\psi_t(z^*)|L^\dagger\frac{\partial}{\partial z_\lambda^*}|\psi_t(z^*)\rangle = \frac{\partial}{\partial z_\lambda^*}\langle L^\dagger\rangle_t\langle\psi_t(z^*)|\psi_t(z^*)\rangle, \tag{3.118}$$

where

$$\langle L^\dagger\rangle_t = \frac{\langle\psi_t(z^*)|L^\dagger|\psi_t(z^*)\rangle}{\langle\psi_t(z^*)|\psi_t(z^*)\rangle}. \tag{3.119}$$

Substituting this for the time evolution of $P_t(z, z^*)$, and using the linear evolution equation for $|\psi_t(z^*)\rangle$ we obtain

$$\partial_t P_t(z, z^*) = -i \sum_\lambda g_\lambda e^{-i\omega_\lambda t} \frac{\partial}{\partial z_\lambda^*} \langle L^\dagger \rangle_t P_t(z, z^*) + \text{c.c.}, \tag{3.120}$$

which has this simple form due to the analyticity of $|\psi_t(z^*)\rangle$ in z^*, and cancellation of conjugate terms. This result shows that the Girsanov transformation is equivalent to the drift of z^*. By looking at Eq. 3.120 the drift velocities may be read off as

$$\dot{z_\lambda^*}(t) = i g_\lambda e^{-i\omega_\lambda t} \langle L^\dagger \rangle_t. \tag{3.121}$$

This equation implies that the most relevant contribution to the full state at a time $t + \Delta t$ corresponds to the coherent state $|z + \dot{z}(t)\Delta t\rangle$. Thus, the expansion of the state should be conducted with respect to $|z(t)\rangle$, instead of a fixed basis, in order to capture the most relevant contributions. Firstly, the drift equation must be solved for trajectories $z_\lambda(t)$, with the initial condition $z_\lambda(0) = z_\lambda$,

$$\tilde{z}_\lambda^*(t) = z_\lambda^* + i \int_0^t g_\lambda e^{-i\omega_\lambda s} \langle L^\dagger \rangle_s \, ds \tag{3.122}$$

where

$$\langle L^\dagger \rangle_t = \frac{\langle \psi_t(\tilde{z}^*(t)) | L^\dagger | \psi_t(\tilde{z}^*(t)) \rangle}{\langle \psi_t(\tilde{z}^*(t)) | \psi_t(\tilde{z}^*(t)) \rangle}. \tag{3.123}$$

The reader may be interested in the more general setting of this solution by looking at the method of characteristics, which is a technique for solving a partial differential equation by reducing it to a family of ordinary differential equations. The Girsanov transformation, along with the time dependent trajectories, provides the equivalent of the original probability distribution with noise

$$P_t(\tilde{z}(t)) d\tilde{z}(t) \equiv \mu(z) dz. \tag{3.124}$$

Thus, the density matrix, and so observable expectation values, can be obtained in three scenarios (sometimes known as stochastic unravelings)

$$\begin{aligned} \rho_t &= \mathbb{E}[|\psi_t(z^*)\rangle\langle\psi_t(z^*)\rangle] \\ &= \tilde{\mathbb{E}}_t[|\tilde{\psi}_t(z^*)\rangle\langle\tilde{\psi}_t(z^*)|] \\ &= \mathbb{E}_t[|\tilde{\psi}_t(\tilde{z}^*(t))\rangle\langle\tilde{\psi}_t(\tilde{z}^*(t))|]. \end{aligned} \tag{3.125}$$

The first represents the linear case, the second is the adjustment for normalised solutions with an associated Girsanov transformed distribution. The final refers to an average over the original untransformed distribution. To achieve this $\psi(\tilde{z}(t))$ must be expressed as a function of the initial amplitudes $z_\lambda = \tilde{z}_\lambda(0)$. Subsequently, the time dependence of the noise results in an additional term such that

$$\begin{aligned}\partial_t\psi_t(\tilde{z}^*(t)) =&\partial_t\psi_t(z^*) + \sum_\lambda \dot{z^*_\lambda}\frac{\partial}{\partial z^*_\lambda}\psi_t(z^*)\\ =&-iH_S|\psi_t(z^*)\rangle - iL\sum_\lambda g^*_\lambda e^{i\omega_\lambda t}\tilde{z}^*_\lambda|\psi_t(z^*)\rangle - iL^\dagger\sum_\lambda g_\lambda e^{-i\omega_\lambda t}\frac{\partial|\psi_t(z^*)\rangle}{\partial z^*_\lambda}\\ &+ i\langle L^\dagger\rangle_t\sum_\lambda g_\lambda e^{-i\omega_\lambda t}\frac{\partial|\psi_t(z^*)\rangle}{\partial z^*_\lambda}.\end{aligned} \tag{3.126}$$

Following the same procedure as the linear derivation the nonlinear version can be rewritten as

$$\partial_t|\psi_t\rangle = -iH_S|\psi_t\rangle + L\tilde{\zeta}^*_t|\psi_t\rangle - \left(L^\dagger - \langle L^\dagger\rangle_t\right)\int_0^t \alpha_{T=0}(t-s)\frac{\delta|\psi_t\rangle}{\delta\zeta^*_s}\,ds, \tag{3.127}$$

where due to Eq. 3.122 the noise has also been shifted to give

$$\tilde{\zeta}^*_t = \zeta^*_t + \int_0^t \alpha_{T=0}(t-s)^*\langle L^\dagger\rangle_s ds. \tag{3.128}$$

Note that this version takes into account the Girsanov transformation and change of probability distribution. Thus, it captures the most relevant contributions and has better convergence than the linear case. However, each trajectory itself is not normalised and the norm must be taken subsequently. To obtain a version for which each trajectory is normalised we must consider the time evolution of,

$$|\tilde{\psi}_t\rangle = \frac{|\psi_t\rangle}{\langle\psi_t|\psi_t\rangle}. \tag{3.129}$$

This follows from

$$\frac{\partial(\langle\psi_t|\psi_t\rangle|\tilde{\psi}_t\rangle)}{\partial t} = \partial_t|\psi_t\rangle, \tag{3.130}$$

which implies

$$\langle\psi_t|\psi_t\rangle\frac{\partial|\tilde{\psi}_t\rangle}{\partial t} = \frac{\partial|\psi_t\rangle}{\partial t} - \left(\frac{\partial\langle\psi_t|}{\partial t}|\psi_t\rangle + \langle\psi_t|\frac{\partial|\psi_t\rangle}{\partial t}\right)|\tilde{\psi}_t\rangle. \tag{3.131}$$

The first term on the right hand side, using the Girsanov shifted result, is given by Eq. 3.127, to obtain the second term note that

$$H^\dagger = H_S + \sum_\lambda (g_\lambda e^{-i\omega_\lambda t} a_\lambda L^\dagger + g_\lambda^* e^{i\omega_\lambda t} a_\lambda^\dagger L), \tag{3.132}$$

then it follows that

$$\begin{aligned}\langle\psi_t|\frac{\partial|\psi_t\rangle}{\partial t} =& -i\langle\psi_t|H_S|\psi_t\rangle - i\sum_\lambda g_\lambda^* e^{i\omega_\lambda t}\tilde{z}_\lambda^*\langle\psi_t|L|\psi_t\rangle \\ &- \langle\psi_t|i\sum_\lambda g_\lambda e^{-i\omega_\lambda t}L^\dagger\frac{\partial|\psi_t\rangle}{\partial\tilde{z}_\lambda^*} \\ &+ \langle\psi_t|i\sum_\lambda g_\lambda e^{-i\omega_\lambda t}\langle\psi_t|L^\dagger|\psi_t\rangle\frac{\partial|\psi_t\rangle}{\partial\tilde{z}_\lambda^*}\end{aligned} \tag{3.133}$$

and

$$\frac{\partial\langle\psi_t|}{\partial t}|\psi_t\rangle = i\langle\psi_t|H_S|\psi_t\rangle \tag{3.134}$$

due to the definition of $H^\dagger$, the conjugate time evolution equation, and analyticity of $|\psi_t\rangle$. Therefore, the second term of Eq. 3.131 is

$$\begin{aligned}\frac{\partial\langle\psi_t|}{\partial t}|\psi_t\rangle + \langle\psi_t|\frac{\partial|\psi_t\rangle}{\partial t} =& -\langle\psi_t|i\sum_\lambda g_\lambda^* e^{i\omega_\lambda t}\tilde{z}_\lambda^* L|\psi_t\rangle \\ &- \langle\psi_t|i\sum_\lambda g_\lambda e^{-i\omega_\lambda t}L^\dagger\frac{\partial|\psi_t\rangle}{\partial\tilde{z}_\lambda^*} \\ &+ \langle\psi_t|i\sum_\lambda g_\lambda e^{-i\omega_\lambda t}\langle\psi_t|L^\dagger|\psi_t\rangle\frac{\partial|\psi_t\rangle}{\partial\tilde{z}_\lambda^*}.\end{aligned} \tag{3.135}$$

Using this result, Eq. 3.127 and the same procedure as the linear derivation, the non-linear NMSSE for normalised trajectories is given by

$$\begin{aligned}\partial_t|\tilde{\psi}_t\rangle =& -iH_S|\tilde{\psi}_t\rangle + (L - \langle L\rangle_t)\tilde{\zeta}_t^*|\tilde{\psi}_t\rangle \\ &- \int_0^t ds\,\alpha_{T=0}(t-s)\Big[(L^\dagger - \langle L^\dagger\rangle)\frac{\delta|\psi_t\rangle}{\delta\tilde{\zeta}_s^*} - \langle(L^\dagger - \langle L^\dagger\rangle_t)\frac{\delta}{\delta\tilde{\zeta}_s^*}\rangle_t\Big]|\tilde{\psi}_t\rangle.\end{aligned} \tag{3.136}$$

This, and Eq. 3.127, requires propagating the quantity $\langle L^\dagger\rangle s$ for $0 \leq s \leq t$ associated with the shifted noise $\tilde{\zeta}_t^*$. However, the additional computational requirements needed for this term are small compared to the improved convergence for the non-linear versions of the NMSSE equation. In Chapter 6 HOPS applied to the non-linear NMSSE is presented alongside a version that is also capable of preserving the norm. Subsequently, it is tested on spin-boson models before applying the method to study condensed phase photoswitch dynamics.

Chapter 4

Linear absorption beyond the standard displaced harmonic oscillator model

In the previous chapters, the harmonic oscillator model was introduced as an example to demonstrate wavepacket dynamics along a potential energy surface (PES). Commonly, theoretical approaches to open quantum systems approximate vibrational degrees of freedom of the environment with a harmonic oscillator bath. In addition, a choice of harmonic system PES is often made. This approximation results in evenly spaced energy levels, and represents gaussian fluctuations in the weak coupling regime [160]. Despite the usefulness of the harmonic model, molecular potentials are, in general, anharmonic and there are many examples that exhibit significant anharmonicity such as light-harvesting and photosynthesis [161–163], photoswitches [8], and small molecules [164, 165]. The feature of anharmonicity can also become pronounced when there is a large displacement between the ground and excited state potentials involving a large nuclear motion. In such cases, parts of the potential far from equilibrium may be explored, and the harmonic approximation is less likely to hold. This is of particular importance when considering the dynamics of photoswitches, as the light induced excitation can displace the system far from equilibrium on the excited PES. As an example of this, a potential that has been used to model the photoisomerisation of retinal [91] is shown in Fig. 4.1. Additionally, for photoswitches the excited state PES may even be repulsive such that there is no equilibrium state until relaxation to the ground electronic state occurs.

The roots of modelling anharmonicity can be found in the work of Osad'ko, and Skinner and Hsu [166, 167]. In addition, Tanimura used a treatment first via perturbation to harmonic potentials [168] and subsequently conducted studies with Morse potentials [169]. Anharmonicity and its effects can manifest itself in numerous ways. The shape of the entire potential can be important, as in the case of the Morse potential and generally in the case of polynomial potentials [170]. Additionally, displaced harmonic oscillators that have different curvatures are accredited with giving rise to non-standard spectral features [171, 172]. Spectroscopy provides an indispensable tool for investigating interactions between electromagnetic fields and matter revealing structural and dynamical properties. Linear absorption spectroscopy provides an elementary tool that reveals the absorption properties as a function of frequency or wavelength. In particular, it gives information on the energy levels of a quantum system and its PES as there is correspondence between absorption frequency and transition between quantum mechanical states. Its non-linear counterpart, and in particular ultrafast spectroscopy

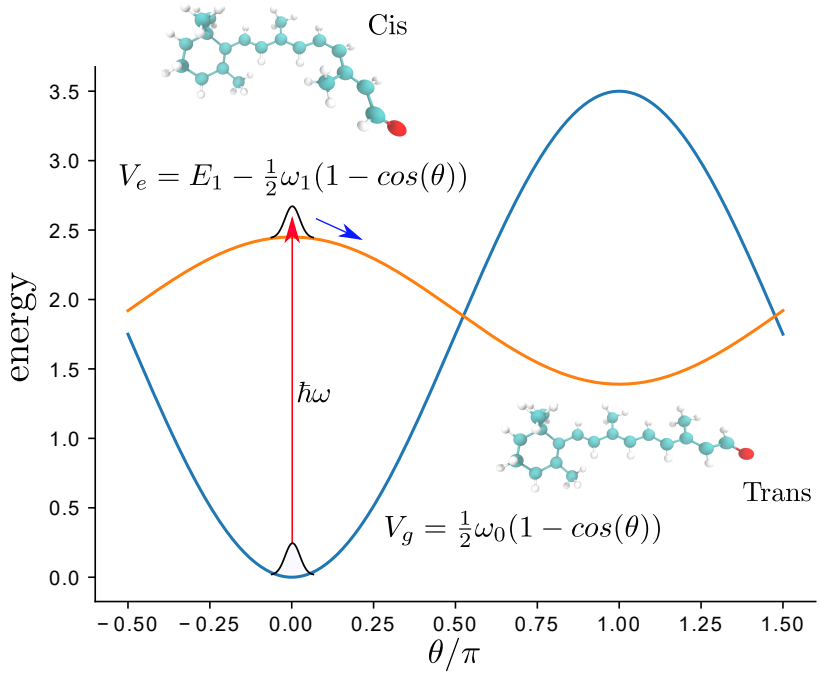

Figure 4.1: Schematic of a potential energy surface used to model the photoisomerisation dynamics of the retinal photoswitch for a bond rotation angle θ. A large displacement from equilibrium is present after photoexcitation of the initial wavepacket via light (red arrow). Subsequent wavepacket dynamics (blue arrow) proceeds along a anharmonic surface shown by V_e where it can undergo further photoexcitation at $\theta = 1$ to the surface V_g.

[173, 174], has provided crucial advances in the study of photoinduced dynamics down to femtosecond and attosecond timescales.

Various effects have been reported in absorption and emission spectra, such as mirror-symmetry breaking between absorption and fluorescence, and splitting of the zero phonon and one phonon peak [170]. In two-dimensional (2D) spectroscopy [175] the analogues of these effects have been studied as well as those not identified by linear spectra [171]. Also, 2D studies have been carried out on skewed spectral lineshapes resulting from non-Gaussian dynamics [176]. Additionally, it has been shown that the ratio between selected cross peaks provides a measure of vibrational anharmonicity and other experimental indicators are possible [177]. The recently introduced Vibrationally Promoted Electronic Resonance (VIPER) experiment [178, 179], a combined electronic-

vibrational spectroscopy technique, offers new ways of probing and controlling molecular systems. A required effect for the VIPER experiment is typically most pronounced when there is large displacement upon electronic transition as featured in the studies of this thesis. Experimental studies have also been conducted using photoelectron spectroscopy to investigate the role of aqueous environments on electronic structure and relaxation dynamics [180].

Realistic systems, in the condensed phase, can include an interplay of all these features in addition to the interaction with the environment. In this chapter the primary focus will be on linear absorption spectral features that arise by going beyond the standard displaced harmonic model, in later chapters the combination of these features and dissipative quantum dynamics is considered. A comprehensive exploration of the topic can be found in textbooks [13, 68, 69, 130]. Using these, we first review the necessary theory of linear absorption. Subsequently, the standard displaced harmonic oscillator model is presented and associated linear absorption spectra. Following this, the model is extended to present original results, featured in [181], on the effect of a difference of curvature between a ground and excited harmonic PES for one coordinate. Through this small adaptation to the model rich spectral features can arise in the case of large curvature difference. This effect is quantified and explained in detail before considering the extension to two coordinate PESs.

4.1 Linear absorption

Fermi's golden rule provides the rates of transitions between discrete eigenstates of the quantum system. However, its form does not provide easy connection to the time-dependent nature of the system. Alternatively, the connection can be made by realising that the features of the spectrum are a frequency representation of the dynamics of the system. The absorption spectrum is then given as a frequency representation of the time-dependent variation of the molecular dipole moment of the system. In Chapter 2, time correlation functions were shown to be a useful tool to represent dynamics of a system. Thus via the correspondence of representations it is possible to describe the absorption spectrum through a time-correlation of the dipole operator. In the

interaction of matter with a field the linear absorption lineshape is defined as [68]

$$\sigma(\omega) = \sum_{ij} p_i |\bar{\mu}_{ij}|^2 \delta(\omega_{ij} - \omega), \tag{4.1}$$

where p_i represents the population and

$$|\bar{\mu}_{ij}|^2 = \left|\langle i|\hat{\epsilon}\cdot\bar{\mu}|j\rangle\right|^2, \tag{4.2}$$

for which $\bar{\mu}$ is the dipole operator, inclusive of magnitude and unit vector, and $\hat{\epsilon}$ represents the polarisation of the field. As the delta function can be represented as the Fourier transform of a complex exponential through the expression

$$\delta(\omega_{ij} - \omega) = \frac{1}{2\pi}\int_{-\infty}^{\infty} dt\, e^{i(\omega_{ij}-\omega)t}, \tag{4.3}$$

Eq. 4.1 can be written as

$$\sigma(\omega) = \frac{1}{2\pi}\int_{-\infty}^{\infty} dt \sum_{ij} p_i \langle i|\bar{\mu}|j\rangle\langle j|\bar{\mu}|i\rangle e^{i(\omega_{ij}-\omega)t}. \tag{4.4}$$

This can be simplified further, by considering the time evolution operator and the projection operator $\sum_j |j\rangle\langle j| = 1$, to give

$$\sigma(\omega) = \frac{1}{2\pi}\int_{-\infty}^{\infty} dt \sum_{ij} p_i \langle i|\bar{\mu}|j\rangle\langle j|U^\dagger\bar{\mu}U|i\rangle e^{-i\omega t} \tag{4.5}$$

$$= \frac{1}{2\pi}\int_{-\infty}^{\infty} dt \sum_{i} p_i \langle i|\bar{\mu}(0)\bar{\mu}(t)|i\rangle e^{-i\omega t}. \tag{4.6}$$

This expression is simply the dipole moment correlation function. Thus the absorption lineshape can be written as

$$\sigma(\omega) = \frac{1}{2\pi}\int_{-\infty}^{\infty} dt\, e^{-i\omega t}\langle\bar{\mu}(0)\bar{\mu}(t)\rangle \tag{4.7}$$

$$= \frac{1}{2\pi}\int_{-\infty}^{\infty} dt\, e^{i\omega t}\langle\bar{\mu}(t)\bar{\mu}(0)\rangle. \tag{4.8}$$

Generally orientation is important and this can be made explicit by writing the expression as

$$\sigma(\omega) = \frac{1}{2\pi}\int_{-\infty}^{\infty} dt\, e^{i\omega t}\langle\hat{\epsilon}\cdot\bar{\mu}(t)\hat{\epsilon}\cdot\bar{\mu}(0)\rangle. \tag{4.9}$$

Thus, the absorption lineshape has been defined in terms of the time-correlation function of the dipole moment. In the next section we will consider a standard example to highlight the dipole correlation functions explicit form and provide comparisons to subsequent studies.

4.2 Standard displaced harmonic oscillator model

The displaced harmonic oscillator (DHO) model provides a standard method of modelling the coupling of nuclear motion and electronic states. It is widely applied and useful in understanding the core concepts of photoinduced wavepacket dynamics which can then be adapted to more complex models. In earlier chapters wavepacket dynamics along a harmonic oscillator PES has been exemplified. In the DHO model there are two electronic states, a ground state g and excited state e, each represented by a harmonic oscillator PES. The excited state of a molecular system usually corresponds to a different equilibrium geometry due to the variation in its electron configuration. This is captured in the DHO model by a displacement of the coordinate q between the ground and excited potentials. Consequently, there is a connection between the electronic and vibrational properties of the system such that the nuclear configuration of the excited electronic state is dependent on the displacement. Furthermore, the electronic energy gap in going from the ground state configuration to the excited state configuration is also dependent on this. In this section, following the notes of Tokmakoff [130], we discuss how these effects arise and their observation through linear absorption spectroscopy.

To construct the model consider two PESs, V_g and V_e, for the ground and excited electronic states respectively. The difference in energy between their ground vibrational configurations is denoted $E_e - E_g$. The Hamiltonian of the overall system is given by

$$H_S = H_G + H_E. \tag{4.10}$$

The state of the system is described through the product states

$$|\Psi_G\rangle = |g, n_g\rangle, \tag{4.11}$$

$$|\Psi_E\rangle = |e, n_e\rangle, \tag{4.12}$$

where g and e represent the electronic states and n_g and n_e the vibrational states. Within this model the adiabatic approximation (also known as the Born-Oppenheimer approximation) [13, 68] is made, which is a simplification based on the difference of timescales of motion with respect to the nucleus and electron. As the mass of the nucleus is much greater than that of the electron, the motion of the nuclei is assumed to be much slower than the electronic motion. This allows a separation in the treatment of the nuclear and electronic systems. This approximation breaks down in regions where

two PESs come close and the coupling between them becomes large. In such regions a conical intersection may be found in more than one dimension, or an avoided crossing in one dimension. Computational studies suggest that such features are present in many chemical systems and that they may play a key role in photochemistry by providing efficient pathways for fast transitions between electronic states [8]. For a system subject to a dissipative environment, the difference between whether the transition occurs via an avoided crossing or conical intersection has been found to be minor [182]. Nonetheless, in this chapter the Born-Oppenheimer approximation suffices for the features analysed because the models presented have well separated PESs. Furthermore, within this approximation the product states are the eigenstates of H_S such that

$$H_G|\Psi_G\rangle = (E_g + E_{n_g})|\Psi_G\rangle \tag{4.13}$$

and

$$H_E|\Psi_E\rangle = (E_e + E_{n_e})|\Psi_E\rangle. \tag{4.14}$$

Each of the Hamiltonians H_G and H_E are related to the respective and independent electronic and vibrational energies, of the ground and excited electronic states. Separating these we have

$$H_G = |g\rangle E_g\langle g| + H_g(q), \tag{4.15}$$

$$H_E = |e\rangle E_e\langle e| + H_e(q), \tag{4.16}$$

where we have the electronic energies E_g and E_e and the nuclear Hamiltonians H_g and H_e which describe the change in energy as a function of the nuclear coordinate. It is the PES associated with the vibronic Hamiltonians which is assumed to be harmonic. In addition to this, it is standard in the DHO model to assume that each of the PESs have equal curvature.

The vibronic Hamiltonians are given by

$$H_g = \frac{p^2}{2m} + \frac{1}{2}m\omega_0^2 q^2, \tag{4.17}$$

$$H_e = \frac{p^2}{2m} + \frac{1}{2}m\omega_0^2 (q-d)^2, \tag{4.18}$$

where $\omega_0 = \omega_g = \omega_e$, and d represents the displacement along coordinate q of the excited PES relative to the ground PES. As discussed in the last section the absorption

lineshape can be obtained if we know the dipole correlation function which is given by

$$\begin{aligned} C_{\mu\mu}(t) &= \langle \bar{\mu}(t)\bar{\mu}(0)\rangle \\ &= \sum_{k=G,E} p_k \langle k|e^{iH_S t/\hbar}\bar{\mu}e^{-iH_S t/\hbar}\bar{\mu}|k\rangle, \end{aligned} \tag{4.19}$$

where p_k represents the probability of occupying a particular electronic and vibrational state. Hereafter, we make the Condon approximation in which it is assumed that the nuclear dependence q is negligible for the dipole operator. This suggests that a transition between electronic surfaces preserves the nuclear configuration, that is to say there is no change in the nuclear coordinate during the transition. This is commonly known as a vertical transition as on a PES diagram the vibrational wavfunction does not change shape but is shifted vertically between the electronic PESs. The approximation is based on the assumption that electronic transitions occur on a time scale that is short compared to nuclear motion. Consequently, the dipole operator becomes an operator that acts solely on the electronic states

$$\bar{\mu} = |g\rangle\mu_{ge}\langle e| + |e\rangle\mu_{eg}\langle g|. \tag{4.20}$$

In addition, it is of use to note that the time evolution of the system can be split as the time-evolution propagator for each surface

$$e^{-iH_S t/\hbar} = |\Psi_G\rangle e^{-iH_G t/\hbar}\langle\Psi_G| + |\Psi_E\rangle e^{-iH_E t/\hbar}\langle\Psi_E|. \tag{4.21}$$

Substituting Eq. 4.20 and Eq. 4.21 into the dipole correlation function Eq. 4.19 gives the result

$$C_{\mu\mu}(t) = |\mu_{eg}|^2 e^{-i(E_e - E_g)t/\hbar}F(t), \tag{4.22}$$

where the dephasing function

$$\begin{aligned} F(t) &= \langle e^{iH_g t/\hbar}e^{-iH_e t/\hbar}\rangle \\ &= \langle U_g^\dagger U_e\rangle \end{aligned} \tag{4.23}$$

has been introduced in which the average is taken over the vibrational states $|n_g\rangle$. Thus, for a two level system within the Condon approximation the correlation function can be split into the product of an oscillation at the electronic energy gap and the

nuclear dynamics of the dephasing function. Furthermore, the dephasing function can be recast into the form

$$F(t) = \langle \varphi_g(t) | \varphi_e(t) \rangle, \tag{4.24}$$

where $|\varphi_g\rangle$ and $|\varphi_g\rangle$ are the nuclear wavefunctions. The motivation for this form is twofold. Firstly, it informs us that the dephasing function is dependent on wavepacket dynamics and the overlap of the time-dependent nuclear wavefunctions. Secondly, if one knows the electronic and nuclear eigenstates, or the dynamics of the nuclear wavefunctions, then it provides a general expression that allows the calculation of the dipole correlation function and in turn the absorption lineshape. This is a useful result that will be used throughout this thesis in the calculation of linear absorption spectra.

Let us turn our attention once again to the harmonic oscillator model and consider the calculation of $F(t)$. The harmonic oscillator provides a problem for which the form of the Hamiltonians are well known. The electronic ground state nuclear Hamiltonian is given by

$$H_g = \hbar\omega_0(a^\dagger a + \frac{1}{2}). \tag{4.25}$$

The electronic excited state nuclear Hamiltonian can also be written similarly if we introduce the displacement operator

$$\hat{D} = e^{-i\hat{p}d/\hbar}. \tag{4.26}$$

This acts on the coordinate operator such as to shift it by d giving

$$\hat{D}\hat{q}\hat{D}^\dagger = \hat{q} - d. \tag{4.27}$$

Using the displacement operator the Hamiltonian H_e becomes

$$H_e = \hat{D}H_g\hat{D}^\dagger, \tag{4.28}$$

which simply relays that the PES of the excited electronic state is shifted by d with respect to the ground electronic state. It follows that this then allows the redefinition of the excited electronic state time-evolution propagator as

$$e^{-iH_e t/\hbar} = \hat{D}e^{-iH_g t/\hbar}\hat{D}^\dagger \tag{4.29}$$

and allows us to write the dephasing function as

$$\begin{aligned} F(t) &= \langle U_g^\dagger e^{-idp/\hbar} U_g e^{idp/\hbar} \rangle \\ &= \langle \hat{D}(t)\hat{D}^\dagger(0) \rangle. \end{aligned} \tag{4.30}$$

This makes apparent the relation of the dipole correlation functions nuclear part to the displacement of the vibrational coordinate. Furthermore, by using the time-evolution propagator the time evolution of $\hat{p}$ is given by

$$\hat{p}(t) = U_g^\dagger \hat{p}(0) U_g, \tag{4.31}$$

which means that the dephasing function can be written as

$$F(t) = \langle e^{-id\hat{p}(t)/\hbar} e^{id\hat{p}(0)/\hbar} \rangle. \tag{4.32}$$

As we did for the Hamiltonian, the operator $\hat{p}$ can be expressed in terms of raising and lowering operators

$$\hat{p} = i\sqrt{\frac{m\hbar\omega_0}{2}}(a^\dagger - a). \tag{4.33}$$

This is a useful form as we can transfer the time dependence to the raising and lowering operators

$$U_g^\dagger a U_g = a e^{-i\omega_0 t}, \tag{4.34}$$

$$U_g^\dagger a^\dagger U_g = a^\dagger e^{i\omega_0 t}, \tag{4.35}$$

which means that $\hat{p}(t)$ may be written as

$$\hat{p}(t) = i\sqrt{\frac{m\hbar\omega_0}{2}}(a^\dagger e^{i\omega_0 t} - a e^{-i\omega_0 t}). \tag{4.36}$$

Therefore the exponential operators become

$$e^{-id\hat{p}(t)/\hbar} = \exp\Big(d\sqrt{\frac{m\omega_0}{2\hbar}}(a^\dagger e^{i\omega_0 t} - a e^{-i\omega_0 t}) \Big), \tag{4.37}$$

$$e^{-id\hat{p}(0)/\hbar} = \exp\Big(- d\sqrt{\frac{m\omega_0}{2\hbar}}(a^\dagger - a) \Big). \tag{4.38}$$

To simplify these expressions the dimensionless displacement may be defined as

$$\Delta = d\sqrt{\frac{m\omega_0}{2\hbar}}. \tag{4.39}$$

Furthermore, as the raising and lowering operators are non-commuting they cannot simply be split. Instead, as a consequence of the Baker-Campbell-Hausdorff formula the operators may be split as

$$e^{\hat{A}+\hat{B}} = e^{\hat{A}}e^{\hat{B}}e^{-\frac{1}{2}\left[\hat{A},\hat{B}\right]}. \tag{4.40}$$

With this the exponential operators are given by

$$e^{-id\hat{p}(t)/\hbar} = \exp\Big(\Delta a^{\dagger}e^{i\omega_0 t}\Big)\exp\Big(-\Delta a e^{-i\omega_0 t}\Big)\exp\Big(-\frac{1}{2}\Delta^2\Big), \tag{4.41}$$

$$e^{-id\hat{p}(0)/\hbar} = \exp(-\Delta a^{\dagger})\exp(\Delta a)\exp\Big(-\frac{1}{2}\Delta^2\Big). \tag{4.42}$$

Further simplification is possible if we take the low temperature approximation, for which the equilibrium state is the ground vibrational state. Remembering the usual raising and lowering operator properties acting on the ground vibrational state it follows that

$$e^{-a}|0\rangle = |0\rangle, \tag{4.43}$$

$$\langle 0|e^{a^{\dagger}} = \langle 0|. \tag{4.44}$$

Therefore, within the low temperature approximation the dephasing function simplifies to

$$F(t) = \langle 0|e^{-id\hat{p}(t)/\hbar}e^{-id\hat{p}(0)/\hbar}|0\rangle \tag{4.45}$$

$$= e^{-\Delta^2}\langle 0|\exp\Big(-\Delta a e^{-i\omega_0 t}\Big)\exp\Big(-\Delta a^{\dagger}\Big)|0\rangle. \tag{4.46}$$

This can be brought into a more practical form by using the operator identity

$$e^{\hat{A}}e^{\hat{B}} = e^{\hat{B}}e^{\hat{A}}e^{-\left[\hat{B},\hat{A}\right]}, \tag{4.47}$$

which can be shown using the previous identity by noting

$$e^{\hat{A}+\hat{B}} = e^{\hat{B}+\hat{A}} = e^{\hat{A}}e^{\hat{B}}e^{-\frac{1}{2}\left[\hat{A},\hat{B}\right]}, \tag{4.48}$$

and

$$e^{-\frac{1}{2}\left[\hat{A},\hat{B}\right]} = e^{\frac{1}{2}\left[\hat{B},\hat{A}\right]}. \tag{4.49}$$

It follows that, using Eq. 4.48, and the first identity of Eq. 4.40 for $\exp(\hat{B}+\hat{A})$, we can write

$$e^{\hat{A}}e^{\hat{B}}e^{-\frac{1}{2}\left[\hat{A},\hat{B}\right]} = e^{\hat{B}}e^{\hat{A}}e^{-\frac{1}{2}\left[\hat{B},\hat{A}\right]}. \tag{4.50}$$

Subsequently, substituting for Eq. 4.49 allows us to derive the operator identity

$$e^{\hat{A}}e^{\hat{B}}e^{-\frac{1}{2}\left[\hat{A},\hat{B}\right]} = e^{\hat{B}}e^{\hat{A}}e^{\frac{1}{2}\left[\hat{A},\hat{B}\right]} \tag{4.51}$$

$$e^{\hat{A}}e^{\hat{B}} = e^{\hat{B}}e^{\hat{A}}e^{\left[\hat{A},\hat{B}\right]} \tag{4.52}$$

Applying this identity to the dephasing function gives

$$\begin{aligned} F(t) &= e^{-\Delta^2}\langle 0|\exp(-\Delta a^\dagger)\exp(-\Delta a e^{-i\omega_0 t})\exp(\Delta^2 e^{-i\omega_0 t})|0\rangle \\ &= \exp(\Delta^2(e^{-i\omega_0 t}-1)), \end{aligned} \tag{4.53}$$

where in going from the first to the second line Eq. 4.43 and Eq. 4.44 have been used. It is of use to define the Huang-Rhys parameter

$$D = \Delta^2 = d^2\frac{m\omega_0}{2\hbar}, \tag{4.54}$$

which is a dimensionless parameter that represents the coupling of the electronic transition to the nuclear coordinate. Lastly, as we have an expression for the dephasing function, the dipole correlation function may be defined as

$$C_{\mu\mu}(t) = |\mu_{eg}|^2\exp\Big(-i\omega_{eg}t + D(e^{-i\omega_0 t}-1)\Big). \tag{4.55}$$

As discussed in the last section, the absorption lineshape can be obtained by Fourier transforming the dipole correlation function

$$\sigma(\omega) = \int_{-\infty}^{\infty} dt\, e^{i\omega t}C_{\mu\mu}(t) \tag{4.56}$$

$$= |\mu_{eg}|^2 e^{-D}\int_{-\infty}^{\infty} dt\, e^{i\omega t}e^{-i\omega_{eg}t}\exp(De^{-i\omega_0 t}). \tag{4.57}$$

Using the series expansion for the exponential function

$$\exp(De^{-i\omega_0 t}) = \sum_0^\infty \frac{1}{n!}D^n(e^{-i\omega_0 t})^n, \tag{4.58}$$

and Fourier transform of the exponential function, an analytic expression for the absorption lineshape is found

$$\sigma(\omega) = |\mu_{eg}|^2\sum_0^\infty e^D\frac{D^n}{n!}\delta(\omega-\omega_{eg}-n\omega_0), \tag{4.59}$$

where δ represents the Dirac delta function.

4.2.1 Linear absorption spectrum and the Franck-Condon principle

Consider the absorption lineshape defined by Eq. 4.59, this generates an absorption spectrum as a function of the frequency. In general, the absorption spectrum consists of a progression of several peaks. For the DHO model these peaks begin at the frequency of ω_{eg} and appear at a regular spacing of ω_0 from this. Such a progression that depends on the electronic transition and vibrational states is called a vibronic progression. The Franck-Condon principle is a rule that explains the amplitude of peaks in the vibronic transition. It states that for a given electronic transition, the change from one vibrational state to another is more likely to happen if there is significant overlap between their vibrational wave functions. Formally, the peak amplitude is given by the so called Franck-Condon coefficients (FCC), also known as Franck-Condon factors, for the overlap of vibrational states of the ground and excited electronic states. For the DHO model discussed these are given by

$$\begin{aligned} |\langle n_g = 0 | n_e = n \rangle|^2 &= |\langle 0 | \hat{D} | n \rangle|^2 \\ &= e^{-D} \frac{D^n}{n!}. \end{aligned} \tag{4.60}$$

From this formula the relation between the displacement, or specifically the Huang-Rhys parameter D, and the vibronic progression can be seen. If there is no displacement then $D = 0$ and there is only an overlap between ground vibrational states. Consequently, one peak is seen in the progression at ω_{eg}, and it is independent of the nuclear coordinate. This peak is known as the $0-0$ transition, or the zero phonon line (ZPL). In the weak coupling regime of $D < 1$ a progression of peaks appears in which the ZPL has the largest amplitude, implying the absorption maximum is at ω_{eg}, and the other peaks decrease in amplitude as D^n. In the strong coupling regime of $D > 1$ the peak with the largest amplitude is given by $n \approx D$. The FC coefficients given by Eq. 4.60 apply to the case of displaced harmonic oscillator PESs with equal curvature. Note, that the FCC provide the vibronic progressions associated with linear absorption spectra and can thus be corresponded with the linear absorption spectra as generated by Eq. 4.8. As we have seen in the last section, this can be calculated by Eq. 4.56, which means if we have knowledge of the ground and excited wavepacket dynamics, we can calculate the absorption spectra. In the next section this is extended to the case of different curvature and original results are presented of the effect on the vibronic progression with a focus on cases where the curvature difference is large.

4.3 Model study of curvature difference

A notable feature in photoswitch potentials, such as stilbene photoswitches, is the large difference in curvature of ground and excited PESs. To isolate, and illustrate, the effect this may have on absorption spectra a model is utilised that has harmonic ground and excited potentials that differ in curvature. It should be noted that such a model has limitations in describing the complete photoswitch dynamics due to deviations from the harmonic approximation that occur in photoswitch PESs, such as potential energy barriers, and coupling between excited and ground electronic states. In the following this is referred to as the harmonic differing curvature model, whereas harmonic potentials with equal curvature is referred to as the standard harmonic model. For the harmonic differing curvature model, a previous study by Fidler and Engel [172] has found that the location of the absorption peak maximum, and the absorption width, are dependent on curvature difference. Specifically, for a shallower excited state, the location of the absorption peak maximum will slightly shift to lower frequencies, whilst the peak width will decrease. Additionally, a four level system which features harmonic PESs with differing curvature has been studied [183].

In this study [181] the restriction of modest curvature difference and displacement of the excited state PES, which are not valid assumptions for some photoswitches such as stiff-stilbene, is lifted to show that new features arise in absorption spectra. To allow focus on the effect of curvature difference, spectral broadening effects of the environment, with this model, will not be included in this section, and instead is reserved to subsequent chapters. The Hamiltonians for this model are thus given by

$$H_g = \frac{p^2}{2m} + \frac{1}{2}m\omega_g^2 q^2, \tag{4.61}$$

$$H_e = \frac{p^2}{2m} + \frac{1}{2}m\omega_e^2 (q-d)^2, \tag{4.62}$$

where contrary to the standard displaced harmonic oscillator model of Eq. 4.17 and Eq. 4.18, the curvature $\omega_g \neq \omega_e$. For comparison, a schematic of the standard model is presented in Fig. 4.2(a), whilst the differing curvature model is presented in Fig. 4.2(b). Under these circumstances the Franck-Condon principle explains the intensity of vibronic transitions that are shown in absorption spectra. As described in the previous section, this principle states that upon excitation, and associated electronic transition, a change from one vibrational energy level to another is dependent on the overlap of the

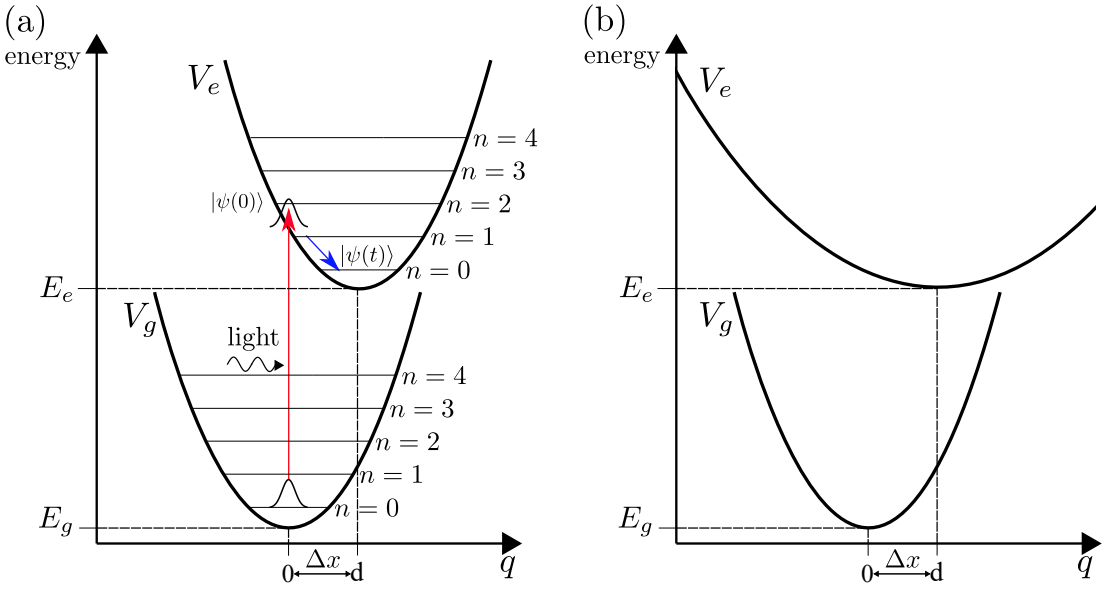

Figure 4.2: Schematic for displaced harmonic oscillator models, with ground electronic PES V_g and excited electronic PES V_e, that are displaced by d along the coordinate q. Vibrational energy levels are represented by n, and the electronic energy gap is given by $E_e - E_g$. (a) The standard harmonic model is shown where the curvature of V_g is equal to the curvature of V_e such that the oscillator frequency $\omega_g = \omega_e$. The wavepacket $|\psi(0)\rangle$ is vertically photoexcited from V_g to V_e (red arrow) where it is no longer in equilibrium and thus undergoes dynamics on the excited electronic PES to $|\psi(t)\rangle$ (blue arrow). (b) The displaced harmonic oscillator model for differing curvature is shown, for which a similar photoexcitation process occurs. However, for this model the curvature of V_g does not equal the curvature of V_e such that $\omega_g \neq \omega_e$.

nuclear wavefunctions, and more likely to occur if the overlap is significant. According to this principle, the amplitudes of absorption peaks are given by the Frank-Condon coefficients $|\langle\psi_g^{n=0}|\psi_e^n\rangle|^2$, where n represents the vibrational state of the nuclear wavepacket, $n = 0$ represents the vibrational ground state wavepacket, and g and e represent the ground and excited electronic wavepackets respectively. This expression represents the overlap between the ground electronic state in the lowest vibrational state, and the excited electronic state in the n^{th} vibrational state. The assumption that the ground state electronic wavepacket is in the lowest vibrational state holds for the low temperature regime, in particular it is valid for room temperature at 298 K. In this case,

the expression represents the intensities of peaks in low temperature absorption spectra. Franck-Condon coefficients for the standard displaced harmonic oscillator are well known and show a dependence on the Huang-Rhys parameter. As discussed in the last section, for $D = 0$ only one peak is expected corresponding to the coefficient

$$|\langle\psi_g^{n=0}|\psi_e^{n=0}\rangle|^2 = 1. \tag{4.63}$$

The peak intensity, corresponding to the respective Franck-Condon coefficient, is shown in Fig. 4.3(a), where the standard harmonic case with $\omega_g = \omega_e = 1$ (black dashed line) is compared to the harmonic potentials with differing curvatures model $\omega_g = 10\omega_e$ and $\omega_e = 1$ (blue line) for zero displacement $D = 0$. In the standard harmonic case the FCC of Eq. 4.60 implies there is only one peak at $n = 0$, however, in the harmonic model with differing curvature a decaying progression of peaks is observed for even n, and the peak intensity is 0 for odd n. In Fig. 4.3(b), for which $D = 30$ and $\omega_g = \omega_e = 1$, this relation is seen to give rise to a Gaussian profile (black dashed line), centered at the Franck-Condon vertical transition. The largest intensity peak is at $n = 30$ and thus D can be associated with the mean number of vibrational quanta excited for $|\psi_e\rangle$. Comparing this to the harmonic differing curvature model, with $\omega_g = 10\omega_e$ and $\omega_e = 1$, there are three notable differences. Firstly, the width of the main vibronic progression decreases and the intensity of central peaks increases. Secondly, the largest intensity peak shifts from $n = 30$ to $n > 30$. Last but not least, there is the appearance of a number of smaller intensity vibronic progressions that occur at larger n than the main vibronic progression, and these decay to zero as n increases. Owing to the sub-structure nature of these progressions, the name given to this feature is the sub-structure vibronic progression or s-progression for short. In the next section we shall derive expressions for the FCC that help to explain the difference in the two models.

Before these expressions are provided, Figure 4.4 allows insight into the appearance of the s-progression. Three excited state vibrational wavefunctions $|\psi_e^n\rangle$ are plotted corresponding to $n = 38, 39$ and $n = 40$, this is compared to the ground state wavefunction $|\psi_g^{n=0}\rangle$ for the standard harmonic model $\omega_g = \omega_e$ and the differing curvature model $\omega_g > \omega_e$. The vibrational state numbers are chosen to correspond to where the first progression in the s-progression starts at approximately $n = 38$ and to where it is at its maximum intensity at $n = 40$. From this it can be seen that the narrow width of the ground wavefunction of the differing curvature model overlaps with close to only one of the oscillations of the excited state vibrational wavefunctions. As a result, the

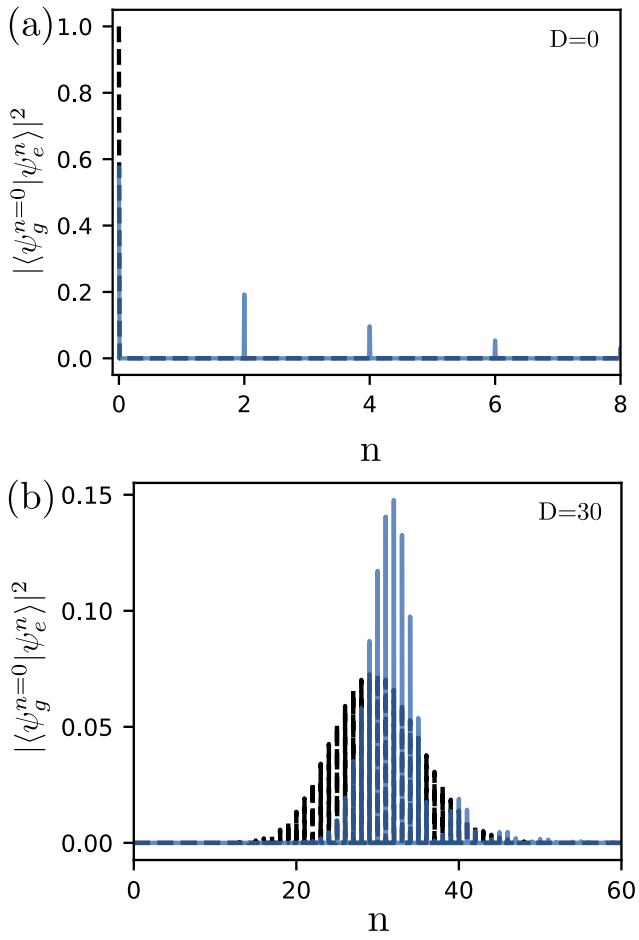

Figure 4.3: Franck-Condon coefficients for the standard harmonic model (black dashed line) with oscillator frequencies $\omega_g = \omega_e = 1$ and differing curvature model with $\omega_g = 10\omega_e$ and $\omega_e = 1$ (blue line) for (a) the case of no displacement ($D = 0$) and (b) displaced potentials ($D = 30$). Notably, in the displaced and un-displaced cases, there is an additional vibronic sub-structure for the differing curvature model, not present in the standard harmonic model. Additionally, for the displaced case, there is a shift in the peak of the main progression to larger n and the width of the progression decreases.

overlap is sensitive to whether, at $x = 0$, the excited state vibrational wavefunction $|\psi_e^n\rangle$ is close to a local minima, maxima, or close to zero. For $n = 38$, the peak of $|\psi_g^{n=0}\rangle$, located at $x = 0$, is nearly aligned with a point where $|\psi_e^{n=38}\rangle = 0$, thus the overlap largely cancels and the Franck-Condon coefficient becomes close to zero. For $n = 40$ the peak of the $|\psi_g^{n=0}\rangle$ is nearly aligned with a local minima of $|\psi_e^{n=40}\rangle$, this results in a

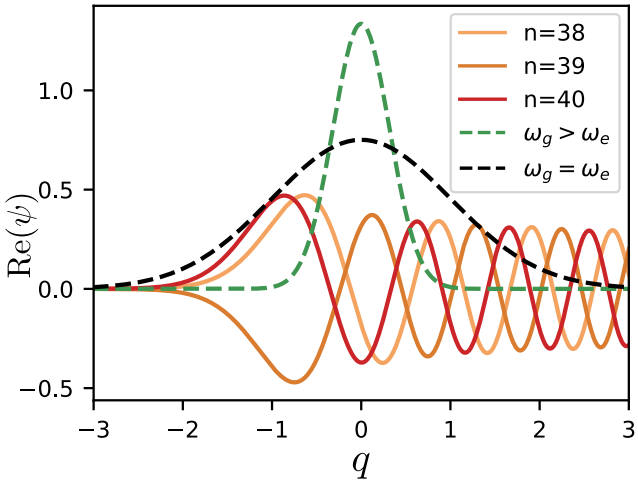

Figure 4.4: The nuclear wavefunctions for the ground and excited potentials are represented by the dashed and solid lines respectively. For the differing curvature model (green dashed line) the overlap is sensitive to individual oscillations of wavefunctions on the excited potential. For $q = 0$, if the excited state vibrational wavefunction $|\psi_e^n\rangle$ is close to a local minima or maxima, as in the case of $n = 40$, the overlap is mainly constructive and leads to the large intensity parts of Fig. 4.3. The converse effect happens if at $q = 0$, $|\psi_e^n\rangle$ is close to 0, as in the case of $n = 38$.

overlap that is large and thus this part of the s-progression is at its maximum intensity. In comparison, $|\psi_g^{n=0}\rangle$ in the standard harmonic model has a large width and does not pick out the fine structure of individual oscillations, therefore the effect is averaged out.

The decay of the progression can also be understood through this figure, as n increases the oscillations of $|\psi_e^n\rangle$, in the region of overlap, become closer together and equal in amplitude. For large n the width of $|\psi_g^{n=0}\rangle$ in the differing curvature model no longer isolates individual oscillations and the effect decays to zero, as in the standard harmonic model. The shift of the main vibronic progression to larger n can also be understood by Fig. 4.4. The overlap occurs first at the edges of $|\psi_e^n\rangle$, and as the width of the differing curvature model is much less than in the standard harmonic model a larger n is required before any overlap is achieved. The decrease in width of the main vibronic progression is also due to overlap with individual oscillations and the small width of $|\psi_g^{n=0}\rangle$, as the overlap increases and decreases more rapidly with increasing n.

Three features have thus far been identified, a shift of the main vibronic progression

to larger n, a decrease in the width of the main progression, and the appearance of an s-progression. These have been explained with the help of Fig. 4.4 that shows the relative overlap.

4.3.1 Franck-Condon coefficients for the differing curvature model

Let us now derive the analytic expressions for the Franck-Condon coefficients that quantify these features and provide deeper insight into their appearance. We start with the case of $D = 0$, for the differing curvature model, where further details of the derivation are contained in Appendix B.1.1. For the differing curvature model the ground state wavefunction is given by

$$|\psi_g^{n=0}\rangle = N_g \exp\Big(-\frac{1}{2}\alpha_g q^2\Big), \tag{4.64}$$

where

$$N_g = \Big(\frac{\alpha_g}{\pi}\Big)^{1/4}, \tag{4.65}$$

and

$$\alpha_g = \frac{m\omega_g}{\hbar}, \tag{4.66}$$

where, m is the mass, and ω_g is the angular frequency of the electronic ground state oscillator. The excited state wavefunction, in the n^{th} vibrational state, is given by

$$|\psi_e^n\rangle = N_n H_n(\sqrt{\alpha_e}q) \exp\Big(-\frac{1}{2}\alpha_e q^2\Big), \tag{4.67}$$

where

$$N_n = \Big(\frac{\sqrt{\alpha_e}}{2^n n!\sqrt{\pi}}\Big)^{1/2}, \tag{4.68}$$

and

$$\alpha_e = \frac{m\omega_e}{\hbar}. \tag{4.69}$$

The object of interest is the overlap integral between $|\psi_g^{n=0}\rangle$ and $|\psi_e^n\rangle$, which is given by

$$\langle\psi_g^{n=0}|\psi_e^n\rangle = N_g N_n \int_{-\infty}^{\infty} dq\, H_n(\sqrt{\alpha_e}q) \exp\Big(-\alpha q^2\Big), \tag{4.70}$$

where

$$\alpha = \frac{\alpha_e + \alpha_g}{2}, \tag{4.71}$$

and $H_n(q)$ is the n^{th} Hermite polynomial. Note that for odd n, $H_n(q)$ is an odd function. The product of this odd function with the even Gaussian function, is odd. Taking the integral of an odd function over a symmetric region results in zero. Thus we have our first result that for odd n, and $D = 0$ the Franck-Condon coefficient is zero, as demonstrated in Fig. 4.3(a).

For the case of even n and $D = 0$ the derivation presented in Appendix B.1.1 results in the expression

$$|\langle\psi_g^{n=0}|\psi_e^n\rangle|^2 = \frac{n!}{2^n((\frac{n}{2})!)^2}\frac{\sqrt{\alpha_e\alpha_g}}{\alpha}\left(1-\frac{\alpha_e}{\alpha}\right)^n, \tag{4.72}$$

for the FCC in the differing curvature model.

Equation 4.72 has some noteworthy features. Firstly, for $\omega_e = \omega_g$ we also have $\alpha_e = \alpha$ and in this case the only non-zero value for the Franck-Condon coefficient is when $n = 0$. Therefore, as expected, in the harmonic limit Eq. 4.72 gives $|\langle\psi_g^{n=0}|\psi_e^{n=0}\rangle|^2 = 1$. In addition, this expression provides the peak intensity of the progression shown in Fig. 4.3(a), and predicts a decay as n increases. Furthermore, the progression will sustain for larger n, if the difference in curvature is increased. In the large curvature difference limit, the shape of the progression will be predominantly determined by

$$\frac{n!}{2^n((\frac{n}{2})!)^2}\frac{\sqrt{\alpha_e\alpha_g}}{\alpha}. \tag{4.73}$$

Following in the same manner we now derive and present an analytic expression for the more general case of when the differing curvature model is displaced. An even more general expression for the Franck-Condon factors of the differing curvature model was derived by Chang [184], which allows for $n \geq 0$ for $|\psi_g^n\rangle$. However, the derivation presented here diverges from that of Chang, implementing the solution found in the un-displaced model, connecting the two solutions. Additionally, the end expression obtained is in a form that allows for the interpretation of the observed features in Fig. 4.3, and provides insight into the appearance of the s-progression. Firstly, the excited state is redefined as

$$|\psi_e^n\rangle = N_n H_n(\sqrt{\alpha_e}(q-d))\exp\left(-\frac{1}{2}\alpha_e(q-d)^2\right), \tag{4.74}$$

where d corresponds to the displacement of the potential. Using this definition the

overlap integral, between $|\psi_g^{n=0}\rangle$ and $|\psi_e^n\rangle$, is given by

$$\begin{aligned}\langle\psi_g^{n=0}|\psi_e^n\rangle =& N_g N_n \int_{-\infty}^{\infty} dq\, H_n(\sqrt{\alpha_e}(q-d)) \\ & \times \exp\Big(-\frac{1}{2}(\alpha_g q^2 + \alpha_e(q-d)^2\Big).\end{aligned} \tag{4.75}$$

Following the derivation in Appendix B.1.2, the FCC for the differing curvature model with non-zero displacement are given by

$$\begin{aligned}|\langle\psi_g^{n=0}|\psi_e^n\rangle|^2 =& \frac{1}{2^n n!}\frac{\sqrt{\alpha_e\alpha_g}}{\alpha}e^{-A} \\ & \times \Big| n! \sum_{l=0}^{\lfloor n/2\rfloor} \frac{(-1)^l}{l!(n-2l)!}(2\beta)^{n-2l} \\ & \times \Big(1-\frac{\alpha_e}{\alpha}\Big)^l \Big|^2 .\end{aligned} \tag{4.76}$$

At this point it is illuminating to consider this equation in limits of interest. Firstly, in the standard displaced harmonic model limit, that is to say of equal curvature, $\alpha_e = \alpha$. In this case, the only term that survives in the summation is when $l = 0$. Furthermore, in this limit $A = D$ the Huang-Rhys parameter, and $\beta = \sqrt{D/2}$. Therefore, making these substitutions we obtain the familiar formula, for harmonic FC coefficients, Eq. 4.60.

The second limit of interest is when the displacement is zero. In this case, the only term that survives the summation in Eq. 4.76, is when $l = n/2$. Substituting this value in and simplifying reproduces Eq. 4.72, the result of the first derivation. A final limit of interest is when the curvature is large, for which the shape of the progression is predominantly determined by

$$\begin{aligned}|\langle\psi_g^{n=0}|\psi_e^n\rangle|^2 =& \frac{1}{2^n n!}\frac{\sqrt{\alpha_e\alpha_g}}{\alpha}e^{-A} \\ & \times \Big| n! \sum_{l=0}^{\lfloor n/2\rfloor} \frac{(-1)^l}{l!(n-2l)!}(2\beta)^{n-2l} \Big|^2 .\end{aligned} \tag{4.77}$$

At this point the motivation for the form given can be found, as the summation in this equation is simply an explicit form of the Hermite polynomial

$$H_n(b) = n! \sum_{l=0}^{\lfloor n/2\rfloor} \frac{(-1)^l}{l!(n-2l)!}(2\beta)^{n-2l}. \tag{4.78}$$

Therefore, substituting this expression gives

$$|\langle\psi_g^{n=0}|\psi_e^n\rangle|^2 = \frac{1}{2^n n!}\frac{\sqrt{\alpha_e\alpha_g}}{\alpha}e^{-A}H_n(\beta)^2, \tag{4.79}$$

for large curvature difference.

The expression of Eq. 4.76 provides the peak intensity of the progression shown in Fig. 4.3(b). Furthermore, by comparing to the limiting cases of this model we see that the s-progression in the displaced case has no corresponding reduction to a single term, and requires more terms of the summation to be accounted for. The summation itself is a modified form of an explicit expression for the Hermite polynomial in which, comparatively, latter terms of the summation contribute less. Thus, as n increases the additional contribution of this summation becomes less important and, along with the other contributions in the equation, leads to the decaying feature of the s-progression. As in the zero displacement case, for a larger difference in curvature, the s-progression sustains for larger n.

4.3.2 Two-coordinate curvature difference

In the previous section we discussed the effect of including curvature difference in the DHO model for a single nuclear coordinate. This shall now be extended to a two-coordinate model, which should be noted only differs from a rotated one-coordinate model if there is a difference in curvature between the two coordinates. We maintain most of the structure of the previous model, but in addition to a coordinate q_1 we include a second coordinate q_2. With this change, the vibronic Hamiltonians are given by

$$H_g = \frac{p^2}{2m} + \frac{1}{2}m\omega_{g_1}^2 q_1^2 + \frac{1}{2}m\omega_{g_2}^2 q_2^2, \tag{4.80}$$

$$H_e = \frac{p^2}{2m} + \frac{1}{2}m\omega_{e_1}^2 (q_1 - d_1)^2 + \frac{1}{2}m\omega_{e_2}^2 (q_2 - d_2)^2, \tag{4.81}$$

where ω_{g_i} and ω_{e_i} represent the frequency of the electronic ground and excited state oscillators for coordinate q_i, and d_i represents the displacement of the PES in that coordinate. In this section the absorption spectra shall be generated using Eq. 4.56 which gives

$$\sigma_{abs}(\omega) = \int_{-\infty}^{\infty} dt\, e^{i\omega t} C_{\mu\mu}(t) \tag{4.82}$$

$$= |\mu_{eg}|^2 \int_{-\infty}^{\infty} dt\, e^{i(\omega-\omega_{eg}t)}\langle\psi_g(t)|\psi_e(t)\rangle, \tag{4.83}$$

where parallel dipoles have been assumed and μ_{eg} is the dipole operator. Furthermore, a small exponential decay is applied to the correlation function to ensure the fourier transform is well behaved, this results in some minor phenomenological broadening in the produced spectra.

The inclusion of the second coordinate increases the number of ways that differing curvature, and displacement, can be included. In what follows we shall discuss these, but restrict ourselves to the case of $\omega_{e_i} < \omega_{g_i}$ for a respective coordinate, and larger displacement in one of the coordinates. This is to mimic physically realistic scenarios of photoswitch PESs, in which the excited state PES is often shallower and there is larger displacement in a particular coordinate. In order to connect with the initial study conducted in this chapter, consider the case of equal curvature $\omega_{g_i} = \omega_{e_i} = \omega_0$, the results of which are shown in Fig. 4.5. Note that for this study the parameters are set to $\hbar = \omega_0 = m = 1$. In the first case where there is no displacement in either coordinate $D_1 = D_2 = 0$ there is only the ZPL as in the previous single coordinate study. Subsequently, two cases are plotted $D_1 = 10, D_2 = 0$ represented by the blue line, and $D_1 = 5, D_2 = 5$ represented by the red dashed line. It can be seen that both of these cases give equivalent results, which means that the two coordinate model can be reduced down to a single coordinate model. The reason for this is that with a symmetry in the curvature of both coordinates one can consider the motion along q_1 and q_2 to instead be modelled along a coordinate q that runs diagonal between them. The relation between the two models displacement is then simply found via the Pythagorean theorem as $d^2 = d_1^2 + d_2^2$. As $d_1 = d_2$ this can be written as $d^2 = 2d_1^2$. With this in mind, the relation to the Huang-Rhys parameter is given by

$$\begin{aligned} D = d^2 \frac{m\omega_0}{2\hbar} &= d_1^2 \frac{m\omega_0}{2\hbar} \\ &= 2D_1. \end{aligned} \tag{4.84}$$

Therefore,

$$\frac{D}{2} = D_1 = D_2 \tag{4.85}$$

Thus for the single coordinate model where $D = 10$, the equivalent two coordinate model is obtained with Hang-Rhys factors $D_1 = D_2 = 5$ as shown in Fig. 4.5.

For the standard DHO model and two coordinates we have seen that, with equal curvature, these do not offer anything more than their single coordinate counterparts.

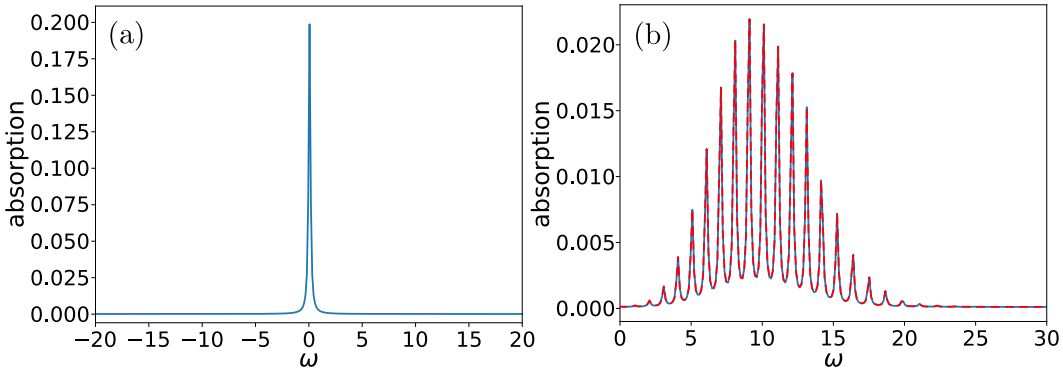

Figure 4.5: The linear absorption spectra of the two coordinate model with equal curvature $\omega_{g_i} = \omega_{e_i}$. (a) Absorption spectra generated from the model with zero displacement in coordinates $D_1 = D_2 = 0$. (b) The linear absorption spectra for a single coordinate model with Huang-Rhys parameter $D = 10$ is shown by the blue line, equivalent results are given by a two coordinate model with $D_1 = D_2 = 5$ as shown by the red dashed line.

We will now extend this to include a difference of curvature. In the first instance consider that there is a difference in curvature in only one of the coordinates such that, $\omega_{g_1} = \omega_{g_2} = \omega_{e_1}$. Furthermore, unless stated otherwise, we will consider displacement in two cases $D_1 > D_2$ and $D_1 < D_2$. If there is a larger displacement in the equal coordinate q_1 then a spectrum similar to the DHO for a single coordinate is observed, shown in Fig. 4.6(a), but there are some larger amplitudes for larger ω giving the appearance of stretching the spectrum. In the case where the larger displacement is in the coordinate q_2, shown in Fig. 4.6(b) a narrow progression is observed with some further peaks at larger wavelength. This further progression is similar to the s-progression but not as distinct. The spectra that is formed from only a single coordinate differing in curvature is distinct from the DHO model but the differences are minor. However, if we instead consider the case of difference in curvature between coordinates $\omega_{g_1} = \omega_{e_1}$ and $\omega_{g_2} = \omega_{e_2}$ complex vibronic progressions are observed (see Fig. 4.6(c) & (d)). As shown in Fig. 4.6(c), if the displacement is greater in the shallow coordinate then several bands are observed each with an associated vibronic progression. Similarly, if the larger displacement is in the steep coordinate, a greater number of vibronic progressions are observed. This is due to a composition effect, in the first instance the

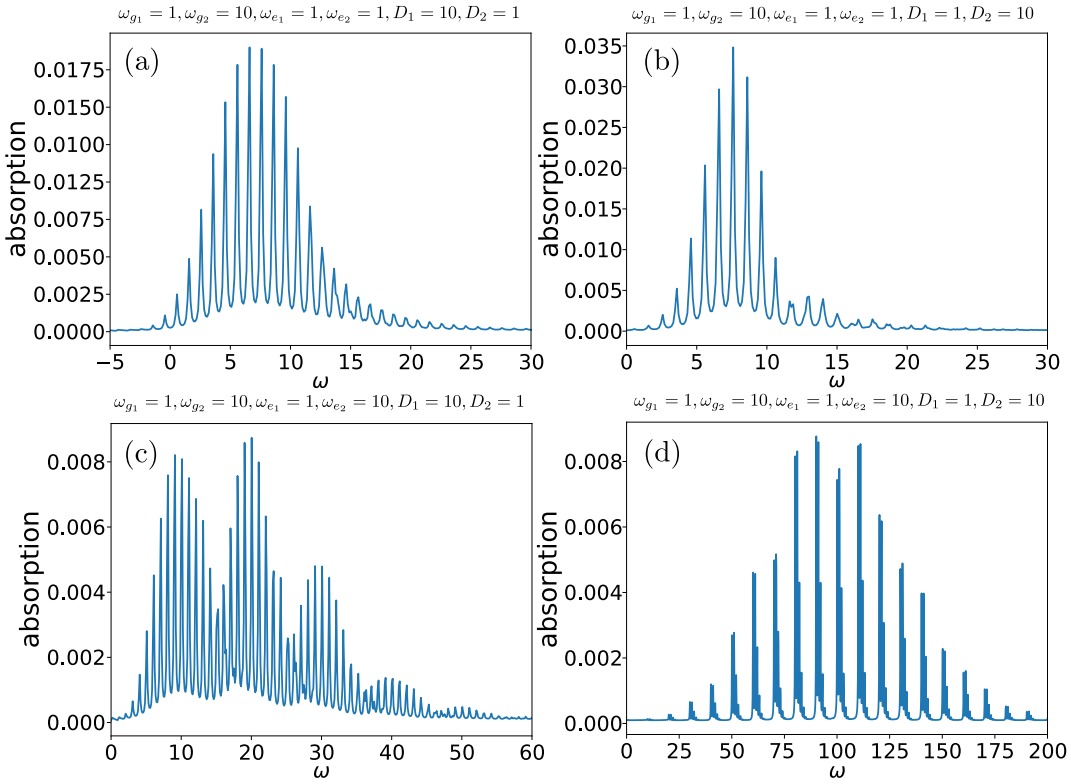

Figure 4.6: Absorption spectra for the two coordinate displaced harmonic oscillator model with differing curvature. Parameter choices are shown above each figure. The left column represents a choice of $D_1 > D_2$ and the right column represents a choice of $D_1 < D_2$. (a)(b) Absorption spectra associated with a difference in curvature with respect to one coordinate only $\omega_{g_1} = \omega_{e_1} = \omega_{e_2}$. (c)(d) Absorption spectra generated using a model with difference in curvature between coordinates $\omega_{g_i} \neq \omega_{e_i}$.

bands are separated in a vibronic progression associated with a Huang-Rhys parameter $D_2 = 1$. For each of the absorption lines associated with this progression there is a sub-progression connected with coordinate q_1 and a Huang-Rhys parameter of $D_1 = 10$. From this point the sub-progression is referred to as the local progression and the wider scale progression is referred to as the global progression. In Fig. 4.6(d) the global progression is generated by the displacement in the steep coordinate q_2 with $D_2 = 10$. On the other hand, the local progression takes the form of a DHO model with $D_1 = 1$.

Proceeding further, in Fig. 4.7(a) & (b) the curvature differs in all but one pair

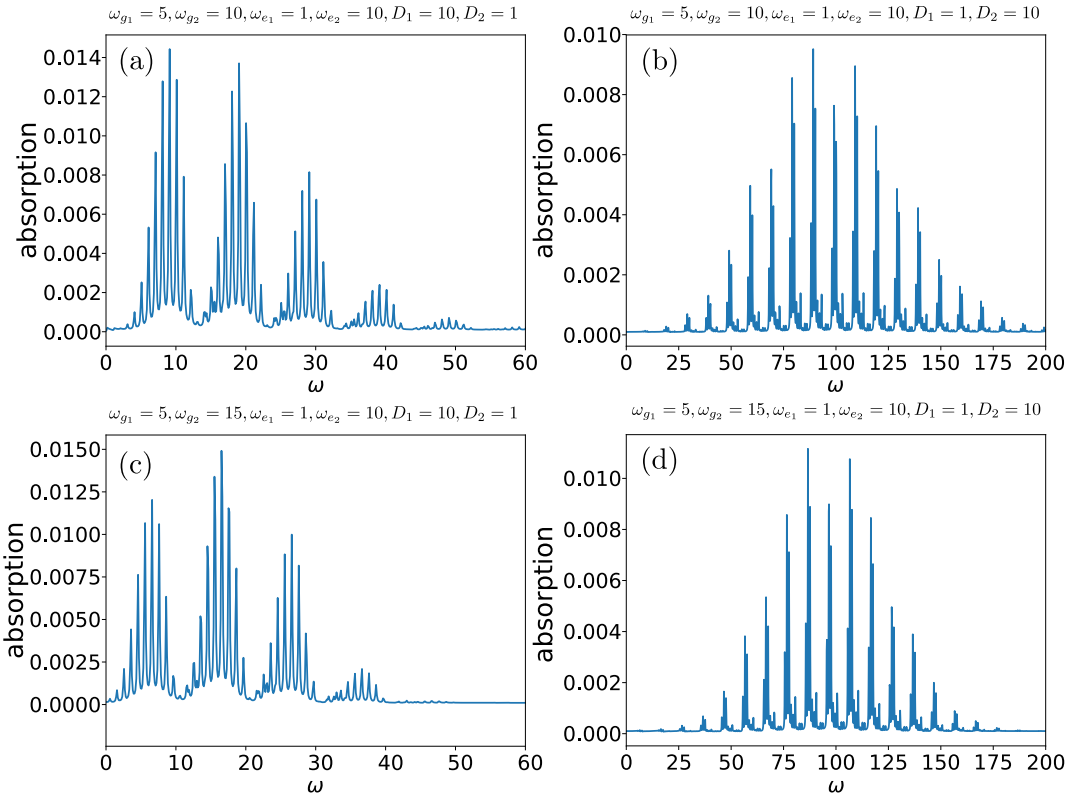

Figure 4.7: Absorption spectra for the two coordinate displaced harmonic oscillator model with differing curvature. Parameter choices are shown above each figure. The left column represents a choice of $D_1 > D_2$ and the right column represents a choice of $D_1 < D_2$. (a)(b) Absorption spectra associated with a choice of $\omega_{g_2} = \omega_{e_2}$ as the only equal oscillator frequencies. (c)(d) Absorption spectra generated using a model with difference in curvature between all coordinates on ground and excited PESs.

$\omega_{g_2} = \omega_{e_2}$. The results are similar to that of Fig. 4.6(c) & (d), meaning that the progression structure is mainly dependent on the composition effect. However, for $D_1 = 10$ and $D_2 = 1$, a narrowing of the local progression is observed. This is similar to what was observed in the single coordinate differing curvature model. However, a clear s-progression is not observed as it is likely obscured by the global progression structure. In the last study, shown in Fig. 4.7(c) & (d) the curvature is different in all coordinates in electronic ground and excited states such that $\omega_{g_1} \neq \omega_{g_2} \neq \omega_{e_1} \neq \omega_{e_2}$. The overall composite spectra is mostly unchanged, however, the global progression is

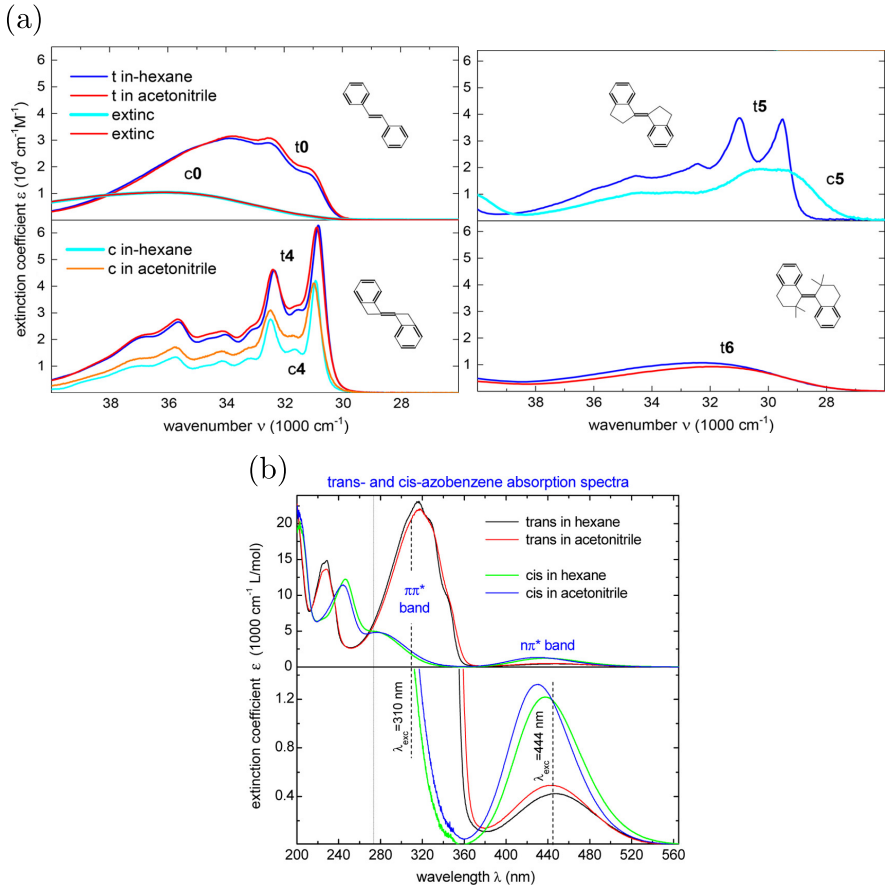

Figure 4.8: (a) Linear absorption spectra of several stiffened stilbene photoswitch variants in solution reprinted (adapted) with permission from reference [2]. Copyright 2019 American Chemical Society. (b) Linear absorption spectra of an azobenzene photoswitch in solution reprinted (adapted) with permission from reference [3]. Copyright 2014 American Chemical Society.

now altered in a similar manner discussed with respect to single coordinate differing curvature models.

Overall the two-coordinate spectra is largely dependent on the composition effect of progressions arising from each coordinate giving rise to a local and global progression. This is the main observable effect, however, by altering the curvature further between electronic ground and excited effects the difference in curvature effects discussed in the last section can also be introduced to the local progression and the global progressions.

Fig. 4.8 demonstrates that complex spectra with several bands may be produced

in the experimental absorption spectra of numerous photoswitches, such as stilbene variants and azobenzene. However, it is important to note that spectral complexity may also arise due to extra electronic excited states.

4.4 Summary

In this chapter we have explored the elementary tool of linear absorption and how it elucidates absorption properties and the nuclear and electronic structure of a quantum system. The standard displaced harmonic oscillator model was reviewed and subsequently extended to include large differences in curvature of ground and electronic PES. This produced increased complexity in the observed absorption spectra of these systems and the appearance of a substructure in the vibronic progression termed the s-progression. The presence of the s-progression in experimental absorption spectra presents a method of verifying, or estimating, the difference in curvature of ground and excited PESs. This is achieved by measuring the width of the s-progression, then comparing and fitting to the derived expressions for the FC coefficients.

Following this, the model was extended to include two coordinates. This generated absorption spectra which was formed by the composition of vibronic progressions for each coordinate, featuring a larger vibronic progression termed the global progression, with sub-progressions termed local progressions. The coordinate with the larger associated oscillator frequency, or curvature, defined the structure of the global vibronic progression. Similarly, the coordinate for which the oscillator frequency was lower defined the structure of the local progressions.

The models developed in this chapter provide a means of understanding the linear absorption of systems with large displacement and curvature difference, which are prominent features of molecular photoswitches. The application of these models assists in the elucidation of vibronic features of photoswitch systems, and in the development of more accurate models. Furthermore, it aids in predicting if there is a large displacement and curvature in a coordinate, and thus informs us on how fast the respective wavepacket dynamics is on a given surface. In the following chapters we discuss these effects in the presence of spectral broadening caused by interaction with an environment of an open quantum system and use the results to interpret spectral features of molecular photoswitches.

Chapter 5

Dissipative quantum dynamics of anharmonic systems

The concept of anharmonicity, introduced in the last chapter, corresponds to a deviation from harmonic models. Whilst the extension of the harmonic model to potential energy surfaces with differing curvature presented was capable of producing complex spectral features, anharmonic models mark a further departure introducing another level of complexity to dynamics and spectroscopy. A harmonic potential energy surface (PES) is quadratic in nature, anharmonic potentials are not restricted to this. Examples include, polynomial potentials, and the Morse oscillator which accounts for bond breaking effects and has been commonly used to model the PES for diatomic molecules providing a better approximation than the harmonic oscillator.

In general, for anharmonic models the energy levels are not evenly spaced as in the harmonic case, which can be observed in linear absorption spectra. Another feature of anharmonic systems is related to finer details of the PES, such as barriers that perturb the energy levels, and give rise to local minima which can trap the wavepacket. In addition, the presence of anharmonicity can have interesting effects on wavepacket dynamics. In the case of the Morse oscillator as displacement is increased, and anharmonic effects become more prevalent, dynamical features emerge. The amplitude of oscillations of the expectation value of the position operator decreases to near zero and after a period of time revives to the near initial oscillation behaviour [165, 185, 186]. Such features can be observed in absorption and emission spectra, and also time-resolved nonlinear spectroscopies.

It is known that spectral features may be broadened by the presence of an environment. Thus a question arises as to how anharmonic and dissipative effects interplay, and the impact on dynamics and spectroscopy results. Systems in which this might be particularly important include photoswitches, where there can be large displacements, and several anharmonic features in the potential. An example of this is found in the stiff-stilbene potential energy surface (PES), for which there is a large difference in curvature on ground and excited potentials, and potential energy barriers on the excited potential which shift energy levels away from the harmonic approximation. These effects can be crucial in identifying spectral observables, wavepacket dynamics, and quantum yields.

Treatment of anharmonic behaviour has been tackled by stochastic environments [187, 188], molecular dynamics simulations [189–191], and by including anharmonicity in the system potential [170, 171, 177]. An extension of a stochastic theory to study

generic quantum environments has also been proposed [192]. In this chapter anharmonic system potentials are used whilst also including an interacting environment via the stochastic Schrödinger equation presented in Chapter 3 [41, 44, 108]. Similarly, there is the quantum jump method capable of simulating nonadiabatic dynamics [193] and methods of simulating conical intersection dynamics in the condensed phase [194]. These become important when the Born-Oppenheimer approximation breaks down and there is a need to account for strongly coupled nuclear and electronic degrees of freedom. Many other such open quantum system methods exist [195] each with their respective advantages and a review has been produced by Breuer [47], and also by de Vega [46]. Alternatively, there exist *ab initio* methods, such as the Multiconfigurational Ehrenfest (MCE) method [36] that provides treatment of a large number of quantum nuclear degrees of freedom. In addition to this, there is the *ab initio* multiple cloning (AIMC) method [196], which is capable of simulating ultrafast excited state quantum dynamics following photo-absorption. There are also semi-classical methods available for studying large systems with anharmonicity [197, 198].

In this chapter original results featured in [181] are presented on the investigation of effects of interaction with an environment on linear absorption spectra and wavepacket dynamics of systems with anharmonicity and differing curvature. Firstly, the photoexcitation model system is introduced where the environment interaction is included through the stochastic Schrödinger equation (SSE). An application of this model for a Morse oscillator is presented to demonstrate the sensitivity of absorption lineshape of anharmonic systems due to asymmetric broadening effects caused by dissipation. Subsequently, to demonstrate relevance to a molecular photoswitch system, absorption spectra and population dynamics are generated using a stiff-stilbene photoswitch PES. The results are then interpreted using the anharmonic and differing curvature model studies for comparison.

5.1 Photoexcitation model in the presence of a bath

The general structure of the photoexcitation model presented in this chapter is that of a electronic two-level system, with a single coordinate, interacting with a bath. The total Hamiltonian representing this was introduced in Chapter 3 and is given by [41]

$$H = H_S + H_B + H_I, \tag{5.1}$$

where H_B represents the bath, H_I is the interaction between system and bath, and the two-level system is represented by

$$H_S = H_g|g\rangle\langle g| + H_e|e\rangle\langle e| + J(|g\rangle\langle e| + |e\rangle\langle g|), \tag{5.2}$$

where $|g\rangle$ and $|e\rangle$ represent ground and excited states respectively and

$$H_g = -\frac{\hbar^2}{2m}\frac{\partial^2}{\partial x^2} + S_0(x), \tag{5.3}$$

$$H_e = E_1 - \frac{\hbar^2}{2m}\frac{\partial^2}{\partial x^2} + S_1(x). \tag{5.4}$$

Here, the coordinate of interest is represented by x, the momentum is given in terms of this coordinate and the mass m, $S_0(x)$ and $S_1(x)$ represent the ground and excited PESs, J is the coupling between them, and E_1 provides the energy difference between the minima of the ground and excited state potentials. For simplicity, we assume that J is independent of x. This is appropriate for the studies conducted in this thesis as we are only interested in transference determined by regions where the PESs are close. H_B and H_I describe the remaining environment degrees of freedom as a harmonic bath, and interaction with the system, which give rise to the effects of relaxation and dephasing.

The SSE, first presented in Chapter 3 for this model is given by

$$d|\Psi(t)\rangle = \left(\Big(-\frac{i}{\hbar}H_S - \frac{1}{2}\Gamma L^\dagger L\Big)dt + \sqrt{\Gamma}dB^\dagger(t)L\right)|\Psi(t)\rangle, \tag{5.5}$$

where Γ represents the strength of coupling to the bath, L is the environment coupling operator, and $dB^\dagger(t)$ is the white noise process. In what follows the Lindblad operator L is chosen to be the lowering operator of the system a, and thus $L^\dagger = a^\dagger$, in order to model damped dynamics and relaxation. The, SSE in this case reads

$$d|\Psi(t)\rangle = \left(\Big(-\frac{i}{\hbar}H_S - \frac{1}{2}\Gamma a^\dagger a\Big)dt + \sqrt{\Gamma}dB^\dagger(t)a\right)|\Psi(t)\rangle. \tag{5.6}$$

For numerical simulations the non-linear version of the equation presented in Chapter 2 is used with a choice of $L = a$, and further details of the computational method can be found in Appendix A.2.

5.2 Morse oscillator

A well known anharmonic PES is the Morse potential

$$V_M(x) = D_e(1 - e^{-\beta(x-\Delta x)})^2, \tag{5.7}$$

Table 5.1: Morse potential parameters of diatomic molecules

Molecule	$D_e(E_h)$	$\omega_x(E_h)$	$\beta(a_0)$
B_2	0.104	0.005	1.89
H_2	0.174	0.020	1.95
O_2	0.190	0.007	2.66
F_2	0.064	0.004	2.75
N_2	0.277	0.011	3.09

where D_e is the well depth defined relative to the dissociation energy, and β is associated with the width. Using the photoexcitation model described in the previous section, a Morse potential is used for the ground electronic state

$$S_0(x) = D_e(1 - e^{-\beta(x)})^2, \tag{5.8}$$

with a displaced Morse potential representing the excited electronic state

$$S_1(x) = D_e(1 - e^{-\beta(x-\Delta_x)})^2. \tag{5.9}$$

To isolate the effects of the anharmonicity of the Morse potential on dynamics and spectra it is assumed that the PESs are well separated and $J = 0$.

To study the effects of anharmonicity on linear absorption spectra a Morse potential is used with a harmonic frequency and dissociation energy aimed to represent the bond vibration of the H_2 molecule [199]. Parameters for H_2 and other molecules [200, 201], for comparison, are contained in Table. 5.1 in atomic units, where ω_x is a parameter used in an alternative definition of the Morse potential, given by [199]

$$V(x) = D_e\left[1 - e^{-\sqrt{\omega_x^2/2D_e}x}\right]^2. \tag{5.10}$$

The absorption spectra, is calculated using Eq. 4.56 via the overlap of ground and excited wavepacket dynamics such that the absorption is given by

$$\sigma_{abs}(\omega) = \int_{-\infty}^{\infty} dt\, e^{i\omega t} C_{\mu\mu}(t) \tag{5.11}$$

$$= |\mu_{eg}|^2 \int_{-\infty}^{\infty} dt\, e^{i(\omega-\omega_{eg}t)} \langle \psi_g(t) | \psi_e(t) \rangle, \tag{5.12}$$

where $C_{\mu\mu}(t)$ is the dipole correlation function, μ_{eg} is the dipole operator, $\hbar\omega_{eg}$ is the energy difference between PES, and $|\psi_g(t)\rangle$, $|\psi_e(t)\rangle$ are the ground electronic and excited electronic state wavepackets respectively. Furthermore, the dynamics on the Morse potentials are simulated with weak dissipation using the SSE, where the computational procedure is described in Appendix A.2. The results for differing values of the Huang-Rhys parameter D, defined in section 4.2 of Chapter 4. are shown in Fig. 5.1, where we define $\omega_{eg} = E_1/\hbar - \omega_0/2$, for which $\omega_0/2$ is subtracted to correct for the zero point energy of the ground state. In the case of the Morse oscillator we find that many of the harmonic absorption spectra relations, described in the previous chapter, no longer hold. Firstly, the Franck-Condon factor for the vibrational ground state is larger and the first vibrational state is lower than in the harmonic case. In the very low limits of the Huang-Rhys parameter D it is expected that results are close to harmonic as only parts of the potential close to the minimum are explored. As the Huang-Rhys parameter is increased towards $D = 1$, as in Fig. 5.1(a), the Morse oscillator vibrational ground state still features a larger FC factor but the first and second states are less populated than in the harmonic case. Furthermore, higher lying states show increased FC factors. These features can be explained due to the asymmetry of the Morse vibrational eigenfunctions that are skewed to the shallow side of the potential. In the weak regime, the higher states thus have greater overlap with a displaced wavefunction that is close to the ground state wavefunction, as is the case for $D < 1$ [199]. Such an effect has been reported for cubic perturbations to excited state harmonic potentials [202].

Another such phenomenon is that a diminishing intensity of the vibronic progression is still observed for $D > 1$, as shown in Fig. 5.1, contrary to harmonic observations. Also, in the strong regime the peak with the largest amplitude, disregarding the zero phonon line (ZPL), occurs at a lower frequency than for harmonic spectra. These observations are due to the effects of asymmetric broadening of the spectra as each eigenstate relaxes at a different rate [185, 186]. In addition, the Morse distribution of the amplitude of FC factors is more uniform which makes the relative amplitudes of spectra more sensitive to asymmetric broadening. This also explains why the ZPL is observed as the largest peak as it features no asymmetric broadening. Analysis with no dissipation shows the peak with largest amplitude is the same as in the harmonic case.

To further exemplify these features we look at the harmonic limit in Fig. 5.2 for

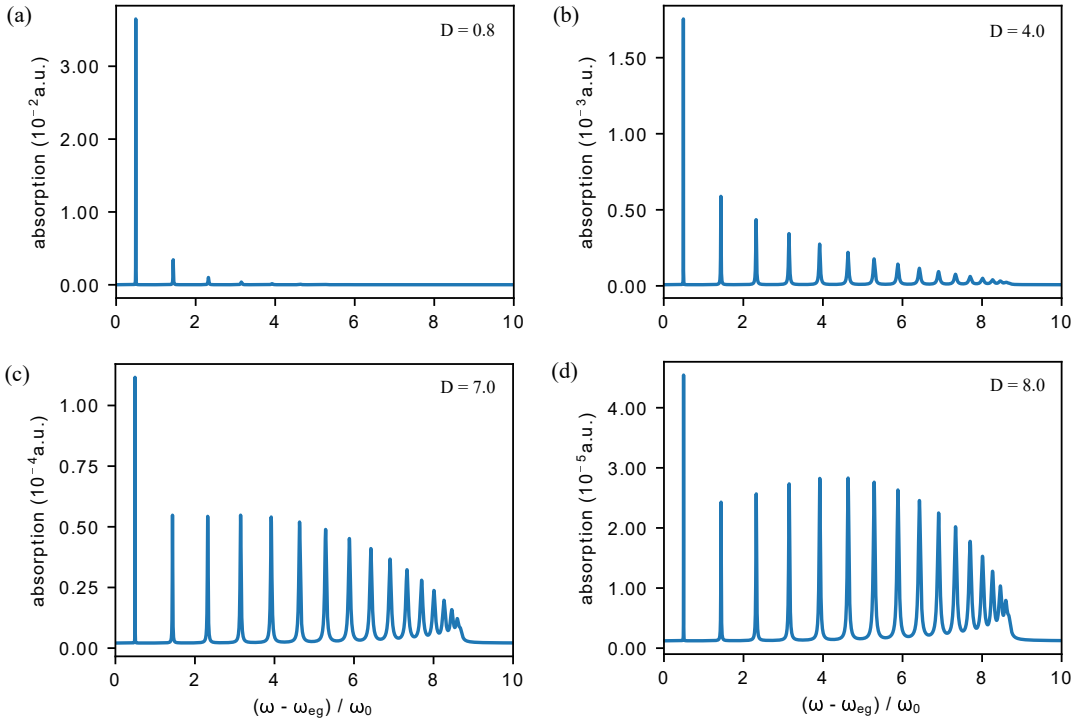

Figure 5.1: A comparison of the linear absorption spectra of H_2 with differing values of Huang-Rhys parameter D. (a) Weak regime of $D = 0.8$. (b) For $D = 4.0$, a decaying vibronic progression is still observed. (c) For $D = 7.0$, the behaviour changes as the amplitude of peaks becomes more uniform. (d) There is now a rise and fall of the amplitude of the vibronic progression. Peaks 5 and 6 have the largest amplitude, disregarding the ZPL.

$D = 7.0$. To approach the harmonic limit the dissociation energy D_e is increased whilst maintaining other parameters. As D_e is increased the spectral lines become more evenly spaced which shifts the higher states to larger frequencies. However, as the results become more harmonic the distribution of amplitudes becomes less uniform, and more peaked around the center of the vibronic progression. For $D_e = 0.6$ the peaks corresponding to energies of eigenstates at $n = 6$ and $n = 7$ have become the largest intensity peaks. The ZPL still remains greater in intensity than the harmonic case as do the wings of the vibronic progression due to a more uniform distribution of FC factors.

As the harmonic limit is achieved the ZPL has decreased as have the wings of the

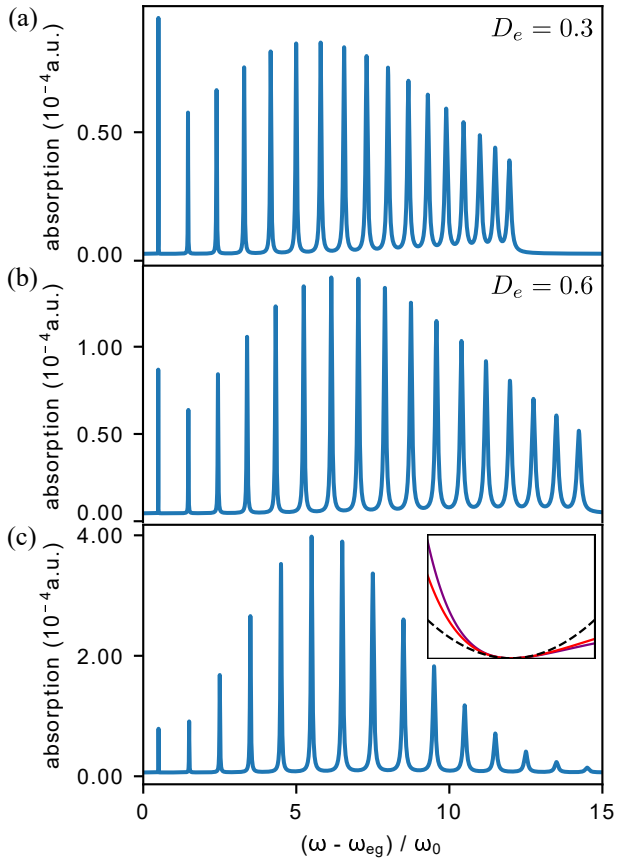

Figure 5.2: Linear absorption spectra for $D = 7.0$ is shown for increasing dissociation energy D_e whilst retaining other parameters of H_2. (a) The increase from $D_e = 0.174$ to $D_e = 0.3$ introduces rise and fall behaviour of the amplitudes of the vibronic progression. (b) For $D_e = 0.6$, the central peak amplitudes increase such that relatively the ZPL no longer has the largest peak amplitude. (c) Harmonic absorption spectra. The inset shows the excited PES as a function of coordinate for the case of $D_e = 0.3$ (purple line), $D_e = 0.6$ (red line), and harmonic (dashed line).

spectra. The tallest peaks do not correspond to $n = 6$ and $n = 7$ due to asymmetric broadening effects but the overall shape of the vibronic progression is still close to a gaussian profile. These results suggest that the features of the Morse spectra are sensitive to the effects of dissipation and asymmetric spectral broadening, especially so in the case when $D > 1.0$.

It is apparent that the nature of dissipation and thus the asymmetric broadening

seen in spectra is connected to the form of Lindblad operator used. It is of interest to determine whether using Morse raising and lowering operators [203] creates significant difference on spectral features. To answer this, a study of Morse raising and lowering operators used as Lindblad operators, as opposed to the commonly used harmonic raising and lowering operators, is now presented.

If we firstly consider the harmonic oscillator and an environment interaction term of the SSE, then harmonic raising and lowering operators give

$$\Gamma L^{\dagger}L|n\rangle = \Gamma n|n\rangle, \tag{5.13}$$

where Γ controls the strength of dissipation, $L^{\dagger}$ and L are Lindblad operators, and we note this choice of Lindbladian causes downwards transitions proportional to n.

For the Morse raising and lowering operators which were derived by [203] acting on an eigenstate we have

$$\Gamma L^{\dagger}L|n\rangle = \Gamma(n - \frac{n}{\nu})|n\rangle, \tag{5.14}$$

where

$$\nu = \sqrt{\frac{8mD_e}{\beta^2\hbar^2}} \tag{5.15}$$

is a measure of the systems harmonicity. The action of the operators is not linearly increasing in n and reflects the fact that energy levels in the Morse oscillator are not evenly spaced and the energy gap between levels is smaller for larger n. This imposes that the higher lying states experience less dissipation than when using harmonic raising and lowering operators. In Eq. 5.14 the harmonic limit is achieved as $\nu \to \infty$ and the the action of $L^{\dagger}L$ on $|n\rangle$ becomes linear in n. A comparison of these terms is shown in Fig. 5.3. As D_e is increased, and the system becomes more harmonic, the dissipation as defined by $L^{\dagger}L$ becomes linear in n.

To study the effects of the different raising and lowering operators on absorption spectra we first choose a Huang-Rhys factor of $D = 1.0$, see Fig. 5.4(a),(b) and (c). This represents relatively low displacement. We study three choices of dissipation: weak $\Gamma = 0.1\omega_0$, medium $\Gamma = \omega_0$, and strong $\Gamma = 10\omega_0$. Results are shown in Fig. 5.4 for harmonic spectra (black dashed line), Morse spectra with harmonic raising and lowering operators (red line), and Morse raising and lowering operators (blue line).

For the weakest dissipation a decaying vibronic progression is observed, with small differences between the Morse and harmonic spectra. The Morse ZPL is larger in

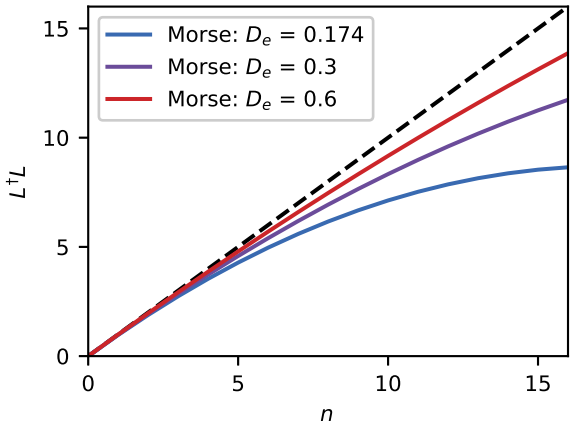

Figure 5.3: The term $L^\dagger L$ which acts on $|n\rangle$ and defines dissipation is shown against the number state for Morse raising and lowering operators. H_2 parameters are used and the dissociation energy is increased to observe the effect of increasing harmonicity. The harmonic case is represented by the black dashed line.

amplitude and the ensuing peaks are smaller than for the harmonic spectra featuring a shift to lower frequencies due to closer vibrational states. For a medium level of dissipation we observe a ZPL which has larger amplitude for the Morse spectra and a phonon sideband with lower amplitude which is shifted to lower frequencies as compared to harmonic. For strong dissipation there is a broad Lorentzian lineshape which is shallower in the wings for the Morse spectra. A common feature among all dissipation levels is that, for $D = 1.0$, there is almost no perceivable difference in using Morse raising and lowering operators. The small observed differences are due to the shape of the potential itself and the dissipation is well approximated via harmonic raising and lowering operators. It is also noteworthy that the harmonic case overestimates the Huang-Rhys factor if used to approximate Morse oscillator results.

We now turn our attention in Fig. 5.4(d),(e) and (f) to the large Huang-Rhys factor $D = 7.0$ to demonstrate the effect of using Morse raising and lowering operators. The results for the Morse spectra have been normalised and much of population of the system, for such a large Huang-Rhys factor, is contained in the continuum of higher states. As we are interested in the anharmonic effects on the bound spectra we restrict ourselves to only the bound states of the system. It should be noted however that

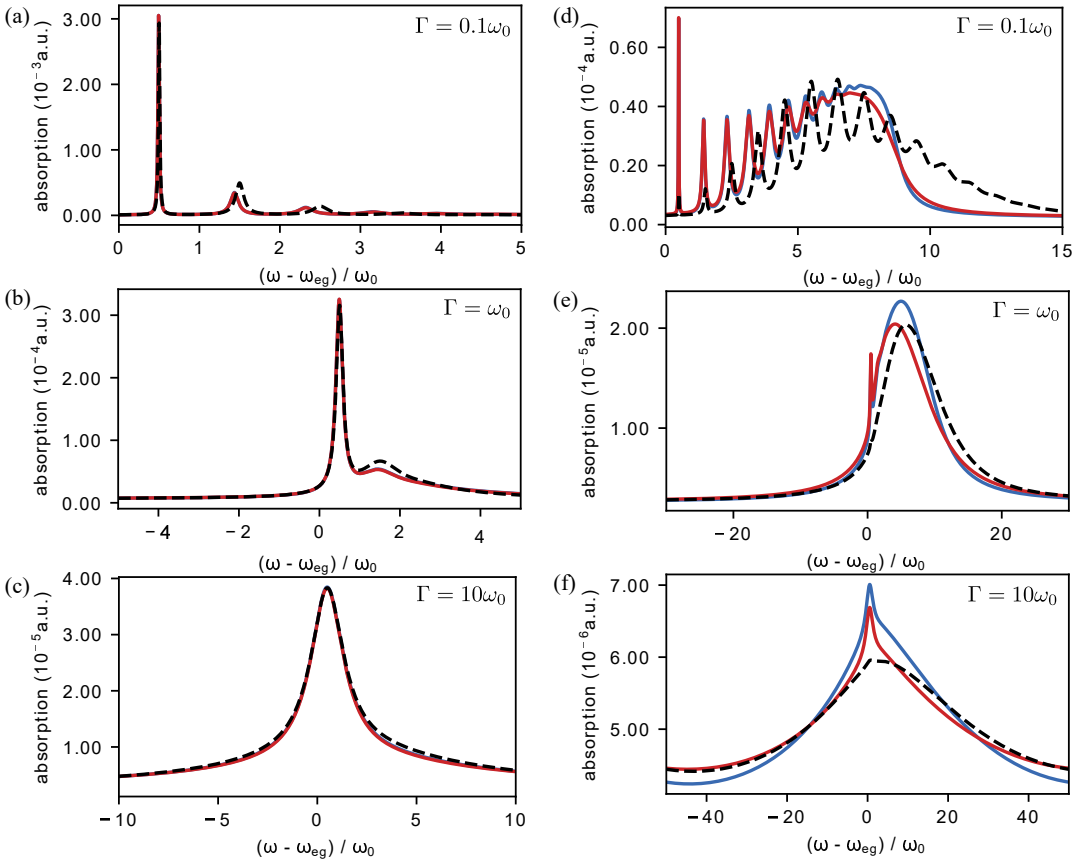

Figure 5.4: Linear absorption lineshape is shown for 3 increasing values of the dissipation parameter Γ. This is conducted for $D = 1.0$ in (a), (b) and (c) and $D = 7.0$ in (d),(e), and (f). The harmonic result (black dashed line), Morse result (blue line), and the Morse result using harmonic raising and lowering operators (red line) are shown to have little difference for the small Huang-Rhys parameter $D = 1.0$. In comparison, for a large value of $D = 7.0$ it is observed that the resulting lineshape is dependent on shape of the potential and the choice of Lindblad operator.

increased spectral broadening can occur due to transition between the ground state and dissociation states [204]. In the low dissipation regime the ZPL for the Morse oscillator has a larger relative amplitude with respect to its vibronic progression. The peak intensity shows only a steady rise in comparison to the harmonic. For the low lying states $n = 0, 1, 2$ there is minimal difference between using Morse raising and lowering operators, as demonstrated when using $D = 1.0$. However, as n increases differences

become more apparent and we see that the peaks and troughs of the spectra, generated using Morse raising and lowering operators, are increased.

For medium dissipation the changes are further exemplified. The harmonic spectra features only a broad lineshape, whereas the Morse spectra still features a visible ZPL with large phonon sideband. The profile for the Morse lineshape is shifted to lower frequencies with respect to the harmonic frequency. The use of Morse raising and lowering operators has significant difference and we observe a lineshape with larger amplitude. The changes are more significant to higher frequencies in the spectra with rough agreement to harmonic raising and lowering operators at low frequencies. Notably the Morse spectra with harmonic raising and lowering operators has a very similar profile to harmonic spectra albeit shifted to lower frequencies and with a more defined ZPL. When the Morse raising and lowering operators are utilised there is less of a shift to lower frequencies and a different profile at higher frequencies such that it is at first steeper than the harmonic profile and then shallower. This overall effect causes the spectra to appear more symmetric about the broadened peak of the sideband. In the large dissipation regime the lineshape is very broad. This is due to asymmetric broadening that is not proportional to n, but instead to $n - n/\nu$. The harmonic spectra features one broad peak and hardly any definition to the ZPL. the Morse spectra features a more defined point to where the ZPL is with a protrusion of the broadening to higher frequencies. Lastly, the Morse raising and lowering operator spectra features a larger steep to shallow transition in its lineshape profile.

5.3 Dissipative dynamics on a photoswitch model PES

Thus far, in the last chapter we have discussed how a large difference in curvature between the displaced ground and excited potentials can produce features in linear absorption spectra. Additionally, we have shown how anharmonicity can alter lineshape by changing the positioning and spacing of the vibronic progression, and how this is influenced by broadening caused by the environment. We will now discuss a condensed phase photoswitch system which exhibits both features of differing curvature and anharmonicity in its PES.

Figure 5.5 shows the developed model PES for stiff-stilbene in hexane, which has been produced using a fit to TD-DFT results [205] to correspond with values of the energies of the trans excitation and energy at the perpendicular conformation. A schem-

atic potential [4, 8] has also been used as inspiration for features such as the double well ground PES and provides potential energy barrier heights. The ground potential surface is given by,

$$S_0(\theta) = \frac{1}{2}(E_P - (\lambda_g - \mu_g))(1 - \cos(2\theta)) + S_{01}(\theta), \tag{5.16}$$

where $E_P = 3.2$ eV is the energy on the $S_0(\theta)$ potential at the perpendicular conformation, for which $\theta = 0.5$, and λ_g, μ_g, and $S_{01}(\theta)$ are involved in the confining well. The coordinate of interest is denoted by θ and represents the rotation about the double bond in stiff-stilbene. The excited potential surface is given by,

$$\begin{aligned} S_1(\theta) =& E_T + \eta_e(\cos(6\theta) - 1) \\ &+ S_{11}(\theta) + S_{12}(\theta) + S_{13}(\theta), \end{aligned} \tag{5.17}$$

where E_T is the energy on the $S_1(\theta)$ surface at the trans conformation $\theta = 0$, and the second term defines three wells and two barriers in the region $0 \leq \theta \leq \pi$ with a height of $2\eta_e$. $S_{11}(\theta)$ defines a confining well, $S_{12}(\theta)$ allows further control over the well depth in the region $0 \leq \theta \leq \pi$, and $S_{13}(\theta)$ allows control over the relative heights of the barriers. Using this model the barrier heights are chosen to be $E_{B1} = 0.0806$ eV and $E_{B2} = 0.105$ eV for the trans and cis barriers respectively [4]. We will now detail the explicit form of the control terms $S_{01}(\theta), S_{11}(\theta), S_{12}(\theta)$ and $S_{13}(\theta)$.

We begin by describing the control terms of the ground potential of Fig. 5.5. The confining well term of Eq. 5.16 is given by

$$S_{01}(\theta) = \lambda_g \sin(\theta) + \mu_g\left(\frac{1 - \cos(1/2(\theta - \pi/2))}{1 - (1/\sqrt{2})} - 1\right), \tag{5.18}$$

where we choose $\lambda_g = 12(1-1/\sqrt{2})$ and $\mu_g = 10(1-1/\sqrt{2})$, which control the steepness of the well and also the position of the minima. This confining well ensures that the wavepacket is confined to the regions of Fig. 5.5. It is possible to reduce the number of equations by setting $\lambda_g = \mu_g + E_P$. In which case, Eq. 5.16 becomes redundant and the ground potential is described by

$$S_{01}(\theta) = (\mu_g + E_P)\sin(\theta) + \mu_g\left(\frac{1 - \cos(1/2(\theta - \pi/2))}{1 - (1/\sqrt{2})} - 1\right). \tag{5.19}$$

If the minima of this potential placed at the points $\theta = 0$ and $\theta = \pi$ is desired, differentiation provides further reduction of parameters to

$$\mu_g = \frac{E_P}{2}(\sqrt{2} - 1). \tag{5.20}$$

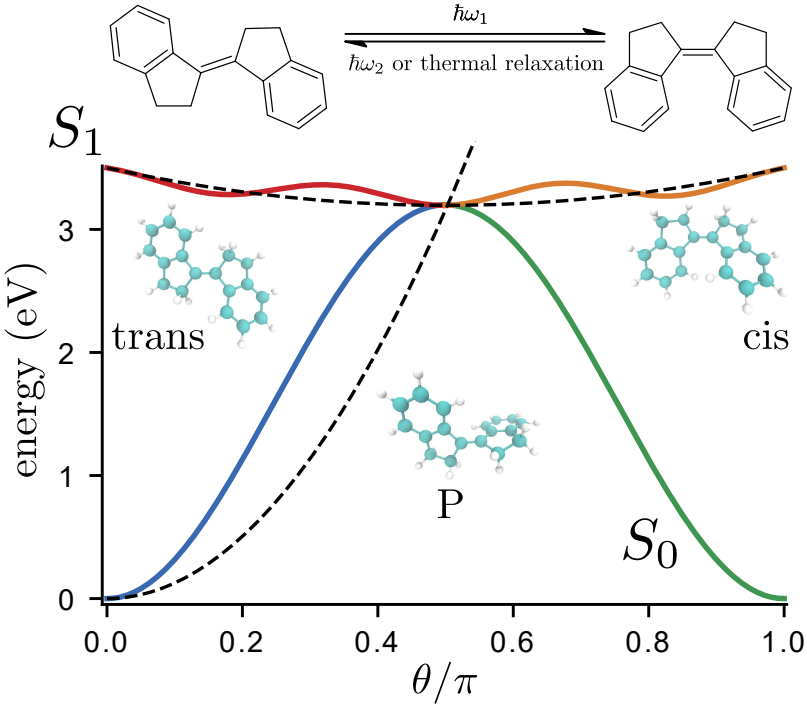

Figure 5.5: Model potential energy surface of stiff-stilbene in hexane as a function of the torsional coordinate θ. The ground PES is represented by the curve S_0 and the excited PES by S_1. To demonstrate the difference in curvature harmonic PESs are plotted, represented by the black dashed lines. Light vertically excites the trans ground state at $\theta = 0$ to the excited state at approximately 3.5 eV. Subsequent rotation to $\theta = 0.5\pi$ takes it to the perpendicular conformation P, where there is a crossing point. Further rotation to $\theta = \pi$ leads to the cis conformation. Two important features are the presence of potential energy barriers on the excited state at $\theta = 0.3\pi$ and $\theta = 0.7\pi$, and the large difference in curvature of ground and excited potentials. The stiff-stilbene PESs are coloured to correspond to regions associated with trans S_0 (blue) and S_1 (red), and cis S_0 (green) and S_1 (orange).

We make use of the unreduced form Eq. 5.16 to allow for a potential that is of the form $1-\cos(2\theta)$ with an additional confining well term. This allows control over the energy at the perpendicular conformation, whilst also allowing control over the symmetry about the minima of the wells at $\theta = 0$ and $\theta = \pi$.

We now describe the additional terms $S_{11}(\theta)$, $S_{12}(\theta)$, and $S_{13}(\theta)$ of the excited potential $S_1(\theta)$, which is displayed in Fig. 5.5. Starting with Eq. 5.17, the cosine amplitude

is chosen as $\eta_e = 0.0702$. The first additional term, which describes the confining well, is given by

$$S_{11}(\theta) = \lambda_e \sin(\theta) + \mu_e \left(\frac{1 - \cos(1/2(\theta - \pi/2))}{1 - (1/\sqrt{2})} - 1 \right), \tag{5.21}$$

where we choose $\lambda_e = 17(1 - 1/\sqrt{2})$ and $\mu_e = 15(1 - 1/\sqrt{2})$. The second term, which allows control over the well depth in the region of interest, is described by

$$S_{12}(\theta) = -\xi_e(1 - \cos(2\theta)), \tag{5.22}$$

which is akin to an inverted form of the ground PES, where $\xi_e = 0.375$ controls the well depth. The final term, is given by

$$S_{13}(\theta) = \zeta_e \sin(4\theta), \tag{5.23}$$

which raises the barrier in the cis conformation, whilst lowering the barrier height in the trans conformation, where $\zeta_e = 0.00807$ controls the barrier height difference.

The model PES of the stiff-stilbene photoswitch shown in Fig. 5.5, possesses both large curvature difference and anharmonicty. In this section the trans-cis population dynamics and absorption spectra of stiff-stilbene, using the developed model PES of Eq. 5.16 and Eq. 5.17, are interpreted using the results of the previous sections. Through this, features that are not captured by the standard harmonic model, of the dissipative dynamics and linear absorption, are explained.

Firstly, the closed system dynamics of the PES in Fig. 5.5 are simulated to allow for comparison, where further detail on computational method can be found in Appendix A.1. To accomplish this, it is assumed that the system starts out in the ground state wavepacket $|\psi_g^{n=0}\rangle$, which is approximated as harmonic by fitting to the ground state potential, as in Eq. 4.64, with a frequency $\omega_g = 0.085$ fs^{-1}. Rotational analogues of motion are taken, such that the coordinate of interest depends on rotation about the double bond in stiff-stilbene θ. In addition to this, the mass is replaced by the moment of inertia $I = 1001$ eVfs^{-1}, and the reduced Planck constant in these units is $\hbar = 4.136/2\pi$ eVfs. A harmonic potential is fitted to the excited PES as in Fig. 5.5, with $\omega_e = 0.01571$ fs^{-1}. Note that the zero temperature approximation used here is valid for the ground state at room temperature, but not quite met for the excited state. This implies that thermal effects could be important and necessary to include for an accurate description. This frequency ensures the desired period of 400 fs, and thus

corresponds to a barrierless isomerisation time of 200 fs [4, 206]. In turn this allows the calculation of the moment of inertia stated,

$$I = \frac{2(S_1(\theta) - E_1)}{\omega_e^2(\theta - \pi/2)^2}, \tag{5.24}$$

where the definition of the excited state harmonic potential has been used with rotational analogues, and $E_1 = 3.195$ eV. Following this, a point on the potential, for example $S_1(0) = 3.5$ eV [205], is substituted to find the value of the moment of inertia that is consistent with the expected period and model PES. It is assumed that the wavepacket is vertically excited from the ground potential, thus maintaining the same shape at $t = 0$ on the excited potential

$$|\psi_e(t=0)\rangle = |\psi_g^{n=0}\rangle. \tag{5.25}$$

Subsequently, the wavefunction is propagated forward in time using the time-dependent Schrödinger equation

$$d|\psi_e(t)\rangle = -\frac{i}{\hbar}\Big(H_e|\psi_e(t)\rangle + J|\psi_g(t)\rangle\Big)dt, \tag{5.26}$$

and

$$d|\psi_g(t)\rangle = -\frac{i}{\hbar}\Big(H_g|\psi_g(t)\rangle + J|\psi_e(t)\rangle\Big)dt, \tag{5.27}$$

which is a limiting case of the SSE Eq. 3.9 for $\gamma = 0$. In the equation H_g and H_e are the Hamiltonians for stiff-stilbene which has a chosen coupling of $J = 0.02$ eV, and potentials are defined by $S_0(\theta)$ and $S_1(\theta)$ in Eq. 5.16 and Eq. 5.17 respectively. The coupling provides transfer of population between $S_0(\theta)$ and $S_1(\theta)$ in the region of $\theta = 0.5\pi$. The simulation is carried out using a fourth-order Runge-Kutta scheme, for $\theta \in [-2\pi, 3\pi]$ to avoid boundary effects, with a spacing of 0.002π. This ensures 500 grid points in the range of interest $\theta \in [0, \pi]$, and a large enough grid to negate boundary effects. The wavepacket dynamics are computed for a time of 400 fs, with a time step of $\Delta t = 0.001$ fs. The population dynamics of S_1 is calculated by

$$P_{S_1}(t) = \int_{-\infty}^{\infty} d\theta\, \psi_e^*(\theta, t)\psi_e(\theta, t), \tag{5.28}$$

and similarly the population dynamics of S_0 is given by

$$P_{S_0}(t) = \int_{-\infty}^{\infty} d\theta\, \psi_g^*(\theta, t)\psi_g(\theta, t). \tag{5.29}$$

To calculate the trans and cis populations, for S_0 and S_1, the limits of integration are restricted to $\theta \in [0, \pi/2]$ and $\theta \in [\pi/2, \pi]$ respectively. The results of the closed dynamics are shown in Fig. 5.6(a) and Fig. 5.6(b), which is colour coordinated to match Fig. 5.5, and can be interpreted as follows. The wavepacket initially starts out in the trans-S_1 conformation and moves along the potential, at approximately 100 fs it reaches the perpendicular conformation. At this point the population transfers to cis-S_1 and also, due to the crossing, to the desired photoswitched state cis-S_0. Following the cis-S_1 population, it takes a further 200 fs to reach the perpendicular conformation again. This occurs at 300 fs, upon which population is transferred from cis-S_1 to the trans-S_0 state and trans-S_1. In addition to this, the population that transferred to cis-S_0 at 100 fs has a faster period of oscillation, and at approximately 250 fs the wavepacket on the ground potential reaches the crossing point, and the population transfers from cis-S_0 to trans-S_0.

To simulate the damped dynamics, the SSE of Eq. 3.9 is used such that the evolution on the ground state PES is determined by

$$d|\psi_g(t)\rangle = D_1[|\psi_g(t)\rangle]dt + D_2[|\psi_g(t)\rangle]dW(t), \tag{5.30}$$

where

$$\begin{aligned} D_1[|\psi_g(t)\rangle] = &-\frac{i}{\hbar}\Big(H_g|\psi_g(t)\rangle + J|\psi_e(t)\rangle\Big) \\ &+ \frac{\gamma}{2}\sum_{i=1,2}\Big(\langle L_i + L_i^\dagger\rangle_{\psi_g} L_i \\ &- L_i^\dagger L_i - \frac{1}{4}\langle L_i + L_i^\dagger\rangle_{\psi_g}^2\Big)|\psi_g(t)\rangle, \end{aligned} \tag{5.31}$$

and

$$D_2[|\psi_g(t)\rangle] = \sqrt{\gamma}\Big(L_i - \frac{1}{2}\langle L_i + L_i^\dagger\rangle_{\psi_g}\Big)|\psi_g(t)\rangle. \tag{5.32}$$

Similarly, evolution on the excited state PES is determined by

$$d|\psi_e(t)\rangle = D_1[|\psi_e(t)\rangle]dt + D_2[|\psi_e(t)\rangle]dW(t), \tag{5.33}$$

where

$$\begin{aligned} D_1[|\psi_e(t)\rangle] = &-\frac{i}{\hbar}\Big(H_e|\psi_e(t)\rangle + J|\psi_g(t)\rangle\Big) \\ &+ \frac{\gamma}{2}\Big(\langle L_3 + L_3^\dagger\rangle_{\psi_e} L_3 \\ &- L_3^\dagger L_3 - \frac{1}{4}\langle L_3 + L_3^\dagger\rangle_{\psi_e}^2\Big)|\psi_e(t)\rangle, \end{aligned} \tag{5.34}$$

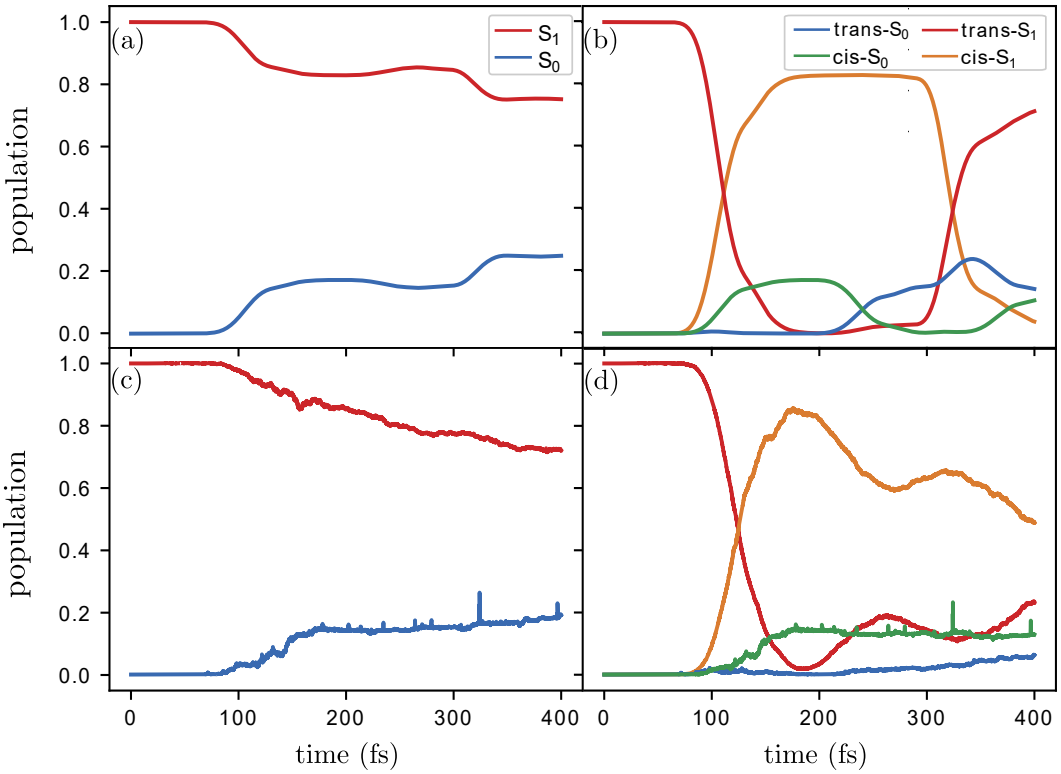

Figure 5.6: Time evolution of the populations are shown for closed dynamics, in (a) and (b), and damped dynamics, in (c) and (d). The left column represents population on either the excited PES, S_1, or the ground PES, S_0. The right column displays the time evolution of finding the system in cis or trans conformations, and is colour coordinated to correspond to Fig. 5.5.

and

$$D_2[|\psi_e(t)\rangle] = \sqrt{\gamma}\Big(L_3 - \frac{1}{2}\langle L_3 + L_3^\dagger\rangle_{\psi_e}\Big)|\psi_e(t)\rangle. \tag{5.35}$$

As before, population can transfer between the PESs near to the crossing point at $\theta = 0.5\pi$ due to a coupling of $J = 0.02$ eV. Also, as in the closed case, the system is assumed to start in the ground state wavepacket $|\psi_g^{n=0}\rangle$, and is then vertically excited to the excited PES. There are some more parameters and operators for the damped case which must be first specified before the dynamics are simulated. These are the dissipation parameter, which is chosen to be $\gamma = 0.2\omega_e$, to ensure appropriate broadening in absorption spectra and significant population trapping in the cis-S_1 state at 400 fs [4].

In addition to this, the Lindblad operators for evolution on S_0 are chosen corresponding to the lowering operator of a harmonic potential fit at $\theta = 0$

$$L_1 = \sqrt{\frac{I\omega_g}{2\hbar}}\left(\hat{\theta} + \frac{i}{I\omega_g}\hat{p}\right) \tag{5.36}$$

and a fit at $\theta = \pi$

$$L_2 = \sqrt{\frac{I\omega_g}{2\hbar}}\left(\left(\hat{\theta} - \pi\right) + \frac{i}{I\omega_g}\hat{p}\right) \tag{5.37}$$

are used to allow for damping towards the minima of the potential corresponding to the trans and cis states respectively. The Lindblad operator for evolution on S_1 is chosen as the lowering operator of the harmonic fit to S_1

$$L_3 = \sqrt{\frac{I\omega_e}{2\hbar}}\left(\left(\hat{\theta} - \frac{\pi}{2}\right) + \frac{i}{I\omega_e}\hat{p}\right), \tag{5.38}$$

which results in damping towards the minima of S_1, corresponding to the perpendicular conformation. This allows a study of damped oscillation on the model PES of stiff stilbene using the SSE method.

The results of the damped dynamics are shown in Fig. 5.6(c) and Fig. 5.6(d), where the simulation implements an adaptation of the fourth-order Runge-Kutta scheme to SSEs [41]. Further details on the computational method can be found in Appendix A.2. The overall population dynamics on S_0 and S_1 behave in a similar manner to the closed evolution, specifically in the sense that at 400 fs the populations are in close agreement. However, there is a difference in the population transfer such that it is more gradual in the damped case, whereas occurs in steps in the closed case, an explanation for this will be provided through consideration of the trans and cis populations. In Fig. 5.6(b) it can be seen that, as in the closed case at $t = 0$ the population is in the trans-S_1 state, then the population dynamics in the first 100 fs proceeds in a similar manner to the closed dynamics. Population transfer at 100 fs has a notable difference in that a small amount of population does not overcome the first barrier, located at approximately $\theta = 0.3\pi$ in Fig. 5.5. This results in a small amount of population maintained in the trans-S_1 state. The majority of the population, is transferred to the cis-S_1 state with some transference, approximately 20%, occurring to the desired cis-S_0 state. There are some notable changes in the ensuing dynamics for the damped case. For example, following the cis-S_1 population, between 200-400 fs there is a decaying transference between cis-S_1 and trans-S_1, accompanied by a small rise in trans-S_0. This is explained by the feature

of the second barrier located at approximately $\theta = 0.7\pi$ in Fig. 5.5, which causes two dynamical effects. The first is that the wavepacket approaching the barrier from the perpendicular confirmation does not pass over it, and thus there is some transference back to trans-S_1 and a small amount of transference to trans-S_0. The second effect is that the wavepacket overcomes the barrier but then becomes partially trapped in the region $0.7\pi \leq \theta \leq 1\pi$. Therefore, in contrast to the closed dynamics, at 400 fs there is a greater cis-S_1 population than trans-S_1. In addition, the population transfer to cis-S_0 at 100 fs remains trapped over the time 100-400 fs. This is due to the damped dynamics of the wavepacket on the ground PES in the region $0.5\pi \leq \theta \leq 1\pi$, the wavepacket is no longer able to reach the vicinity of the crossing point and instead relaxes to the minima of the potential at $\theta = \pi$. To summarise, the damped dynamics causes a larger cis population on both excited and ground PES at 400 fs. Inclusion of finite temperature effects via the thermofield method [65] would also induce absorption from the bath, which has to be described by additional Lindblad operators defined by raising operators. Inclusion of these processes may promote wavepackets overcoming potential energy barriers.

The features of the PES of Fig. 5.5 can also be assessed by analysing linear absorption spectra. To generate the absorption spectra, the wavepacket dynamics are first simulated using the SSE procedure described in Appendix A.2. This is then used to calculate the dephasing function, from which the absorption lineshape is found using Eq. 5.12. Coupling of the states is included with J, as described in the population dynamics, and provides a loss of excited state population leading to further decay of the dipole correlation function and thus increased broadening in the spectra. Parallel dipoles are assumed and $|\mu_{eg}|^2 = 1$. The results are presented in Fig. 5.7. For comparison, absorption spectra for the standard displaced harmonic oscillator model is plotted as the black dashed line in Fig. 5.7, assuming that $\omega_g = \omega_e = 0.01571$ fs^{-1}. Additionally, the absorption spectra for the differing curvature model is plotted as the red dashed line, with $\omega_g = 0.085$ fs^{-1} and $\omega_e = 0.01571$ fs^{-1}. The spectra of stiff-stilbene, generated using dynamics on the model PES of Fig. 5.5, is represented by the blue line in Fig. 5.7. The stiff-stilbene spectra presents some features which are not captured by the standard displaced harmonic oscillator model. Firstly, the width of the peak is much narrower and the peak maximum is shifted to larger wavelength. Both of these features are a result of different curvature in ground and excited PES, and are present

in the spectra of the differing curvature model. Secondly, there is the appearance of the s-progression described in the last chapter, at $\lambda = 350$ nm, which is also a result of different curvature and present in the differing curvature model spectra. The results presented in this section do not give rise to the well resolved vibronic progressions of closed system results due to the presence of the environment which causes spectral broadening. In the case of the differing curvature model spectra, this broadening can make it difficult to observe the s-progression. Additionally, the s-progression feature is diminished further due to asymmetric broadening which results in a larger amount of broadening for smaller wavelength. We also note that, as harmonic raising and lowering operators are used, the extent of this asymmetric broadening may be different than if the raising and lowering operators of the system manifold were used. This is dependent on the spacing of the eigenenergies, and if the anharmonicity makes the spacing smaller or larger.

Although the differing curvature model allows some explanation for the rise of features of the stiff-stilbene spectra, it does not completely capture all spectral features. For example, the stiff-stilbene spectra is less shifted towards larger wavelength. This is a result of the anharmonicity of the excited state PES, whereby the potential energy barriers, cause a shift of the eigenenergies above the barrier to larger energies [207]. This, in turn, causes the spectra to be shifted to smaller wavelengths. Furthermore, the s-progression is enhanced for the stiff-stilbene spectra. This is due to the widening of the excited state PES in the model before it rises steeply to act as a confining well. The eigenfunctions thus become elongated creating a greater overlap with higher lying states than in the differing curvature model. It should be noted that the experimental absorption spectra for stiff-stilbene exhibits more complexity due to the presence of other modes which are not directly involved in the isomerisation pathway. As a consequence, the additional peaks can also obscure spectral features for the presented band generated by torsion about the carbon double bond in stiff-stilbene. Comparing the lineshape to experimental spectra [4] provides a number of insights. Firstly, the energy at $\theta = 0$ on the excited PES should be closer to 3.65 eV, which provides a wavelength of 340 nm for the absorption spectra peak of the torsion band. Additionally, the harmonic spectra is too broad and symmetric to match the experimental torsion band. The differing curvature model in part corrects this. For the lineshape at large wavelengths of $\lambda \geq 350$ nm in Fig. 5.7 the best agreement is found with the simulated stiff stilbene

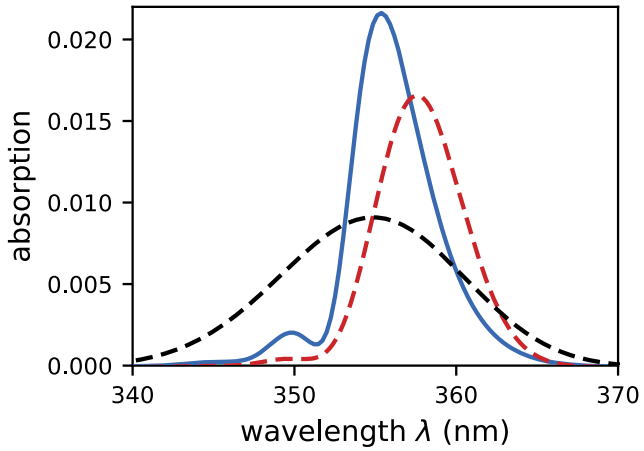

Figure 5.7: Linear absorption spectra of stiff-stilbene using a model PES (blue line). To analyse the features of the spectra, the standard displaced harmonic model spectra (black dashed line) and differing curvature model spectra (red dashed line) are plotted. Notably, there is the appearance of the s-progression, described in the last chapter, at $\lambda = 350$ nm.

spectra, for which the standard harmonic spectra overestimates the absorption. The differing curvature model agrees well for this region but as the wavelength increases it underestimates the absorption whilst the simulated stiff stilbene spectra still features good agreement. At lower wavelengths of 340 nm there is less agreement between the experimental spectra and the lineshape fit of the simulated spectra. This is largely due to the spectral overlap of a band centred at approximately 320 nm in the experimental spectra [4]. However, it could also be in part due to the spectral broadening caused by the environment and the approximate harmonic form of the Lindblad operators as demonstrated in the Morse model study.

5.4 Summary

In this chapter the effects of an interacting environment and dissipation were incorporated through the SSE approach on wavepacket dynamics, and the resulting absorption spectra for anharmonic systems was discussed. Firstly, linear absorption spectra of an anharmonic dissipative system was demonstrated using the Morse potential. This revealed the sensitivity of spectral features due to the combined effects of asymmetric

broadening, and alteration of vibronic progression intensity and spacing caused by anharmonicity. Furthermore, the assumption of harmonic raising and lowering operators used as the Lindblad operators that define interaction with the environment was tested using analytic expressions. This provided the observation that using harmonic raising and lowering operators causes a greater broadening for higher frequencies than using the Morse counterpart raising and lowering operators, though such a feature was only prominent for large displacements. Following this, a model PES for stiff-stilbene was presented, inspired by a schematic diagram and TD-DFT data [4, 205]. Two prominent features of the PES were identified. The first was the large difference in curvature of the excited and ground PES accompanied by a large displacement. The second feature was anharmonicity in the form of potential energy barriers, and an overall deviation from quadratic potentials. The population dynamics, and absorption spectra, generated using the model PES for stiff-stilbene was subsequently analysed. The former displayed the importance of an interplay of anharmonicity in the form of potential energy barriers, and damped dynamics. This suggests damping of the dynamics is important in stabilising the photoswitched state. Furthermore, it implies the potential of photoselectability of cis and trans states that is dependent on a tuning of interaction with the environment and anharmonicity. The absorption spectra presented spectral features, of the model stiff-stilbene PES, in the form of the s-progression presented in the last chapter, a decrease of peak width, and shift of peak maximum to larger wavelengths. These features were largely accounted for by the difference in curvature in ground and excited PES and the large displacement between potentials. However, the presence of the potential energy barriers additionally caused the spectra to be less shifted to larger wavelengths than in the differing curvature model.

The results here demonstrate population dynamics generated using a stochastic Schrödinger equation and spectral features present in a model PES for stiff-stilbene. The form of the SSE presented has some limitations in that it does not allow for an accounting of memory effects of the environment, or an accurate treatment of thermal effects. Such effects can be important, particularly when considering the rotational speed of molecular motors [182]. In order to accurately describe the full dynamical processes and spectral features of photoswitching an extension of the method is required. This is the focus of the next chapter in which we shall extend the method using the non-Markovian stochastic Schrödinger equation and solution via HOPS. This

provides an increase in the accuracy of simulations and allows for a rigorous assessment of spectral features and dynamical processes of photoswitches, and analysis of the importance of potential energy barriers and environment effects.

Chapter 6

Numerically exact quantum stochastic modelling of molecular photoswitches

In the previous chapters we have discussed the simulation of wavepacket dynamics and absorption spectra for closed system dynamics and an interacting environment within the Markovian approximation included via stochastic Schrödinger equations (SSE). Such studies provide insight into the effects of quantum dissipation and damping on wavepacket dynamics of molecular photoswitches, and the associated broadened absorption spectra. However, there are limitations that impact an accurate modelling of the complete photoswitch dynamics.

Firstly, the initial form of the stochastic Schrödinger equations, the quantum state diffusion equation [41, 44, 152], represents dynamics under a zero-temperature approximation. For molecular photoswitches and motors, it has been shown that thermal fluctuations represent a key step in dynamics determining the average rotational speed [182]. Furthermore, for systems of biological relevance, such as retinal [90, 91, 93], the dynamics takes place within a protein environment at finite temperature necessitating a treatment that can account for these effects.

A second limitation is that within the Markovian approximation the memory of the interaction of the environment is neglected. In the initial classical studies conducted on photoswitches it was found in some cases, such as when modelling the photoisomerisation of trans-stilbene, an accounting of non-Markovianity, via a frequency dependent friction model and generalised Langevin equation [113, 114], was important in matching experimental observations [8, 110]. For the quantum analogue the importance of incorporating non-Markovian effects in photoswitch dynamics remains an open question, however, a recent study suggests that non-Markovianity can boost the efficiency of bio-molecular switches [208].

In this chapter original results are presented on the development of a numerically exact quantum stochastic method, that extends the hierarchy of stochastic pure states (HOPS) [59] presented in Chapter 3, to model the dynamics of molecular photoswitches in the condensed phase whilst accounting for non-Markovian and thermal effects. In the first section we discuss the extension of the non-linear HOPS approach to normalised trajectories and its implementation is demonstrated using the spin-boson model. Following this, the HOPS approach is developed for a reaction coordinate representation which is tested against the Lindblad equation in the Markovian limit. The coordinate based HOPS approach is subsequently applied to a double well model to investigate barrier crossing that mimic the first stages of stiff-stilbene photoisomerisation. The model

is then extended to account for dynamics on the complete stiff-stilbene potential energy surface. Using the extended model wavepacket dynamics are simulated and compared against the results of transient absorption spectroscopy experiments [4]. The effects of the environment interaction are considered for several physically realistic parameter choices, and linear absorption spectra is compared to experimental results. Lastly, the results are summarised and future directions and open questions for the research are discussed.

6.1 Non-linear HOPS for normalised trajectories

The overall form of the non-linear non-Markovian stochastic Schrödinger (NMSSE) equations is similar to the linear versions except for the appearance of the shifted noise associated with the Girsanov transformation and subtraction of the operator expectation values associated with normalisation [65]. Thus, the non-linear NMSSE, in particular the Girsanov transformed version, naturally adapts to the HOPS solution of the linear NMSSE. In the non-linear form that only involves the Girsanov transformation a similar derivation of HOPS to the linear case is possible, following the same procedure as in Chapter 3, the Girsanov non-linear HOPS equation [59] for unnormalised trajectories is given by

$$|\dot{\psi}_t^{(k)}\rangle = (-iH_S - kw + \tilde{\zeta}_t L)|\psi_t^{(k)}\rangle + k\alpha_{T=0}(0)L|\psi_t^{(k-1)}\rangle - (L^\dagger - \langle L^\dagger\rangle_t)|\psi_t^{(k+1)}\rangle. \quad (6.1)$$

For the NMSSE it was also possible to derive a version that preserves the norm for each trajectory given by Eq. 3.136. For this normalised form, it is more challenging to derive a HOPS solution due to the term

$$\left\langle (L^\dagger - \langle L^\dagger\rangle_t)\int_0^t ds\, \alpha_{T=0}(t-s)\frac{\delta}{\delta\tilde{\zeta}_s^*}\right\rangle_t |\tilde{\psi}_t\rangle. \quad (6.2)$$

The presence of this term means that in deriving HOPS for the NMSSE with normalised trajectories we must consider

$$D_t\Big\langle (L^\dagger - \langle L^\dagger\rangle_t)D_t\Big\rangle_t |\tilde{\psi}_t\rangle, \quad (6.3)$$

which can be rearranged to give

$$\begin{aligned}\Big\langle (L^\dagger - \langle L^\dagger\rangle_t)D_t\Big\rangle_t D_t|\tilde{\psi}_t\rangle &= \Big\langle (L^\dagger - \langle L^\dagger\rangle_t)D_t\Big\rangle_t |\tilde{\psi}_t{}^{(1)}\rangle \\ &= \frac{\langle\psi_t|(L^\dagger - \langle L^\dagger\rangle_t)D_t|\psi_t\rangle}{\langle\psi_t|\psi_t\rangle}|\tilde{\psi}_t{}^{(1)}\rangle \\ &= \frac{\langle\psi_t|(L^\dagger - \langle L^\dagger\rangle_t)|\psi_t^{(1)}\rangle}{\langle\psi_t|\psi_t\rangle}|\tilde{\psi}_t{}^{(1)}\rangle. \end{aligned} \tag{6.4}$$

In addition to this another term that appears in the normalised version is

$$\frac{-\langle\psi_t|i\sum_\lambda g_\lambda^* e^{i\omega_\lambda t}\tilde{z}_\lambda^* L|\psi_t\rangle}{\langle\psi_t|\psi_t\rangle} = \langle\tilde{\zeta}_t{}^* L\rangle_t|\tilde{\psi}_t\rangle. \tag{6.5}$$

When considering the NMSSE, as in the study by Diósi et al [65], this is written as

$$\langle L\rangle_t\tilde{\zeta}_t|\tilde{\psi}_t\rangle. \tag{6.6}$$

This form is appropriate and valid for conducting the $\hat{O}$ operator substitution, which replaces the functional derivative with an ansatz. However, for the purpose of deriving HOPS for normalised trajectories the form of Eq. 6.5 is desired. Thus, in the derivation of non-linear HOPS for normalised trajectories one obtains the term

$$\begin{aligned} D_t\langle\tilde{\zeta}_t{}^* L\rangle_t|\tilde{\psi}_t\rangle &= \langle\tilde{\zeta}_t{}^* L\rangle_t D_t|\tilde{\psi}_t\rangle \\ &= \langle\tilde{\zeta}_t{}^* L\rangle_t|\tilde{\psi}_t{}^{(1)}\rangle. \end{aligned} \tag{6.7}$$

Note that if the form $\tilde{\zeta}_t{}^*\langle L\rangle_t|\tilde{\psi}_t\rangle$ is assumed, then the HOPS derivation results in the incorrect term

$$\begin{aligned} D_t\langle L\rangle_t\tilde{\zeta}_t{}^*|\tilde{\psi}_t\rangle &= \langle L\rangle_t\tilde{\zeta}_t{}^* D_t|\tilde{\psi}_t\rangle + \langle L\rangle_t\alpha_{T=0}(0)|\tilde{\psi}_t\rangle \\ &= \langle L\rangle_t\tilde{\zeta}_t{}^*|\tilde{\psi}_t{}^{(1)}\rangle + \langle L\rangle_t\alpha_{T=0}(0)|\tilde{\psi}_t\rangle, \end{aligned} \tag{6.8}$$

in which the commutation relation of Eq. 3.105 has been used as in the linear HOPS derivation. Following the correct derivation, and substituting the additional terms of Eq. 6.4 and Eq. 6.7, the non-linear HOPS for normalised trajectories is given by

$$\begin{aligned} |\dot{\tilde{\psi}}_t^{(k)}\rangle = &\left(-iH_S - kw + \tilde{\zeta}_t^* L - \langle\tilde{\zeta}_t{}^* L\rangle_t + \frac{\langle\psi_t|(L^\dagger - \langle L^\dagger\rangle_t)|\psi_t^{(1)}\rangle}{\langle\psi_t|\psi_t\rangle}\right)|\tilde{\psi}_t^{(k)}\rangle \\ &+ k\alpha_{T=0}(0)L|\tilde{\psi}_t{}^{(k-1)}\rangle - (L^\dagger - \langle L^\dagger\rangle_t)|\tilde{\psi}_t{}^{(k+1)}\rangle. \end{aligned} \tag{6.9}$$

To demonstrate the differences between the non-linear form of HOPS and the version that also has normalised trajectories, it is useful to consider the spin-boson model as an example. The spin-boson model constitutes a particular dissipative two-level realisation of the Caldeira-Leggett model [160, 209] which is of interest in the field of open quantum systems and is capable of describing a range of phenomena [41]. The model constitutes a two-level system coupled to a bath, where the system part is given by

$$H = -\frac{1}{2}\Delta\sigma_x + \frac{1}{2}\epsilon\sigma_z \tag{6.10}$$

and the environment coupling operator is given by

$$L = \sigma_z, \tag{6.11}$$

where σ_x and σ_z correspond to Pauli operators. In the first test of this form of the equation we take the limiting case of a Markovian environment and compare against the Lindblad master equation. In this instance HOPS is taken at a zero depth order with the terminator introduced in Chapter 3 and a choice of large γ in the bath correlation function (BCF) [59] such that one approaches

$$\alpha(t) = \Gamma\delta(t) = \Gamma \lim_{\gamma\to\infty} \frac{\gamma}{2} e^{-\gamma t}, \tag{6.12}$$

where Γ represents the strength of coupling. Results of the expectation value of σ_z for this model are shown in Fig. 6.1 for 1000 iterations, a choice of $\gamma = 100$, $\Delta = 1$, $\epsilon = 0$, and two strengths of dissipation $\Gamma = 0.25$ and $\Gamma = 0.5$. Good agreement is found between the Lindblad results, represented by the black dashed line, and the HOPS results, represented by the blue solid line.

To demonstrate results beyond the Markovian limit, system parameters are chosen as $\Delta = 1$, $\epsilon = 0$, with a bath correlation function given by

$$\alpha(t) = ge^{-wt}, \tag{6.13}$$

where $g = 2$ and $w = 0.5 + 2i$ and a hierarchy depth of 8 is chosen. This parameter choice provides a comparison to the results of the linear and non-linear HOPS results found by Suess et al [59]. Firstly, it is of use to discuss the differences in results in using the normalised trajectory version. The results of single trajectories for this choice of parameters are shown in Fig. 6.2. In Fig. 6.2(a) the expectation value of σ_z is shown using the non-linear equation for unnormalised trajectories. These represent the

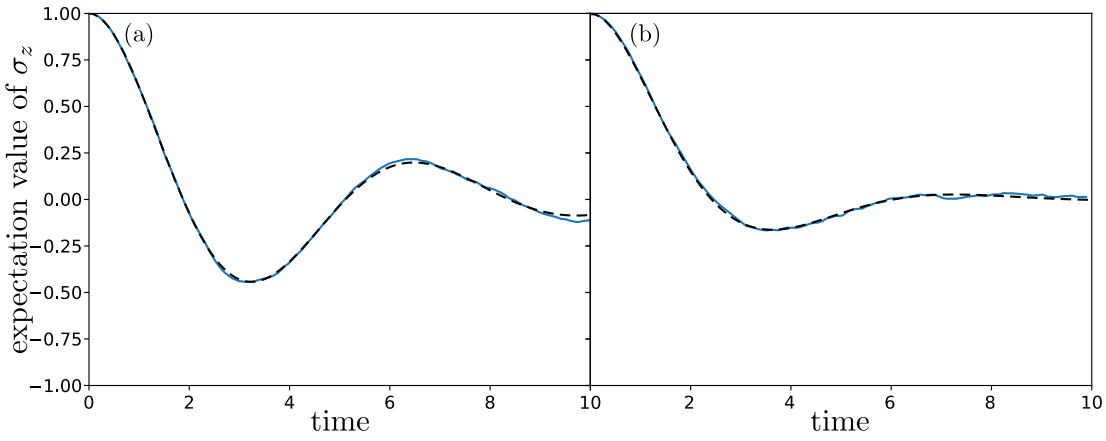

Figure 6.1: Comparison of non-linear HOPS with normalised trajectories in the Markovian limit, represented by the blue solid line, and the Lindblad equation, represented by the black dashed line, for a choice of $\Gamma = 0.25$ in (a) and $\Gamma = 0.5$ in (b).

preconditioned expectation values that must be renormalised using the norm of $|\psi_t\rangle$. Thus, the post-normalised values are given by

$$\langle \tilde{\sigma_z} \rangle = \frac{\langle \psi_t | \sigma_z | \psi_t \rangle}{\langle \psi_t | \psi_t \rangle}, \tag{6.14}$$

where $|\psi_t\rangle = |\psi_t^{(0)}\rangle$ represents the zeroth order term of the hierarchy. The results of post-normalised values are shown by the dashed lines in Fig. 6.2(b). Alternatively, using the normalised trajectory version of HOPS, no renormalisation is required as $|\psi_t^{(0)}\rangle$ remains normalised and so taking the expectation value with respect to this immediately gives the desired result, as shown by the solid lines of Fig. 6.2(b). An advantage of the normalised trajectory form is that the potentially large preconditioned values, as shown in Fig. 6.2(a), are avoided thus improving the accuracy and stability of simulations.

Using the same parameters the average of many trajectories is shown in Fig. 6.3 for both the unnormalised (black dashed line), and normalised trajectory (blue solid line) form of HOPS. In Fig. 6.3(a)(b) a hierarchy depth of 4 is used, whereas in Fig. 6.3(c)(d) a depth of 8 is chosen. An average of 1000 trajectories is chosen for Fig. 6.3(a)(c) and an average of 10000 trajectories is shown in Fig. 6.3(b)(d). Excellent agreement is found between the normalised trajectory form and unnormalised form at both choices

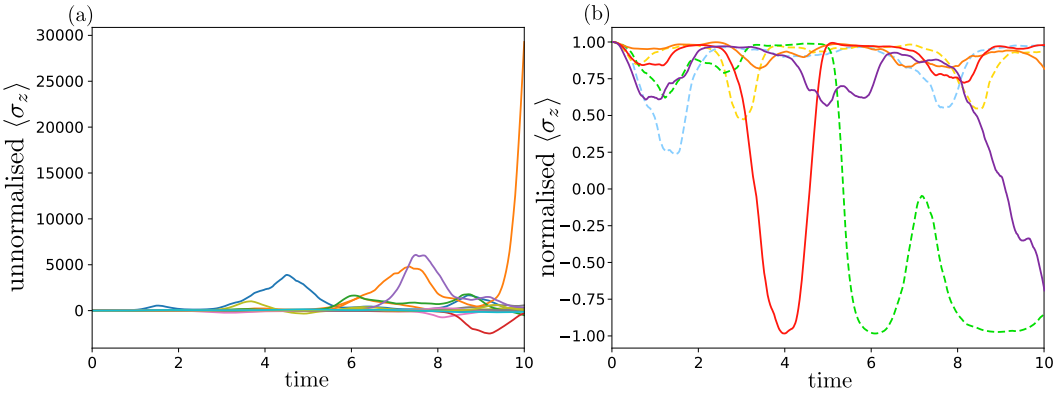

Figure 6.2: Expectation values of σ_z using a spin-boson model for single trajectories of non-linear forms of HOPS, with $\Delta = 1$, $\epsilon = 0$, $g = 2$ and $w = 0.5 + 2i$ and a hierarchy depth of 8. (a) Preconditioned expectation values of the unnormalised non-linear form of HOPS. (b) Post-normalised expectation values (dashed lines) and expectation values of the normalised trajectory form of HOPS (solid lines) are compared. Note that these are independent trajectories and dashed lines are not expected to agree with solid lines. Preconditioned values are seen to involve potentially large values, which must then be normalised to give the post-normalised results, whereas normalised trajectories maintain values of $-1 \leq \sigma_z \leq 1$.

of depth and an average of 10000 trajectories. A good agreement is already found for only 1000 trajectories and all results shown agree with the results of Suess et al [59]. Given that this is a two-state system, and populations consist of only spin up or down states, it is remarkable that results that approach the converged results are found for the average over just 100 trajectories [59], with fine details converging over a larger ensemble. The results presented here demonstrate the validity of the normalised trajectory form of HOPS that has been derived. This provides a simulation method that is more accurate and stable for large trajectories. Such considerations are important for the ensuing studies of this chapter which involve larger system sizes and a higher degree of computational complexity.

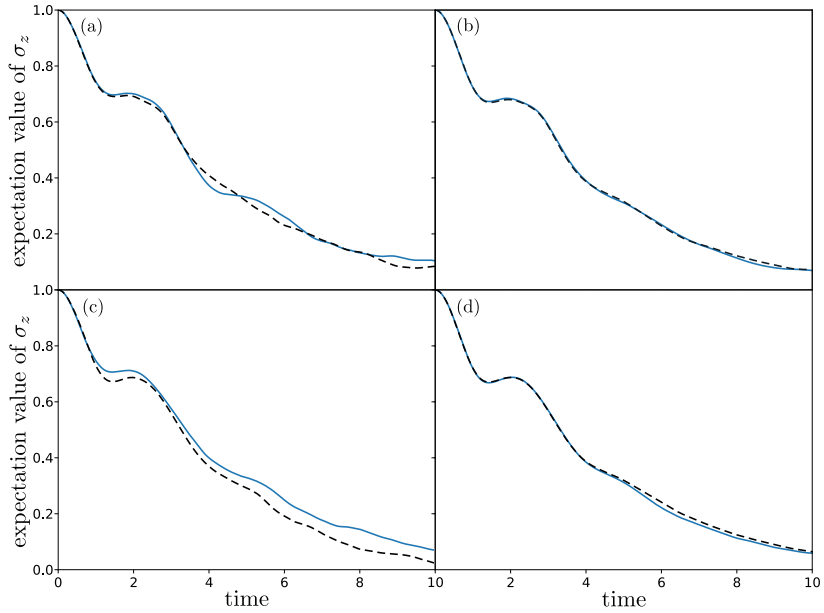

Figure 6.3: Expectation values of σ_z using a spin-boson model for the average of several trajectories with $\Delta = 1$, $\epsilon = 0$, $g = 2$ and $w = 0.5 + 2i$. Normalised trajectory results are represented by the solid blue lines whereas the unnormalised form of HOPS results are represented by the dashed black lines. (a)(b) Represent expectation values for a hierarchy depth of 4, whereas (c)(d) represent expectation values for a hierarchy depth of 8. In (a)(c) the average is taken over 1000 trajectories, whereas in (b)(d) the average is taken over 10000 trajectories.

6.2 Reaction coordinate hierarchy of stochastic pure states

In the stochastic Schrödinger equation method considered in earlier chapters the coupling to the environment was defined by a lowering operator, which was valid for defining quantum dissipation and naturally arose in the derivation through taking the zero temperature approximation. For the spin-boson model considered in the last section the environment coupling operator is of the form

$$\sigma_z = \begin{bmatrix} 1 & 0 \\ 0 & -1 \end{bmatrix}, \tag{6.15}$$

which defines a dynamical evolution that takes the system to equal populations such that the expectation value of σ_z decays to 0. Thus for a two-level system, or under

some assumptions regarding temperature, the coupling operator can be defined with relative ease. However, for the inclusion of finite temperature in systems with several accessible states, such as energy states, we know that the thermal equilibrium state is represented as a weighted combination of these states. Furthermore, for interaction with a bath at thermal equilibrium there is not only a process that takes energy from the system through dissipation, but another process that provides a transfer of energy back into the system. In the context of raising and lowering operators this requires that, with respect to the environment coupling, there is not only a lowering operator a that couples to dissipate energy from the system, but also a second environment coupling operator given by the raising operator $a^\dagger$ that represents transfer of energy into the system. With respect to this picture, the processes must be weighted accordingly in a phenomenological manner in order to satisfy detailed balance and achieve the thermal equilibrium state. Alternatively, the coupling operator can be defined in terms of the coordinate q which represents processes that transfer energy from and to the system. In this section, for the purpose of modelling photoswitch dynamics, we shall describe HOPS in terms of this choice of coupling operator, using a coordinate representation, and discuss subtleties regarding non-Markovianity.

The starting point for the reaction coordinate with environment coordinate coupling form of HOPS is once again the non-Markovian stochastic Schrödinger equation (NMSSE). However, as in the initial presentation of the NMSSE provided by Diósi and Strunz [64] the system is coupled linearly via coordinate coupling to an environment of harmonic oscillators [160, 210]. The total Hamiltonian representing the system, environment, and interaction is given by

$$H = H_S + H_B + H_I \tag{6.16}$$

$$= H_S(q,p) + \sum_\lambda \Big(\frac{P_\lambda^2}{2m_\lambda} + \frac{1}{2} m_\lambda \omega_\lambda^2 Q_\lambda^2 \Big) - q \sum_\lambda g_\lambda Q_\lambda, \tag{6.17}$$

where p and q represent the system momentum and coordinate respectively and P_λ, Q_λ, and m_λ represent the bath momentum, coordinate, and mass for mode λ. The harmonic environment Hamiltonian is given by

$$H_B = \sum_\lambda \Big(\frac{P_\lambda^2}{2m_\lambda} + \frac{1}{2} m_\lambda \omega_\lambda^2 Q_\lambda^2 \Big), \tag{6.18}$$

and the interaction Hamiltonian is

$$H_I = -q\sum_\lambda g_\lambda Q_\lambda. \tag{6.19}$$

Using a Bargmann coherent state basis for the environmental degrees of freedom [63], the same procedure that was used to derive the NMSSE in Chapter 3 (Eq. 3.45) can be implemented for the coordinate coupling form to give

$$\partial_t|\psi_t\rangle = -iH_S(q,p)|\psi_t\rangle + q\zeta_t^*|\psi_t\rangle - q\int_0^t \alpha_{T=0}(t-s)\frac{\delta|\psi_t\rangle}{\delta\zeta_s^*}\,ds. \tag{6.20}$$

The coordinate coupling form of the NMSSE is thus of a similar form to the NMSSE used as the starting point for the derivation of HOPS, with L and $L^\dagger$ replaced with q. Therefore, the derivation of HOPS presented in Chapter 3 and by Suess et al [59] holds for the coordinate coupling form. Following this derivation we obtain the reaction coordinate HOPS in the coordinate representation of the system as

$$|\dot{\psi}_t^{(k)}\rangle = (-iH_S(q,p) - w + q\zeta_t^*)|\psi_t^{(k)}\rangle + \alpha_{T=0}(0)q|\psi_t^{(k-1)}\rangle - q|\psi_t^{(k+1)}\rangle. \tag{6.21}$$

Similarly, the non-linear form of reaction coordinate HOPS is given by

$$|\dot{\psi}_t^{(k)}\rangle = (-iH_S(q,p) - kw + \tilde{\zeta}_t q)|\psi_t^{(k)}\rangle + k\alpha_{T=0}(0)q|\psi_t^{(k-1)}\rangle - (q-\langle q\rangle_t)|\psi_t^{(k+1)}\rangle, \tag{6.22}$$

and the non-linear form of HOPS that preserves the norm of each trajectory is given by

$$\begin{aligned}|\dot{\tilde{\psi}}_t^{(k)}\rangle =& \left(-iH_S(q,p) - kw + \tilde{\zeta}_t^* q - \langle \tilde{\zeta}_t^{\,*} q\rangle_t + \frac{\langle\psi_t|(q-\langle q\rangle_t)|\psi_t^{(1)}\rangle}{\langle\psi_t|\psi_t\rangle}\right)|\tilde{\psi}_t^{(k)}\rangle \\ &+ k\alpha_{T=0}(0)q|\tilde{\psi}_t{}^{(k-1)}\rangle - (q-\langle q\rangle_t)|\tilde{\psi}_t{}^{(k+1)}\rangle.\end{aligned} \tag{6.23}$$

The coordinate representation of the system with coordinate coupling between system and environment is well suited to quantum dynamics studies in which the reaction proceeds along a coordinate such as a molecular vibration or rotation, an example of which is in modelling the dynamics of molecular photoswitches. Potential energy surfaces of such systems are often defined in terms of coordinates important to the reaction. Thus, the coordinate representation of HOPS permits the use of such potentials, implemented either as a model or as a set of data points taken from a pre-determined potential, without a need to calculate the energy states and raising and lowering operators (RLO).

In addition the energy states and RLO would have to be recalculated when adjusting features of the potential such as barrier heights. Furthermore, extension to several coordinates of the system is possible with ease providing a means by which complex non-adiabatic dynamics can be incorporated via conical intersections.

An important finding arises when considering the system coordinate coupling to the environment form of HOPS in the Markovian limit with finite temperature. The derivation in this limit results in an incorrect form of dissipation that is free from damping in the coordinate. The explanation for this becomes apparent when considering the energy representation. The coordinate that couples the environment and system is formed by the summation of a raising and lowering operator, and so represents both processes in which the system receives and dissipates energy. In the Markovian limit each of these processes is weighted equally and the system evolves such as to populate its energy states evenly, this results in an evolution that is free from damping in the coordinate. In the non-Markovian form of the equation the memory term containing the bath correlation function provides a dynamical quantity for the dissipation in which memory of the processes are retained. This allows the processes to be weighted according to the bath correlation function, satisfy detailed balance, and thus provide a correct form of dissipation and damped dynamics.

This finding shows that it is crucial to consider non-Markovian dynamics at finite temperature using coordinate system-environment coupling. Nonetheless, it is possible to find a Markovian limit of the coordinate coupling HOPS if one takes the zero-temperature approximation. As shown in the derivation of the Markovian stochastic Schrödinger equation in Chapter 3, when making the zero-temperature approximation the bath lowering operator in the interaction term acts upon the vacuum state and thus annihilates to give zero. This leaves only the term involving the lowering operator of the system in the interaction Hamiltonian

$$H_I = \sum_\lambda g_\lambda^* L a_\lambda^\dagger. \tag{6.24}$$

Therefore, under the zero-temperature approximation the environment interaction only involves the single process that dissipates energy from the system. This means that the issue of equal raising and lowering operations of the system energy states is avoided and a dynamical quantity that accounts for all processes is no longer required. To demonstrate this with the coordinate representation of HOPS consider a harmonic

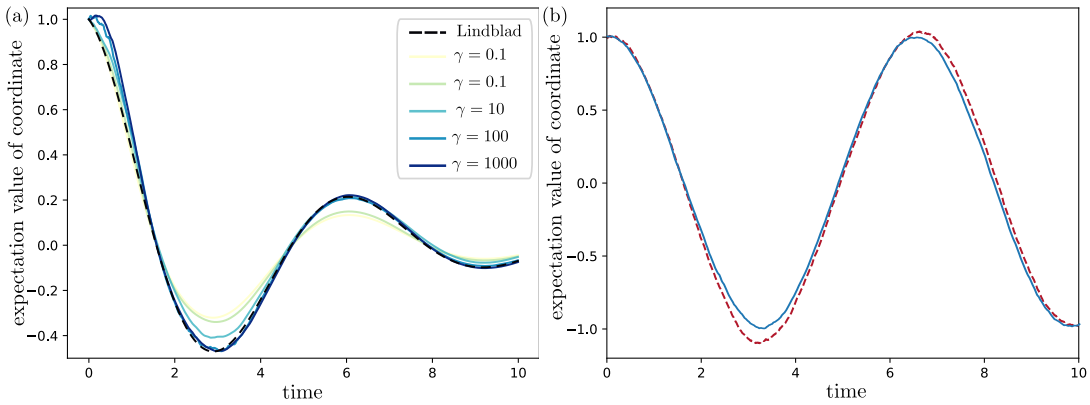

Figure 6.4: Expectation value of coordinate for a harmonic oscillator model system in the Markovian limit for a coupling strength of $\Gamma = 0.5$. (a) The results of HOPS in Markovian limit with zero-temperature approximation are compared against Lindblad results for increasing BCF parameter γ. (b) Coordinate environment coupling in the Markovian limit results are shown for HOPS (solid blue line) and compared to results of the Markovian SSE (dashed red line), featuring no damping in the coordinate.

oscillator model in which

$$H_S(q,p) = \frac{p^2}{2m} + \frac{1}{2}m\omega^2(q-d)^2. \tag{6.25}$$

Taking the zero-temperature approximation, the form of the environment coupling operator in the coordinate representation is given by

$$L = \sqrt{\frac{\hbar}{2m\omega}}a = \frac{1}{2}(q + \frac{i}{m\omega}p). \tag{6.26}$$

The bath correlation function is chosen to be of the approximate Markovian form of Eq. 6.12 presented in the last section. Simulation results for this system using HOPS with 1000 trajectories, a coupling strength of $\Gamma = 0.5$, and for several choices of the BCF parameter γ are shown against the Lindblad master equation in Fig. 6.4(a). As the parameter γ is increased, we approach the Markovian form of the BCF, and results of HOPS begin to converge to the Lindblad results. For better agreement at short times γ would need to be increased further. Full convergence would be achieved, for sufficient number of trajectories, in the limit of $\gamma \to \infty$. Using the same parameter

choices, in Fig. 6.4(b) the environment coupling operator is chosen to be the coordinate q to demonstrate the issues corresponding with not making the zero-temperature approximation with the Markovian limit. The solid blue line represents the results of HOPS in the Markovian limit and shows that no damping is present in the coordinate dynamics. In addition, a choice of coordinate coupling operator is demonstrated for the Markovian SSE and shown in Fig. 6.4(b) by the dashed red line. Up to convergence of trajectories, results are equivalent to the HOPS simulation in the Markovian limits demonstrating issues with using environment coordinate coupling for Markovian methods are not isolated to HOPS in the Markovian limit.

The results of this section suggest that one must be careful when taking the Markovian limit, and support the findings of Ferialdi concerning dissipation in the Caldeira-Leggett model [211]. In this study Ferialdi claims that, treating a microscopic description with position environment coupling as a more fundamental perspective, dissipation is a purely non-Markovian feature. Beyond the theoretical significance of the fundamental nature of dissipation, the findings of this section further show the importance of including non-Markovian dynamics under practical considerations. For Markovian dynamics, in these studies one must either make approximations that are potentially not physically realistic such as the zero-temperature approximation, or adopt a phenomenological approach in which the raising and lowering operations are separately weighted in order to achieve detailed balance. This is in contrast to the classical methods used to study molecular photoswitch dynamics such as the Langevin equation, for which both Markovian and non-Markovian versions with coordinate environment coupling are possible [211].

6.3 Barrier crossing in a double well potential

In order to apply the reaction coordinate form of HOPS to a potential more appropriate for modelling photoswitching, consider the double well potential shown in Fig. 6.5 which is given by

$$V = a(\theta - \Delta)^4 - b(\theta - \Delta)^2 - c(\theta - \Delta) + d, \tag{6.27}$$

where parameters are chosen as $a = 0.375$, $b = 1.25$, $c = 1$, $d = 3.29$, and $\Delta = 1.39$. This choice of parameters is chosen such as to mimic the initial dynamics of the stiff-stilbene photoswitch for the torsional coordinate and gives an initial energy of 3.66 eV at $\theta = 0$ [205], with a barrier height of 700 cm^{-1} located at $\theta = 0.93$. Dynamics

are generated using the HOPS method, with a depth of 2 unless otherwise stated, a coordinate grid of 1000 points in the range $-2\pi \leq \theta \leq 2\pi$, a time step of $\Delta t = 0.001$ fs, and a fourth-order Runge-Kutta method as described in Appendix A.3. To investigate barrier crossing dynamics two initial wavepacket positions are chosen, represented by red circles in Fig. 6.5, with the first at $\theta = 0$ and the second at $\theta = 0.1375$ for which the potential is level to the barrier height. In the first set of results discussed the environment coupling operator is chosen to correspond with the well at $\theta = 2.85$, where the positions of the wells are marked by green circles in Fig. 6.5, such that

$$L_2 = q - 2.85. \tag{6.28}$$

This corresponds to dynamics in which the equilibrium position, with respect to environment interaction, corresponds to the position of the well at $\theta = 2.85$. The BCF is implemented using a Drude spectral density

$$J(\omega) = \frac{2\lambda}{\pi} \frac{\gamma\omega}{\omega^2 + \gamma^2}, \tag{6.29}$$

which allows an exponential form of the BCF required for HOPS to be written as [60, 158, 159]

$$\alpha(t) = \sum_{n=0}^{\infty} g_n e^{-\gamma_n t}. \tag{6.30}$$

For low temperature, higher order terms of $n > 0$ may be required, but for the purposes of studies in this chapter a temperature of $T = 300$ K and the relaxation times involved mean that the low temperature correction terms may be dropped. In this case Eq. 6.30 becomes a single exponential with

$$\gamma_0 = \gamma \tag{6.31}$$

and

$$g_0 = \gamma\lambda\Big(\cot\left(\frac{\beta\hbar\gamma}{2}\right) - i\Big), \tag{6.32}$$

where $\beta = 1/k_B T$, and $\hbar = 4.136/2\pi$ eVfs. The reorganisation energy of the bath λ is estimated to be between 0.313 eV and 0.322 eV from the Stokes shift S [130], where

$$S = 2\lambda, \tag{6.33}$$

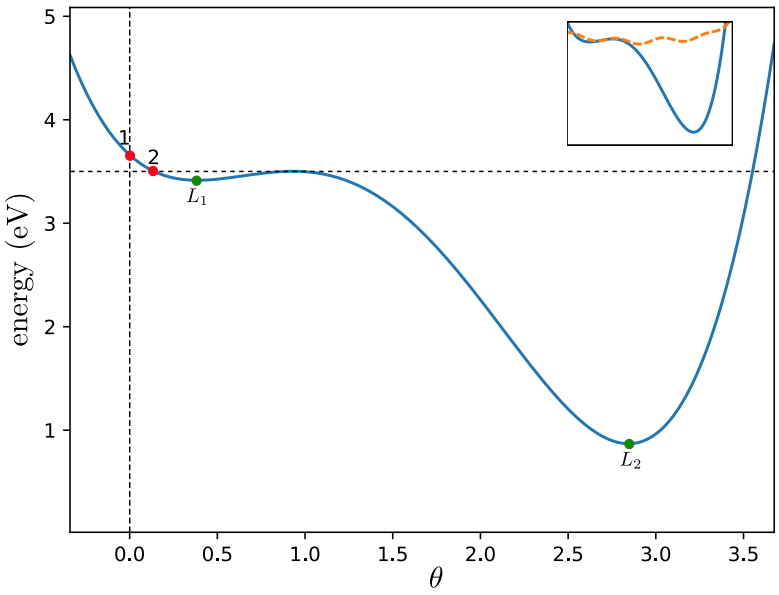

Figure 6.5: Double well PES that mimics first stages of stiff-stilbene photoisomerisation. Red circles represent two positions for the initial state, and green circles represent positions of the wells used for environment interaction operators L_i. The inset shows the comparison to a full model of the stiff-stilbene excited state PES.

and the Stokes shift was found using the difference between stiff-stilbene absorption and fluorescence spectra of Quick et al [4]. The reorganisation energy is representative of all vibrational degrees of freedom and so we must account for the energy of the torsional degree of freedom that is taken into the system which is given by

$$\lambda_S = \frac{1}{2} m\omega^2 d^2, \tag{6.34}$$

where m is the mass, ω is the harmonic oscillator frequency, and d is the displacement in the torsional coordinate. Thus for stiff-stilbene we have $m = 1001$ eV fs^{-1}, $\omega = 0.01571$ fs^{-1}, $d = \pi/2$, and so $\lambda_S = 0.305$ eV. Therefore, the reorganisation of the bath is in the range $\lambda_B = 0.313 - 0.305 = 0.008$ eV and $\lambda_B = 0.322 - 0.305 = 0.017$ eV. The inverse relaxation time is varied around $\gamma = 106$ cm^{-1}, which corresponds to $\gamma = 0.02$ fs^{-1}. The range of γ reflects values that are in a physically plausible range for light absorbing open quantum systems such as light-harvesting systems and the retinal photoswitch [59, 91, 212].

Firstly, simulation of the closed system dynamics is shown in Fig. 6.6 for above

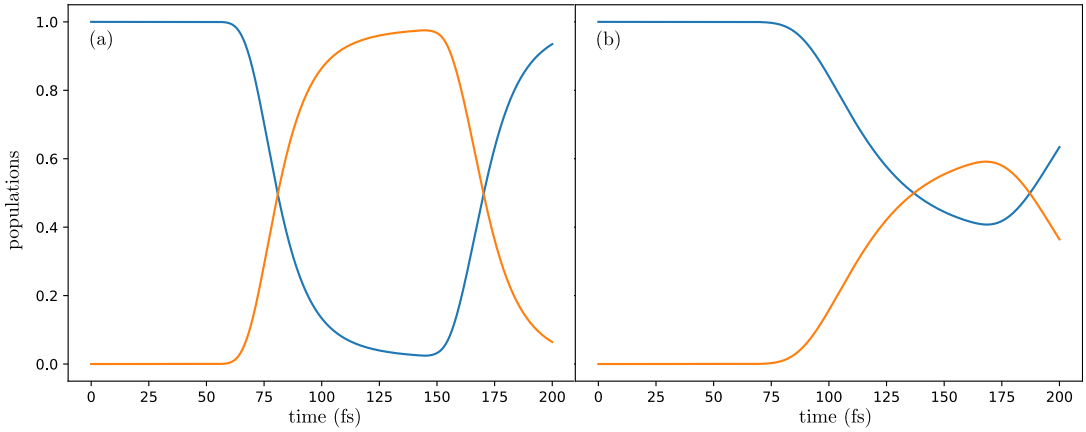

Figure 6.6: Closed system population dynamics for the barrier crossing model PES of Fig. 6.5. The blue line represents trans population in the region $0 \leq \theta \leq \pi/2$, and the orange line represents the cis population in the region $\pi/2 \leq \theta \leq \pi$. (a) Population dynamics for an initial state that is above the barrier height (represented by the first red circle in Fig. 6.5). (b) Population dynamics for an initial state that is level with the barrier (represented by the second red circle in Fig. 6.5).

barrier and at barrier height starting positions of the initial system state that lie at respective energies of 3.66 eV and 3.5 eV. Populations $P(t)$ are calculated using

$$P(t) = \int_{-\infty}^{\infty} d\theta \, \psi^*(\theta, t)\psi(\theta, t). \tag{6.35}$$

For trans and cis populations, the limits of integration are restricted to $\theta \in [0, \pi/2]$ and $\theta \in [\pi/2, \pi]$ respectively. Population dynamics are seen to have significant variation for the two different initial state choices with the barrier height initial state transferring less population to the cis state. However, for both initial state choices the majority of the population transfers from trans to cis before transferring back.

Subsequently, consider the open quantum system dynamics with a variation of λ for values 0.008 eV, 0.017 eV, and 0.036 eV where the latter value is chosen according to parameters for the retinal photoswitch [91]. Simulation results are shown in Fig. 6.7 where λ is increased in each panel from left to right, Fig. 6.7 (a)(b)(c) corresponds to an initial state above barrier height, and Fig. 6.7 (d)(e)(f) corresponds to an initial state at barrier height. By including interaction with the environment, $\lambda = 0.008$ eV, the dynamics become damped and less population is transferred from trans to cis. As λ is

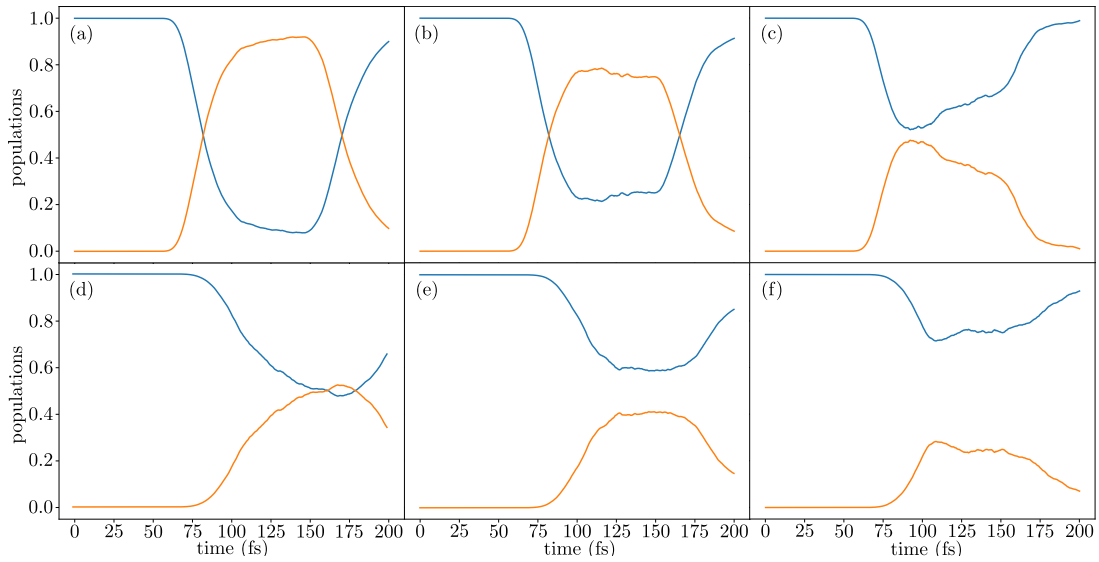

Figure 6.7: Population dynamics in the presence of an interacting environment, for varying λ, using the double well potential of Fig. 6.5. Blue lines represent the trans population in the region $0 \leq \theta \leq \pi/2$, and the orange lines represents the cis population in the region $\pi/2 \leq \theta \leq \pi$. Panels (a)(b)(c) represent population dynamics for an initial state above barrier height whilst panels (d)(e)(f) represent population dynamics for an initial state at barrier height. The coupling strengths are $\lambda = 0.008$ eV for (a)(d), $\lambda = 0.017$ eV for (b)(e) and $\lambda = 0.036$ eV for (c)(f).

increased the damping effects become more prominent as the wavepacket becomes less likely to overcome the barrier and so less population is transferred from trans to cis. For a choice of initial state at barrier height, the population is either equal or remains mostly in the trans state for each choice of λ. Conversely, this larger trans retained population is only observed in the initial state above the barrier height for the largest choice of $\lambda = 0.036$ eV. Therefore, there is significant difference in the dominant population over time for the different choices of initial wavepacket with environment interaction. This suggests that both the initial wavepacket height with respect to the barrier and λ are crucial in determining the population dynamics. To match experimental observations [4], using the double well potential model, either an initial state that is close to the barrier height is required with coupling strengths $\lambda = 0.008$ eV or $\lambda = 0.017$ eV, or strong coupling $\lambda = 0.036$ eV.

The second BCF parameter is varied between physically plausible values of $\gamma = 0.02$

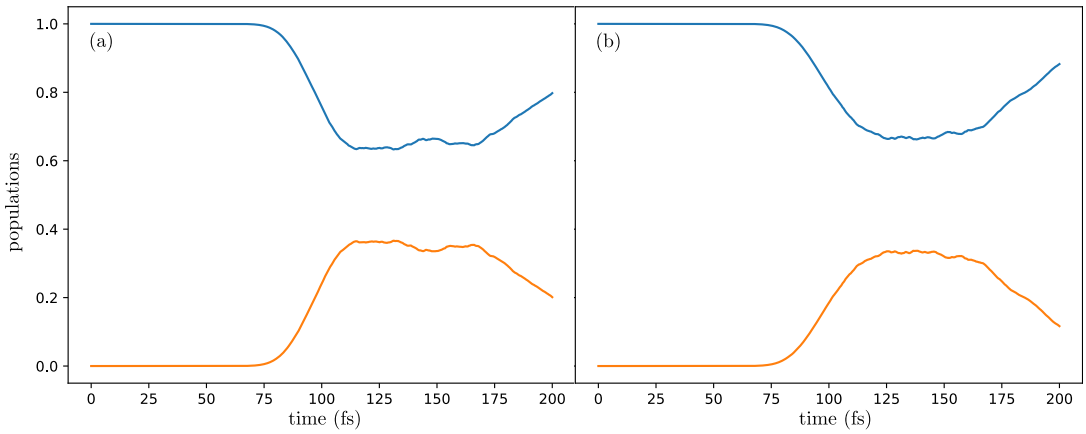

Figure 6.8: Population dynamics in the presence of an interacting environment, for varying γ with a fixed value of $\lambda = 0.017$ eV, using the double well potential of Fig. 6.5. (a) Results are shown for $\gamma = 0.02$ fs^{-1}. (b) Results are shown for $\gamma = 0.04$ fs^{-1}.

fs^{-1} and $\gamma = 0.04$ fs^{-1}, $\lambda = 0.017$ eV is fixed to the upper estimate calculated from the stokes shift of stiff-stilbene. The initial wavepacket is chosen to be at barrier height, which provides population dynamics that are in better agreement with experiment. Results are shown in Fig. 6.8, and demonstrate that for the increase in γ from 0.02 fs^{-1} to 0.04 fs^{-1}, a smaller increase in the damping is observed in comparison to a variation of λ within physically plausible values.

Beyond analysis of the effect of changing parameters of the BCF, it is of use to consider the convergence with respect to depth. This allows an analysis of the convergence with respect to terms that incorporate the non-Markovianity of the memory integral of the NMSSE. For larger depth sizes of HOPS, more terms are included that account for the non-Markovianity of the memory integral. The terminator term that truncates HOPS at a finite size, treats the remainder of the interaction as Markovian. The depth convergence is analysed under the choice of $\lambda = 0.017$ eV, $\gamma = 0.02$ fs^{-1}, and for the two choices of initial state above the barrier and at barrier height, for depth sizes of 2, 4, and 8. Results are shown in Fig. 6.9, where the top panels represent an initial state above the barrier height and the lower panels represent an initial state at barrier height. Depth size is increased from the leftmost panels to the rightmost and demonstrate a change in the respective population dynamics for both choices of initial state. Firstly, for the initial state above the barrier the increase in depth size is shown

to have a restoring effect to the coherent dynamics, with a depth size of 4 (Fig. 6.9(b)) altering population dynamics to resemble the case of weaker coupling $\lambda = 0.008$ eV shown in Fig. 6.7(a). Further increase of depth size to 8 alters population dynamics to resemble the coherent closed system population dynamics of Fig. 6.6. Secondly, consider the initial state at barrier height shown in the lower panels of Fig. 6.9. Similar to the initial state above the barrier a restoration effect can be seen as depth size is increased to 4 (Fig. 6.9(e)), that alters the population dynamics to resemble coherent closed system dynamics. However, the depth increase to 8, (Fig. 6.9(f)) does not have an associated further restoration effect of coherent dynamics. These results demonstrate that a larger depth size, and more accurate accounting of the non-Markovianity of system-environment interaction, can have significant effect on population dynamics. In general the resulting effect is a restoration of coherent dynamics, however, the interplay of a barrier on the PES can reduce this effect for initial states that are closer to the barrier height. For such initial states the coherent dynamics does not dominate as much as initial states that are above the barrier height. Therefore, damping effects and convergence with respect to non-Markovianity become important in determining the population dynamics and whether trans or cis conformations are the most likely.

Lastly, the choice of environment coupling operator is investigated. Thus far, the environment coupling operator has been chosen as $L_2 = \theta - 2.85$ to correspond with an equilibrium position associated with the second well in the cis conformation, at which point no damping is experienced. Instead consider an additional environment coupling operator $L_1 = \theta - 0.39$, that corresponds to an equilibrium position of the well at $\theta = 0.39$. The overall coupling to the environment can thus be represented as

$$L = L_1 + L_2 = 2\theta - 3.24, \tag{6.36}$$

which corresponds to an equilibrium position of $\theta = 3.24/2 = 1.62$, the point half way between the equilibrium positions associated with L_1 and L_2. The overall coupling is additive as the extra environment operators create new terms in the HOPS equation that can then be collected in like terms. There is also a doubling in the coupling, as compared to if $L = \theta - 1.62$, due to the dynamics being damped towards two equilibrium positions. However, if the wavepacket is at the equilibrium position with respect to L_1 it still encounters damping with respect L_2. If each of these interactions are considered to have equal strength then the new equilibrium point $\theta = 1.62$ represents the point at which damping is equal from L_1 and L_2. However, the true equilibrium coordinate

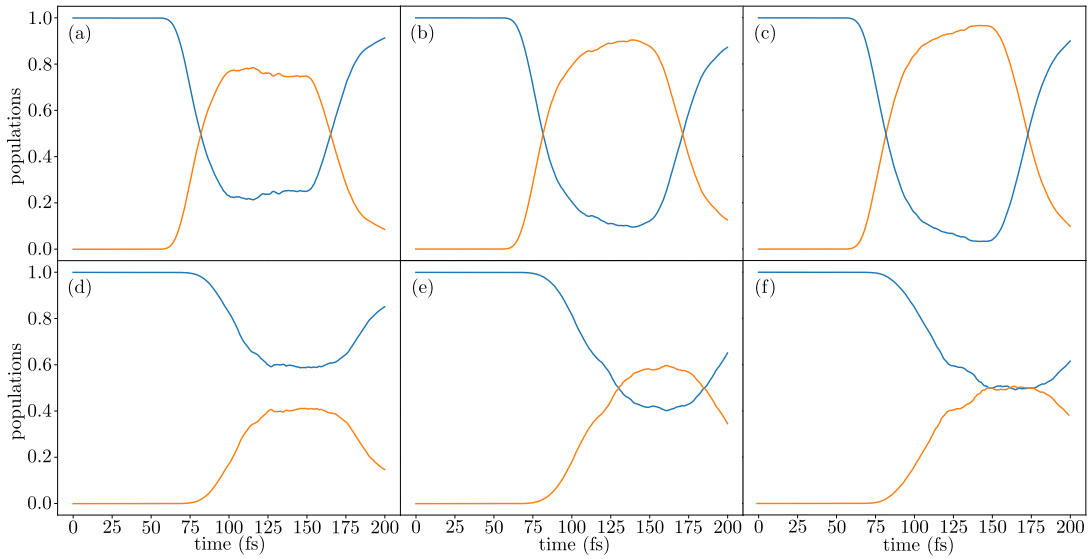

Figure 6.9: Population dynamics in the presence of an interacting environment, with $\lambda = 0.017$ eV and $\gamma = 0.02$ fs^{-1} for varying depth sizes of the HOPS method, using the double well potential of Fig. 6.5. Blue lines represent the trans population in the region $0 \leq \theta \leq \pi/2$, and the orange lines represents the cis population in the region $\pi/2 \leq \theta \leq \pi$. Panels (a)(b)(c) represent population dynamics for an initial state above barrier height whilst panels (d)(e)(f) represent population dynamics for an initial state at barrier height. The depth sizes are 2 for (a)(d), 4 for (b)(e) and 8 for (c)(f).

of the system will also depend on the shape of the system potential and parameters of the environment. In Fig. 6.10 population dynamics are shown for an environment coupling operator of $L = 2\theta - 3.24$ and a fixed value of $\gamma = 0.02$ fs^{-1}. The top panels represent an initial choice of state above the barrier, whilst the lower panels represent a choice of initial state at barrier height. In the leftmost panels population dynamics are generated for $\lambda = 0.017$ eV, and in the rightmost panels $\lambda = 0.034$ eV. The population dynamics for the case of $\lambda = 0.017$ eV (Fig. 6.10(a) & (c)) show similar results to the previous choice of single environment coupling operator L_2. This is also the case for $\lambda = 0.034$ eV and a choice of initial state at barrier height (Fig. 6.10(d)), however, there is greater stabilisation with respect to crossing the barrier as the coupling operator increases more, relative to the a choice of single coupling operator L_2, after crossing $\theta = 1.62$. The largest difference is observed (Fig. 6.10(b)) for a choice of $\lambda = 0.34$ eV and initial state that is above the barrier height, for which the dominant population

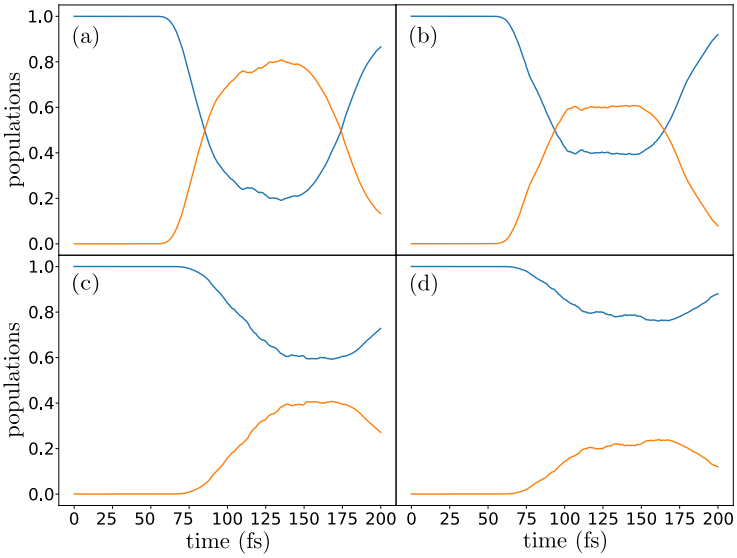

Figure 6.10: Population dynamics in the presence of an interacting environment, for two equilibrium positions and environment coupling operator $L = L_1 + L_2$, using the double well potential of Fig. 6.5. Blue lines represent the trans population in the region $0 \leq \theta \leq \pi/2$, and the orange lines represents the cis population in the region $\pi/2 \leq \theta \leq \pi$. For panels (a)(b) the initial state is above the barrier height, and for panels (c)(d) the initial state is at barrier height. For panels (a)(c) $\lambda = 0.017$ eV, whilst in panels (b)(d) $\lambda = 0.034$ eV.

after barrier crossing is altered to the cis conformation. This effect can be explained by the symmetric damping about the central point of the wells which decreases the damping in the left well as compared to a choice of environment coupling operator L_2. Therefore, a larger population is able to cross via coherent dynamics over the barrier to the cis conformation.

This section has analysed open quantum system barrier crossing dynamics of a double well potential that models the first steps of the photoisomerisation of stiff-stilbene using the HOPS method for a range of parameter choices. Summarising the key results, it was found that non-Markovian dynamics in interplay with the presence of a barrier, can be crucial in determining the population dynamics and yields. In general this occurs through a restoration of coherent dynamics which is most prominent for cases where the coherent dynamics dominates, as in the case of an initial state above barrier height. A similar effect occurs for an initial state at barrier height, but there

is not an associated restoration for each increase in depth size of HOPS. This could be due to population crossing back over the barrier after passing it if there is a reduction in the damping near the crossing point due to the restoration of coherent dynamics. The choice of equilibrium positions and environment coupling operators has been shown to range from subtle to significant, is sensitive to the coupling strength through changes in λ, and dependent on the location of barriers. Barrier crossing stabilisation can be observed dependent on the choice of environment coupling operator, and a change in the damping such that more population is able to cross the barrier. It is important to note that in order to prevent population from transferring back through coherent dynamics a much larger coupling strength would be required than the physically plausible range of values chosen. Thus the model, akin to early barrier crossing models of photoswitching [8, 110, 112–114], is best suited if one is not concerned with the ensuing dynamics after the barrier is crossed. If the post-barrier crossing dynamics are of importance either a larger coupling strength or modification of the system potential is required. In this case it is important to note that although the double well model potential mimics the stiff-stilbene PES such that the initial wavepacket is at 3.66 eV and the barrier height is 0.0806 eV, the inital state height above barrier is overestimated by 0.021 eV and the PES is not as shallow. Thus, while the inset of Fig. 6.5 shows a relatively good fit for a double well model, subtle differences could contribute to significant changes in the dynamics.

6.4 Numerically exact simulation dynamics of stiff-stilbene

In the last section a double well potential was used as a simplified model representative of the first stages of stiff-stilbene photoisomerisation. Whilst useful for testing HOPS and analysing barrier crossing dynamics relevant for photoswitches such as stiff-stilbene, such a model is insufficient in accurately modelling the complete quantum dynamics as a function of coordinates important to the reaction. For example, it is unable to model the excited state dynamics in the cis conformation, and is instead used to represent barrier crossing from the electronic excited state trans population to the electronic ground state cis population. In this section we will explore the application of HOPS to a two electronic state PES that was first introduced in Chapter 5 Fig. 5.5.

In the early time dynamics of 400 fs of stiff-stilbene, transient grating spectroscopy suggests that the excited electronic state (S_1) is the most relevant [4]. Consequently,

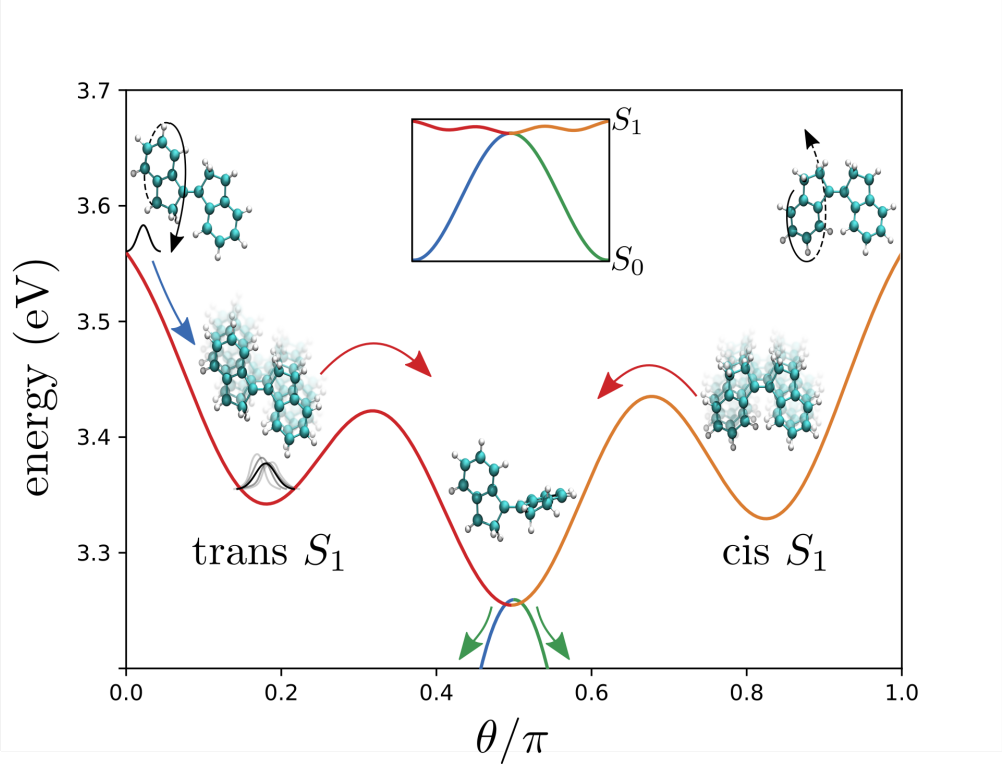

Figure 6.11: PES diagram of the S_1 surface of stiff-stilbene as a function of torsional coordinate. The inset shows both the S_1 and S_0 surfaces. The initial state is vertically excited to 3.56 eV on the S_1 surface at $\theta = 0$. The blue arrow represents subsequent dynamics due to the system and interacting environment incorporated through HOPS. In the perpendicular conformation $\theta = 0.5\pi$ the wavepacket can be transferred to the S_0 surface, as shown by the green arrows. Trapped wavepackets in the trans S_1 region $0 \leq \theta \leq 0.3\pi$ and the cis region $0.7\pi \leq \theta \leq \pi$ can overcome the barriers to the perpendicular conformation over the course of several picoseconds.

Fig. 6.11 represents the features of the S_1 surface in more detail. Upon photo-excitation the initial wavepacket undergoes a vertical transition from trans S_0 to the trans S_1 state at $\theta = 0$ with an energy difference of 3.56 eV, which has been chosen according to absorption spectra [4]. This initial state is propagated using HOPS which, following the blue arrow of Fig. 6.11, undergoes an evolution due to the system and fluctuations and damping caused by interaction with the environment. Transient grating spectroscopy results [4] have suggested that in the initial evolution a small population overcomes a

barrier of 650 cm^{-1} located at approximately $\theta = 0.3\pi$, passing through the perpendicular conformation at $\theta = 0.5\pi$ without significant transfer to the S_0 surface, and overcoming another barrier of 850 cm^{-1} at approximately $\theta = 0.7\pi$ to become trapped in the the cis S_1 region between $0.7\pi \leq \theta \leq \pi$. Over several picoseconds the trapped populations overcome the barriers due to thermal fluctuations to the perpendicular conformation at $\theta = \pi$. In what follows the observed transient grating spectroscopy and associated interpretation, is compared against the wavepacket dynamics generated using the coordinate representation of HOPS for the torsional coordinate. Comparisons to the double well potential model are drawn at the end of the section.

Wavepacket dynamics along the ground and excited PES of Fig. 5.5 are generated using the HOPS method for 100 trajectories, with a depth of 4 unless otherwise stated, a coordinate grid of 1000 points in the range $-2\pi \leq \theta \leq 2\pi$, a time step of $\Delta t = 0.001$ fs, and a fourth-order Runge-Kutta method as described in Appendix A.3. The BCF parameters introduced in the last section, which represent physically plausible values for stiff-stilbene in hexane at temperature $T = 300$ K, are used with a Drude spectral density for $\lambda = 0.008$ eV and $\gamma = 0.03$ fs^{-1}. Coupling between ground and excited surfaces is chosen as $J = 0.02$ eV such that transference only occurs in the region of $\theta = 0.5\pi$. Motivated by the findings of the double well potential model, environment coupling operators are included for each potential energy well such that for the excited state surface $L_1^{S_1} = \theta - 0.567$, $L_2^{S_1} = \theta - 1.56$, and $L_3^{S_1} = \theta - 2.59$. Similarly, the ground state surface has environment operators $L_1^{S_0} = \theta$, and $L_2^{S_0} = \theta - 3.14$. The overall coupling operators for S_0 and S_1 surfaces are expressed as

$$L^{S_1} = L_1^{S_1} + L_2^{S_1} + L_3^{S_1} = 3\theta - 4.72, \tag{6.37}$$

$$L^{S_0} = L_1^{S_0} + L_2^{S_0} = 2\theta - 3.14, \tag{6.38}$$

which corresponds to an S_1 equilibrium position of $\theta = 4.72/3 = 1.57$ and an S_0 equilibrium position of $\theta = 3.14/2 = 1.57$ i.e. approximately $\pi/2$.

It is of interest to understand how sensitive the population dynamics are to a change in environment parameters. In the first case we consider a change of the BCF parameter λ with results shown in Fig. 6.12. Upper panels of the figure show population dynamics as λ is increased from the value estimated from stokes shift $\lambda = 0.008$ eV (Fig. 6.12(a)), to the upper estimate from stokes shift $\lambda = 0.017$ eV (Fig. 6.12(b)), and lastly to $\lambda = 0.036$ eV (Fig. 6.12(c)) which corresponds to a value used in model studies of the retinal photoswitch [91]. The lower panels of Fig. 6.12 show the spectral densities

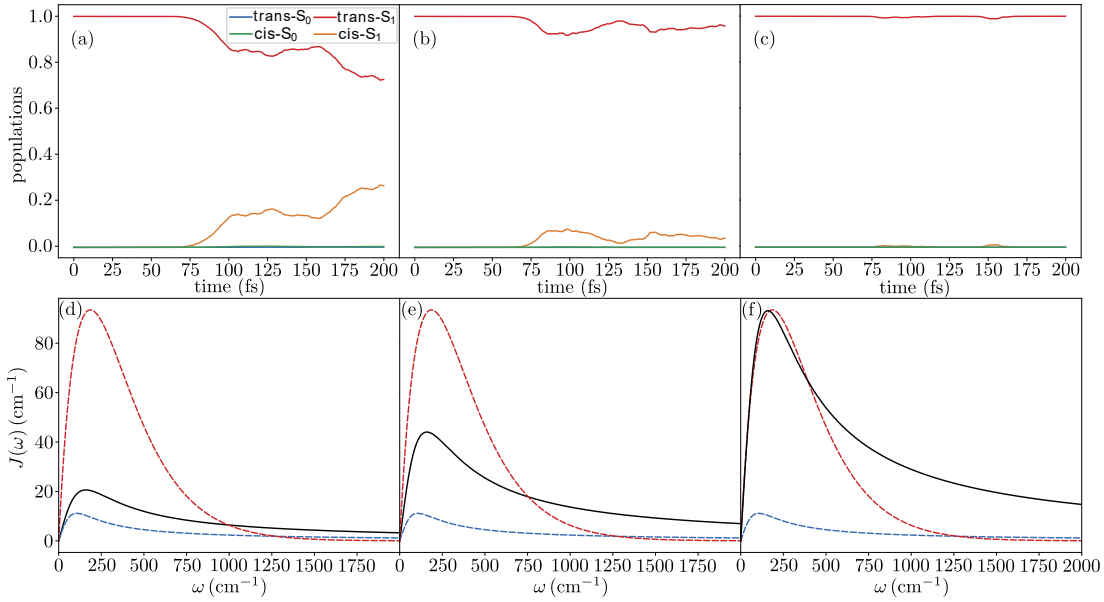

Figure 6.12: Upper panels (a)(b)(c) show population dynamics in the presence of an interacting environment, for a variation of λ, using the stiff-stilbene PES of Fig. 5.5. Lower panels (d)(e)(f) show the corresponding spectral density, represented by the solid black line. The dashed red and blue lines are included for comparison and represent an Ohmic spectral density used for the retinal photoswitch and a Drude spectral density used for the photosynthetic FMO complex respectively. For the coupling strengths an estimate obtained from stokes-shift is used in (a)(d) with $\lambda = 0.008$ eV, for (b)(e) an upper estimate obtained from the stokes-shift is used with $\lambda = 0.017$ eV. In panels (c)(f) the parameter is chosen as $\lambda = 0.036$ eV which corresponds to a value used in retinal model studies.

associated with each of these parameter choices shown by the black line. For reference, a Drude spectral density used for the photosynthetic Fenna-Matthews-Olson (FMO) complex [59], is shown by the blue dashed line. Additionally, an Ohmic spectral density used for retinal [91] is shown by the red dashed line. For $\lambda = 0.008$ eV, the population dynamics suggest a portion of the wavepacket overcomes the barrier at $\theta = 0.3\pi$ and $t = 75$ fs passing through the perpendicular conformation, without significant transference to the S_0 surface, and overcoming the barrier at 0.7π as t approaches 200 fs. This is in good agreement with transient absorption spectroscopy results [4] that suggest a decay in the trans excited state absorption (ESA) and a rise in the cis ESA. The

increase to $\lambda = 0.017$ eV leads to stronger damping resulting in a only a small portion of the wavepacket overcoming the barrier at approximately $\theta = 0.3\pi$. Following this, an increase in the trans S_1 population for $t = 100$ fs suggests that the less of the portion of the wavepacket that crossed the barrier at $\theta = 0.3\pi$ is able to cross the barrier at $\theta = 0.7\pi$ than for the case of $\lambda = 0.008$ eV. Lastly, for $\lambda = 0.036$ eV strong damping is observed such that the wavepacket unable to overcome the barrier at $\theta = 0.3\pi$ becoming trapped in the well corresponding to the trans S_1 conformation. The early femtosecond timescale dynamics of stiff-stilbene is often referred to as frictionless, the results here suggest an interpretation of this as a regime of damped coherent dynamics rather than free of interaction with the environment. An increased interaction with the environment, achieved through changing λ within a physically plausible parameter choice, demonstrates sensitivity in the damped coherent dynamics leading to trapping in different conformations. For the largest choice of λ the coherent dynamics is rapidly damped such that escape over the barrier is possible only on a longer timescale determined by thermal fluctuations. Interaction with the environment, friction, and damping thus plays a significant role in determining early time dynamics and wavepacket trapping. However, population transference from trans S_1 to cis S_1 via barrier crossing on the femtosecond timescale can be largely attributed to the coherent, yet damped, wavepacket dynamics.

The second BCF parameter that may be varied with the Drude spectral density is the inverse relaxation time γ. The population dynamics for such a variation are shown in the upper panels (a)(b)(c) of Fig. 6.13, and the corresponding spectral densities are shown in the lower panels (d)(e)(f). A change of γ translates the location of the peak of the spectral density, in Fig. 6.13 a vertical dashed line has been used to clarify its position with respect to the reference retinal and FMO spectral densities. The inverse relaxation time is varied between that of the FMO spectral density with $\gamma = 0.02$ fs^{-1} (Fig. 6.12(a)), to $\gamma = 0.03$ fs^{-1} (Fig. 6.12(b)), and lastly to the that of the retinal spectral density $\gamma = 0.04$ fs^{-1} (Fig. 6.12(c)). In contrast to a variation of λ, varying γ within a parameter regime corresponding to real systems has a more subtle effect on population dynamics. There is a small increase in damping as γ is increased, leading to lower population transfer from trans S_1 to cis S_1. For all cases the dominant population over 200 fs is trans S_1, in agreement with experimental observations [4]. However, there is a greater population transference for $\gamma = 0.02$ fs^{-1}, suggesting that a value of $\gamma = 0.03$

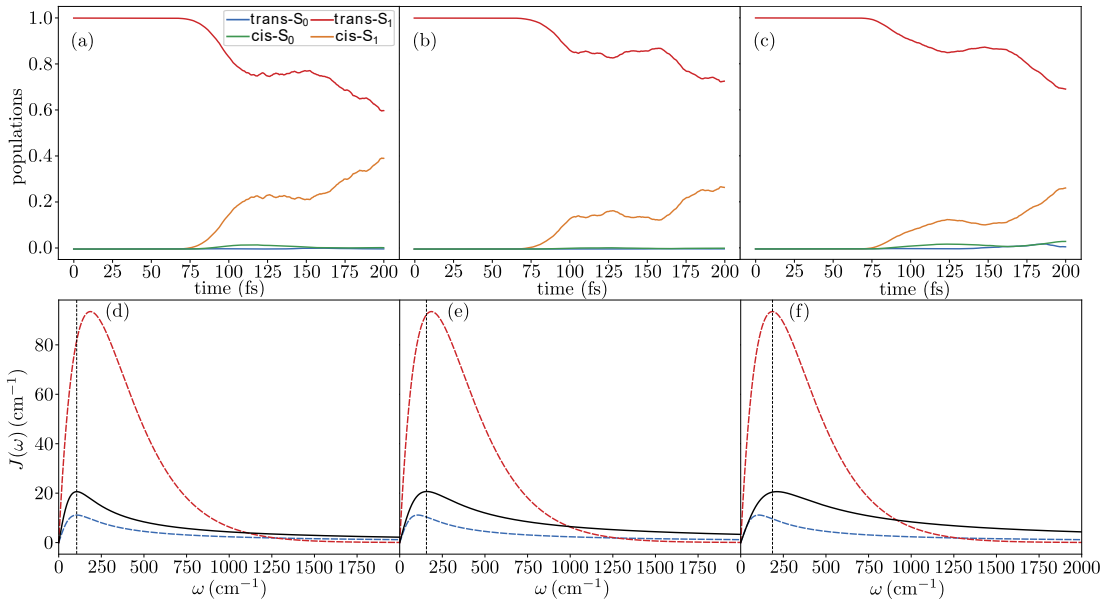

Figure 6.13: Upper panels (a)(b)(c) show population dynamics in the presence of an interacting environment, for a variation of γ, using the stiff-stilbene PES of Fig. 5.5. Lower panels (d)(e)(f) show the corresponding spectral density, represented by the solid black line. The dashed red and blue lines are included for comparison and represent an Ohmic spectral density used for the retinal photoswitch and a Drude spectral density used for the photosynthetic FMO complex respectively. The vertical dashed line clarifies the location of the peak of the spectral density. The inverse relaxation times are $\gamma = 0.02$ fs^{-1} in (a)(d) corresponding to a peak location of 106 cm^{-1}, $\gamma = 0.03$ fs^{-1} in (b)(e) corresponding to a peak location of 159 cm^{-1}, and $\gamma = 0.04$ fs^{-1} in (c)(f) corresponding to a peak location of 212 cm^{-1}.

fs^{-1} or $\gamma = 0.04$ fs^{-1} is more appropriate for better agreement with experiment, and also corresponds closer to values used for photoswitches such as retinal.

In addition to the BCF parameters considered above, the temperature T and the coupling J between the ground and the excited PES may influence population dynamics. It is thus of importance to consider a variation of these parameters to understand the effect on wavepacket dynamics. For the temperature this is conducted for increases of 100 K for $T = 200$ K, $T = 300$ K, and $T = 400$ K, the last of which lies approximately 60 K above the phase change point of hexane. Thus results at $T = 400$ K are purely for comparison of the generated dynamics and should not strictly be attributed

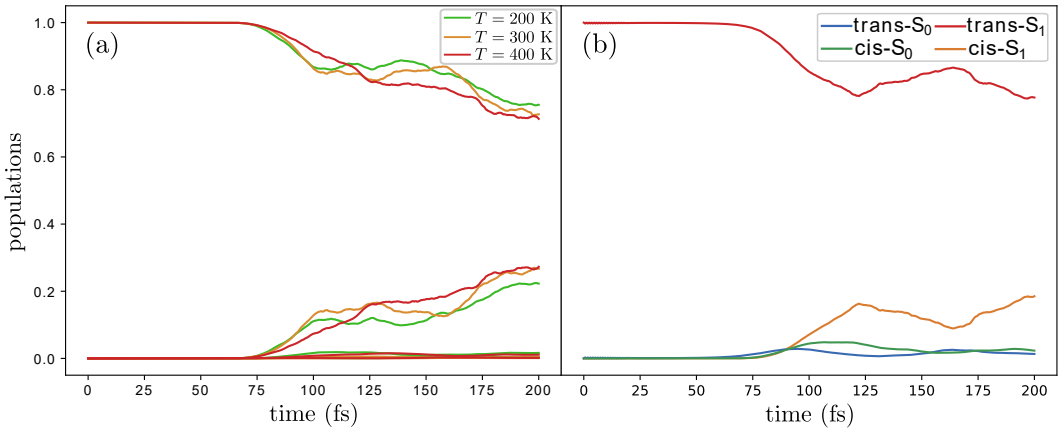

Figure 6.14: Population dynamics generated through HOPS, for 100 trajectories with $\lambda = 0.008$ eV and $\gamma = 0.03$ fs^{-1}. (a) Demonstrates the small change on dynamics of increasing temperature from 200 K to 400 K. (b) Coupling between S_0 and S_1 is increased to $J = 0.1$ eV which shows a minor increase in transference between surfaces.

to a physical system. Results at each of the temperatures, for a choice of $\lambda = 0.008$ eV, and $\gamma = 0.03$ fs^{-1}, can be seen in 6.14(a) and show similar population dynamics. There is a potential increase in barrier crossing observed as the temperature is increased. However, as the differences in population dynamics are only slight, a large number of trajectories would be required to verify this observation. Regardless, on the femtosecond timescale there is at most only a minute change in the barrier crossing dynamics due to temperature increase. It is anticipated that a change in temperature leads to a larger difference in the thermal fluctuation dynamics for the long term picosecond barrier crossing, whereas for the damped coherent dynamics it has a smaller impact. In addition to the temperature, J may be varied, in simulations thus far a value of $J = 0.02$ eV was chosen such that transfer between S_0 and S_1 surfaces occur in the region of $\theta = 0.5\pi$. Minimal transference has been observed in agreement with experimental observation [4], this is in contrast to the closed system dynamics for stiff-stilbene presented in Chapter 5 [181] in which significant population transfer of 0.2 was observed. In Fig. 6.14(b) results are shown for a choice of $J = 0.1$ eV and demonstrate that results are robust to changes in J with only a small increase in the population transfer from S_1 to S_0. Comparison to closed system dynamics suggests that the interaction with the environment inhibits transfer to the S_0 surface from S_1, this is in part due to less of the wavepacket passing through the perpendicular conformation at

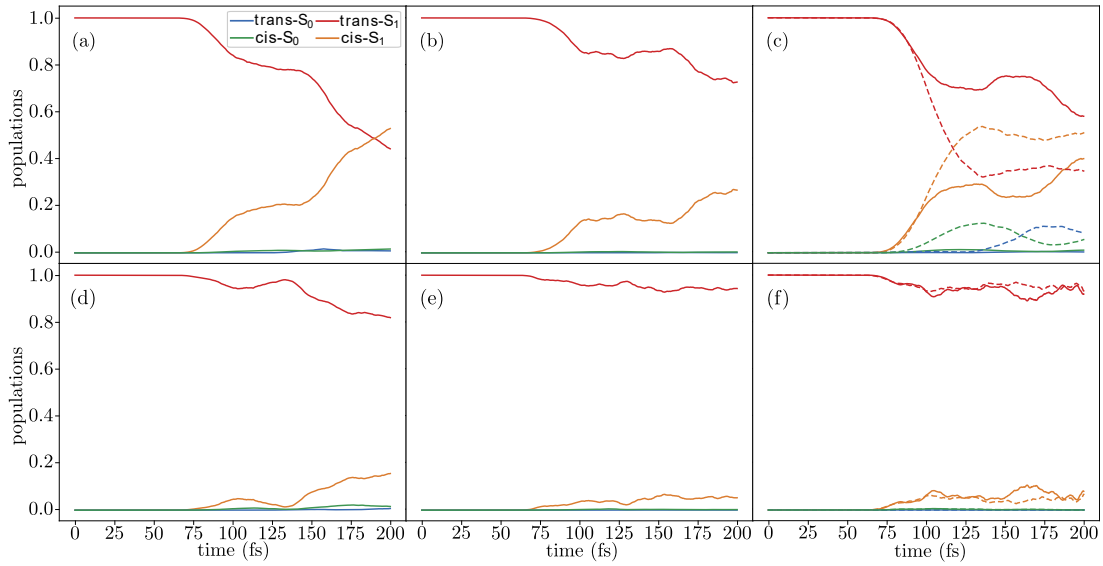

Figure 6.15: Population dynamics generated through HOPS, for 100 trajectories with $\lambda = 0.008$ eV (a)(b)(c), $\lambda = 0.017$ eV (d)(e)(f), and $\gamma = 0.03$ fs^{-1}, for an increase in hierarchy depth. Results are shown for depth 2 in panels (a)(d), depth 4 in panels (b)(e), and depths 8 (solid line) and 12 (dashed line) in panels (c)(f). Results show good convergence for $\lambda = 0.017$ eV by a depth of 4, whereas population dynamics still have not converged by a depth of 12 for $\lambda = 0.008$ eV

$\theta = 0.5\pi$ where the internal conversion occurs. In addition to this, fluctuations from the interaction with the environment may play a role by causing the wavepacket to fluctuate out of the region where internal conversion occurs as it passes through the perpendicular conformation.

In addition to the parameters that may be altered within the HOPS approach, the convergence with respect to hierarchy depth must also be considered which accounts for the memory term within the NMSSE. For larger hierarchy depths there is a more accurate accounting of non-Markovian dynamics that comes at the expense of increased computational cost. In Fig. 6.15 depth sizes of 2, 4, 8, and 12 are considered. For a depth of 4 there is relatively good convergence of the overall population dynamics within 200 fs for $\lambda = 0.017$ eV, but poor convergence of population dynamics for $\lambda = 0.008$ eV by a depth of 12. Furthermore, as the depth size is increased results for $\lambda = 0.008$ eV predict that the majority of the wavepacket is able to cross the barrier at $\theta = 0.3\pi$, deviating from experimental observation. This is likely due to the

restoration of coherent dynamics that arises from the non-Markovian interaction with the environment and is shown to also increase S_0 populations. Thus, at deeper layers of the hierarchy, finer details of the non-Markovian dynamics are resolved as the increase in auxiliary states tracks more of the state of the bath and system-bath interaction. The terminator acts to truncate the hierarchy at a sufficient depth at such a point that the rest of the interaction can be assumed to be Markovian [213]. However, if the depth is insufficient then a significant part of the memory integral of the NMSSE may be unaccounted for and consequently non-Markovian dynamics may be missed. For $\lambda = 0.008$ eV the depth of 4 is insufficient as non-Markovian interactions are still unaccounted for as shown by increased depth size. Thus, if results with $\lambda = 0.008$ eV are to agree better with experiment the parameter γ, which was estimated from similar systems, would have to be altered.

The results presented thus far inform on the time dynamics up to 200 fs and represents the point at which part of the damped coherent wavepacket dynamics has passed over the barrier at $\theta = 0.7\pi$ to the potential energy well corresponding to the cis S_1 conformation. In the transient absorption spectroscopy this corresponds to a decay in the trans ESA signal and a rise in the cis ESA [4]. We now turn our attention to the subsequent dynamics up to 400 fs to investigate barrier trapping of the wavepacket. Motivated by the findings of this section, the BCF parameters are chosen as, $\lambda = 0.008$ eV and $\lambda = 0.017$ eV which are lower and upper estimates found from the stokes-shift of stiff-stilbene in hexane [4], and $\gamma = 0.03$ fs $^{-1}$ which corresponds to a physically plausible choice for photoswitches such as retinal [91]. Dynamics are generated, up to 400 fs at a temperature of $T = 300$ K, using HOPS with 1000 trajectories and a depth of 4. Results are presented in Fig. 6.16, where for comparison the population dynamics for two sets of 100 trajectories are shown by the transparent solid and dashed lines demonstrating similar results. The damped coherent wavepacket dynamics up to 200 fs has already been analysed and represents a partial crossing of the barrier at $\theta = 0.3\pi$, with subsequent passage through the perpendicular conformation presenting minor transfer to the S_0 surface, and lastly a partial crossing of the barrier at $\theta = 0.7\pi$. Following this, population dynamics for $\lambda = 0.008$ eV in Fig. 6.16(a) shows that there is a small increase in the cis S_1 population as further transference occurs, but population transfer plateaus between 300 fs and 400 fs representing a trapping of the wavepacket. For population dynamics of $\lambda = 0.017$ eV (Fig. 6.16(b)) the plateau in

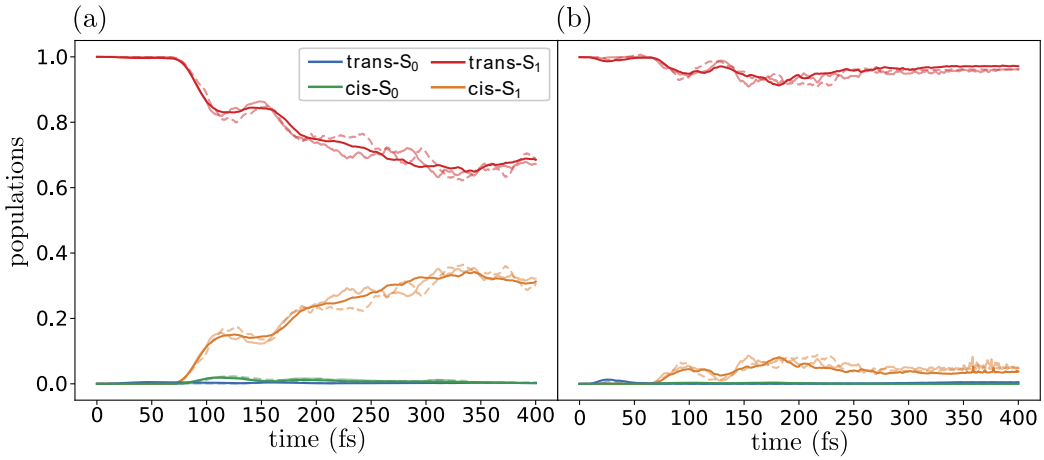

Figure 6.16: Population dynamics up to 400 fs generated through HOPS with a depth of 4 at $T = 300$ K, for 1000 trajectories. BCF parameters are chosen as $\lambda = 0.008$ eV (a), $\lambda = 0.017$ eV (b), and $\gamma = 0.03$ fs^{-1}. Transparent solid and dashed lines represent results of two alternative sets of 100 trajectories.

population transfer occurs at an earlier time due to stronger damping and wavepacket trapping, demonstrating significant influence of the environment on dynamics. A small rise in cis-S_1 population subsequent to 200 fs is supported by the transient absorption spectroscopy [4], which suggests there is a rise in the cis ESA signal between 200 fs and 400 fs. Thus, a value for λ that captures this feature, and converges with respect to depth, lies between the two estimates of $\lambda = 0.008$ eV and $\lambda = 0.017$ eV. Alternatively, for a depth of 4 with $\lambda = 0.008$ eV, an increase in γ would reduce the transfer slightly to cis-S_1, as demonstrated in Fig. 6.13. Crucially, for this parameter choice it could also reduce the bath correlation time such that better convergence of non-Markovian dynamics may be found. Nonetheless, both results show a small transfer in population from trans S_1 to cis S_1, followed by a plateau within 400 fs, which is in good agreement with the experimental observations of minor change in the cis ESA signal from 500 fs to 1 ps. Furthermore, the results predict that over the 400 fs, there is little population transfer to S_0 as suggested by transient absorption findings. The overall wavepacket dynamics here thus agree with the interpretation of the transient absorption results by Quick et al [4] that the early sub-picosecond dynamics leads to wavepacket trapping in regions corresponding to the cis and trans S_1 conformations that would then undergo a thermally activated barrier crossing on the picosecond timescale, which is claimed to

be completed within 16 ps.

Beyond these results, an additional feature is observed in the population dynamics of Fig. 6.16(a) identified by the rise in the trans S_1 population at approximately 150 fs and 275 fs. This is attributed to wavepacket trapping in the central well corresponding to the perpendicular conformation. As trans population is associated with the wavepacket in the region $0 \leq \theta \leq 0.5\pi$ and cis population in the region $0.5\pi \leq \theta \leq \pi$, a portion of the wavepacket trapped in the central region about 0.5π would result in a small oscillatory population transfer between trans S_1 and cis S_1 that would decay over time due to further barrier crossing and transfer to the S_0 surface. This feature would not be resolved in the transient absorption spectroscopy due to an inability to probe the perpendicular conformation. However, it could be identified by a decrease in the trans ESA that is not accompanied by the associated equivalent increase in the cis ESA representing trapping in the perpendicular conformation.

In addition to the wavepacket dynamics that have been generated, which was compared to existing transient absorption spectroscopy, linear absorption spectroscopy provides a means by which to test the model and HOPS method. It also presents a tool to optimise parameters, such as those of the BCF, in order to fit to experimental data. HOPS provides an efficient method to generate the linear absorption spectra [59, 212, 214], with further reduction in computation possible by simulating with only one zero noise trajectory. In Fig. 6.17 the absorption spectra for stiff-stilbene in hexane has been generated with HOPS using [68, 130]

$$\sigma_{abs}(\omega) = |\mu_{eg}|^2 \int_{-\infty}^{\infty} dt\, e^{i\omega t} \langle \psi_g(t) | \psi_e(t) \rangle, \tag{6.39}$$

assuming perpendicular dipoles and $|\mu_{eg}|^2 = 1$, with BCF parameters $\lambda = 0.008$ eV, and $\gamma = 0.03$ fs^{-1} and the single coordinate PES of Fig. 6.11. Dynamics are generated for 400 fs to allow the correlation function to decay sufficiently. Solid lines of Fig. 6.17 represent simulated absorption spectra for depths 4, 8 and 16 using a single zero noise trajectory, whilst the black dashed line represents the results of the full approach of simulating 100 trajectories with noise at a depth of 8. Only minor differences are observed as the depth is increased from a depth of 8 to 16, and reasonable convergence of the broadened lineshape is observed for 100 trajectories. However, the simulated spectra is unable to reproduce the complexity of several broadened bands observed in experiment [4]. Thus, whilst the one dimensional PES model is able to produce

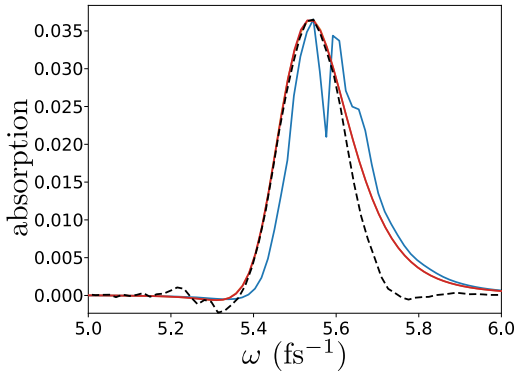

Figure 6.17: Linear absorption spectra for stiff-stilbene in hexane generated using HOPS with a single noise free trajectory for depth 4 (blue line), depth 8 (orange line), and depth 16 (red line). The black dashed line shows the absorption spectra generated using the complete HOPS method for depth 8 with noise and 100 trajectories.

wavepacket dynamics in good agreement with transient absorption spectroscopy results, it is unable to generate the complete linear absorption spectra.

Motivated by the two coordinate linear absorption spectra findings of Chapter 3 shown in Fig. 4.6 and Fig. 4.7, and a schematic of a two coordinate model PES presented in a study on cis stilbene [215], the model PES of Fig. 6.18 is proposed. In this figure θ represents the torsional motion of the single coordinate model [181] presented in this section and Chapter 5, and q represents a second higher frequency harmonic mode of $\omega = 0.085$ fs^{-1} that is displaced with a Huang-Rhys parameter of $D_q = 1$. Blue arrows represent the direction of the initial damped coherent wavepacket dynamics, red arrows represent the thermally activated escape over barriers, and green arrows represent the internal conversion processes that take the wavepacket from the S_1 surface to the S_0. The inset of Fig. 6.18 shows the S_0 and S_1 surfaces, where the arrow represents the vertical excitation to trans S_1, and the vertical line with black circles represents the point of internal conversion at $\theta = 0.5\pi$. With respect to dynamics, at $t = 0$ fs, the wavepacket is vertically excited to 3.56 eV on the two coordinate S_1 PES. It then undergoes high frequency oscillatory motion in the q coordinate whilst the wavepacket dynamics that correspond to the reaction mechanism occurs in the shallow coordinate θ. As before, barriers are encountered at $\theta = 0.3\pi$ and $\theta = 0.7\pi$ which may trap the wavepacket. The additional coordinate q is not anticipated to play a role in the

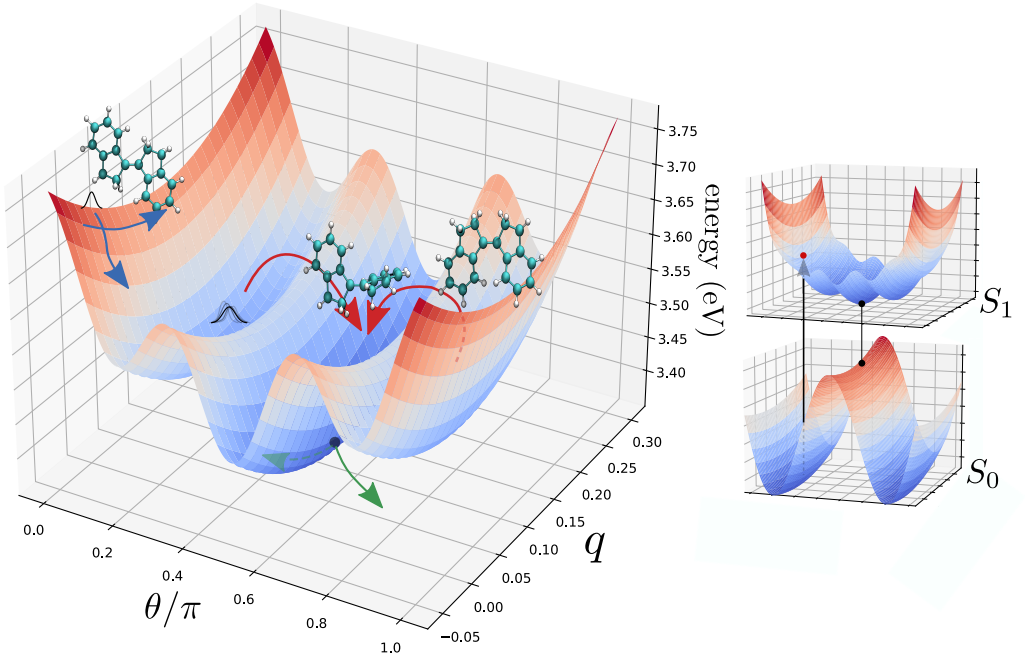

Figure 6.18: S_1 PES for stiff-stilbene as a function of coordinates θ and q. The initial wavepacket is vertically excited, as shown by the arrow in the inset, to an energy of 3.56 eV on the S_1 surface. Blue arrows represent the initial coherent yet damped wavepacket dynamics on the S_1 surface, red arrows represent thermally activated barrier crossing, and green arrows represent internal conversion processes taking the wavepacket from the S_1 surface to the S_0 surface. The point of internal conversion is shown in the inset by the black circles connected by a vertical line at approximately 0.5π.

photoisomerisation reaction of stiff-stilbene [4, 8, 110] and the population dynamics presented for the single coordinate model are expected to hold for the two coordinate model. However, the results of this section and Chapter 4 suggest that the inclusion of the coordinate q is crucial in accounting for the full complexity of linear absorption spectra.

For an initial investigation of the two coordinate absorption spectra a two coordinate harmonic model, such as those presented in Chapter 4, is used with frequencies $\omega_g(\theta) = \omega_g(q) = \omega_e(q) = 0.085$ fs^{-1} and $\omega_e(\theta) = 0.01571$ fs^{-1}. Dynamics are generated using a split operator method, as described in Appendix. A.3, with a 1000 grid points in each coordinate for a grid size of 1000×1000, and a time-step of $\Delta t = 0.001$

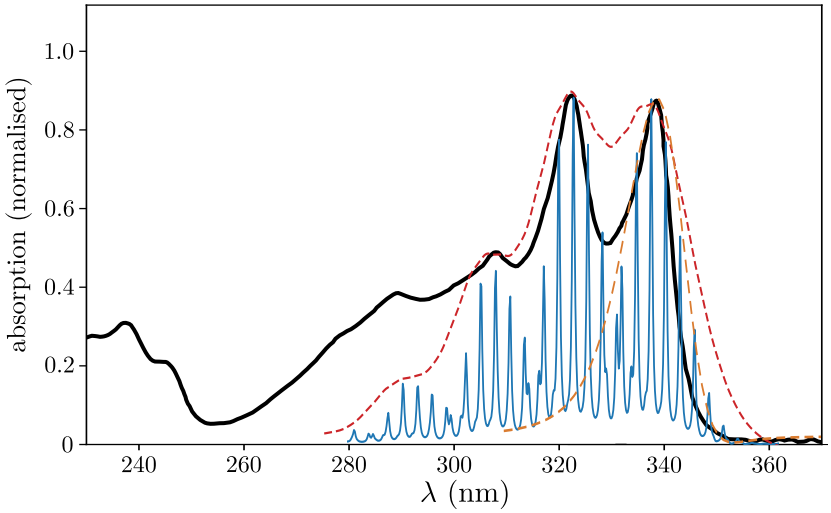

Figure 6.19: Linear absorption spectra is shown for a two coordinate harmonic model with frequencies $\omega_g(\theta) = \omega_g(q) = \omega_e(q) = 0.085$ fs^{-1} and $\omega_e(\theta) = 0.01571$ fs^{-1} and split operator method (blue line), the equivalent spectra artificially broadened (red dashed line), and single coordinate model with dynamics generated through HOPS with a depth of 16 (orange dashed line). For comparison experimental spectra is shown by the black line reprinted (adapted) with permission from reference [4]. Copyright 2014 American Chemical Society.

fs^{-1}. Figure 6.19 compares the resolved absorption spectra generated using the two coordinate model (blue line), with the experimental absorption spectra (black line). In addition, artificial broadening of the spectra is achieved via exponentially decaying the correlation function (red dashed line), and the single coordinate model spectra generated through the HOPS method with a depth of 16 has been included for comparison (orange dashed line). The two coordinate resolved spectra produces multiple bands, the centres of which are in good agreement with the experimental spectra. Application of artificial broadening is unable to recreate the lineshape of experimental spectra and overestimates the broadening of the vibronic progression associated with each band whilst underestimating the broadening of the overall lineshape. The single coordinate spectra correctly predicts the peak location of the first band but is unable to produce the correct lineshape due to the lack of the additional coordinate which alters features of the first band lowering the width at the longer wavelength side of the band whilst increasing it at the shorter wavelength side of the band. The results thus far suggest

that the correct broadening features may be captured through HOPS with two coordinates by producing damping in each coordinate θ and q. This would result in an asymmetric broadening for each band through damping in coordinate θ such that the shorter wavelength side of each band is broadened more. Furthermore, via asymmetric broadening in coordinate q the overall lineshape is broadened in the range of 260 nm to 360 nm, with greater broadening produced at shorter wavelengths. It is predicted that these effects, in combination with the numerically exact dynamics generated via HOPS, will produce the correct lineshape features. In connection to this, the two coordinate model used with HOPS provides a means of testing the parameters, such as those of the BCF.

6.5 Summary

In this chapter the numerically exact method of HOPS has been extended to a coordinate representation to model molecular photoswitching in a condensed phase environment. Firstly, the derivation of HOPS was revisited in order to derive a version that preserves the norm of each trajectory to improve the stability of simulations and the accuracy over the unnormalised version for large values of the norm. This normalised version of HOPS was verified by using a spin-boson model and comparing to the unnormalised version, and a Lindblad master equation in the Markovian limit. Subsequently, the coordinate representation of HOPS was developed and tested against the Lindblad master equation using a harmonic oscillator model in the Markovian limit. Additionally, for a coordinate coupling of the system to the environment, it was found that the Markovian limit incorrectly predicts an evolution free from damping. Instead, one must either make approximations, such as the zero-temperature approximation, or take a phenomenological approach. The coordinate representation of HOPS was then applied to a barrier crossing model to represent the initial stages of stiff-stilbene, and investigate different parameter choices and position of initial state with respect to the barrier. The model was subsequently extended to a full single coordinate PES for ground and excited electronic surfaces. In the latter study the developed normalised version of HOPS was crucial for a tractable implementation, allowing for stronger system-environment coupling and longer simulation times to be used. Findings from both studies suggest a sensitivity of population dynamics and yields to non-Markovian effects with respect to barrier crossing dynamics. The barrier crossing model was less

accurate than the two state single coordinate stiff-stilbene model in its predictions requiring stronger coupling to the bath for agreement with experiment, this suggests that the damped coherent wavepacket dynamics are highly sensitive to the curvature of the potential. Good agreement was found between the stiff-stilbene PES model population dynamics over the course of 400 fs and observed transient absorption spectroscopy results [4]. In the first 400 fs the dynamics is dominated by coherent evolution, that is damped due to interaction with the environment resulting in the trapping of the wavepacket in potential energy wells with minimal transfer to the S_0 surface. The subsequent evolution is then determined by thermally activated barrier crossing which results in transfer to the S_0 surface. However, portions of the wavepacket trapped in the regions associated with the cis or trans S_1 conformations is likely to influence the transfer to the S_0 surface due to the associated motion of the wavepacket as it either travels from trans to cis, or cis to trans. This suggests that the overall photoswitch dynamics involves an interplay of damped coherent wavepacket dynamics and thermally activated barrier crossing. In addition to providing support for interpretation of experimental data, the generated wavepacket dynamics gives insight into the evolution in regions inaccessible by transient absorption spectroscopy. Lastly, linear absorption spectra was generated using the HOPS method and it was found that, although a single coordinate model can accurately predict population dynamics, it is insufficient in generating the several spectral bands that arise and a two coordinate model is required. Future research could consider the generation of absorption spectra, and population dynamics, using HOPS with a two coordinate model by making use of the parallel computing capabilities of the method to address the increased computational cost. This would provide the foundation for the study of photoswitches with complex dynamics in which the reaction mechanism relies on more than one coordinate. Furthermore, one could consider the extension to the simulation of nonlinear spectroscopy which would provide an explicit comparison to experimental results.

Chapter 7

Conclusion

Throughout this thesis efficient methods of open quantum system methods have been developed for the simulation and analysis of quantum dynamics and features of molecular photoswitches, with a focus on interaction with condensed phase environments. The underlying aim of the work has been on developing tools that provide a better understanding of phenomena, the prediction and interpretation of experimental data, and in the extension of accurate yet tractable methods for the purposes of simulation. Although these were applied primarily for the study of photoswitch dynamics, the findings and methods are anticipated to have wide applicability and impact in the study of dynamics and properties of complex quantum systems.

In the introductory chapters, I reviewed the background theory. Following this, in Chapter 4 I investigated properties of linear absorption spectra for systems beyond the standard displaced harmonic oscillator model with equal surface curvature. Using a displaced harmonic model with large difference in surface curvature to mimic features of a photoswitch potential energy surface, a substructure in the vibronic progression of absorption spectra was identified. This was quantified via analytic expressions and provided not only a means to interpret linear absorption features, but also a predictive tool of the difference in curvature between ground and excited potential energy surfaces. Furthermore, I investigated the linear absorption spectra of two coordinate harmonic potential energy surfaces that differ in curvature demonstrating that such models were capable of producing rich spectral detail and a composition effect in the observed vibronic progressions. An extension of this work could consider the derivation of analytic expressions for the two coordinate harmonic model absorption spectra using Franck-Condon factors. This would allow quantification, and further insight, into the composition effect in absorption spectra when two or more coordinates are involved.

Subsequently in Chapter 5, the effects of an interacting environment, that causes the wavepacket dynamics to become damped, was included via a stochastic Schrödinger equation (SSE) approach. I investigated the effects of anharmonicity in the system, in combination with an interacting environment, on linear absorption spectra. This demonstrated asymmetric broadening effects for which anharmonic surfaces, such as the Morse potential, were sensitive to. In addition, I investigated the application of the SSE to a model potential energy surface (PES) for the stiff-stilbene photoswitch to understand effects of damping on wavepacket dynamics along an anharmonic surface. It was found that damping has the ability of stabilising photoswitched states by

inhibiting coherent wavepacket motion. This result suggested the possibility of tuning the environment of molecular photoswitches to achieve a change in dynamics and yield. A possible extension of this work would be to include finite temperature effects, through phenomenological means and the inclusion of two environment coupling operators that respectively correspond to processes that take energy from the system to the environment and processes that provide energy to the system from the environment. This would provide a Markovian method with results that could be more easily compared to non-Markovian methods, in order to assess and understand the importance of non-Markovian effects.

In Chapter 6 I extended the hierarchy of stochastic pure states (HOPS), a numerically exact open quantum system method capable of including non-Markovianity, to a coordinate representation for the study of condensed phase molecular photoswitch dynamics. Firstly, I developed a version of HOPS that is capable of preserving the norm of each trajectory, providing a more stable and accurate version over the unnormalised counterpart for large norm cases. Subsequently, I used the developed method to analyse barrier crossing dynamics in a double well PES, and a model PES of stiff stilbene. Findings suggested dynamics are highly sensitive to the curvature of the PES, with a greater effect of damping on wavepacket dynamics observed on the shallower stiff-stilbene PES. In addition to this, I found significant changes to dynamics dependent on the convergence of non-Markovianity. Consequently, an interplay of damped coherent dynamics, thermally activated dynamics, and non-Markovianity was determined to be crucial for photoswitch dynamics and yield. This suggests several potentially tunable elements to achieve desired changes to wavepacket dynamics and thus photoswitching. Furthermore, the results of population dynamics generated through HOPS was compared to transient absorption spectroscopy results with good agreement found supporting HOPS as a viable method to model condensed phase photoswitch dynamics. In addition, the results supported the existing interpretation of experimental results whilst also providing further insight into the wavepacket dynamics in regions of the PES inaccessible to the experiment. Lastly, I identified that a single system coordinate model with dynamics generated through HOPS is incapable of reproducing the linear absorption spectroscopy results. This suggested that the model must be extended and initial results generated with the split operator method and a two system coordinate harmonic PES model show promise for better agreement of a two coordinate model

with experiment. Thus a natural extension of the work would be to extend the HOPS method to explicitly model two sytem coordinates. This would allow for a better assessment of the parameters used in the HOPS method by comparing the fit of the absorption lineshape produced to that of the experimental absorption lineshape.

The work presented in this thesis provides tools and the foundations of methods that allow one to investigate and better understand the quantum dynamics of molecular photoswitches. Furthermore, the generality of the method allows it to be adapted to study a wide range of open quantum systems. Examples include open quantum systems of relevance to biological function and chemical reactions such as photosynthesis, the proposed quantum compass of avian magnetoreception, and the retinal photoswitch of vision. Beyond these examples, it provides an accurate setting to rigorously analyse: non-Markovian effects on spectral lineshape [216], quantum dissipation and role of an environment in the quantum-classical boundary, and resources quantified by quantum information theoretic tools that may be utilised by solid-state quantum devices. A motivational aim in this would be to better understand natural systems and fundamental physics, to use findings for medical applications, and to improve and design technology. There are clear paths forward in the research, such as application of the HOPS method to more complex photoswitch dynamics for which the reaction mechanism potentially depends on several coordinates, such as the azobenzene and retinal photoswitches. In this effort the HOPS method provides an efficient and numerically exact approach to rigorously assess non-Markovian effects in such systems. Such considerations are gaining interest with results suggesting the possibility of non-Markovian improvements to the efficiency of bio-molecular switches [208] supported by the findings of this thesis. Future studies could consider this further using resource theories [97] to quantify improvements, and test observations against experiment such as nonlinear spectroscopy, using theory to assist in interpretation [217]. Beyond these themes, it would be of interest to consider hybridisation of the HOPS method with open quantum system approaches that have close relations such as the coupled coherent state method. Through an interplay of these methods it may be possible to achieve a tunable balance for desired efficiency and accuracy. The large scope for the development and application of the methods and findings of this thesis suggest that approaches, such as the coordinate representation HOPS, will be fruitful in the future research of molecular photoswitches and open quantum system dynamics.

Appendix A

Computational methodology

A.1 Simulating closed quantum dynamics

In the closed system we have seen that the unitary time evolution operator of Eq. 1.77 can be used as the propagator of the wavefunction. Restating this in a way motivated for numerical implementation we obtain

$$U(\Delta t) = e^{-\frac{i}{\hbar}H\Delta t}, \tag{A.1}$$

where Δt is a time step. Having access to the propagator $U(\Delta t)$ gives knowledge of the propagator at longer times via the composition property

$$U(t) = [U(\Delta t)]^{N_t}, \tag{A.2}$$

where the propagator for Δt has been applied successively for $N_t = t/\Delta t$ steps.

The numerical implementation of this propagator can be done through several methods such as the discrete variable representation, Chebyshev, and the split-operator (SO) methods [218, 219]. Here we focus on the SO method in which the propagator is approximated as

$$\begin{aligned} U(\Delta t) =& e^{-\frac{i}{\hbar}(T_N+V)\Delta t} \\ \approx& e^{-\frac{i}{\hbar}V\frac{\Delta t}{2}} e^{-iT_N\Delta t} e^{-iV\frac{\Delta t}{2}}, \end{aligned} \tag{A.3}$$

which is approximate as in general $[T_N, V] \neq 0$. To be precise this is the symmetrised version of the SO method whereby the split of the potential at the beginning and the end of the interval gives a $\mathcal{O}(\Delta t^3)$ error for small Δt. This provides greater stability than the normal split operator method $U(\Delta t) \approx e^{-iV\Delta t}e^{-iT_N\Delta t}$ which gives an $\mathcal{O}(\Delta t^2)$ error [218]. The propagator has been partitioned in terms of the kinetic energy (T_N) and potential energy (V) terms which has the advantage that T_N acts locally in nuclear momentum space and the potential term acts locally in position space. Thus, the exponential operators can be implemented as pointwise multiplications of the wavefunction in respective spaces. The transformation between spaces can be efficiently achieved by invoking the fast Fourier transform (FFT), and its inverse, in the routine

$$\begin{aligned} U(\Delta t)|\psi\rangle =& e^{-\frac{i}{\hbar}(T_N+V)\Delta t} \\ \approx& e^{-\frac{i}{\hbar}V\frac{\Delta t}{2}} FFT^{-1}\Big(e^{-iT_N\Delta t} FFT\Big(e^{-iV\frac{\Delta t}{2}}|\psi\rangle\Big)\Big). \end{aligned} \tag{A.4}$$

There also exist many different finite difference methods that can be utilized. One of the most simple to implement is the explicit Euler scheme

$$\frac{d|\psi\rangle}{dt} \approx \frac{|\psi^{n+1}\rangle - |\psi^n\rangle}{\Delta t}, \tag{A.5}$$

which leads to

$$|\psi^{n+1}\rangle - |\psi^n\rangle \approx -\frac{i}{\hbar} H|\psi^n\rangle \Delta t \tag{A.6}$$

$$|\psi^{n+1}\rangle \approx |\psi^n\rangle - \frac{i}{\hbar} H|\psi^n\rangle \Delta t, \tag{A.7}$$

where the truncation error is $\mathcal{O}(\Delta t, \Delta x^2)$. The error in Δx arises due to the finite difference approximation of the kinetic term in the Hamiltonian

$$-\frac{\hbar^2}{2m}\frac{\partial^2|\psi\rangle}{\partial x^2} \approx \frac{|\psi^n_{j+1}\rangle - 2|\psi^n_j\rangle + |\psi^n_{j-1}\rangle}{\Delta x^2}, \tag{A.8}$$

where the superscript represents discretisation in time and the subscript in space. The same method can be obtained from a Taylor expansion of $e^{-i\Delta t H}$ keeping only the leading terms to obtain

$$|\psi^{n+1}\rangle = (1 - i\Delta t H)|\psi^n\rangle. \tag{A.9}$$

It is known however that the explicit Euler scheme is unconditionally unstable for the Schrödinger equation [220, 221]. There are many more finite difference methods available however of higher order. These can be explicit, as in the Euler scheme, in which iterations are calculated using the value at t to obtain the value at $t + \Delta t$. Or implicit in which a complex system of algebraic equations have to be solved. The explicit schemes have the advantage that they are generally easier to implement and take less storage, however, many conventional explicit schemes for the Schrödinger equation are unstable.

A.2 Simulating open quantum dynamics with SSEs

In Chapter 3 the non-linear Markovian SSE was presented (Eq. 3.31). In this section we shall review the fourth order Runge-Kutta numerical method presented in [41] and computational procedure for simulating open quantum dynamics with this SSE. Firstly, we restate the equation as

$$d\psi(t) = D_1(\psi(t))dt + D_2(\psi(t))dW(t), \tag{A.10}$$

where the drift term is given by

$$D_1(\psi) = \Big[-\frac{i}{\hbar} H\psi(t) + \frac{\Gamma}{2}\Big(\langle a + a^\dagger\rangle_\psi a - a^\dagger a - \frac{1}{4}\langle a + a^\dagger\rangle_\psi^2\Big)\psi(t)\Big]dt \tag{A.11}$$

and the diffusion term

$$D_2(\psi) = \Big[\sqrt{\Gamma}\Big(a - \frac{1}{2}\langle a + a^\dagger\rangle_\psi\Big)\psi(t)\Big]dW(t). \tag{A.12}$$

The RK4 numerical scheme is then performed by integrating in each time step the drift with the RK4 method, and the diffusion term with a simple Euler scheme as follows

$$\psi_{t+\Delta t} = \psi_t + \frac{1}{6}(\psi_t^1 + 2\psi_t^2 + 2\psi_t^3 + \psi_t^4)\Delta t + D_2(\psi_t)\Delta W_t, \tag{A.13}$$

with

$$\psi_t^1 = D_1(\psi_t), \tag{A.14}$$

$$\psi_t^2 = D_1(\psi_t + \frac{1}{2}\Delta t\psi_t^1), \tag{A.15}$$

$$\psi_t^3 = D_1(\psi_t + \frac{1}{2}\Delta t\psi_t^2), \tag{A.16}$$

$$\psi_t^4 = D_1(\psi_t + \Delta t\psi_t^3). \tag{A.17}$$

Using this a computational procedure is as follows:

1. **Input parameters and initialisation**: input time grid, basis grid (e.g. energy or coordinate), and system parameters. Input bath parameters such as coupling strength Γ, and coupling operator to bath L .

2. Generate potential energy surfaces and Hamiltonian.

3. Define the initial state $|\psi_0\rangle$ and allocate arrays.

4. **Stochastic routine**: This part of the procedure loops over steps 4–10 until the desired total number of stochastic iterations is met. Initialise arrays for the trajectory, iteration results, and RK4 terms. Set the initial state as $|\psi_0\rangle$.

5. **Generate white noise**: Generate time domain Gaussian random numbers $\xi(t)$ with mean zero and unit variance associated with white noise. Convert to a Wiener increment $\Delta W_t = \sqrt{\Delta t}\xi_t$, which is a Gaussian random variable with zero mean and variance Δt, with index t corresponding to different realisations at each time step.

6. **Time propagation routine**: This part of the procedure loops over steps 6-9 until the desired total simulation time is met. Firstly, set noise variables at t_1, t_2 and t_3 for the RK4 routine.

7. RK4 propagation for one time step: As outlined above generate four RK terms for the trajectory.

8. Store the time propagated trajectory, compute the density matrix, and/or expectation values.

9. If the total number of time steps is not met repeat from step 6.

10. If the total number of stochastic iterations is not met repeat from step 4.

11. **Completion**: Divide the sum total of trajectory expectation values and density matrix by the number of stochastic iterations providing the output results.

A.3 Simulating open quantum dynamics with HOPS

The linear HOPS method was introduced in Chapter 2 (Eq. 3.107), and subsequently non-linear (Eq. 6.1), and non-linear trajectory norm preserving versions (Eq. 6.9) were introduced in Chapter 6. In this section a computational procedure is demonstrated that implements these using a RK4 numerical scheme. The procedure is as follows:

1. **Input parameters and initialisation**: input time grid, basis grid (e.g. energy or coordinate), system parameters, bath correlation function parameters g, $w = \gamma + i\omega$ associated with the exponential form $\alpha_{T=0}(t) = g\ \exp(-wt)$, and the definition of coupling operator to bath L. Also input hierarchy parameters such as depth and number of stochastic iterations.

2. Generate potential energy surfaces and Hamiltonian.

3. Define the initial state $|\psi_0\rangle$ and allocate arrays.

4. **Stochastic routine**: This part of the procedure loops over steps 4–10 until the desired total number of stochastic iterations is met. Initialise arrays for the hierarchy $|\psi_t^{(k)}\rangle$, iteration results, RK4 terms, and set the initial state of hierarchy $|\psi_t^{(0)}\rangle = |\psi_0\rangle$.

5. **Generate noise**: Firstly, generate time domain Gaussian random numbers $x(t)$ and $y(t)$ with mean zero and unit variance to create the complex random number $\epsilon(t) = x(t) + iy(t)$ associated with white noise. Compute the time dependent bath correlation function $\alpha_{T=0}(t)$ between $-2t$ and $2t$. Use the fast Fourier transform (FFT) to transform the BCF and white noise random variables to the frequency domain $\epsilon(\omega) = \text{FFT}[\epsilon(t)]$, $J(\omega) = \text{FFT}[\alpha_{T=0}(t)]$. Multiply these as follows to obtain the correctly weighted noise $\eta(\omega) = \sqrt{J(\omega)}\epsilon(\omega)$. Lastly, use the inverse fast Fourier transform to obtain the time dependent weighted noise $\eta(t) = \text{IFFT}[\eta(\omega)]$. This generates $2t/2 = t$ independent random numbers, where in the simulation time is discretised into steps. Calculate the conjugate of the noise, corresponding to Eq. 3.93, $\zeta_t^* = \eta(t)^*$.

6. **Time propagation routine**: This loops over steps 6-9 until the desired total simulation time is met. Firstly set noise variables from the noise array ζ_t^* at t_1, t_2, and t_3 for the RK4 routine.

7. RK4 propgation for one time step: Obtain four RK4 terms for the hierarchy and four for the memory terms (in non-linear versions). Compute all required norm terms such as $\langle L^\dagger \rangle_t$. An exponential BCF also simplifies the treatment of the memory term in Eq. 3.122. The memory term $h(t)$ is propagated according to

$$\dot{h}(t) = \alpha_{T=0}(0)\langle L^\dagger \rangle_t - w^* h(t), \tag{A.18}$$

where

$$h(t) = \int_0^t \alpha_{T=0}(t-s)^* \langle L^\dagger \rangle_s \, ds. \tag{A.19}$$

Calculate each level of the hierarchy using Eq. 3.107 in the linear case, with additional terms for non-linear cases as in the Girsanov-shifted case (Eq. 6.1) and Girsanov-shifted with normalised trajectory case (Eq. 6.9) along with the terminator of Eq. 3.108 for the input depth. Compute the hierarchy for all levels k and memory term at the new time step using RK4

$$|\psi_{t+\Delta t}^{(k)}\rangle = |\psi_t^{(k)}\rangle + \frac{1}{6}(|\psi_1^{(k)}\rangle + 2|\psi_2^{(k)}\rangle + 2|\psi_3^{(k)}\rangle + |\psi_4^{(k)}\rangle)\Delta t, \tag{A.20}$$

$$h_{t+\Delta t} = h_t + \frac{1}{6}(h_1 + 2h_2 + 2h_3 + h_4)\Delta t. \tag{A.21}$$

8. Store the time propagated state trajectory, given by $|\psi^{(0)}_{t+\Delta t}\rangle$, and compute the density matrix and/or expectation values. For the un-normalised trajectory divide through by the norm $\|\psi^{(0)}_t\|^2$. For the normalised trajectory propagation no normalisation of expectation or density matrix is required.

9. If the total number of time steps is not met repeat from step 6

10. If the total number of stochastic iterations is not met repeat from step 4

11. **Completion**: Divide the sum total of trajectory expectation values and density matrix by the number of stochastic iterations providing the output results.

Appendix B

Further theory

B.1 Derivation of FCC for the differing curvature model

B.1.1 Zero displacement: $D = 0$

For the derivation of FC coefficients in the case of $D = 0$ and even n the explicit representation of the Hermite polynomial for even n [222]

$$H_n(q) = n! \sum_{l=0}^{\frac{n}{2}} \frac{(-1)^{\frac{n}{2}-l}}{(2l)!(\frac{n}{2}-l)!}(2q)^{2l} \tag{B.1}$$

is required. Substituting this expression into Eq. 4.70 gives

$$\begin{aligned}\langle \psi_g^{n=0} | \psi_e^n \rangle =& N_g N_n n! \sum_{l=0}^{\frac{n}{2}} \frac{(-1)^{\frac{n}{2}-l}}{(2l)!(\frac{n}{2}-l)!} \\ &\times \int_{-\infty}^{\infty} dq \, (2\sqrt{\alpha_e} q)^{2l} \exp\Big(-\alpha q^2 \Big).\end{aligned} \tag{B.2}$$

The integral in Eq. B.2 is a gaussian integral with a known result

$$\int_{-\infty}^{\infty} dq \, q^{2n} \exp\Big(-aq^2 \Big) = \frac{(2n-1)!!}{2^n a^n} \sqrt{\frac{\pi}{a}}, \tag{B.3}$$

where !! represents the double factorial, for which by definition $(-1)!! = 0!! = 1$. Substituting the solution to the integral gives

$$\begin{aligned}\langle \psi_g^{n=0} | \psi_e^n \rangle =& N_g N_n n! \sum_{l=0}^{\frac{n}{2}} \frac{(-1)^{\frac{n}{2}-l}}{(2l)!(\frac{n}{2}-l)!} \\ &\times (2\sqrt{\alpha_e})^{2l} \frac{(2l-1)!!}{2^l \alpha^l} \sqrt{\frac{\pi}{\alpha}}\end{aligned} \tag{B.4}$$

Further simplification can be achieved by using the following definition for the double factorial

$$(2n-1)!! = \frac{(2n)!}{2^n n!}. \tag{B.5}$$

Substituting this expression into Eq. B.4 and simplifying gives

$$\langle \psi_g^{n=0} | \psi_e^n \rangle = N_g N_n n! \sqrt{\frac{\pi}{\alpha}} \sum_{l=0}^{\frac{n}{2}} \frac{(-1)^{\frac{n}{2}-l}}{(l)!(\frac{n}{2}-l)!} \left(\frac{\alpha_e}{\alpha}\right)^l \tag{B.6}$$

By taking a factor of $(n/2)!$ out of the summation we can recast the equation in terms of a binomial coefficient

$$\langle \psi_g^{n=0} | \psi_e^n \rangle = N_g N_n \frac{n!}{(\frac{n}{2})!} \sqrt{\frac{\pi}{\alpha}} \sum_{l=0}^{\frac{n}{2}} \binom{\frac{n}{2}}{l} \left(\frac{\alpha_e}{\alpha}\right)^l. \tag{B.7}$$

The binomial formula

$$\sum_{k=0}^{n} \binom{n}{k} q^{n-k} y^k = (x+y)^n \tag{B.8}$$

is now used to further simplify the equation to give

$$\langle \psi_g^{n=0} | \psi_e^n \rangle = N_g N_n \frac{n!}{(\frac{n}{2})!} \sqrt{\frac{\pi}{\alpha}} \left(\frac{\alpha_e}{\alpha} - 1 \right)^{\frac{n}{2}}. \tag{B.9}$$

Substituting Eq. 4.65 and Eq. 4.68, simplifying, and taking the square absolute value provides the final expression for the FCC

$$|\langle \psi_g^{n=0} | \psi_e^n \rangle|^2 = \frac{n!}{2^n ((\frac{n}{2})!)^2} \frac{\sqrt{\alpha_e \alpha_g}}{\alpha} \left(1 - \frac{\alpha_e}{\alpha} \right)^n, \tag{B.10}$$

B.1.2 Non-zero displacement: $D \geq 0$

For the more general case of $D \geq 0$ and $\omega_g \neq \omega_e$ Eq. 4.75 can be recast into the form [184]

$$\begin{aligned} \langle \psi_g^{n=0} | \psi_e^n \rangle = & N_g N_n \exp\left(-\frac{A}{2} \right) \int_{-\infty}^{\infty} dq\, H_n(\sqrt{\alpha_e}(q-d)) \\ & \times \exp\left(-\frac{\alpha_g + \alpha_e}{2} \left(q - \frac{\alpha_e d}{\alpha_g + \alpha_e} \right)^2 \right), \end{aligned} \tag{B.11}$$

where

$$A = \frac{\alpha_g \alpha_e d^2}{\alpha_g + \alpha_e}. \tag{B.12}$$

Next let

$$y = q - \frac{\alpha_e d}{\alpha_g + \alpha_e}, \tag{B.13}$$

and substitute this expression into Eq. B.11 to give

$$\begin{aligned} \langle \psi_g^{n=0} | \psi_e^n \rangle = & N_g N_n \exp\left(-\frac{A}{2} \right) \int_{-\infty}^{\infty} dy\, H_n(\sqrt{\alpha_e} y + \beta) \\ & \times \exp\left(-\alpha y^2 \right), \end{aligned} \tag{B.14}$$

where

$$\alpha = \frac{\alpha_g + \alpha_e}{2}, \tag{B.15}$$

as before and

$$\beta = \frac{\alpha_g \sqrt{\alpha_e} d}{\alpha_g + \alpha_e}. \tag{B.16}$$

A Taylor expansion of the Hermite polynomial provides the useful property

$$H_n(x+y) = \sum_{k=0}^{n} H_k(\sqrt{\alpha_e}y)(2\beta)^{n-k}. \tag{B.17}$$

Using this property, for the Hermite polynomial in Eq. B.14, gives

$$\begin{aligned}\langle \psi_g^{n=0} | \psi_e^n \rangle =& N_g N_n \exp\left(-\frac{A}{2}\right) \sum_{k=0}^{n} (2\beta)^{n-k} \\ &\times \int_{-\infty}^{\infty} dy\, H_k(\sqrt{\alpha_e}y) \exp\left(-\alpha y^2\right),\end{aligned} \tag{B.18}$$

where the integral in the equation is of the same form as Eq. 4.70. Therefore, by using the result in Eq. B.9, of the derivation for the case of no displacement we obtain

$$\begin{aligned}\langle \psi_g^{n=0} | \psi_e^n \rangle =& N_g N_n \sqrt{\frac{\pi}{\alpha}} \exp\left(-\frac{A}{2}\right) \sum_{k=0}^{n} \binom{n}{k} (2\beta)^{n-k} \\ &\times \frac{k!}{(\frac{k}{2})!} \left(\frac{\alpha_e}{\alpha} - 1\right)^{k/2},\end{aligned} \tag{B.19}$$

for even k. For the purpose of clarity, we now replace k with $2l$ for $l \in \mathbb{N}_0$ to give,

$$\begin{aligned}\langle \psi_g^{n=0} | \psi_e^n \rangle =& N_g N_n \sqrt{\frac{\pi}{\alpha}} \exp\left(-\frac{A}{2}\right) \sum_{l=0}^{\lfloor n/2 \rfloor} \binom{n}{2l} (2\beta)^{n-2l} \\ &\times \frac{2l!}{(l)!} \left(\frac{\alpha_e}{\alpha} - 1\right)^{l},\end{aligned} \tag{B.20}$$

where the floor function of $n/2$ has been taken in the upper limit of the summation such that double counting does not occur, and to ensure that $2l$ represents an even number. Using the binomial coefficient formula, rearranging and simplifying, gives

$$\begin{aligned}\langle \psi_g^{n=0} | \psi_e^n \rangle =& N_g N_n \sqrt{\frac{\pi}{\alpha}} \exp\left(-\frac{A}{2}\right) \\ &\times n! \sum_{l=0}^{\lfloor n/2 \rfloor} \frac{(-1)^l}{l!(n-2l)!} (2\beta)^{n-2l} \left(1 - \frac{\alpha_e}{\alpha}\right)^{l},\end{aligned} \tag{B.21}$$

where the motivation for this form is discussed in Chapter 4. Firstly, we substitute for N_g and N_n, using Eq. 4.65 and Eq. 4.68,

$$\begin{aligned}\langle \psi_g^{n=0} | \psi_e^n \rangle =& \frac{1}{\sqrt{2^n n!}} \left(\frac{\sqrt{\alpha_e \alpha_g}}{\alpha}\right)^{1/2} \exp\left(-\frac{A}{2}\right) \\ &\times n! \sum_{l=0}^{\lfloor n/2 \rfloor} \frac{(-1)^l}{l!(n-2l)!} (2\beta)^{n-2l} \left(1 - \frac{\alpha_e}{\alpha}\right)^{l}.\end{aligned} \tag{B.22}$$

Thus, the Franck-Condon coefficients for the differing curvature model, that admits displacement, is given by

$$\begin{aligned}|\langle\psi_g^{n=0}|\psi_e^n\rangle|^2 =& \frac{1}{2^n n!}\frac{\sqrt{\alpha_e\alpha_g}}{\alpha}e^{-A} \\ &\times \left| n! \sum_{l=0}^{\lfloor n/2\rfloor} \frac{(-1)^l}{l!(n-2l)!}(2\beta)^{n-2l} \right. \\ &\times \left. \left(1-\frac{\alpha_e}{\alpha}\right)^l \right|^2 . \end{aligned} \tag{B.23}$$

Bibliography

[1] T. Madej, C. J. Lanczycki, D. Zhang, P. A. Thiessen, R. C. Geer et al., MMDB and VAST+: tracking structural similarities between macromolecular complexes, *Nucleic acids research* **42** (2014)

[2] O. A. Krohn, M. Quick, I. N. Ioffe, O. N. Mazaleva, D. Lenoir et al., Time-Resolved Photochemistry of Stiffened Stilbenes, *Journal of Physical Chemistry B* **123**, 4291 (2019)

[3] M. Quick, A. L. Dobryakov, M. Gerecke, C. Richter, F. Berndt et al., Photoisomerization dynamics and pathways of trans - And cis -azobenzene in solution from broadband femtosecond spectroscopies and calculations, *Journal of Physical Chemistry B* **118**, 8756 (2014)

[4] M. Quick, F. Berndt, A. L. Dobryakov, I. N. Ioffe, A. A. Granovsky et al., Photoisomerization dynamics of stiff-stilbene in solution, *Journal of Physical Chemistry B* **118**, 1389 (2014)

[5] D. A. Micha and I. Burghardt, *Quantum Dynamics of Complex Molecular Systems*, Springer-Verlag Berlin Heidelberg, 1st edition (2007)

[6] R. S. of Chemistry, *Quantum Effects in Complex Systems: Faraday Discussion 221*, Faraday Discussion, Royal Society of Chemistry (2020)

[7] A. Acín, I. Bloch, H. Buhrman, T. Calarco, C. Eichler et al., The quantum technologies roadmap: A European community view, *New Journal of Physics* **20**, 080201 (2018)

[8] T. Kumpulainen, B. Lang, A. Rosspeintner and E. Vauthey, Ultrafast Elementary Photochemical Processes of Organic Molecules in Liquid Solution, *Chemical Reviews* **117**, 10826 (2017)

[9] R. E. Blankenship, *Molecular Mechanisms of Photosynthesis*, Wiley (2002)

[10] S. Gozem, H. L. Luk, I. Schapiro and M. Olivucci, Theory and Simulation of the Ultrafast Double-Bond Isomerization of Biological Chromophores, *Chemical Reviews* **117**, 13502 (2017)

[11] P. J. Johnson, M. H. Farag, A. Halpin, T. Morizumi, V. I. Prokhorenko et al., The Primary Photochemistry of Vision Occurs at the Molecular Speed Limit, *Journal of Physical Chemistry B* **121**, 4040 (2017)

[12] K. Palczewski, Chemistry and biology of vision, *Journal of Biological Chemistry* **287**, 1612 (2012)

[13] L. Valkunas, D. Abramavicius and T. Mancal, *Molecular Excitation Dynamics and Relaxation*, Wiley-VCH (2013)

[14] A. O. Caldeira, *An Introduction to Macroscopic Quantum Phenomena and Quantum Dissipation*, Cambridge University Press (2014)

[15] M.-M. Russew and S. Hecht, Photoswitches: From Molecules to Materials, *Advanced Materials* **22**, 3348 (2010)

[16] W. Szymański, J. M. Beierle, H. A. Kistemaker, W. A. Velema and B. L. Feringa, Reversible photocontrol of biological systems by the incorporation of molecular photoswitches, *Chemical Reviews* **113**, 6114 (2013)

[17] Z. L. Pianowski, Recent Implementations of Molecular Photoswitches into Smart Materials and Biological Systems, *Chemistry - A European Journal* **25**, 5128 (2019)

[18] A. Goulet-Hanssens, F. Eisenreich and S. Hecht, Enlightening Materials with Photoswitches, *Advanced Materials* **32**, 1905966 (2020)

[19] W. R. Browne and B. L. Feringa, Making molecular machines work, *Nature Nanotechnology* **1**, 25 (2006)

[20] D. Dattler, G. Fuks, J. Heiser, E. Moulin, A. Perrot et al., Design of Collective Motions from Synthetic Molecular Switches, Rotors, and Motors, *Chemical Reviews* **120**, 310 (2020)

[21] D. Roke, S. J. Wezenberg and B. L. Feringa, Molecular rotary motors: Unidirectional motion around double bonds, *Proceedings of the National Academy of Sciences of the United States of America* **115**, 9423 (2018)

[22] P. Hänggi and F. Marchesoni, Artificial Brownian motors: Controlling transport on the nanoscale, *Reviews of Modern Physics* **81**, 387 (2009)

[23] A. Lennartson, A. Roffey and K. Moth-Poulsen, Designing photoswitches for molecular solar thermal energy storage, *Tetrahedron Letters* **56**, 1457 (2015)

[24] C.-L. Sun, C. Wang and R. Boulatov, Applications of Photoswitches in the Storage of Solar Energy, *ChemPhotoChem* **3**, 268 (2019)

[25] W. A. Velema, W. Szymanski and B. L. Feringa, Photopharmacology: Beyond proof of principle, *Journal of the American Chemical Society* **136**, 2178 (2014)

[26] I. Tochitsky, A. Polosukhina, V. E. Degtyar, N. Gallerani, C. M. Smith et al., Restoring visual function to blind mice with a photoswitch that exploits electrophysiological remodeling of retinal ganglion cells, *Neuron* **81**, 800 (2014)

[27] I. Tochitsky, J. Trautman, N. Gallerani, J. G. Malis and R. H. Kramer, Restoring visual function to the blind retina with a potent, safe and long-lasting photoswitch, *Scientific Reports* **7**, 1 (2017)

[28] I. Tochitsky, M. A. Kienzler, E. Isacoff and R. H. Kramer, Restoring Vision to the Blind with Chemical Photoswitches, *Chemical Reviews* **118**, 10748 (2018)

[29] R. N. Van Gelder, Photochemical approaches to vision restoration, *Vision Research* **111**, 134 (2015)

[30] T. C. Berkelbach and M. Thoss, Special topic on dynamics of open quantum systems, *The Journal of Chemical Physics* **152**, 020401 (2020)

[31] D. V. Shalashilin and M. S. Child, Time dependent quantum propagation in phase space, *Journal of Chemical Physics* **113**, 10028 (2000)

[32] D. V. Shalashilin and M. S. Child, The phase space CCS approach to quantum and semiclassical molecular dynamics for high-dimensional systems, *Chemical Physics* **304**, 103 (2004)

[33] D. V. Shalashilin, Quantum mechanics with the basis set guided by Ehrenfest trajectories: Theory and application to spin-boson model, *Journal of Chemical Physics* **130**, 244101 (2009)

[34] D. V. Shalashilin, Nonadiabatic dynamics with the help of multiconfigurational Ehrenfest method: Improved theory and fully quantum 24D simulation of pyrazine, *Journal of Chemical Physics* **132**, 244111 (2010)

[35] D. V. Shalashilin, Multiconfigurational Ehrenfest approach to quantum coherent dynamics in large molecular systems, *Faraday Discussions* **153**, 105 (2011)

[36] D. V. Makhov, C. Symonds, S. Fernandez-Alberti and D. V. Shalashilin, Ab initio quantum direct dynamics simulations of ultrafast photochemistry with Multiconfigurational Ehrenfest approach, *Chemical Physics* **493**, 200 (2017)

[37] O. Bramley, C. Symonds and D. V. Shalashilin, Quantum system-bath dynamics with quantum superposition sampling and coupled generalized coherent states, *Journal of Chemical Physics* **151**, 064103 (2019)

[38] J. A. Green, A. Grigolo, M. Ronto and D. V. Shalashilin, A two-layer approach to the coupled coherent states method, *Journal of Chemical Physics* **144**, 024111 (2016)

[39] J. A. Green and D. V. Shalashilin, Simulation of the quantum dynamics of indistinguishable bosons with the method of coupled coherent states, *Physical Review A* **100**, 013607 (2019)

[40] A. Grigolo, T. F. Viscondi and M. A. De Aguiar, Multiconfigurational quantum propagation with trajectory-guided generalized coherent states, *Journal of Chemical Physics* **144**, 094106 (2016)

[41] H.-P. Breuer and F. Petruccione, *The Theory of Open Quantum Systems*, OUP, Oxford (2007)

[42] Á. Rivas and S. F. Huelga, *Open Quantum Systems An Introduction*, Springer-Verlag Berlin Heidelberg, 1st edition (2012)

[43] K. H. Hughes, *Dynamics of Open Quantum Systems*, Collaborative Computational Project on Molecular Quantum Dynamics (CCP6) (2006)

[44] C. W. Gardiner and P. Zoller, *Quantum Noise A Handbook of Markovian and Non-Markovian Quantum Stochastic Methods with Applications to Quantum Optics*, Springer-Verlag Berlin Heidelberg, 3rd edition (2004)

[45] A. Barchielli and M. Gregoratti, *Quantum Trajectories and Measurements in Continuous Time*, Springer-Verlag Berlin Heidelberg (2009)

[46] I. De Vega and D. Alonso, Dynamics of non-Markovian open quantum systems, *Reviews of Modern Physics* **89**, 015001 (2017)

[47] H.-P. Breuer, E.-M. Laine, J. Piilo and B. Vacchini, Colloquium: Non-Markovian dynamics in open quantum systems, *Reviews of Modern Physics* **88**, 021002 (2016)

[48] H. P. Breuer, Foundations and measures of quantum non-Markovianity, *Journal of Physics B: Atomic, Molecular and Optical Physics* **45**, 154001 (2012)

[49] A. Strathearn, P. Kirton, D. Kilda, J. Keeling and B. W. Lovett, Efficient non-Markovian quantum dynamics using time-evolving matrix product operators, *Nature Communications* **9**, 1 (2018)

[50] D. Gribben, A. Strathearn, J. Iles-Smith, D. Kilda, A. Nazir et al., Exact quantum dynamics in structured environments, *Phys. Rev. Research* **2**, 13265 (2020)

[51] Y. Tanimura and R. Kubo, Time Evolution of a Quantum System in Contact with a Nearly Gaussian-Markoffian Noise Bath, *Journal of the Physical Society of Japan* **58**, 101 (1989)

[52] Y. Tanimura, Stochastic Liouville, Langevin, Fokker-Planck, and master equation approaches to quantum dissipative systems, *Journal of the Physical Society of Japan* **75** (2006)

[53] Y. Tanimura, Numerically "exact" approach to open quantum dynamics: The hierarchical equations of motion (HEOM), *The Journal of Chemical Physics* **153**, 020901 (2020)

[54] A. G. Dijkstra and A. Beige, Efficient long-distance energy transport in molecular systems through adiabatic passage, *Journal of Chemical Physics* **151**, 034114 (2019)

[55] I. S. Dunn, R. Tempelaar and D. R. Reichman, Removing instabilities in the hierarchical equations of motion: Exact and approximate projection approaches, *Journal of Chemical Physics* **150**, 184109 (2019)

[56] H. Rahman and U. Kleinekathöfer, Chebyshev hierarchical equations of motion for systems with arbitrary spectral densities and temperatures, *Journal of Chemical Physics* **150**, 244104 (2019)

[57] L. Chen, M. F. Gelin and W. Domcke, Orientational relaxation of a quantum linear rotor in a dissipative environment: Simulations with the hierarchical equations-of-motion method, *Journal of Chemical Physics* **151**, 034101 (2019)

[58] C. Schinabeck, A. Erpenbeck, R. Härtle and M. Thoss, Hierarchical quantum master equation approach to electronic-vibrational coupling in nonequilibrium transport through nanosystems, *Physical Review B* **94**, 201407 (2016)

[59] D. Suess, A. Eisfeld and W. T. Strunz, Hierarchy of stochastic pure states for open quantum system dynamics, *Physical Review Letters* **113**, 150403 (2014)

[60] R. Hartmann and W. T. Strunz, Exact open quantum system dynamics using the hierarchy of pure states (HOPS), *Journal of Chemical Theory and Computation* **13**, 5834 (2017)

[61] R. Hartmann, M. Werther, F. Grossmann and W. T. Strunz, Exact open quantum system dynamics: Optimal frequency vs time representation of bath correlations, *Journal of Chemical Physics* **150**, 234105 (2019)

[62] P. P. Zhang, C. D. Bentley and A. Eisfeld, Flexible scheme to truncate the hierarchy of pure states, *Journal of Chemical Physics* **148**, 134103 (2018)

[63] L. Diósi, Exact semiclassical wave equation for stochastic quantum optics, *Quantum Semiclass. Opt.* **8**, 309 (1996)

[64] L. Diosi and W. T. Strunz, The non-Markovian stochastic Schrijdinger equation for open systems, *Physics Letters A* **235**, 569 (1997)

[65] L. Diosi, N. Gisin, W. T. Strunz and L. Dio, Non-Markovian quantum state diffusion, *Physical Review A* **58**, 1699 (1998)

[66] W. T. Strunz, Linear quantum state diffusion for non-Markovian open quantum systems, *Physics Letters A* **224**, 25 (1996)

[67] T. Yu, Non-Markovian quantum trajectories versus master equations: Finite-temperature heat bath, *Physical Review A* (2004)

[68] S. Mukamel, *Principles of Nonlinear Optical Spectroscopy*, Oxford University Press (1995)

[69] J. Yuen-Zhou, J. J. Krich, I. Kassal, A. S. Johnson and A. Aspuru-Guzik, *Ultrafast Spectroscopy*, IOP Publishing (2014)

[70] N. Lambert, Y. N. Chen, Y. C. Cheng, C. M. Li, G. Y. Chen et al., Quantum biology, *Nature Physics* **9**, 10 (2013)

[71] G. D. Scholes, G. R. Fleming, L. X. Chen, A. Aspuru-Guzik, A. Buchleitner et al., Using coherence to enhance function in chemical and biophysical systems, *Nature* **543**, 647 (2017)

[72] A. Marais, B. Adams, A. K. Ringsmuth, M. Ferretti, J. M. Gruber et al., The future of quantum biology, *Journal of the Royal Society Interface* **15** (2018)

[73] Y. Kim, F. Bertagna, E. M. D'Souza, D. J. Heyes, L. O. Johannissen et al., Quantum biology: An update and perspective, *Quantum Reports* **3**, 80 (2021)

[74] J. Al-Khalili and J. McFadden, *Life on the Edge: The Coming of Age of Quantum Biology* (2014)

[75] K. Schulten, H. Staerk, A. Weller, H. J. Werner and B. Nickel, Magnetic field dependence of the geminate recombination of radical ion pairs in polar solvents, *Zeitschrift fur Physikalische Chemie* **101**, 371 (1976)

[76] R. Haberkorn, Density matrix description of spin-selective radical pair reactions, *Molecular Physics* **32**, 1491 (1976)

[77] M. Tiersch, U. E. Steiner, S. Popescu and H. J. Briegel, Open quantum system approach to the modeling of spin recombination reactions, *Journal of Physical Chemistry A* **116**, 4020 (2012)

[78] H. G. Hiscock, S. Worster, D. R. Kattnig, C. Steers, Y. Jin et al., The quantum needle of the avian magnetic compass, *Proceedings of the National Academy of Sciences of the United States of America* **113**, 4634 (2016)

[79] D. R. Kattnig, J. K. Sowa, I. A. Solov'Yov and P. J. Hore, Electron spin relaxation can enhance the performance of a cryptochrome-based magnetic compass sensor, *New Journal of Physics* **18**, 063007 (2016)

[80] B. Adams, I. Sinayskiy and F. Petruccione, An open quantum system approach to the radical pair mechanism, *Scientific Reports* **8**, 1 (2018)

[81] R. H. Keens and D. R. Kattnig, Monte-Carlo wavefunction approach for the spin dynamics of recombining radicals, *New Journal of Physics* **22**, 83064 (2020)

[82] G. S. Engel, T. R. Calhoun, E. L. Read, T.-K. Ahn, T. Mancal et al., Evidence for wavelike energy transfer through quantum coherence in photosynthetic systems., *Nature* **446**, 782 (2007)

[83] F. Caruso, A. W. Chin, A. Datta, S. F. Huelga and M. B. Plenio, Highly efficient energy excitation transfer in light-harvesting complexes: The fundamental role of noise-assisted transport, *The Journal of Chemical Physics* **131**, 105106 (2009)

[84] E. Collini, C. Y. Wong, K. E. Wilk, P. M. Curmi, P. Brumer et al., Coherently wired light-harvesting in photosynthetic marine algae at ambient temperature, *Nature* **463**, 644 (2010)

[85] G. Panitchayangkoon, D. V. Voronine, D. Abramavicius, J. R. Caram, N. H. Lewis et al., Direct evidence of quantum transport in photosynthetic light-harvesting complexes, *Proceedings of the National Academy of Sciences of the United States of America* **108**, 20908 (2011)

[86] E. Romero, R. Augulis, V. I. Novoderezhkin, M. Ferretti, J. Thieme et al., Quantum coherence in photosynthesis for efficient solar-energy conversion, *Nature Physics* **10**, 676 (2014)

[87] J. Iles-Smith, A. G. Dijkstra, N. Lambert and A. Nazir, Energy transfer in structured and unstructured environments: Master equations beyond the Born-Markov approximations, *Journal of Chemical Physics* **144**, 044110 (2016)

[88] J. Cao, R. J. Cogdell, D. F. Coker, H. G. Duan, J. Hauer et al., Quantum biology revisited, *Science Advances* **6**, eaaz4888 (2020)

[89] J. S. Higgins, L. T. Lloyd, S. H. Sohail, M. A. Allodi, J. P. Otto et al., Photosynthesis tunes quantum-mechanical mixing of electronic and vibrational states to steer exciton energy transfer, *Proceedings of the National Academy of Sciences* **118**, e2018240118 (2021)

[90] S. Hahn and G. Stock, Quantum-Mechanical Modeling of the Femtosecond Isomerization in Rhodopsin, *Journal of Physical Chemistry B* **104**, 1146 (2000)

[91] S. Hahn and G. Stock, Ultrafast cis-trans photoswitching: A model study, *The Journal of Chemical Physics* **116**, 1085 (2002)

[92] M. Abe, Y. Ohtsuki, Y. Fujimura and W. Domcke, Optimal control of ultrafast cis-trans photoisomerization of retinal in rhodopsin via a conical intersection, *Journal of Chemical Physics* **123** (2005)

[93] M. Mohseni, Y. Omar, G. S. Engel and M. B. Plenio, *Quantum effects in biology*, Cambridge University Press (2014)

[94] P. J. Johnson, A. Halpin, T. Morizumi, V. I. Prokhorenko, O. P. Ernst et al., Local vibrational coherences drive the primary photochemistry of vision, *Nature Chemistry* **7**, 980 (2015)

[95] D. Polli, P. Altoè, O. Weingart, K. M. Spillane, C. Manzoni et al., Conical intersection dynamics of the primary photoisomerization event in vision, *Nature* **467**, 440 (2010)

[96] T. V. Tscherbul and P. Brumer, Quantum coherence effects in natural light-induced processes: Cis-trans photoisomerization of model retinal under incoherent excitation, *Physical Chemistry Chemical Physics* **17**, 30904 (2015)

[97] N. Yunger Halpern and D. T. Limmer, Fundamental limitations on photoisomerization from thermodynamic resource theories, *Physical Review A* **101**, 042116 (2020)

[98] L. D. Landau and E. Lifshitz, *Mechanics*, Butterworth-Heinemann, 3rd edition (1982)

[99] C. Lanczos, *The Variational Principles of Mechanics*, Dover Publications Inc., 4th edition (1986)

[100] V. Arnol'd, *Mathematical Methods of Classical Mechanics*, Springer, 4th edition (1997)

[101] D. T. Greenwood, *Classical Dynamics*, Dover Publications Inc., new edition (2003)

[102] H. Goldstein, *Classical Mechanics*, Pearson, 3rd edition (2013)

[103] H. Young and R. Freedman, *University Physics with Modern Physics*, Pearson, 15th edition (2019)

[104] I. Gelfand and S. Fomin, *Calculus of Variations*, Dover Publications Inc. (2003)

[105] R. Weinstock, *Calculus of Variations With Applications to Physics and Engineering*, Weinstock Press (2007)

[106] F. B. Hildebrand, *Methods of Applied Mathematics*, Dover Publications Inc. (1992)

[107] N. Van Kampen, *Stochastic Processes in Physics and Chemistry*, North Holland, 3rd edition (2007)

[108] C. Gardiner, *Stochastic Methods: A Handbook for the Natural and Social Sciences*, Springer-Verlag Berlin Heidelberg, 4th edition (2009)

[109] P. E. Kloeden and E. Platen, *Numerical Solution of Stochastic Differential Equations*, Springer-Verlag Berlin Heidelberg (1992)

[110] D. H. Waldeck, Photoisomerization Dynamics of Stilbenes, *Chemical Reviews* **91**, 415 (1991)

[111] H. A. Kramers, Brownian motion in a field of force and the diffusion model of chemical reactions, *Physica* **7**, 284 (1940)

[112] G. Rothenberger, D. K. Negus and R. M. Hochstrasser, Solvent influence on photoisomerization dynamics, *J. Chem. Phys* **79**, 5360 (1983)

[113] R. F. Grote and J. T. Hynes, The stable states picture of chemical reactions. II. Rate constants for condensed and gas phase reaction models, *The Journal of Chemical Physics* **73**, 2715 (1980)

[114] R. F. Grote and J. T. Hynes, Reactive modes in condensed phase reactions, *The Journal of Chemical Physics* **74**, 4465 (1981)

[115] M. S. Green, Markoff random processes and the statistical mechanics of time-dependent phenomena, *The Journal of Chemical Physics* **20**, 1281 (1952)

[116] R. Kubo, The fluctuation-dissipation theorem, *Reports on Progress in Physics* **29**, 255 (1966)

[117] D. J. Griffiths, *Introduction to Quantum Mechanics*, Cambridge University Press, 3rd edition (2018)

[118] A. Phillips, *Introduction to Quantum Mechanics*, Wiley, 1st edition (2003)

[119] P. W. Atkins and R. S. Friedman, *Molecular Quantum Mechanics*, OUP Oxford, 5th edition (2010)

[120] D. J. Tannor, *Introduction to Quantum Mechanics: a time-dependent perspective*, University Science Books, 1st edition (2008)

[121] A. I. Rae and J. Napolitano, *Quantum Mechanics*, Routledge, 6th edition (2015)

[122] M. A. Nielsen and I. L. Chuang, *Quantum Computation and Quantum Information*, Cambridge University Press, 10th edition (2010)

[123] H. D. Meyer, U. Manthe and L. S. Cederbaum, The multi-configurational time-dependent Hartree approach, *Chemical Physics Letters* **165**, 73 (1990)

[124] U. Manthe, H. D. Meyer and L. S. Cederbaum, Wave-packet dynamics within the multiconfiguration Hartree framework: General aspects and application to NOCl, *The Journal of Chemical Physics* **97**, 3199 (1992)

[125] W. Haobin and M. Thoss, Quantum dynamical simulation of electron-transfer reactions in an anharmonic environment, *Journal of Physical Chemistry A* **111**, 10369 (2007)

[126] H. D. Meyer, F. Gatti and G. A. Worth, *Multidimensional Quantum Dynamics*, Wiley (2009)

[127] A. W. Chin, Á. Rivas, S. F. Huelga and M. B. Plenio, Exact mapping between system-reservoir quantum models and semi-infinite discrete chains using orthogonal polynomials, *Journal of Mathematical Physics* **51**, 092109 (2010)

[128] J. Prior, A. W. Chin, S. F. Huelga and M. B. Plenio, Efficient simulation of strong system-environment interactions, *Physical Review Letters* **105**, 050404 (2010)

[129] R. Rosenbach, J. Cerrillo, S. F. Huelga, J. Cao and M. B. Plenio, Efficient simulation of non-Markovian system-environment interaction, *New Journal of Physics* **18**, 23035 (2016)

[130] A. Tokmakoff, Time-Dependent Quantum Mechanics and Spectroscopy (2014)

[131] A. Streltsov, G. Adesso and M. B. Plenio, Colloquium: Quantum coherence as a resource, *Reviews of Modern Physics* **89** (2017)

[132] M. Toda, R. Kubo and N. Saito, *Statistical Physics I*, Springer-Verlag Berlin Heidelberg, 2nd edition (1992)

[133] W. Greiner, L. Neise and H. Stöcker, *Thermodynamics and Statistical Mechanics*, Springer-Verlag New York (1995)

[134] M. Glazer and J. Wark, *Statistical Mechanics: A Survival Guide*, Oxford University Press (2001)

[135] T. Guenault, *Statistical Physics*, Springer, revised edition (2007)

[136] S. J. Blundell and K. M. Blundell, *Concepts in Thermal Physics*, Oxford University Press, 2nd edition (2009)

[137] Y. Takahashi and H. Umezawa, Thermo field dynamics, *International Journal of Modern Physics B* **10**, 1755 (1996)

[138] G. Harsha, T. M. Henderson and G. E. Scuseria, Thermofield theory for finite-temperature quantum chemistry, *Journal of Chemical Physics* **150**, 154109 (2019)

[139] P. Shushkov and T. F. Miller, Real-time density-matrix coupled-cluster approach for closed and open systems at finite temperature, *Journal of Chemical Physics* **151**, 134107 (2019)

[140] S. M. Barnett, A. Beige, A. Ekert, B. M. Garraway, C. H. Keitel et al., Journeys from quantum optics to quantum technology, *Progress in Quantum Electronics* **54**, 19 (2017)

[141] S. Mukamel, Non-markovian theory of molecular relaxation. I. Vibrational relaxation and dephasing in condensed phases, *Chemical Physics* **37**, 33 (1979)

[142] J. Bretn, A. Hardisson, F. Mauricio and S. Velasco, Relaxation of quantum systems weakly coupled to a bath. I. Total-time-ordering-cumulant and partial-time-ordering-cumulant non-Markovian theories, *Physical Review A* **30**, 542 (1984)

[143] J. Bretn, A. Hardisson, F. Mauricio and S. Velasco, Relaxation of quantum systems weakly coupled to a bath. II. Formal analysis of the total-time-ordering-cumulant and partial-time-ordering-cumulant spectral line shapes, *Physical Review A* **30**, 553 (1984)

[144] K. Song, L. Song and Q. Shi, An alternative realization of the exact non-Markovian stochastic Schrödinger equation, *Journal of Chemical Physics* **144**, 224105 (2016)

[145] Y. Ke and Y. Zhao, Hierarchy of forward-backward stochastic Schrödinger equation, *The Journal of Chemical Physics* **145**, 024101 (2016)

[146] K. Nakamura and Y. Tanimura, Hierarchical Schrödinger equations of motion for open quantum dynamics, *Physical Review A* **98**, 012109 (2018)

[147] C. W. Gardiner, A. S. Parkins and P. Zoller, Wave-function quantum stochastic differential equations and quantum-jump simulation methods, *Physical Review A* **46**, 4363 (1992)

[148] I. Semina, V. Semin, F. Petruccione and A. Barchielli, Stochastic schrödinger equations for markovian and non-markovian cases, *Open Systems and Information Dynamics* **21**, 1440008 (2014)

[149] M. B. Plenio and P. L. Knight, The quantum-jump approach to dissipative dynamics in quantum optics, *Reviews of Modern Physics* **70**, 101 (1998)

[150] N. Gisin and I. C. Percival, The quantum-state diffusion model applied to open systems, *Journal of Physics A* **25**, 5677 (1992)

[151] N. Gisin and I. C. Percival, The quantum state diffusion picture of physical processes, *Journal of Physics A* **26**, 2245 (1993)

[152] Ian Percival, *Quantum State Diffusion*, Cambridge University Press, Cambridge (1998)

[153] T. Ikeda and Y. Tanimura, Low-Temperature Quantum Fokker-Planck and Smoluchowski Equations and Their Extension to Multistate Systems, *Journal of Chemical Theory and Computation* **15**, 2517 (2019)

[154] R. Kosloff, M. A. Ratner and W. B. Davis, Dynamics and relaxation in interacting systems: Semigroup methods, *The Journal of Chemical Physics* **106**, 7036 (1997)

[155] J. R. Johansson, P. D. Nation and F. Nori, QuTiP 2: A Python framework for the dynamics of open quantum systems, *Computer Physics Communications* **184**, 1234 (2013)

[156] L. Diósi and W. T. Strunz, The non-Markovian stochastic Schrödinger equation for open systems, *Physics Letters, Section A: General, Atomic and Solid State Physics* **235**, 569 (1997)

[157] D. Suess, Hierarchy of Quantum Trajectories applied to Photosynthetic Complexes, Technical report, Dresden University of Technology (2013)

[158] C. Meier and D. J. Tannor, Non-Markovian evolution of the density operator in the presence of strong laser fields, *Journal of Chemical Physics* **111**, 3365 (1999)

[159] G. Ritschel and A. Eisfeld, Analytic representations of bath correlation functions for ohmic and superohmic spectral densities using simple poles, *The Journal of Chemical Physics* **141**, 094101 (2014)

[160] R. P. Feynman and F. L. Vernon, The theory of a general quantum system interacting with a linear dissipative system, *Annals of Physics* **281**, 547 (2000)

[161] G. D. Scholes and G. R. Fleming, On the Mechanism of Light Harvesting in Photosynthetic Purple Bacteria: B800 to B850 Energy Transfer, *Journal of Physical Chemistry B* **104**, 1854 (2000)

[162] J. Meldaikis, O. Zerlauskiene, D. Abramavicius and L. Valkunas, Manifestation of protein conformations in the B850 absorption band of light-harvesting complex LH2, *Chemical Physics* **423**, 9 (2013)

[163] O. Rancova and D. Abramavicius, Static and dynamic disorder in bacterial light-harvesting complex LH2: A 2DES simulation study, *Journal of Physical Chemistry B* **118**, 7533 (2014)

[164] R. J. Le Roy, Y. Huang and C. Jary, An accurate analytic potential function for ground-state N2 from a direct-potential-fit analysis of spectroscopic data, *The Journal of Chemical Physics* **125**, 164310 (2006)

[165] P. Földi, A. Czirják, B. Molnár and M. G. Benedict, Formation of Schrödinger-cat states in the Morse potential: Wigner function picture, *Optics Express* **10**, 376 (2002)

[166] I. S. Osad'ko, Determination of electron-phonon coupling from structured optical spectra of impurity centers, *Soviet Physics Uspekhi* **22**, 311 (1979)

[167] J. L. Skinner and D. Hsu, Pure dephasing of a two-level system, *Journal of Physical Chemistry* **90**, 4931 (1986)

[168] K. Okumura and Y. Tanimura, Femtosecond two-dimensional spectroscopy from anharmonic vibrational modes of molecules in the condensed phase, *The Journal of Chemical Physics* **107**, 2267 (1997)

[169] Y. Tanimura and Y. Maruyama, Gaussian-Markovian quantum Fokker-Planck approach to nonlinear spectroscopy of a displaced Morse potentials system: Dissociation, predissociation, and optical Stark effects, *The Journal of Chemical Physics* **107**, 1779 (1997)

[170] A. Anda, L. De Vico, T. Hansen and D. Abramavičius, Absorption and Fluorescence Lineshape Theory for Polynomial Potentials, *Journal of Chemical Theory and Computation* **12**, 5979 (2016)

[171] A. Anda, D. Abramavičius and T. Hansen, Two-dimensional electronic spectroscopy of anharmonic molecular potentials, *Physical Chemistry Chemical Physics* **20**, 1642 (2018)

[172] A. F. Fidler and G. S. Engel, Nonlinear spectroscopic theory of displaced harmonic oscillators with differing curvatures: A correlation function approach, *Journal of Physical Chemistry A* **117**, 9444 (2013)

[173] M. Maiuri, M. Garavelli and G. Cerullo, Ultrafast Spectroscopy: State of the Art and Open Challenges, *Journal of the American Chemical Society* **142**, 3 (2020)

[174] J. Yuen-Zhou, J. J. Krich, M. Mohseni and A. Aspuru-Guzik, Quantum State and Process Tomography of Energy Transfer Systems Via Ultrafast Spectroscopy, *Proceedings of the National Academy of Sciences* **108**, 17615 (2011)

[175] J. D. Hybl, A. W. Albrecht, S. M. G. Faeder and D. M. Jonas, Two-dimensional electronic spectroscopy, *Chemical Physics Letters* **297**, 307 (1998)

[176] M. H. Farag, B. J. Hoenders, J. Knoester and T. L. C. Jansen, Spectral line shapes in linear absorption and two-dimensional spectroscopy with skewed frequency distributions, *The Journal of Chemical Physics* **146**, 234201 (2017)

[177] A. Galestian Pour, C. N. Lincoln, V. Perlík, F. Šanda and J. Hauer, Anharmonic vibrational effects in linear and two-dimensional electronic spectra, *Physical Chemistry Chemical Physics* **19**, 24752 (2017)

[178] L. J. G. W. van Wilderen, A. T. Messmer and J. Bredenbeck, Mixed IR/Vis Two-Dimensional Spectroscopy: Chemical Exchange beyond the Vibrational Lifetime and Sub-ensemble Selective Photochemistry, *Angewandte Chemie International Edition* **53**, 2667 (2014)

[179] J. von Cosel, J. Cerezo, D. Kern-Michler, C. Neumann, L. J. G. W. van Wilderen et al., Vibrationally resolved electronic spectra including vibrational pre-excitation: Theory and application to VIPER spectroscopy, *The Journal of Chemical Physics* **147**, 164116 (2017)

[180] J. W. Riley, B. Wang, J. L. Woodhouse, M. Assmann, G. A. Worth et al., Unravelling the Role of an Aqueous Environment on the Electronic Structure and Ionization of Phenol Using Photoelectron Spectroscopy, *Journal of Physical Chemistry Letters* **9**, 678 (2018)

[181] L. D. Smith and A. G. Dijkstra, Quantum dissipative systems beyond the standard harmonic model: Features of linear absorption and dynamics, *Journal of Chemical Physics* **151**, 164109 (2019)

[182] T. Ikeda, A. G. Dijkstra and Y. Tanimura, Modeling and analyzing a photo-driven molecular motor system: Ratchet dynamics and non-linear optical spectra, *The Journal of Chemical Physics* **150**, 114103 (2019)

[183] Y. Tanimura and S. Mukamel, Multistate quantum Fokker-Planck approach to nonadiabatic wave packet dynamics in pump-probe spectroscopy, *The Journal of Chemical Physics* **101**, 3049 (1994)

[184] J. L. Chang, A new formula to calculate Franck-Condon factors for displaced and distorted harmonic oscillators, *Journal of Molecular Spectroscopy* **232**, 102 (2005)

[185] P. Földi, M. Benedict, A. Czirják and B. Molnár, Wave packet motion and decoherence in an anharmonic potential, *Fortschritte der Physik* **51**, 122 (2003)

[186] P. Földi, M. G. Benedict, A. Czirják and B. Molnár, Decoherence of wave packets in an anharmonic oscillator, *Physical Review A* **67**, 32104 (2003)

[187] D. M. Packwood and Y. Tanimura, Non-Gaussian stochastic dynamics of spins and oscillators: A continuous-time random walk approach, *Physical Review E* **84**, 061111 (2011)

[188] T. L. C. Jansen and J. Knoester, Calculation of two-dimensional infrared spectra of ultrafast chemical exchange with numerical Langevin simulations, *The Journal of Chemical Physics* **127**, 234502 (2007)

[189] C. Olbrich, T. L. Jansen, J. Liebers, M. Aghtar, J. Strümpfer et al., From atomistic modeling to excitation transfer and two-dimensional spectra of the FMO light-harvesting complex, *Journal of Physical Chemistry B* **115**, 8609 (2011)

[190] K. Kwac, H. Lee and M. Cho, Non-Gaussian statistics of amide I mode frequency fluctuation of N-methylacetamide in methanol solution: Linear and nonlinear vibrational spectra, *The Journal of Chemical Physics* **120**, 1477 (2004)

[191] S. Garrett-Roe and P. Hamm, Three-point frequency fluctuation correlation functions of the OH stretch in liquid water, *Journal of Chemical Physics* **128**, 104507 (2008)

[192] C.-Y. Hsieh and J. Cao, A unified stochastic formulation of dissipative quantum dynamics. I. Generalized hierarchical equations, *The Journal of Chemical Physics* **148**, 14103 (2018)

[193] A. J. Schile and D. T. Limmer, Studying rare nonadiabatic dynamics with transition path sampling quantum jump trajectories, *The Journal of Chemical Physics* **149**, 214109 (2018)

[194] A. J. Schile and D. T. Limmer, Simulating conical intersection dynamics in the condensed phase with hybrid quantum master equations, *The Journal of Chemical Physics* **151**, 14106 (2019)

[195] J. Shao, Decoupling quantum dissipation interaction via stochastic fields, *The Journal of Chemical Physics* **120**, 5053 (2004)

[196] J. A. Green, D. V. Makhov, N. C. Cole-Filipiak, C. Symonds, V. G. Stavros et al., Ultrafast photodissociation dynamics of 2-ethylpyrrole: adding insight to experiment with ab initio multiple cloning, *Physical Chemistry Chemical Physics* **21**, 3832 (2019)

[197] T. L. C. Jansen and S. Mukamel, Semiclassical mode-coupling factorizations of coherent nonlinear optical response, *The Journal of Chemical Physics* **119**, 7979 (2003)

[198] R. F. Loring, Mean-trajectory approximation for electronic and vibrational-electronic nonlinear spectroscopy, *The Journal of Chemical Physics* **146**, 144106 (2017)

[199] M. Micciarelli, R. Conte, J. Suarez and M. Ceotto, Anharmonic vibrational eigenfunctions and infrared spectra from semiclassical molecular dynamics, *The Journal of Chemical Physics* **149**, 64115 (2018)

[200] H. M. Hulburt and J. O. Hirschfelder, Potential energy functions for diatomic molecules, *The Journal of Chemical Physics* **9**, 61 (1941)

[201] K. Huber, *Molecular Spectra and Molecular Structure*, Springer US (1979)

[202] Y. Tanimura and K. Okumura, First-, third-, and fifth-order resonant spectroscopy of an anharmonic displaced oscillators system in the condensed phase, *The Journal of Chemical Physics* **106**, 2078 (1997)

[203] S.-H. Dong, R. Lemus and A. Frank, Ladder operators for the Morse potential, *International Journal of Quantum Chemistry* **86**, 433 (2002)

[204] T. Ikeda and Y. Tanimura, Probing photoisomerization processes by means of multi-dimensional electronic spectroscopy: The multi-state quantum hierarchical Fokker-Planck equation approach, *The Journal of Chemical Physics* **147**, 014102 (2017)

[205] R. Improta and F. Santoro, Excited-state behavior of trans and cis isomers of stilbene and stiff stilbene: A TD-DFT study, *Journal of Physical Chemistry A* **109**, 10058 (2005)

[206] S. A. Kovalenko and A. L. Dobryakov, On the excitation wavelength dependence and Arrhenius behavior of stilbene isomerization rates in solution, *Chemical Physics Letters* **570**, 56 (2013)

[207] A. M. Pupasov-Maksimov, Analytical simulations of double-well, triple-well and multi-well dynamics via rationally extended Harmonic oscillator, *Journal of Physics: Conference Series* **670**, 012042 (2016)

[208] G. Spaventa, S. F. Huelga and M. B. Plenio, Non-Markovianity boosts the efficiency of bio-molecular switches (2021)

[209] A. J. Leggett, S. Chakravarty, A. T. Dorsey, M. P. Fisher, A. Garg et al., Dynamics of the dissipative two-state system, *Reviews of Modern Physics* **59**, 1 (1987)

[210] A. O. Caldeira and A. J. Leggett, Path integral approach to quantum Brownian motion, *Physica A: Statistical Mechanics and its Applications* **121**, 587 (1983)

[211] L. Ferialdi, Dissipation in the Caldeira-Leggett model, *Phys. Rev. A* **95**, 52109 (2017)

[212] G. Ritschel, D. Suess, S. Möbius, W. T. Strunz and A. Eisfeld, Non-markovian quantum state diffusion for temperature-dependent linear spectra of light harvesting aggregates, *The Journal of Chemical Physics* **142**, 034115 (2015)

[213] A. G. Dijkstra and V. I. Prokhorenko, Simulation of photo-excited adenine in water with a hierarchy of equations of motion approach, *The Journal of Chemical Physics* **147**, 64102 (2017)

[214] P. P. Zhang, Z. Z. Li and A. Eisfeld, Hierarchy of equations to calculate the linear spectra of molecular aggregates: Time-dependent and frequency domain formulation, *International Journal of Quantum Chemistry* **117**, e25386 (2017)

[215] A. Z. Szarka, N. Pugliano, D. K. Palit and R. M. Hochstrasser, Vibrational coherence in the solution phase photoisomerization reaction of cis-stilbene, *Chemical Physics Letters* **240**, 25 (1995)

[216] D. Green, B. S. Humphries, A. G. Dijkstra and G. A. Jones, Quantifying non-Markovianity in underdamped versus overdamped environments and its effect on spectral lineshape, *The Journal of Chemical Physics* **151**, 174112 (2019)

[217] D. Green, *Modelling Ultrafast Two-Dimensional Spectroscopy of Vibronic Systems using non-Markovian Hierarchical Equations of Motion*, Ph.D. thesis, University of East Anglia (2020)

[218] M. D. Feit, J. A. Fleck and A. Steiger, Solution of the Schrödinger equation by a spectral method, *Journal of Computational Physics* **47**, 412 (1982)

[219] C. Leforestier, R. H. Bisseling, C. Cerjan, M. D. Feit, R. Friesner et al., A comparison of different propagation schemes for the time dependent Schrödinger equation, *Journal of Computational Physics* **94**, 59 (1991)

[220] A. Askar and A. S. Cakmak, Explicit integration method for the time-dependent Schrodinger equation for collision problems, *The Journal of Chemical Physics* **68**, 2794 (1978)

[221] T. F. Chan, D. Lee and L. Shen, Stable Explicit Schemes for Equations of the Schrodinger Type, *SIAM Journal on Numerical Analysis* **23**, 274 (1986)

[222] E. W. Weisstein, http://mathworld.wolfram.com/HermitePolynomial.html